



School of Pharmacy and Pharmaceutical Sciences

Developing a 3D bio-printed human skin model

A thesis submitted for the degree of

Doctor of Philosophy (PhD)

by

Ahmad Moukachar

June 2021



Abstract

Unravelling the pathophysiological mechanisms of skin disease relies on representative skin models. However, current laboratory skin models have acknowledged limitations which impede translation to the clinic. The need for a stratified 3D cellular co-culture with control over spatial organization to represent the complexities of human skin more realistically is therefore highly desirable. 3D bio printing has recently generated physiologically relevant human skin models (Baltazar et al. 2020). However, current bio printing technologies are typically expensive, difficult to operate, and have low customisation ability, thus hindering widespread accessibility (Ioannidis et al. 2020). Custom-built, low-cost 3D bio-printing platforms have been recently reported for the production of 3D cell culture and tissue models (Cubo et al. 2016a; Reid et al. 2016; Kahl et al. 2019; Ioannidis et al. 2020). It is therefore hypothesised that recreating the structure of human skin through developing a cost-effective flexible 3D bio-printing technology is feasible. The aim of this study is to develop a 3D-bio-printed human skin model using a low-cost flexible cell-printing platform.

Preliminary 2D cell culture studies were conducted using an immortalized keratinocyte cell line to establish the optimum culture conditions. Cells were maintained in a proliferative or differentiated state by varying the calcium concentration to mimic the physiological epidermal calcium gradient (Wilson et al. 2007; Bikle et al. 2012). Morphology and specific biochemical markers of differentiation were studied in each condition. A bespoke LEGO® 3D bio-printer, capable of encapsulating high cell densities and creating 2D and 3D arrangements of cells, was built in parallel to the cell culture experiments.

Cells maintained in low calcium exhibited proliferative characteristics whereas cells in higher concentrations of calcium were induced to become more differentiated, recapitulating the effect of the calcium gradient in the epidermis. The programmed custom-built LEGO® 3D bio-printer was optimized to generate high-resolution 2D and 3D complex patterns of bio-ink. Using the custom-built 3D bio-printer, the cells were successfully encapsulated in bio-material droplets and printed. Microscopy images and a cell viability assay indicated homogenous cell dispersion and high cell viability (87.5%) within the bio-printed material. Keratinocytes were successfully 3D bio-printed in an 18-layered squared lattice and imaged showing high cell viability. These initial results provide a platform for manufacture of single and mixed cell

culture populations with a defined 3D organization, akin to the human skin. The adaptability and flexibility of the custom-built LEGO® 3D bio-printer has the potential to enhance the complexity of the skin tissue model. Therefore, a first prototype of the LEGO® 3D bio-printing platform has been developed demonstrating a printing resolution at the sub-millimeter scale, providing a cost-effective novel 3D bio-printing technology for the production of human skin models.

Table of Contents

Abstract	<i>i</i>
Table of Contents	<i>iii</i>
List of Figures	<i>xi</i>
List of Tables	<i>xv</i>
Abbreviations	<i>xvi</i>
Acknowledgments	<i>xviii</i>
Chapter 1 General Introduction	<i>1</i>
1.1 The human skin	<i>4</i>
1.1.1 The epidermis	<i>5</i>
1.1.1.1 Stratum basale (viable epidermis).....	<i>9</i>
1.1.1.2 Stratum spinosum (viable epidermis)	<i>10</i>
1.1.1.3 Stratum granulosum (viable epidermis).....	<i>10</i>
1.1.1.4 Stratum corneum (non-viable epidermis).....	<i>11</i>
1.1.2 The dermal-epidermal junction	<i>12</i>
1.1.3 The dermis	<i>13</i>
1.1.4 The hypodermis	<i>15</i>
1.2 Laboratory skin models	<i>15</i>
1.2.1 2D monolayer cell culture models	<i>19</i>
1.2.2 Excised ex vivo skin models	<i>21</i>
1.2.3 3D skin models.....	<i>23</i>
1.2.3.1 Spheroid-based models.....	<i>24</i>
1.2.3.2 Human skin equivalents (HSE).....	<i>25</i>
1.3 3D bio-printing	<i>29</i>
1.3.1 Overview	<i>29</i>
1.3.1.1 Advantages of 3D bio-printing.....	<i>33</i>
1.3.1.2 Limitations of 3D bio-printing.....	<i>34</i>

1.3.2	Strategies for 3D bio-printing skin	35
1.3.2.1	Droplet-based bio-printing	36
1.3.2.2	Laser-assisted bio-printing (LAB)	38
1.3.2.3	Extrusion-based bio-printing	40
1.4	Bio-inks for 3D bio-printing	41
1.4.1	Alginate	42
1.4.1.1	General properties	43
1.4.1.2	Hydrogel crosslinking.....	44
1.4.1.2.1	Ionic crosslinking	45
1.4.1.3	Alginate degradation	46
1.4.1.4	Alginate applications in 3D bio-printing	47
1.5	Microfluidics.....	48
1.5.1	Overview	48
1.5.2	Droplet-based microfluidics.....	50
1.5.2.1	Overview.....	50
1.5.2.2	Strategies in droplet formation	51
1.5.2.2.1	T-junction	51
1.5.2.2.2	Co-flowing	52
1.5.2.2.3	Flow focusing.....	53
1.5.2.3	Applications in tissue engineering.....	54
	<i>Aim and objectives</i>	57
Chapter 2 <i>Establishing the optimal culture conditions for 2D and 3D cultures of</i>		
<i>keratinocytes 59</i>		
2.1	Introduction	60
2.2	Aim and objectives	64
2.3	Materials and Methods.....	65
2.3.1	Cell culture	65
2.3.1.1	HaCaT cell culture.....	65
2.3.1.2	Low/high-calcium media and cell culture	65
2.3.1.3	Routine subculture	67
2.3.1.4	Cryopreservation and cell culture from frozen stock.....	67

2.3.1.5	Determination of cell count	68
2.3.1.6	Cell growth curves	68
2.3.2	Imaging of cells and time-lapse acquisition.....	68
2.3.3	Human skin sample preparation and cryo-sectioning	69
2.3.4	Evaluating expression of epidermal markers in HaCaT cells	69
2.3.4.1	Western blot.....	70
2.3.4.1.1	Cell preparation for protein extraction	70
2.3.4.1.2	Preparation of lysate from cells	70
2.3.4.1.3	Bradford assay	71
2.3.4.1.4	SDS-PAGE.....	73
2.3.4.1.5	Protein transfer and blocking.....	74
2.3.4.1.6	Antibody staining.....	75
2.3.4.1.7	Protein detection.....	76
2.3.4.1.8	Blot analysis.....	76
2.3.4.2	Immunofluorescence staining	77
2.3.4.2.1	Immunohistochemistry on skin samples.....	77
2.3.4.2.2	Cell preparation and fixation.....	78
2.3.4.2.3	Cell blocking, permeabilization and antibody incubation	79
2.3.4.3	Confocal imaging	80
2.3.5	Statistics	80
2.4	Results	81
2.4.1	Effect of extracellular Ca ²⁺ changes on cell morphology	81
2.4.2	Effect of extracellular Ca ²⁺ change on cell growth rate	84
2.4.3	Effect of extracellular Ca ²⁺ changes on the biochemical properties of HaCaT cells ...	89
2.5	Discussion	93
Chapter 3 <i>Optimisation of alginate droplet production for keratinocyte encapsulation</i>		
– <i>Development of the bio-ink</i>..... 102		
3.1	Introduction	103
3.2	Aim and objectives	106
3.3	Materials and Methods.....	107
3.3.1	Preparation of microfluidic device and reagents.....	107

3.3.1.1	Microfluidic device and syringe preparation.....	107
3.3.1.2	Alginate droplet generation – Preparation of the bio-material	109
3.3.2	Alginate droplet generation imaging and analysis	111
3.3.2.1	Evaluating alginate droplet frequency production.....	113
3.3.2.2	Evaluating alginate droplet length	113
3.3.2.3	Evaluating alginate droplet gelling quality	114
3.3.2.4	Measuring alginate droplet length post-extrusion.....	115
3.3.3	Generating keratinocyte-laden alginate hydrogels – Preparation of the bio-ink.....	115
3.3.4	Determining count and viability of encapsulated keratinocytes.....	116
3.3.5	Imaging cell-laden alginate droplets – Bio-ink.....	117
3.3.5.1	Phase contrast microscopy.....	117
3.3.5.2	Confocal microscopy	117
3.3.5.3	Light sheet microscopy.....	118
3.4	Results	119
3.4.1	Preparation of the bio-material: Characterising alginate droplet formation using microfluidics	119
3.4.1.1	Investigating the relationship between alginate droplet production frequency and flow rates	119
3.4.1.2	Investigating the relationship between alginate droplet length and flow rates..	120
3.4.2	Preparation of the bio-material: Investigating the relationship between alginate droplet gelling quality, flow rates, and concentration of reagents	122
3.4.2.1	Investigating the impact of flow rate changes on alginate droplet gelling quality	122
3.4.2.2	Investigating the impact of reagent concentration changes on alginate droplet gelling quality.....	127
3.4.3	Preparation of the bio-material: Characterising the dimensions of droplets produced under optimal microfluidic parameters	131
3.4.4	Preparation of the bio-ink: Characterising microfluidic encapsulation of a keratinocyte cell line (HaCaT).....	133
3.4.4.1	Qualitative assessment of cell viability, cell dispersion, and encapsulation efficiency in the bio-ink.....	133
3.4.4.2	Quantitative assessment of cell viability upon encapsulation in the bio-ink.....	138
3.5	Discussion	140

Chapter 4	<i>Exploring the spatial capabilities of the custom-built LEGO® 3D bio-printer stage</i>	148
4.1	Introduction	149
4.2	Aim and objectives	152
4.3	Materials and Methods.....	153
4.3.1	LEGO® Bio-printer Design	153
4.3.2	LEGO® Bio-printer Build (Hardware).....	156
4.3.3	Printer Control (Software)	158
4.3.4	Measuring lateral and perpendicular movements of the LEGO® stage	161
4.3.5	Measuring the lateral speeds of the LEGO® stage.....	162
4.4	Results	163
4.4.1	Defining the LEGO® 3D bio-printer hardware dimensions	163
4.4.2	Exploring and controlling the movements (distance and speed) of the LEGO® 3D bio-printer stage	164
4.4.2.1	Measuring and controlling the lateral and perpendicular distances moved by the LEGO® 3D bio-printer stage	164
4.4.2.2	Measuring and controlling the speed of lateral movements of the LEGO® 3D bio-printer stage.....	166
4.4.3	Defining the default positions and parameters of the LEGO® 3D bio-printer stage	168
4.4.4	Modifying the default print height, starting position and speed for the LEGO® 3D bio-printer stage	169
4.4.4.1	Modifying the default print height for the LEGO® 3D bio-printer stage	170
4.4.4.2	Modifying the default starting lateral (x/y) position for the LEGO® 3D bio-printer stage	171
4.4.5	Modifying the default starting speed for the LEGO® 3D bio-printer stage	171
4.5	Discussion	172
Chapter 5	<i>Evaluating the bio-printing capabilities of the custom-built LEGO® 3D bio-printer platform</i>	177
5.1	Introduction	178
5.2	Aim and objectives	181

5.3	Materials and Methods.....	182
5.3.1	Designing a 2D pattern programme to evaluate the relationship between the LEGO® stage movements and droplet deposition printability quality	182
5.3.2	Evaluating the relationship between stage movement/speed and droplet printability quality	183
5.3.3	Preparation of a visible bio-ink for optimisation of multi-layered bio-printing	184
5.3.4	Longitudinal sectioning of bio-printed constructs and macroscale imaging	185
5.3.5	Dual bio-ink microfluidic setup	185
5.3.6	LEGO® syringe driver build and droplet production characterisation.....	186
5.4	Results	189
5.4.1	Combining the LEGO® stage and microfluidic droplet production to explore printability	189
5.4.1.1	Evaluating the relationship between the lateral movement of the LEGO® 3D bio-printer stage and droplet line continuity, packing, and spacing quality	190
5.4.1.2	Evaluating the relationship between the lateral movement of the LEGO® 3D bio-printer stage and printed droplet shapes	192
5.4.2	Programming and evaluating different 2D and 3D print patterns and shapes using the LEGO® custom-built 3D bio-printer	193
5.4.2.1	Programming and evaluating 2D print patterns using the LEGO® 3D bio-printer	195
5.4.2.2	Programming and evaluating 3D print patterns using the LEGO® 3D bio-printer	197
5.4.2.3	Programming and evaluating outline and concentric shapes using the LEGO® 3D bio-printer	201
5.4.3	Investigating the sequential print of multiple bio-inks using the LEGO® 3D bio-printer	204
5.4.4	Developing multiple nozzles for extrusion and a LEGO® syringe driver for future iterations of the LEGO® 3D bio-printer prototype	209
5.4.4.1	Developing multiple nozzle prototypes for multiple bio-ink printing using the LEGO® 3D bio-printer	209
5.4.4.2	Developing a LEGO® syringe driver prototype to create a fully integrated LEGO® 3D bio-printer	210
5.5	Discussion	213

Chapter 6	<i>Towards bio-printing a human skin model: processing and post-processing</i>	224
6.1	Introduction	225
6.2	Aims and objectives.....	228
6.3	Materials and Methods.....	229
6.3.1	Preparation for imaging multi-bio-ink 3D bio-printed structures via Lightsheet Microscopy (LSFM)	229
6.3.1.1	hTERT/Ker-CT Keratinocyte staining.....	229
6.3.1.2	Experimental 3D bio-printing of encapsulated cells	229
6.3.1.3	Light Sheet Microscopy material preparation for image acquisition.....	229
6.3.2	Alginate droplet degradation with EDTA and sodium citrate.....	232
6.3.3	Investigating the biocompatibility of the dissolved bio-material (alginate/calcium chelator solutions) on keratinocytes.....	233
6.3.4	Statistics.....	234
6.4	Results	235
6.4.1	Multi-bio-ink 3D bio-printing of a patterned structure containing live keratinocytes	235
6.4.2	Evaluating the degradation rates of a 2D patterned alginate structure using calcium chelators	238
6.4.2.1	Sodium Citrate	238
6.4.2.2	EDTA	242
6.4.2.3	Exploring the effect of pH variations on alginate degradation rates	245
6.4.3	Investigating the effect of the dissolved bio-material solution on keratinocyte viability	247
6.4.4	Evaluating the degradation rates of large 3D bio-printed structures using calcium chelators	249
6.5	Discussion	253
Chapter 7	<i>General discussion.....</i>	264
7.1	General Commentary	265
7.2	Future work and Limitations	271

References..... 276

List of Figures

Figure 1.1 3-Dimensional schematic representation of the skin.....	4
Figure 1.2 Layers and components of the human epidermis.....	7
Figure 1.3 Human skin epidermal layers and calcium distribution.....	8
Figure 1.4 Histologic photomicrograph of the human dermis.....	15
Figure 1.5 Number of publications on 3D cell cultures from 1968 – 2020.....	16
Figure 1.6 Architectural comparison of human and mouse skin.....	23
Figure 1.7 Approaches to generate reconstructed human skin equivalents (HSE).....	28
Figure 1.8 Schematic representations of commonly used 3D bio-printer platforms for tissue bio-printing.....	31
Figure 1.9 3D bio-printing steps.....	32
Figure 1.10 A histological comparison of H&E stained native skin with a 3D bio-printed human skin model.....	34
Figure 1.11 Chemical structures of G- and M-residues, and alternating sequence of G- and M-residues of alginate.....	44
Figure 1.12 Ionic cross-linking of sodium alginate through the formation of egg-box structures.....	45
Figure 1.13 Schematics demonstrating the laminar and turbulent flow regimes.....	49
Figure 1.14 Droplet formation with a T-junction.....	52
Figure 1.15 Droplet formation in a co-flow system.....	53
Figure 1.16 Droplet formation in flow-focusing devices.....	54
Figure 2.1 In vitro extracellular Ca^{2+} conditions for HaCaT cell culture mimicking the physiological non-linear Ca^{2+} gradient in the epidermis.....	66
Figure 2.2 Examples of Bovine Albumin Serum (BSA) Standard Curves.....	73
Figure 2.3 Representative scheme of the transfer sandwich setup.....	75
Figure 2.4 Morphological changes of HaCaT cells cultured in different calcium concentrations shown by phase-contrast microscopy.....	82
Figure 2.5 Morphological changes of HaCaT cells at different confluence percentages following the extracellular Ca^{2+} switch.....	83
Figure 2.6 Proliferation rate of HaCaT cells grown in very low (VLC), low (LC), normal (NC), and high (HC) calcium-containing medium.....	86

<i>Figure 2.7 Time-lapse micrographs of HaCaT cell proliferation in different Ca²⁺ conditions.</i>	<i>88</i>
<i>Figure 2.8 Expression of epidermal molecular markers of proliferation and differentiation in in vitro cultured KC and in human skin.....</i>	<i>91</i>
<i>Figure 2.9 Expression levels of Involucrin in human skin and in HaCaT cells grown in different Ca²⁺ concentrations.</i>	<i>92</i>
<i>Figure 3.1 Alginate droplet cross-linking strategies.....</i>	<i>105</i>
<i>Figure 3.2 Accessories used for the microfluidic device.</i>	<i>108</i>
<i>Figure 3.3 Alginate droplet production using a microfluidic t-junction device and infusion-only dual syringe pump.....</i>	<i>110</i>
<i>Figure 3.4 Experimental setup and analysis of microfluidic droplet generation.....</i>	<i>112</i>
<i>Figure 3.5 Schematic design of alginate droplet measurements inside a microfluidic tube.</i>	<i>114</i>
<i>Figure 3.6 Effect of flow rate change on droplet frequency.</i>	<i>120</i>
<i>Figure 3.7 Effect of flow rate change on droplet length.</i>	<i>121</i>
<i>Figure 3.8 Droplet gelling quality assessment at a constant mineral oil flow rate of 20 mL/hr and different alginate flow rates.</i>	<i>124</i>
<i>Figure 3.9 Droplet gelling quality assessment at a constant mineral oil flow rate of 10 mL/hr and different alginate flow rates.</i>	<i>125</i>
<i>Figure 3.10 Droplet gelling quality assessment at equal flow rates of alginate and mineral oil.....</i>	<i>126</i>
<i>Figure 3.11 Droplet gelling quality assessment using 0.25 mM CaCO₃ and varying levels of acetic acid.</i>	<i>128</i>
<i>Figure 3.12 Droplet gelling quality assessment using 2% alginate, 0.5 mM CaCO₃, and varying levels of acetic acid.</i>	<i>129</i>
<i>Figure 3.13 Droplet gelling quality assessment using 2% alginate, 0.75 mM CaCO₃, and varying levels of acetic acid.</i>	<i>130</i>
<i>Figure 3.14 Typical droplet morphology produced under the optimal microfluidic parameters.</i>	<i>131</i>
<i>Figure 3.15 3D bio-printing of HaCaT cell-encapsulated biomaterial.....</i>	<i>134</i>
<i>Figure 3.16 Microscopic images of bio-ink units: microfluidic generated alginate droplets with encapsulated HaCaT cells.....</i>	<i>136</i>
<i>Figure 3.17 Lightsheet microscopic images of the bio-ink units: microfluidic generated alginate droplets with Live/Dead stained encapsulated HaCaT cells.</i>	<i>137</i>
<i>Figure 3.18 Cell viability assessment 2 hours post cell-encapsulation in the bio-ink.....</i>	<i>139</i>
<i>Figure 4.1 The original LEGO® 3D printer: EV3Dprinter.....</i>	<i>155</i>
<i>Figure 4.2 The 3D bio-printer concept.</i>	<i>156</i>
<i>Figure 4.3 The adapted LEGO® 3D bio-printer.</i>	<i>158</i>

<i>Figure 4.4 Mindstorms visual programming language (VPL).</i>	160
<i>Figure 4.5 Method development for measuring the LEGO® stage lateral distances.</i>	161
<i>Figure 4.6 The dimensions of the LEGO® x/y/z stage.</i>	163
<i>Figure 4.7 Measuring and controlling the lateral movements of the LEGO® stage.</i>	166
<i>Figure 4.8 Measuring and controlling the lateral stage speed.</i>	167
<i>Figure 4.9 “Programme_Run” calibration programme.</i>	169
<i>Figure 4.10 Main menu and Parameter menu options.</i>	170
<i>Figure 5.1 The “4 parallel lines” programme sequence and resulting movement concept.</i>	183
<i>Figure 5.2 A 4 parallel lines programme designed to evaluate the relationship between LEGO® stage movements/speeds and droplet printability.</i>	184
<i>Figure 5.3 Developing strategies for multiple bio-ink bio-printing.</i>	186
<i>Figure 5.4 Developing strategies for multiple bio-ink bio-printing.</i>	188
<i>Figure 5.5 Testing the printability at a constant bio-material flow rate of 4 mL/hr when altering the speed of the lateral movements of the LEGO® stage (mm/s).</i>	191
<i>Figure 5.6 Effect of the stage speeds on printed droplet shapes extruded at equal flow rates of 4 mL/hr.</i>	193
<i>Figure 5.7 Main menu interface of the LEGO® x/y/z stage as shown on the EV3 programmable brick.</i>	194
<i>Figure 5.8 Programming sequence of the “Basic Prints”, available shapes, and a 4 parallel lines bio-print.</i>	196
<i>Figure 5.9 Schematics of the two-layered square lattice printing process and the resulting print.</i>	199
<i>Figure 5.10 The printing process of an 8-layered “Pyramid Lattice 1”.</i>	200
<i>Figure 5.11 Pyramid lattice 1 programme.</i>	201
<i>Figure 5.12 Generating 3D lattices of different shapes using the concentric function.</i>	203
<i>Figure 5.13 Multi-bio-ink bio-printing: Example of a three-bio-ink multi-layered cube lattice.</i>	206
<i>Figure 5.14 Multi-bio-ink bio-printing: Example of a dual bio-ink cube encased within a larger cube.</i>	208
<i>Figure 5.15 Preliminary data showing a multi-bio-ink construct bio-printed using the dual parallel nozzle device.</i>	210
<i>Figure 5.16 Developing LEGO® syringe drivers for alginate droplet production.</i>	211
<i>Figure 5.17 Fully integrated setup of a LEGO® 3D bio-printer connected to a dual LEGO® syringe driver.</i>	212
<i>Figure 6.1 FEP tube preparation for Light Sheet Fluorescent Microscopy imaging.</i>	231

<i>Figure 6.2 Schematic representation of blank alginate droplet degradation bio-printed in Millicell® hanging inserts.....</i>	<i>233</i>
<i>Figure 6.3 Multi-bio-ink bio-printing with encapsulated live hTERT/Ker-CT cells imaged by light-sheet microscopy.</i>	<i>237</i>
<i>Figure 6.4 Time lapse images of alginate droplet degradation at 5, 10, and 19 minutes, using 5 mM and 10 mM sodium citrate solutions.</i>	<i>239</i>
<i>Figure 6.5 Time lapse images of alginate droplet degradation at 0, 2.5, and 5 minutes, using 50mM and 100mM sodium citrate solutions.</i>	<i>240</i>
<i>Figure 6.7 Alginate droplet degradation times with varying concentrations of sodium citrate.....</i>	<i>241</i>
<i>Figure 6.6 Control time lapse images of alginate droplets exposed to dH₂O and Ca²⁺-free DMEM for 60 minutes.....</i>	<i>241</i>
<i>Figure 6.8 Time lapse images of alginate degradation at 5, 10, and 18 minutes using 1 mM and 2.5 mM EDTA solutions.</i>	<i>243</i>
<i>Figure 6.9 Time lapse images of alginate degradation at 5, 10, and 15 minutes using 4 mM and 8 mM EDTA solutions.</i>	<i>244</i>
<i>Figure 6.10 Alginate droplet degradation times with varying concentrations of EDTA.</i>	<i>245</i>
<i>Figure 6.11 Effect of pH adjustments for 4 mM and 8 mM EDTA solutions on the average alginate droplet degradation times.</i>	<i>246</i>
<i>Figure 6.12 Effect of dissolved alginate-calcium chelator solutions (bio-material) on keratinocyte viability over time.....</i>	<i>248</i>
<i>Figure 6.13 Time lapse images showing the degradation of large 3D bio-printed alginate structures using 2.5 mM EDTA and 50 mM sodium citrate solutions.....</i>	<i>251</i>
<i>Figure 6.14 Time lapse images showing the degradation of a large 3D bio-printed alginate structure using 50 mM sodium citrate.</i>	<i>252</i>

List of Tables

<i>Table 1.1 Comparison of 2D and 3D cell culture</i>	<i>17</i>
<i>Table 2.1 Lysis Buffer Recipe (100 mL) (RIPA Buffer)</i>	<i>71</i>
<i>Table 2.2 Preparation of Diluted Albumin (BSA) Standards.....</i>	<i>72</i>
<i>Table 2.3 List of primary antibodies used for Western Blot.....</i>	<i>76</i>
<i>Table 2.4 List of primary antibodies used for immunofluorescence</i>	<i>78</i>
<i>Table 2.5 List of secondary antibodies used for immunofluorescence</i>	<i>78</i>
<i>Table 2.6 BLOCK+ Solution Recipe.....</i>	<i>80</i>
<i>Table 6.1 Reports of alginate degradation approaches using sodium citrate and EDTA.</i>	<i>259</i>

Abbreviations

2D	Two-Dimensional
3D	Three-dimensional
AU	Arbitrary Unit
BSA	Bovine Serum Albumin
Ca ²⁺	Calcium Ion
CaCl ₂	Calcium Chloride
CaCO ₃	Calcium Carbonate
dH ₂ O	Distilled water
DMEM	Dulbecco's Modified Eagle Medium
DMSO	Dimethyl Sulfoxide
DOR	Degree(s) of Rotation
ECM	Extracellular Matrix
EDTA	Ethylenediaminetetraacetic acid
EGF	Epidermal Growth Factor
FBS	Foetal Bovine Serum
FEP	Fluorinated ethylene-propylene
HC	High Calcium
HSE	Human Skin Equivalent
hTERT	Human Telomerase Reverse Transcriptase
ID	Internal Diameter
INV	Involucrin
K10	Intermediate Filament Protein Cytokeratin 10 (Keratin 10)
K5	Intermediate Filament Protein Cytokeratin 5 (Keratin 5)
KBM	Keratinocyte Growth Basal Medium
LAB	Laser-based Bio-printing/Bio-printer
LC	Low Calcium
LSFM	Lightsheet Fluorescence Microscopy
MW	Molecular Weight

NC	Normal Calcium
NHEK	Primary Normal Human Epidermal Keratinocytes
OD	Outer Diameter
PBS	Phosphate Buffer Saline
PBS-T	Phosphate Buffer Saline – Tween™ 20
PET	Polyethylene Terephthalate
PS	Penicillin Streptomycin
PSG	Penicillin Streptomycin Glutamine
ROI	Region of Interest
RT	Room Temperature
SB	Stratum Basale
SC	Stratum Corneum
SCC	Squamous Cell Carcinoma
SD	Standard Deviation
SG	Stratum Granulosum
SS	Stratum Spinosum
TE	Tissue Engineering/Engineered
VLC	Very Low Calcium

Acknowledgments

First and foremost, I would like to express my sincerest gratitude to my supervisors, Dr Sion Coulman, Dr Oliver Castell, and Dr Christopher Thomas for their invaluable guidance, encouragements, support, and presence throughout my PhD. I cannot thank them enough for providing me with such a unique PhD opportunity and the chance to attend several conferences. It has been an absolute pleasure working under their leadership. I would also like to thank my PGR advisor, Pr. James Birchall, for his invaluable advice and insight during my thesis. I also thank the British Skin Foundation (BSF) for funding my project.

A huge thanks to Dr Anthony Hayes and Dr Peter Watson for teaching me how to use the Lightsheet microscopy platform, which was an invaluable tool for my research. Also, a huge thanks to Dr James Burston for providing me with the immunofluorescence protocol and materials.

I am extremely grateful to every student who chose this project as part of their internship or research curriculum. Without their valuable contributions, this project would not have progressed to where it is now.

To the members of the Birchall and Castell labs, I cannot thank them enough for their friendship and for providing such a wonderful and enjoyable environment to work in. I am sincerely grateful for their friendship and support on both the professional and personal level.

Un énorme merci à tous mes amis en France et ailleurs dans le monde pour votre soutien, pour tous les bons moments et surtout pour une amitié formidable. Merci du fond du cœur.

I would like to express my sincerest love and gratitude to my family. I am and will always be indebted to my mother, father, and brother, for their endless support, prayers, love, patience, and for continuously believing in me, even when I doubted myself. I would like to express my heartfelt gratitude to my beloved wife for her love and outstanding patience for the past year.

Above all, I would like to thank Allah for blessing me with the strength and health to complete my thesis.

This thesis is dedicated to my mother and father, who sacrificed everything for our achievements.

Chapter 1 General Introduction

● GENERAL INTRODUCTION ●

As of 2017, skin diseases were ranked as the 4th leading cause of non-fatal disease burden worldwide, contributing to 1.79% to the global burden of disease (GBD) (Karimkhani et al. 2017; Seth et al. 2017). However, due to a relatively small burden of mortality, skin diseases continue to receive little attention at the global scale (Hay et al. 2014). Whilst some skin diseases significantly reduce the quality of life for extended periods of time (e.g. psychological morbidity due to disfigurement), other skin diseases, such as skin cancers, can be life-threatening (Hay et al. 2014; Karimkhani et al. 2017; Seth et al. 2017). Additionally, chronic skin injuries with limited regenerative capacities can result in amputations and death. Investigating the physiological processes associated with skin disease, injury and regeneration is key in identifying suitable therapeutic strategies that may mitigate patients' disabilities. This relies heavily on the development and availability of relevant laboratory skin models.

The three dimensional (3D) spatial cytoarchitecture of tissues *in vivo* is crucial for physiological cell-cell and cell-microenvironment communication and function, and the skin is no exception to this dogma. Whilst 2D monolayer cell culture has provided a valuable tool for cell behavioural studies over the years, it has also paved the way to create more complex 3D reconstructed skin models. Thus, researchers have been developing 3D human skin equivalents (HSE) using innovative methods for clinical and research purposes for more than three decades (Sugihara et al. 1991; Szymański et al. 2020). From the establishment of keratinocyte culture in 2D more than 40 years ago to the development of full-thickness reconstructed skin models *in vitro*, HSE have made tremendous leaps in generating relevant models that mimic the *in vivo* microanatomy and the physiology of the skin. Applications of HSE include skin replacements, grafts, pharmaceutical, biomedical studies, and cosmetic purposes (Guiraud et al. 2014; Szymański et al. 2020). Additionally, there are a few studies focused on developing diseased models, such as melanoma or psoriasis, in the aim to investigate interactions between diseased and healthy cells (Donetti et al. 2020). Despite these advances, recapitulating the complexity of the skin anatomy remains challenging and is yet to be achieved.

Amongst the different methods for HSE development, 3D bio-printing has made the furthest advances in generating physiologically and anatomically relevant skin models (Yan et al. 2018). Nonetheless, the limited accessibility of commercially available bio-printers

● GENERAL INTRODUCTION ●

continues to hinder potential progress in biological research (Okubo et al. 2019). In this study, a versatile and bespoke 3D bio-printing platform was built, capable of producing a variety of 2D/3D structures with high spatial control. This was achieved by building a low-cost LEGO® x/y/z programmable stage combined with a t-junction microfluidic droplet dispensing device, allowing for precise geometrical positioning of viable keratinocyte-encapsulated alginate droplets. The LEGO® 3D bio-printer is also capable of printing complex multi-layered tissue-like structures with distinct layers, potentially mimicking biological micro and macrostructures of the skin.

1.1 The human skin

The skin is the largest organ of the human body accounting for 15% of the total body mass in adults. It is organized into a complex and elaborate multi-layered structure consisting predominantly of two layers : the **epidermis** and the **dermis** (McGrath and Uitto 2010; Kolarsick et al. 2011) (**Figure 1.1**). The skin also rests on a fatty layer called the hypodermis, also known as the subcutaneous tissue. Various other appendages present in the skin include sweat glands, hair follicles, blood vessels and nerves. The natural compartmentalization of different cell types interacting with each other along with the presence of multiple accessory appendages provide the skin with many vital functions involved in maintaining body homeostasis. Some of these functions include acting as a protective barrier against external assailants and infections, preventing excessive water loss, thermoregulation, metabolic functions and immune-regulatory functions (Brohem et al. 2011; Kolarsick et al. 2011).

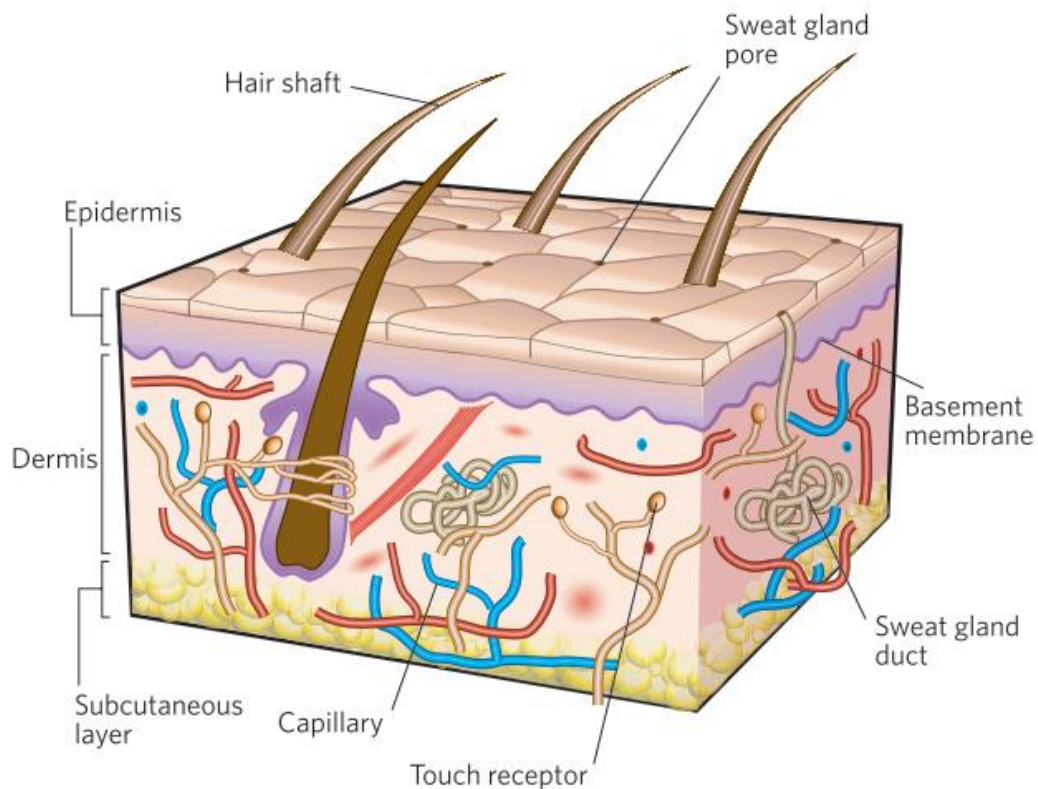


Figure 1.1 3-Dimensional schematic representation of the skin.
Taken from (MacNeil 2007).

1.1.1 The epidermis

The outer most layer of the skin, the epidermis, is a stratified keratinized squamous epithelium overlying the dermis. The epidermis is divided into four histologically distinct layers: the basal cell layer or stratum basale (SB) which lies just above the dermis, stratum spinosum (SS), stratum granulosum (SG), and the stratum corneum (SC) (the outermost layer) (**Figure 1.2**). The epidermis, composed largely of keratinocytes (keratin-producing cells), is formed by cell proliferation within the basal layer which then undergo progressive differentiation as they move upwards through the epidermis to the SC where they are terminally differentiated and enucleated. The distinct transitional stages of differentiation effect keratinocyte morphology resulting in several distinguishable layers of the epidermis (McGrath and Uitto 2010; Kolarsick et al. 2011). The human skin epidermis can therefore be considered as a two-layered structure of viable, nucleated keratinocytes underlying the non-viable outermost layer, the SC composed of corneocytes. Cells within the epidermis are linked intercellularly to adjacent and overlying cells to form a three-dimensional (3D) lattice of tightly adhering cells. This relies on several types of membrane junctions including hemidesmosomes, desmosomes, adherens junctions, gap junctions and tight junctions (**Figure 1.2 & 1.3 A**) (McGrath and Uitto 2010; Simpson et al. 2011). Apart from keratinocytes, the epidermis harbours several other cell populations, such as melanocytes which produce melanin and have a role in ultraviolet protection, Langerhans' cells which are implicated in immunological functions and the mechanoreceptor Merkel cells which are specialized in sensory functions (**Figure 1.2**) (Kolarsick et al. 2011; Zhang and Michniak-Kohn 2012).

Although the structural organization of the epidermis provides the skin with stability and an environmental barrier, its cellular components must remain highly dynamic to allow constant tissue regeneration and renewal. Keratinocytes therefore undergo a continual process of proliferation and differentiation derived from keratinocyte stem-cells present in the basal layer. The differentiation process that occurs as the cells move from the basal layer through the SS, SG to the SC is known as keratinization, a process in which cells accumulate distinct keratin filament proteins that serve as part of the cell's cytoskeleton (Kolarsick et al.

● GENERAL INTRODUCTION ●

2011). Keratinocytes at different stages of differentiation express distinct keratins which serve as markers of differentiation (**Figure 1.3 A**).

Many other proteins are expressed as keratinocytes further differentiate, including Involucrin, Fillagrin and loricrin (Tobin 2006). The process of proliferation and differentiation is highly involved in skin homeostasis and is regulated by pro-mitotic and pro-differentiation factors including calcium (Ca^{2+}) (Hennings et al. 1980; Menon et al. 1985; Tobin 2006; Bikle et al. 2012; Elsholz et al. 2014), hormones, vitamins (e.g. vitamin D3) growth factors, and cytokines (Tobin 2006; McGrath and Uitto 2010; Kolarsick et al. 2011).

Amongst different regulatory factors involved in epidermal stratification, Ca^{2+} stands out as one of the key factors involved in this process *in vivo* (Hennings et al. 1980; Menon et al. 1985; Menon and Elias 1991; Tu and Bikle 2013; Elsholz et al. 2014). The epidermal Ca^{2+} gradient has been shown to form a steep gradient in the human and mouse skin from the basal layer to the outer granular layer (or lower layer of the SC) (**Figure 1.3 A**) (Menon et al. 1985; Menon and Elias 1991; Tobin 2006). Although early studies demonstrate a steep Ca^{2+} gradient with lowest levels in the basal layer, a more recent study conducted by A. Celli *et al.* using fluorescence-lifetime imaging microscopy, revealed a more tempered Ca^{2+} gradient in the human epidermis, generating potentially novel hypotheses in Ca^{2+} -dependant epidermal regulation (**Figure 1.3 B**) (Malmqvist et al. 1983; Menon and Elias 1991; Celli et al. 2010). Although the factors involved in the formation and regulation of the Ca^{2+} gradient remain unidentified, it is widely accepted that this gradient plays a pivotal role in epidermal differentiation. The distinct organisation and presence of diverse cell types and regulatory factors within each layer of the epidermis highlights a clear relationship between structure and function.

● GENERAL INTRODUCTION ●

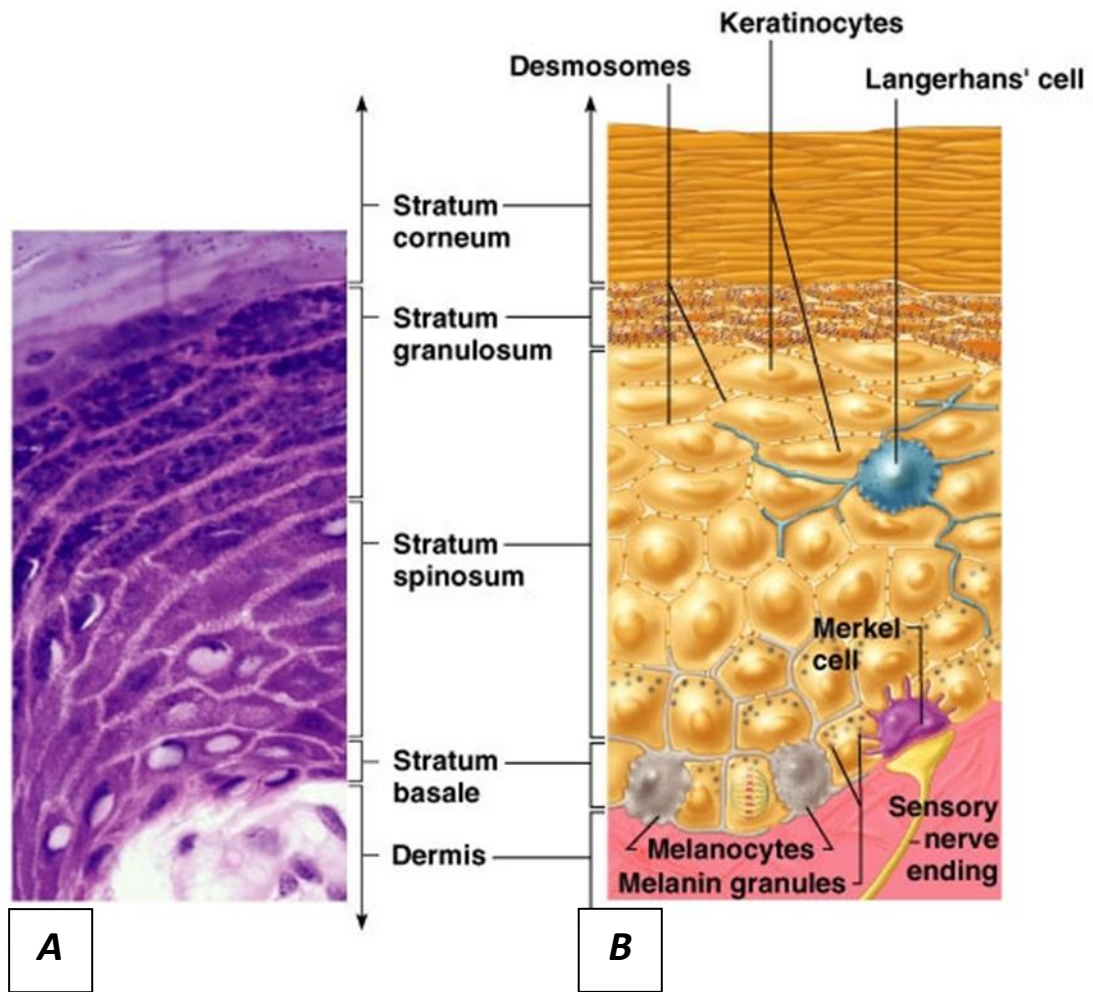


Figure 1.2 Layers and components of the human epidermis.

(A) Histologic photomicrograph of the human epidermis and (B) a schematic representation indicating the different layers and components. (Taken from Copyright © 2004 Pearson Education, Inc., publishing as Benjamin Cummings).

● GENERAL INTRODUCTION ●

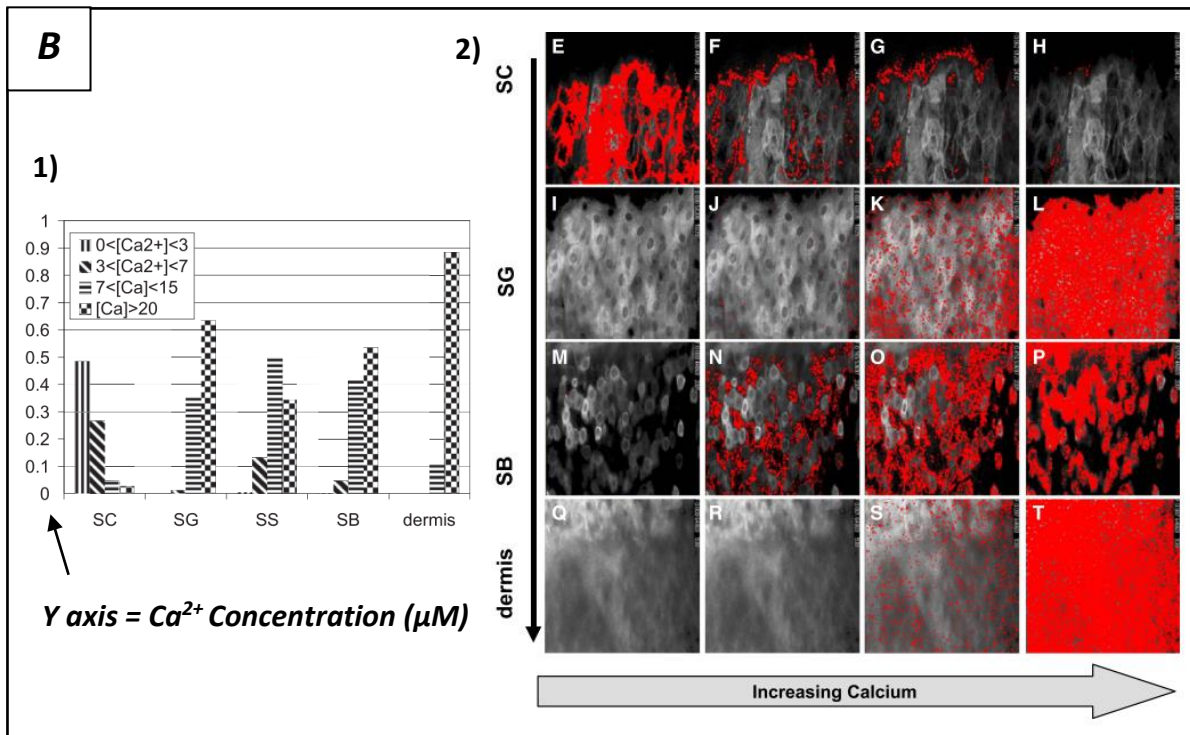
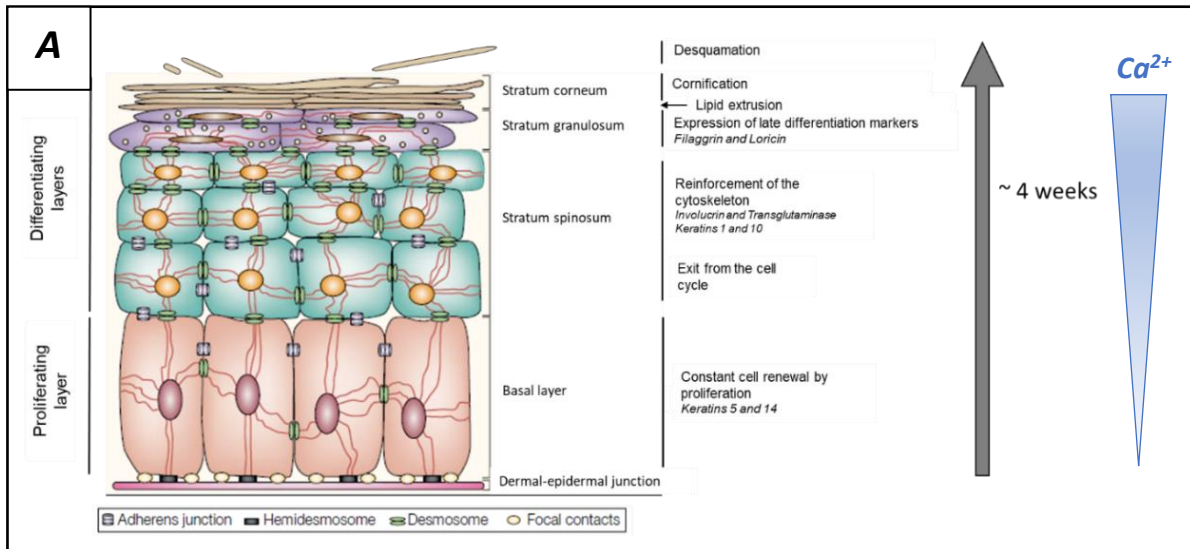


Figure 1.3 Human skin epidermal layers and calcium distribution.

(A) A schematic representation of the human skin epidermal layers with indication of the differentiation process, the expression of specific proteins and the calcium gradient. Each stage of epidermal differentiation is characterised by the expression of specific proteins. Some examples of these proteins are indicated in *italic* (Adapted from (Fuchs and Raghavan 2002)). (B) Calcium distributions in the adult human skin epidermal layers using the phasor representation of fluorescent lifetime imaging (FLIM). The intensity of Ca^{2+} is highlighted by a red colour in (2). (Images taken from (Celli et al. 2010)). (SC: Stratum Corneum, SG: Stratum Granulosum, SS: Stratum Spinosum and SBL SB).

1.1.1.1 *Stratum basale (viable epidermis)*

The stratum basale (SB), or basal layer, is a monolayer of columnar-shaped basal keratinocytes lying above the dermal-epidermal junction, which is anchored to the basement membrane via membrane junctions known as hemidesmosomes (**Figure 1.2**) (Menon 2002). Keratinocytes present in the basal layer are the only mitotically active cells within the epidermis due to the presence of highly proliferative stem cells. To maintain a stable stem-cell population and ensure constant epidermal renewal, half of the basal cells will remain behind in continual mitosis whilst the other half will progress upwards to differentiate. Proliferative keratinocytes in the SB express the keratin filaments K5 and K14 (Tobin 2006; Moll et al. 2008). Differentiation initiates only when basal keratinocytes are displaced from their hemidesmosome link on the basement membrane, allowing migration into the suprabasal layers (Tobin 2006). Ca^{2+} plays a pivotal role in the initiation of epidermal differentiation reflected by an prominent heterogeneity in the average calcium concentrations in the basal keratinocytes, contrary to early studies showing lowest Ca^{2+} levels in the basal layer (Celli et al. 2010). This heterogeneity may be key in maintaining the cells in a proliferative state whilst allowing for initiation of differentiation and transition to the SS. It takes approximately four weeks for the cell to reach the epidermal surface.

The basal layer harbours additional cell types that contribute to the epidermal function including: melanin producing melanocytes, which contribute to skin pigmentation and ensure protection against UV radiation, and Merkel-Ranvier cells which participate in the regulation of sensory reception (**Figure 1.2**) (Zhang and Michniak-Kohn 2012). Stem cells are not only present in the basal layer of the epidermis, but also in hair follicles embedded in the dermis.

Melanocytes are found within the basal layer, with a 1:10 melanocyte to keratinocyte ratio (Cichorek et al. 2013). Melanocytes form a tight relationship with keratinocytes known as the melanin-epidermal unit, whereby one melanocyte transports melanin-containing melanosomes through its extended dendrites to approximately 30 – 40 neighbouring keratinocytes (**Figure 1.2**) (Cichorek et al. 2013; Wang et al. 2016). Melanin is transferred to keratinocytes where its accumulation plays an important role in skin pigmentation and protection against UV radiation. The relationship between melanocytes and keratinocytes is

● GENERAL INTRODUCTION ●

symbiotic, as studies have shown that keratinocytes regulate melanocyte phenotype, growth kinetics, migration, adhesion and differentiation through the paracrine secretion of different growth factors (Wang et al. 2016). In addition to paracrine crosstalk, both cell populations communicate via cell-cell contact in the basal layer. Early findings demonstrated that undifferentiated basal keratinocytes control the growth of melanocytes and can prevent transformation into melanoma cells (Valyi-Nagy et al. 1993). Overall, these results indicate a tight reciprocal regulation of distinct cellular populations within the epidermis, owing to the strategic location of melanocytes in relation to the surrounding keratinocytes.

1.1.1.2 *Stratum spinosum (viable epidermis)*

The SS is a suprabasal layer overlying the SB (**Figure 1.2**). The shape of the keratinocytes in this layer change from columnar to more flattened as they migrate upwards. Keratinocytes arising from the basal layer in the SS start to gradually exit the cell cycle. They start synthesising stiffer bundles of keratin filaments, namely K1 and K10 during early stages of maturation/differentiation (Tobin 2006; Moll et al. 2008). As the cells differentiate, the keratins aggregate and form desmosomes which tightly connect to the cell membranes of adjacent keratinocytes. Ca^{2+} is again a key factor in the regulation of keratinocyte differentiation as it regulates the expression of several intercellular connections including desmosomal junctions (Tobin 2006). Several other proteins are expressed in keratinocytes present in this layer, namely Involucrin and the transglutaminase enzyme. Lamellar granules containing high amounts of lipids are present in the upper spinous layer (Kolarsick et al. 2011).

Langerhans cells, a dendritic cell, and macrophages, are present in the epidermis and dermis, but have a prominent presence in the spinous and basal layer of the epidermis. These play vital roles in both innate and adaptive immune responses of the skin (Clayton et al. 2017).

1.1.1.3 *Stratum granulosum (viable epidermis)*

The most superficial layer of the viable epidermis is the granular layer, or SG, named after the granules, that form in the cells (**Figure 1.2**). Keratinocytes in this layer mature further, accumulate more keratins and synthesise proteins and markers of late differentiation

● GENERAL INTRODUCTION ●

(e.g. profillagrin and loricrin) (Tobin 2006). Progressive keratinocyte differentiation in this layer is also accompanied by lipogenesis increase, resulting in the presence of lipid rich lamellar granules (Menon 2002). The lamellar granules reach their highest density in the upper granular layer, which then fuse with the cell membrane and eventually extrude the lipid contents into the extracellular space of the SC (Menon 2002; Tobin 2006). This process contributes to the formation of the lipid permeability barrier of the epidermis. Cell viability begins to decrease when cells of the upper granular layer undergo dissolution of cellular organelles, keratin filaments aggregation to form microfibrils, and cell membranes are replaced by a cornified envelope; this leads to the irreversible process of cornification to form terminally differentiated cells in the SC named corneocytes (Menon 2002; McGrath and Uitto 2010; Kolarsick et al. 2011). Ca^{2+} accumulation in the intercellular space of the lower/mid granular layer along with a cytosolic influx in the apical granular cells is believed to regulate and prompt the differentiation of granulocytes to corneocytes (Menon et al. 1985). Furthermore, the extruded lamellar bodies also demonstrated high amounts of Ca^{2+} (Menon et al. 1985).

1.1.1.4 *Stratum corneum (non-viable epidermis)*

The final product of the differentiation process is a non-viable cornified layer made of corneocytes, or terminally differentiated keratinocytes, and secreted contents of the lamellar bodies, known as the SC (**Figure 1.2**) (Menon 2002). The corneocytes are flat, keratin-filled cells which have lost their nuclei and are embedded in a continuous extracellular lipid matrix (Tobin 2006; Kolarsick et al. 2011). This layer provides a physical barrier due to a hard protein envelope, tight cell packing via desmosomes and a surrounding lipid matrix. Eventually the desmosomes undergo degradation and the corneocytes shed, or desquamate, which is also constantly balanced by the continual cell growth and renewal by the viable epidermis. Ca^{2+} is believed to play a pivotal role in the process of keratinocyte differentiation having significant amounts in the upper granular layer and lower corneum layer, but has very low to no presence in the upper SC (Menon et al. 1985; Tu et al. 2008; Celli et al. 2010).

Keratinocytes from the different epidermal layers have shown to express different calcium-sensing receptors (CaSR) and non-selective calcium ion channels, providing various

● GENERAL INTRODUCTION ●

strategies and entry points of Ca^{2+} into the cells. Studies have shown that detection of high Ca^{2+} levels evokes the activation of the Phosphoinositide 3-kinase (PI3K) pathway which empties the intracellular Ca^{2+} stores, and activating Ca^{2+} entry through the ion channels (Elsholz et al. 2014). This in turn allows Ca^{2+} to mediate the differentiation of keratinocytes through various strategies. Indeed, calcium-mediated keratinocyte differentiation is a multifactorial mechanism that involves both genomic and non-genomic pathways (Elsholz et al. 2014). The mobilisation of intracellular Ca^{2+} has previously been reported to increase formation of desmosomes which may in turn provide signalling events for keratinocyte differentiation (Niessen 2007). Additionally, this mobilisation has also been reported to be involved in the activation of calcium-responsive promoters, up-regulating genes involved in differentiation whilst down-regulation proliferative genes (Seo et al. 2005; Elsholz et al. 2014). The physiological balance of the epidermal Ca^{2+} gradient and type of Ca^{2+} receptors and ions found on keratinocytes from the different epidermal layers plays an essential role in maintaining a healthy epidermis and cornified protective layer.

1.1.2 The dermal-epidermal junction

The interface between the dermis and epidermis is formed by a non-cellular cutaneous basement membrane known as the dermal-epidermal junction (DEJ). The DEJ separates the two distinct compartments of the skin. It also provides epidermal-dermal adherence through junctional protein complexes found in the basal cell membranes of the epidermis called hemidesmosomes. Besides structural properties, the dermal-epidermal junction functions as a porous semi-permeable barrier allowing exchange of cells, fluids and bioactive molecules across the junction (Burgeson and Christiano 1997; Kolarsick et al. 2011).

The DEJ plays several important roles in skin homeostasis. It regulates the migration of soluble factors and invading cells between the dermis and epidermis under normal and pathological conditions (Burgeson and Christiano 1997; Breitkreutz et al. 2013). It is composed of a network of interconnecting proteins which confer this zone with important roles in morphogenesis, wound healing and skin remodelling (Burgeson and Christiano 1997; Breitkreutz et al. 2013). Furthermore, it helps to regulate growth, adhesion, and movement

● GENERAL INTRODUCTION ●

of keratinocytes and fibroblasts, by allowing the paracrine communication of both cell populations, as explained in the following section (**Section 1.1.3**).

1.1.3 The dermis

The deeper layer of the skin, the dermis, is the major component of the skin at 3-5 mm thick. It is an integrated system of fibrous connective tissue and several cell populations, including fibroblasts, mast cells, macrophages and dendritic cells (Kolarsick et al. 2011; Haniffa et al. 2015). The dermal layer provides the skin with most of its structural support, its strength and flexibility owing to the presence of a network of collagen and elastin fibrils. Although predominantly composed of connective tissue, the fibroblasts, which constitute the major cell type of the dermis, play an important role in constantly secreting and maintaining connective fibres to form a supporting extracellular matrix (ECM). Collagen is the major connective tissue component of the dermis providing stress-resistant properties to the skin, whereas elastin plays a role in maintaining elasticity (Kolarsick et al. 2011). Other structures embedded in the dermis include blood vessels, nerves, sweat glands and hair follicles (**Figure 1.1**).

The human dermis is divided into two distinct layers: a thin superficial papillary layer lying immediately beneath the epidermis, and a thick deeper reticular region (**Figure 1.4**). The papillary dermis consists of loosely arranged fine collagenous and elastic fibres, that extend toward the epidermis forming the papillae (**Figure 1.4**). The reticular region, which is attached to the hypodermis, is more acellular with a denser connective tissue meshwork than the papillary layer. Scattered fibroblasts and various other cells such as macrophages are present in both regions of the dermis. The rich dermal vasculature is provided by a deep plexus lying at the dermal-hypodermal junction and a superficial papillary plexus beneath the epidermis. This supplies the skin with nutrients and oxygen via blood vessels and capillaries extending from the plexuses into the epidermal ridges.

The role of dermal fibroblasts is not confined to ECM secretion and structural support, but also plays a pivotal role in skin homeostasis. Extensive studies have shown that a physiological intercommunication between the dermal fibroblasts and epidermal

● GENERAL INTRODUCTION ●

keratinocytes is a key factor in wound healing and maintaining skin homeostasis (Boehnke et al. 2007; Werner et al. 2007; Kolarsick et al. 2011). More specifically, fibroblasts and keratinocytes communicate through the synthesis and release of soluble factors, such as growth factors and cytokines, including keratinocyte growth factor (KGF) or interleukin-6 (IL-6), influencing their growth kinetics and activity (Werner et al. 2007). The co-culturing of dermal fibroblasts and keratinocytes in 2D monolayers and 3D organotypic skin cell cultures, demonstrated that efficient keratinocyte proliferation and differentiation highly depends on paracrine crosstalk between both cell populations (Parenteau et al. 1992; Schoop et al. 1999; Boehnke et al. 2007; Werner et al. 2007; Wang et al. 2012; Schumacher et al. 2014; Wojtowicz et al. 2014; Berning et al. 2015; Sriram et al. 2015). These results emphasise the importance of dimensionality, structural and microanatomical proximity between two distinct cell populations from different layers of the same tissue. This concept is further stressed by studies showing that papillary and reticular dermal fibroblasts differ in morphology and function, contributing differently to the ECM composition and organisation between the two dermal compartments (Sriram et al. 2015). For example, the work of Sorrell, Baber, and Caplan showed that papillary dermal fibroblasts secreted higher levels of KGF and granulocyte-macrophage colony stimulating factor (GM-CSF), than reticular fibroblasts (Sorrell et al. 2004). This would suggest that the natural proximity of the papillary layer to the epidermis is essential for growth factor production and release, to ensure physiological keratinocyte growth kinetics. Furthermore, epidermal tissue function has been previously shown to be dependent on the microenvironment composition (Boehnke et al. 2007).

Whilst the dermis is commonly known as a structural compartment of the skin, wound healing studies have revealed a far more diverse and complex role (Werner et al. 2007). In fact, dermal fibroblasts and ECM play pivotal roles in maintaining healthy skin physiology and promoting cutaneous wound healing, owing to the tissue-specific architecture. The specific dimensionality and cellular arrangements found in tissues are critical for normal homeostasis (Knight and Przyborski 2015; Ryan et al. 2016; Marcom 2017).

● GENERAL INTRODUCTION ●

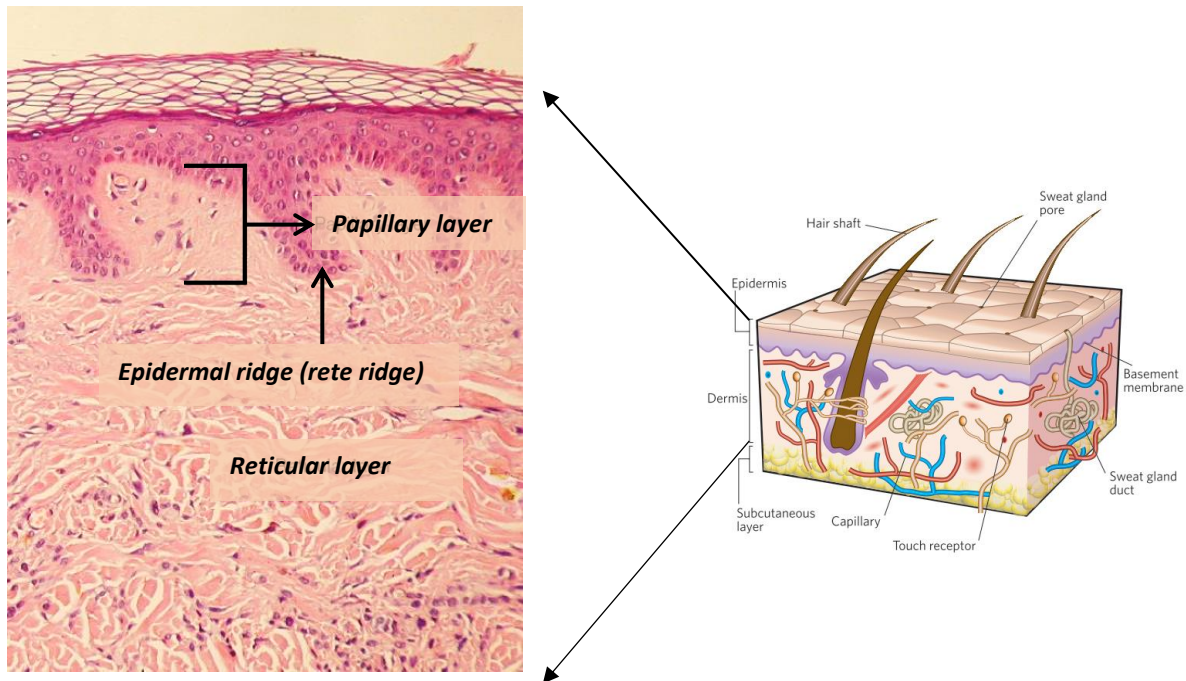


Figure 1.4 Histologic photomicrograph of the human dermis.

The dermis consists of the papillary layer and reticular layer. Adapted from (MacNeil 2007) and (OpenStax, Anatomy and Physiology, Layers of the Skin).

1.1.4 The hypodermis

The hypodermis, or the subcutaneous tissue, is a fatty layer underlying the skin which binds it to the bones and muscles. The hypodermis consists primarily of adipose tissue and blood vessels embedded in a loose connective tissue comprised of collagenous fibres (**Figure 1.1**). Although not strictly part of the skin, this layer functions as a storehouse of energy and fat, and provides insulation and cushioning of the body (Kolarsick et al. 2011).

1.2 Laboratory skin models

Cell and tissue culture models are paramount research tools in investigating mechanisms underlying tissue and organ physiology, pathophysiology, drug response, improving precision in drug discovery, and the development of tissue engineering (TE) (Vertrees et al. 2009). Traditionally, cell culture models isolate and grow cells on a flat surface, outside a living organism, in an effort to recapture biological processes that occur *in vivo* in

● GENERAL INTRODUCTION ●

order to investigate skin biology and pathophysiology. It is undeniable that traditional 2D monolayer cell culture systems contributed to countless breakthroughs in fundamental biology and biomedical research over the years (Jensen and Teng 2020). Despite this, scientists have acknowledged the limitations of growing cells in an oversimplified 2D physical and chemical environment (Baker and Chen 2012; Jensen and Teng 2020).

Cells grown in a 2D environment do not accurately recapture the complex 3D *in vivo* architecture and possible cell-cell and cell-microenvironment interplay. The lack of an ECM, 3D cell-cell contact, 3D cellular morphology, cellular polarity, appropriate proximity between heterogenous cell populations, and vasculature, has generated scepticism around interpretable physiological responses observed in 2D cell culture (Duval et al. 2017; Langhans 2018). Indeed, an extensive body of studies has demonstrated drawbacks and unreliability of 2D culture models regarding several vital characteristics, including drug efficacy prediction or drug sensitivity, gene and protein expression, response to stimuli, cell differentiation, morphology, and growth kinetics (Duval et al. 2017; Arezou Teimouri et al. 2018; Hoarau-Véchet et al. 2018; Jensen and Teng 2020). Recognising the limitations of a 2D environment, has stimulated a range of 3D cell culture methods, (**Figure 1.5**) (Baker and Chen 2012; Anton et al. 2015; Kapałczyńska et al. 2016; Arezou Teimouri et al. 2018; Jensen and Teng 2020; Mapanao and Voliani 2020). A table comparing 2D and 3D cell culture methods is shown in **Table 1.1**.

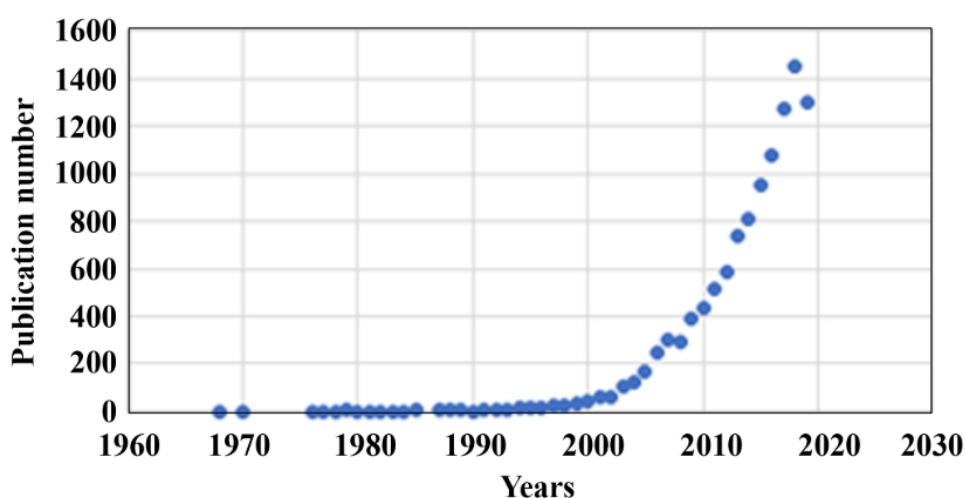


Figure 1.5 Number of publications on 3D cell cultures from 1968 – 2020.
Taken from (Jensen and Teng 2020).

● GENERAL INTRODUCTION ●

Type of culture	2D	3D
Time of culture formation	Within minutes to 24 hours	From a few days to several weeks
Culture quality	High reproducibility, long-term culture, simplicity in culture, accessible interpretation.	Lower reproducibility, difficult to interpret
<i>In vivo</i> relevance	Lacks the natural structure of tissue in 3D	Closely replicates the 3D anatomy and micro-anatomy
Cells interaction	Deprived of cell-cell and cell-ECM interactions, no <i>in vivo</i> -like microenvironment and no “niches”	Improved interactions of cell-cell and cell-ECM environment, possibility to produce environmental “niches”
Cell characteristics	Loss of natural cellular morphology /polarity and cell division; divergence from natural phenotype	Relatively well-preserved morphology/polarity and way of division; relatively well conserved phenotype
Access to nutrition and compounds	Unlimited access to oxygen, nutrients, metabolites and signalling molecules	Variable access to oxygen, nutrients, metabolites and signalling molecules (depending on size)
Molecular mechanisms	Changes in gene expression, mRNA splicing, topology, and biochemistry of cells	Expression of genes, splicing, topology and biochemistry of cells similar to <i>in vivo</i>
Cost of maintaining culture	Low-cost, widely accessible, and commercially available	More demanding in materials, more expensive, time-consuming.

Table 1.1 Comparison of 2D and 3D cell culture
Adapted from (Kapałczyńska et al. 2016).

Much of the knowledge surrounding the skin’s biological function, pathogenesis mechanisms, and microanatomy, stemmed from the continual development of 2D and 3D skin cell culture methods, and 3D TE *in vitro* skin models over the past 4 decades (Prunieras et al. 1976; Bell et al. 1981; Arezou Teimouri et al. 2018). The gradual improvement of laboratory skin cell culture models over the years has allowed expansion of not only the understanding of fundamental biological processes, but also to generate laboratory grown skin substitutes for skin defect replacements and wound healing (Coulomb and Dubertret 2002). Indeed, a key factor that has driven scientists’ interest in improving keratinocyte cultivation *in vitro* was the need for epidermal transplantation for skin defects, recognised by Billingham and Reynolds in 1953 (Billingham and Reynolds 1953). Twenty years later, Rheinwald and Green significantly improved keratinocyte culture methods, allowing for serial cultivation, resulting in the first stratified colonies of human keratinocytes or “epidermal sheets” (Rheinwald and Green 1975; Rheinwald and Green 1977). It was not long after, that the first cultured epidermal sheet autograft, combined with a dermal allograft, were

● GENERAL INTRODUCTION ●

fabricated *in vitro* and successfully grafted onto a burn victim (Cuono et al. 1986). This was a pivotal time for skin biology as these preliminary studies paved the way for improved 2D skin cell culture techniques and demonstrated the potential of 3D TE skin development. Early studies showed that whilst 2D monolayer skin cell culture development was initially aimed for non-clinical use, it rapidly developed into clinical practical applications for tissue substitution (Green et al. 1979). Complete reconstruction of the skin *in vitro* by culturing keratinocytes, fibroblasts, and preadipocytes onto a collagen matrix, was reported in 1991, demonstrating micro-anatomically relevant full thickness skin tissue model, i.e., consisting of an epidermis, dermis, and hypodermis (Sugihara et al. 1991). This provided a promising platform for both clinical practice and model system to study skin diseases. One year later, Parenteau et al. demonstrated that TE skin models can also mimic several *in vivo* physiological processes, like establishing a functional barrier, further evidencing its potential for *in vitro* non-clinical research (Parenteau et al. 1992). In the following years, the incorporation of different cell types and appendages, such as Langerhans cells, melanocytes, melanoma cells, endothelial cells, and pilosebaceous units, resulted in increasingly relevant healthy and diseased models (Archambault et al. 1995; Régnier et al. 1997; Michel et al. 1999; Meier et al. 2000). In the past few years, skin TE has become more standardised due to technical advances in scaffold-based systems and 3D culture strategies, as evidenced from high numbers of commercially available TE skin systems (Zhang and Michniak-Kohn 2012; Randall et al. 2018; Roger et al. 2019). Finally, the advent of 3D bio-printing in the 21st century is currently setting a new standard for the generation of increasingly relevant skin tissue models (Baltazar et al. 2020).

Despite notable efforts, skin models that faithfully recapture the physiological complexity and architecture of the human skin are still lacking. This is crucial for the development of skin replacements, drug testing, disease modelling, and circumventing animal testing and models (MacNeil 2007). Limiting factors in current established models are generally associated to the difficulty in incorporation of ancillary appendages, immune cells, functional vasculature, and pigmentation (Chau et al. 2013; Groeber et al. 2016; Min et al. 2017; Boyce and Lalley 2018). Furthermore, the absence of standardised methodologies can lead to increased inter-laboratory variability and decreased reproducibility in skin structure recapitulation (Roger et al. 2019). Current skin models are therefore considered

● GENERAL INTRODUCTION ●

oversimplified and can result in functionally aberrant *in vitro* tissue models. Therefore, it is important to maintain efforts to develop models that closely resemble the skin microanatomy and subsequently physiological functions. However, this relies on the ability to grow skin cells in 3D biomimetic environments and precisely position cells and extracellular matrix (ECM) in defined locations, akin to the native tissue structure. Indeed, it is widely acknowledged that physiological functions of tissues and organs heavily rely on their native microarchitecture and cellular localisation, such as the stratified and layered epidermis (Lee et al. 2009), rete ridge topography at the dermal-epidermal junction (Kumamoto et al. 2018) or hepatic lobules found in liver (Ma et al. 2016).

Established laboratory skin models *in vitro* are broadly categorised into 2D and 3D skin cell culture models (Arezou Teimouri et al. 2018). While 2D monolayer cell culture models involve growing skin cells (mostly keratinocytes or fibroblasts) in a flat environment, 3D models consist of culturing skin cells in a 3D environment, which are currently categorised in spheroid-based models, human skin equivalents, or organ-on-a-chip models (Klicks et al. 2017).

1.2.1 2D monolayer cell culture models

2D cell cultures involve growing cells in a two-dimensional flat environment as monolayers. Cells grown in 2D monolayers will typically adhere to the plastic flat surface and contact neighbouring cells solely at their periphery. To ensure high cell viability and division outside an organism, cells require a strictly controlled environment *in vitro*. This typically includes a cell-specific culture medium containing essential amino acids, vitamins, buffering systems, growth factors etc., incubations at 37°C with a CO₂ level at 5%, and sterile culture hoods.

Optimisation of keratinocyte isolation, expansion and culture conditions was reported nearly 50 years ago (Rheinwald and Green 1975; Prunieras et al. 1976). Providing a robust 2D *in vitro* keratinocyte model was a pre-requirement in expanding knowledge on skin physiology and pathophysiology. To this day, 2D cell culture of healthy and malignant skin cells is the most widely used method to model skin biology and pathogenesis mechanisms in

● GENERAL INTRODUCTION ●

laboratories. Typical 2D skin cell cultures involves growing and maintaining keratinocytes or fibroblasts, the major cell populations found in the epidermis and dermis, respectively. However, many studies have also reported the cell culture of other cell types found in the skin, such as melanocytes and melanoma cells (Valyi-Nagy et al. 1993; Golan et al. 2015; Kodet et al. 2015). 2D skin cell cultures have provided researchers with extensive knowledge of gene expression patterns and molecular mechanisms involved in skin function and pathologies over the years (Golan et al. 2015; Wang et al. 2016; Colombo et al. 2017). Monolayer cell cultures provide a simple, flexible, and cost-effective model to monitor cell responses to various mediators, inducing factors, or treatments. Furthermore, this is facilitated by the flexibility in altering the culture medium composition. For example, much of the understanding surrounding the role of Ca^{2+} in epidermal differentiation was achieved through growing keratinocytes in culture medium with varying Ca^{2+} concentrations (Hennings et al. 1980; Lemaître et al. 2004; Wilson et al. 2007; Micallef et al. 2008). Hence, Ca^{2+} is routinely used as a pro-differentiating factor to maintain keratinocytes in proliferative basal-like or differentiated phenotypes, mimicking the different levels of differentiation found in the epidermis (Wilson et al. 2007; Colombo et al. 2017). In addition to these studies, 2D monolayer cultures have also contributed to the understanding of cell-cell crosstalk in both healthy and diseased models. Indeed studies have shown that melanocyte division, proliferation, growth, migration, and differentiation are tightly regulated by keratinocyte-melanocyte crosstalk, through 2D co-culture models (Wang et al. 2016). In a diseased co-culture model, melanoma cells have been shown to influence the differentiation pattern of keratinocytes (Kodet et al. 2015). In 1975, Rheinwald et al. showed a significant increase in keratinocyte proliferation when co-cultured in presence of 3T3 mouse embryonic fibroblasts (Rheinwald and Green 1975). This was later confirmed in 2012 by Wang et al., who demonstrated enhanced wound healing when both cell types were co-cultured (Wang et al. 2012).

2D skin monolayer cell culture provides several advantages, including, simple culturing methods, rapid monitoring, inexpensiveness, and extensive knowledge serving as comparative analysis. However, 2D skin cell culture does not recapitulate the complexity of the 3D skin tissue architecture and lacks presence of other cells, structures, and extracellular milieu, all which are vital for representative culture conditions (Knight and Przyborski 2015).

● GENERAL INTRODUCTION ●

Under such simplified conditions, cell-cell and cell-ECM communication, biochemical and mechanical signalling, and spatial organization are lost (Gibot et al. 2013). This in turn can significantly influence the physiological responses and sensitivity to drug and dermatocytotoxic testing. Indeed, a study demonstrated that keratinocytes cultured in 3D showed a decrease of 50% in cell loss compared to 2D cultures, when exposed to cytotoxic agents (Sun et al. 2006).

1.2.2 Excised *ex vivo* skin models

Excised human skin models are obtained by removal of a specific tissue from a subject following a surgical procedure, such as mastectomy, breast reduction, or abdominoplasty (Ng et al. 2009; Ranamukhaarachchi et al. 2016). Excised human skin models provide a representative 3D model of the skin which closely reflects *in vivo* responses, and can also be cultured in laboratories (Yang et al. 2015; Abd et al. 2016). This model has been previously used to investigate drug delivery systems, fungal infections, and testing of topical products for bioequivalence assessment (Coulman et al. 2009; Franz et al. 2009; Abd et al. 2016; Corzo-León et al. 2019). However, evaluation of skin permeation for targeted transdermal drug delivery or derma-toxicological assessments are the most common experiments conducted on excised human skin models, due to their resemblance to their *in vivo* counterparts (Coulman et al. 2009; Franz et al. 2009; Yang et al. 2015; Abd et al. 2016). Although excised human skin maintains its 3D structural integrity, this model has some key limitations. Generally, availability of healthy excised human skin samples is low and diseased skin biopsies even less readily available (Abd et al. 2016). Inter-subject variability, due to different ages and pigmentation, is another drawback which may contribute to inconsistent results (Franz et al. 2009; Abd et al. 2016). Furthermore, excised tissue is known to have a limited viable lifetime which restricts extended studies. The removal of the tissue from a vascularised and innervated *in vivo* environment can also contribute to a loss of essential functions. Finally, the infrastructure, equipment, and procedures required to comply with the human tissue act and ensure safe and ethical use of human tissue is associated with practical restrictions that also hinder the use of excised human tissue in some laboratories.

● GENERAL INTRODUCTION ●

A lack of readily available excised human skin biopsies has driven researchers to rely on animal *ex vivo* for experimentation. The most common animal skin models used as alternatives include pig, rodent, and snake skin (Kerimoğlu and Şahbaz 2018). Studies have shown that pig skin architecture, thickness, hair-follicle density, and permeability are similar to human skin (Abd et al. 2016). Rodents provide a more readily and cheaper alternative to pig skin models. Amongst rodents, rat skin showed the best resemblance to human skin architecture (Abd et al. 2016). However, permeation studies revealed high permeability of rat skin compared to human skin.

Access to, and availability of, diseased human biopsies is significantly lower than healthy samples. Therefore, *ex vivo* animal models for skin diseases have been widely developed to study prevalent skin diseases such as melanoma, psoriasis, atopic dermatitis, squamous cell carcinoma (SCC), and basal cell carcinoma (BCC) (Elias et al. 2008; Singh et al. 2015; Filocamo et al. 2016; Roszbach et al. 2016; Schröder et al. 2016). Mouse is the most common model used to study common skin cancers. The key advantage is the capacity to genetically manipulate one or several genes of interest to stimulate tumorigenesis in the skin, whilst maintaining a physiological lymph system and peripheral circulation. Conditional and inducible transgenic mouse models allow fine controlled gene expression or knock-out in specific tissues. Transgenic animal models have been specifically developed against BCC, SCC and melanoma (Khavari 2006; Avci et al. 2013). Alternatively, regenerated transgenic human skin for specific cancer drivers can also be grafted in immune-deficient mice and monitored for cancer-like structure development (Khavari 2006; Avci et al. 2013). However, several limitations of mouse models of skin disease exist. Mouse skin is inherently different from the human skin in terms of architecture, biochemical signalling, biomechanics, cell profile, cellular spatial organization, immunology and genetics (**Figure 1.6**) (Khavari 2006; Avci et al. 2013). For example, whilst the human epidermis is comprised of 6 – 10 layers with a >100 µm thickness, mouse epidermis contains only 3 layers at <25 µm thickness (Khavari 2006). The process of cancer development between mice and humans differ in several ways: whereas most human skin tumours arise in the epithelia, most murine tumours occur in the form of non-epithelial cancers (Khavari 2006). It is also more desirable to find alternatives to animal

● GENERAL INTRODUCTION ●

models to study disease progression in the scientific research, as described by the National Centre for the Replacement Refinement and Reduction of Animals in Research (NC3Rs).

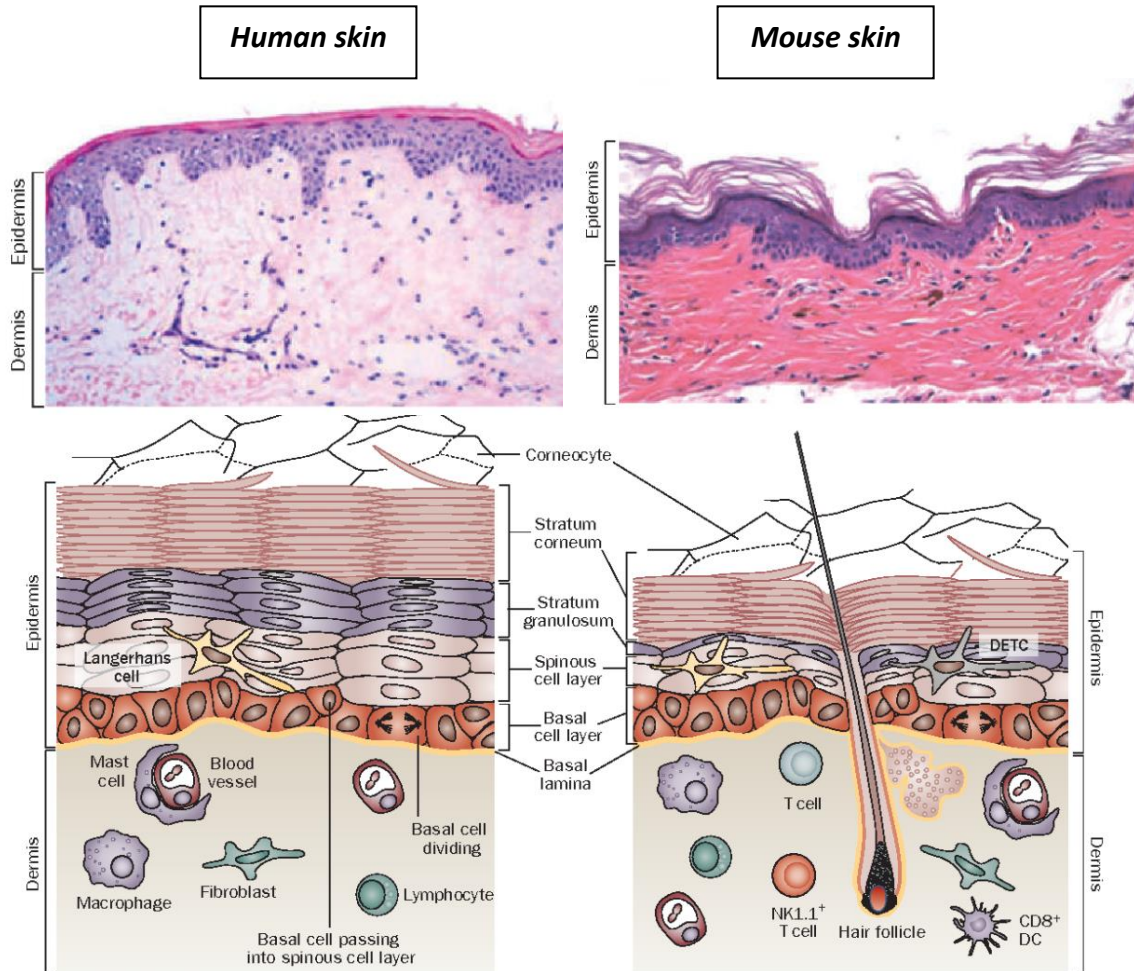


Figure 1.6 Architectural comparison of human and mouse skin.
Taken from (Wagner et al. 2010).

1.2.3 3D skin models

3D skin modelling involves the culture of skin cells in systems that mimic the *in vivo* 3D environment, which aims to achieve one or more of the following: (1) produce and retain microarchitectural similarities to the *in vivo* skin, (2) recapitulate important physiological mechanisms and respond physiologically to various stimuli and the surrounding environment, and (3) represent a diseased model, when necessary. Subsequently, the produced models can be evaluated for their relevance by direct comparison to the established knowledge

● GENERAL INTRODUCTION ●

surrounding the native skin function and architecture. Strategies to develop 3D skin cell cultures depend heavily on the study aim (Klicks et al. 2017). Ongoing development of 3D skin cell cultures, like other tissues, stem from the extensive literature recognising a lack of architectural and physiological recapitulation in 2D monolayer cultures and animal *ex vivo* models (Klicks et al. 2017). Currently established *in vitro* 3D skin cell culture models include, spheroids, skin-on-a-chip, reconstructed human skin equivalents (HSE) or organotypic cultures, and 3D bio-printed models (Klicks et al. 2017). Spheroids and HSE will be described in more detail in the next sections and 3D bio-printed skin models will be explored in **Section 1.3.2**.

1.2.3.1 Spheroid-based models

Spheroids are spherical 3D cellular aggregates formed from one or multiple cultures (mono- or multicellular spheroids, respectively) (Pampaloni et al. 2007; Chatzinikolaidou 2016). Spheroids can be formed by using different techniques, including the hanging drop technique, ultra-low-attachment surface methods, magnetic levitation, microfluidics, scaffold-based methods, or bio-printing (Chatzinikolaidou 2016; Hoarau-Véchet et al. 2018). A main attraction of using spheroids is that scaffolds are not needed, and cells aggregate on their own, which more closely resembles the *in vivo* state. Spheroids have been established as a reliable, accessible, and cost-effective 3D culture model, specifically in the study of tumour biology and anti-cancer drug screening (Mapanao and Voliani 2020). Multicellular spheroids allow the establishment and study of cell-cell and cell-ECM interactions. Indeed, the heterogenous cell population within a single culture model has shown significant differences in growth kinetics, drug resistance, and motility when compared to 2D monolayer culture (Imamura et al. 2015).

Despite not being a popular method for skin 3D cell culture, a few studies have exhibited promising results by using spheroid-based models (Klicks et al. 2017). For example, Klicks et al. generated HaCaT spheroids using the non-adherent method (Klicks et al. 2017). The inner layer showed positive staining for Keratin 14, a marker found predominantly in the basal layer, whereas the outer layer showed Keratin 10 expression, showing a more differentiated layer. Therefore, this spheroid model exhibited typical epidermal differentiation patterns *in vitro*.

● GENERAL INTRODUCTION ●

This demonstrates the ability of keratinocytes to rearrange in a physiological pattern when cultured as spheroids. Upon co-culturing keratinocytes and melanoma cells as spheroids, each cell population formed separate spheroid units which remained attached, as opposed to mixing when cultured in a chip system (Klicks et al. 2017). In 2016, InSphero 3D Insight™ reported a spheroid skin model exhibiting outer epidermal stratified layers with the inner core composed of fibroblast and fibroblast-derived ECM, akin to the dermal layer (Ströbel et al. 2016). Generating tumour models by co-culturing keratinocytes or fibroblasts with melanoma cells using spheroids have also been reported (Marrero et al. 2009; Okochi et al. 2013; Vörsmann et al. 2013; Müller and Kulms 2018).

Spheroid production for 3D skin cell culture provide a potentially attractive model, owing to its accessibility, simplicity, cost-effectiveness, and high reproducibility. In addition to evaluating individual spheroids, studies have also combined them to other bioengineering strategies. For example, Vörsmann et al. developed a melanoma model by incorporating melanoma spheroids into reconstructed human skin equivalents, improving *in vitro* drug screening and mimicking pathophysiological functions and structure (Vörsmann et al. 2013). 3D bio-printing of endothelial and stem cell spheroids has previously been reported (Faulkner-Jones et al. 2013; Benning et al. 2018; Sasmal et al. 2018). Spheroids can also be embedded in hydrogel scaffolds to better mimic the tumour microenvironment (Hoarau-Véchet et al. 2018). Droplet-based microfluidics has also demonstrated a strong potential in generating hydrogel encapsulated cell populations tailored to form spheroids in culture (Huang et al. 2017).

1.2.3.2 Human skin equivalents (HSE)

Over the past two decades, a high demand in the development of *in vitro* tissue-engineered skin substitutes for either grafts in wound healing or *in vitro* models for research, known as reconstructed human skin equivalents (HSE) or organotypic cultures, have driven a host of innovations (Schoop et al. 1999; Carlson et al. 2008; Brohem et al. 2011; Berning et al. 2015). To this day, HSE is the most widespread and common technique to generate relevant 3D human skin models *in vitro*. HSE consist mainly of primary or immortalised keratinocytes cultured on a dermal substitute which is submerged in culture medium for 1 or 2 days, then

● GENERAL INTRODUCTION ●

lifted to the air-liquid interface for approximately two to four weeks, allowing for epidermal differentiation and stratification (Schoop et al. 1999; Ghalbzouri et al. 2008; Berning et al. 2015). The dermal substitutes can be generated from acellular biocompatible natural polymers (collagen, alginate, chitosan, fibrin, or elastin), synthetic polymers, de-epidermized dermis (DED), fibroblast-dermal equivalents or fibroblast-populated collagen matrices (Ghalbzouri et al. 2008; Xie et al. 2010; Berning et al. 2015; Kober et al. 2015; Nicholas et al. 2016). Epidermal equivalents can be generated by culturing keratinocytes on a acellular dermis or a plastic hanging insert (Niehues et al. 2018). A figure recapitulating the different approaches to generating HSE models is demonstrated in **Figure 1.7**. Additionally, full-thickness skin models have been reported by incorporating adipocytes to recapitulate the hypodermis (Sugihara et al. 1991; Huber et al. 2016). Reconstituted human full-thickness and epidermal skin equivalents provide a 3D architecture which recapitulates some biochemical, structural, and functional aspects of the human skin *in vivo*. Organotypic models of skin disease in the past two decades have focussed on melanoma, SCC, and psoriasis (Meier et al. 2000; Smalley et al. 2006; Brohem et al. 2011; Berning et al. 2015; Niehues and van den Bogaard 2018; Donetti et al. 2020).

One of the earliest 3D skin cell culture methods was developed by Leighton, through culturing tissues explants onto a sponge matrix support, allowing for culture media nutrient and oxygen diffusion (Leighton 1951; Leighton et al. 1967). This model was termed “histoculture” and could be generated from normal and cancer tissues with architectural and phenotypical resemblance to *in vivo* tissue (Hoffman 2010). Soon after, a “living skin equivalent” was produced by seeding keratinocytes on top of fibroblast-seeded collagen substrate, reported by Bell et al. (Bell et al. 1979; Bell et al. 1981). From then, a standardised method was implemented for HSE generation that allowed further development of relevant healthy models (Sugihara et al. 1991; Parenteau et al. 1992; Black et al. 1998; Lee et al. 2000).

Advances in scaffolding systems over the years has led to implementing different polymers, other than collagen, such as fibrin or the development of electrospinning for the use of the synthetic poly(D,L-lactide-co-glycolide) (PLGA) (Li et al. 2002; Kober et al. 2015). Mieremet et al. developed a human skin model for barrier-related studies by modulating collagen matrix with chitosan (Mieremet et al. 2017). Such advances in methodologies with

● GENERAL INTRODUCTION ●

an improved understanding of skin physiology have led to a significant increase in commercialised skin models (Carlson et al. 2008; Randall et al. 2018).

Despite major advances in HSE development, these models are still considered oversimplified. Current approaches of HSE rarely incorporate more than keratinocytes, cancer cells and fibroblasts, despite the complex cellular composition of the skin. The reconstructed skin model therefore loses critical cell-cell interactions and signalling events which are vital for cell differentiation and growth. Furthermore, the absence of functioning vasculature and the immune system may significantly impact physiological responses *in vitro*. However, recent studies have demonstrated immune-competent models and vascularized systems that promise to overcome such limitations (Gibot et al. 2013; Groeber et al. 2016; Pupovac et al. 2018). A considerable amount of work has resulted in widespread models developed in different labs and these models use different cell lines, scaffolds, and methodologies. This has led to lab-to-lab variabilities and the absence of standardised methods (Roger et al. 2019). For example, barrier-related studies have demonstrated that HaCaT cells do not allow for SC development in HSE models, whilst N/TERT keratinocytes do (Schoop et al. 1999; Smits et al. 2017). Hence, cell line choices depending on the study aims can highly impact the study's reliability. In skin disease models, incorporating skin cancer cells in a 3D scaffold can only ever mimic cancer and not the disease process, thus hindering investigation of the pathological mechanisms involved in the transition from healthy to diseased cells. Finally, a major limitation of available HSE methods is the loss of control in precise spatial positioning and arrangement of the cells and biomaterial, which 3D bio-printing promises to overcome (Lee et al. 2014). Lee et al. associated the challenge of incorporating immune cells in HSE to the difficulty in maintaining them in their naïve state. This is most likely due to a lack of spatial control and the ability to precisely place a specific cell population within a specific skin layer. Organotypic 3D skin models clearly present several advantages over other models as they are highly reproducible, readily accessible and mimic the *in vivo* skin structure faithfully. However, developing a representative skin model which allows high-throughput studies, higher accuracy, increased adaptability and which faithfully mimics the *in vivo* structures and disease processes is therefore highly desirable.

● GENERAL INTRODUCTION ●

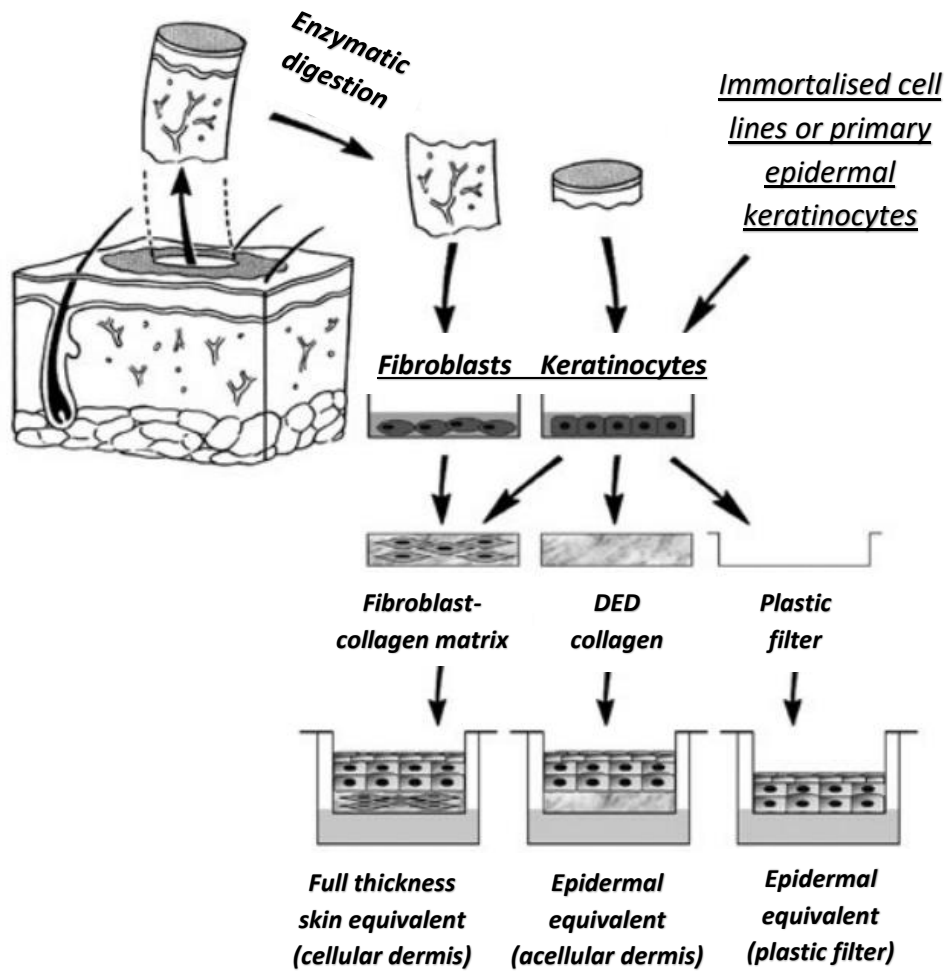


Figure 1.7 Approaches to generate reconstructed human skin equivalents (HSE). Keratinocytes are grown on a dermal substrate for a few days in submerged cell culture conditions. Keratinocytes are then lifted to the air-liquid-interface (ALI) where they are allowed to differentiate and stratify into a multi-layered epithelium for 2 to 4 weeks. Taken and adapted from (Niehues et al. 2018).

1.3 3D bio-printing

1.3.1 Overview

In the last decade, additive manufacture, more commonly referred to as 3D printing, has made significant technical advances, e.g. improved printing resolution and higher geometric accuracy both at the macroscale and microscale (Sears et al. 2016). This has been accompanied by significant reductions in the cost of goods, making it an affordable and accessible technology that has been adopted and adapted by a diverse range of industries for a range of innovative applications (Morgan et al. 2016; Graham et al. 2017; Aljohani et al. 2018). This has undoubtedly paved the path for the development of 3D bio-printing, which facilitates the layer-by-layer positioning of biocompatible material and living cells in a 3D structure akin to a functional living tissue (Billiet et al. 2014; Lee et al. 2014; England et al. 2017). 3D bio-printing platforms, therefore, have potential to establish tissue models that more closely mimic the human *in vivo* microanatomy, offering improved alternatives to 2D monolayered cell cultures, animal models, and manually engineered tissue models (Murphy and Atala 2014; Sears et al. 2016; Pedde et al. 2017; Zhang et al. 2017; Xia et al. 2018).

Several commonly used bio-printing techniques are currently available which are classified in three broad categories : micro-extrusion, laser-assisted (LAB), and droplet-based bio-printing (**Figure 1.8**) (Gudapati et al. 2016; Ng et al. 2016; Sears et al. 2016; Pedde et al. 2017; Xia et al. 2018). Each technique adapts to cell printing using different materials and deposition methods, but more importantly, all methods aim recreate tissue structure and function with minimal impact on cell viability and function. It is widely recognized that each bio-printer presents several drawbacks. Such drawbacks include complex bio-ink preparation procedures, limited structural or mechanical bio-printed integrity, restricted selection of appropriate bio-inks due to different viscosities, or printing speeds (Aljohani et al. 2018).

3D bio-printing can be described as the precise deposition of cells and/or biomaterials in a layer-by-layer or patterned fashion to generate 3D tissue-like structures. 3D bio-printing aims to replicate the tissue architecture through direct biomimicry or self-assembly.

● GENERAL INTRODUCTION ●

Biomimicry is described as the direct bio-printing of identically recapitulated tissues, including all cellular and extracellular components, whilst self-assembly relies on the bio-printed cells to self-organise and self-rearrange into a functional tissue *in vitro*. A 3D bio-printer is comprised of four major compartments: a cartesian robot (also known as the programmable x-y-z stage), a recipient (typically a Petri dish holder), nozzle or syringe, and a computer (Pereira et al. 2018). 3D bio-printed process can be divided into three essential steps: (1) pre-processing, (2) processing, and (3) post-processing (**Figure 1.9**). Pre-processing is the first step in preparation for 3D bio-printing, which involves designing a 3D model using computer software and selecting the appropriate cell populations/biomaterials to produce the bio-ink. Tissue models are commonly designed through computer-aided design and computer-aided manufacturing (CAD-CAM) tools as blueprint models and saved as digital files. Alternatively, other software that dictate stage and/or nozzle coordinates, such as visual programming language (VPL) can be used. These files are subsequently processed by the bio-printer and dictate printing paths of the nozzle or printing stage for layer-by-layer and patterned movements and deposition. The processing step is the actual bio-printing of the bio-ink in defined patterns which ideally provides optimal parameters for high cell viability, structural integrity, and high-resolution patterning. These parameters include bio-ink viscosity, printing temperature, extrusion speed, and cross-linking properties. Post-processing provides the optimal culture conditions to ensure tissue maturation, which requires regular culture supplementation and, in some cases, scaffold degradation. The matured tissue can subsequently be evaluated for microarchitectural and functional similarities to native tissues, informing on the relevance of the bio-printed tissue model.

● GENERAL INTRODUCTION ●

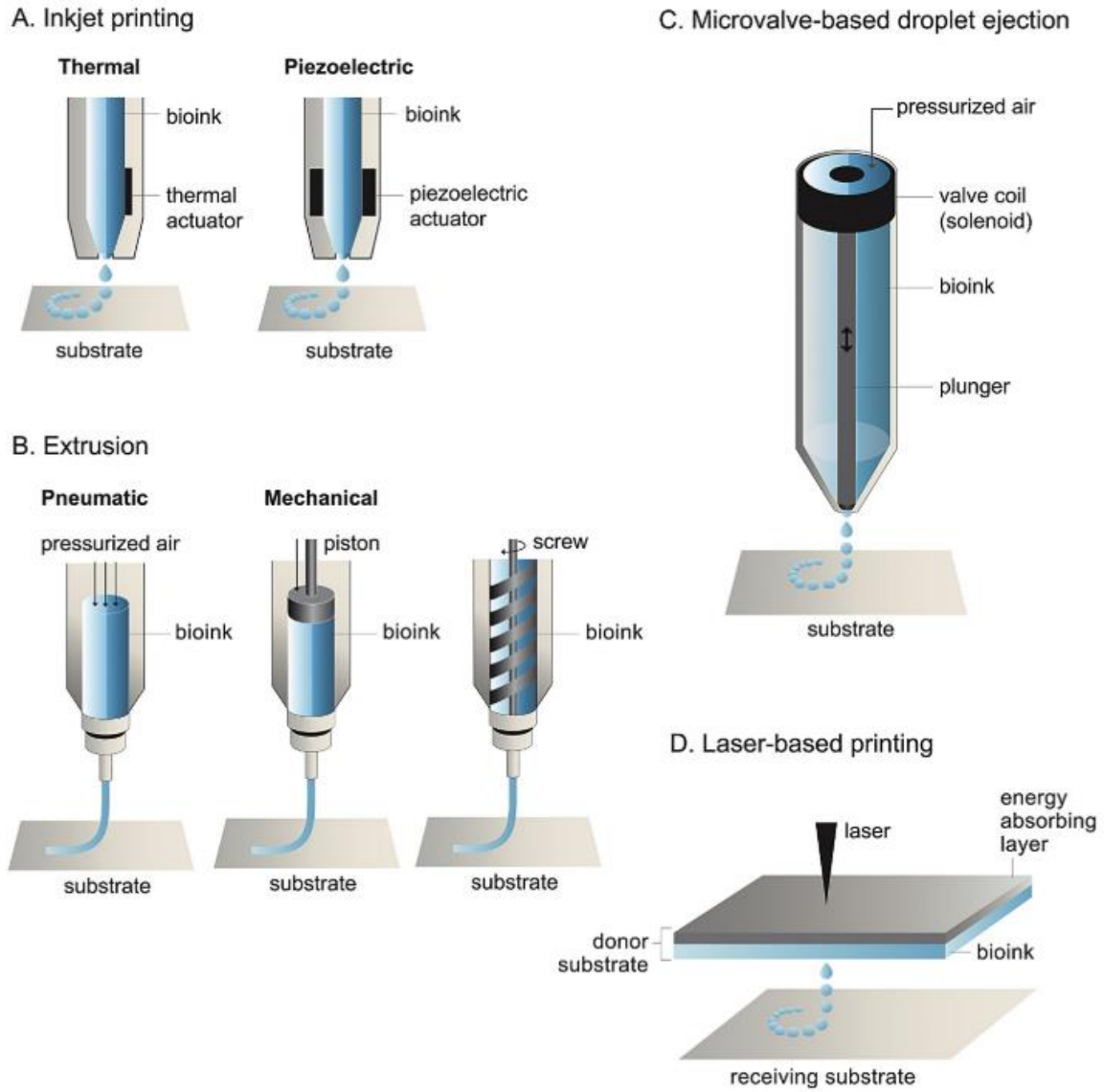


Figure 1.8 Schematic representations of commonly used 3D bio-printer platforms for tissue bio-printing.

(A) Inkjet bio-printing (droplet-based bio-printing): Bio-inks are bio-printed in forms of droplets through thermal or piezoelectric printing heads. (B) Extrusion-based bio-printing: Bio-inks are extruded in a continuous form through pneumatic or mechanical printing heads. (C) Micro-valve-based bio-printing (droplet-based bio-printing) (D) LAB: Bio-ink droplets are expelled onto a receiving substrate using a laser pulse without the use of a nozzle. Taken from (Włodarczyk-Biegun and del Campo 2017).

● GENERAL INTRODUCTION ●

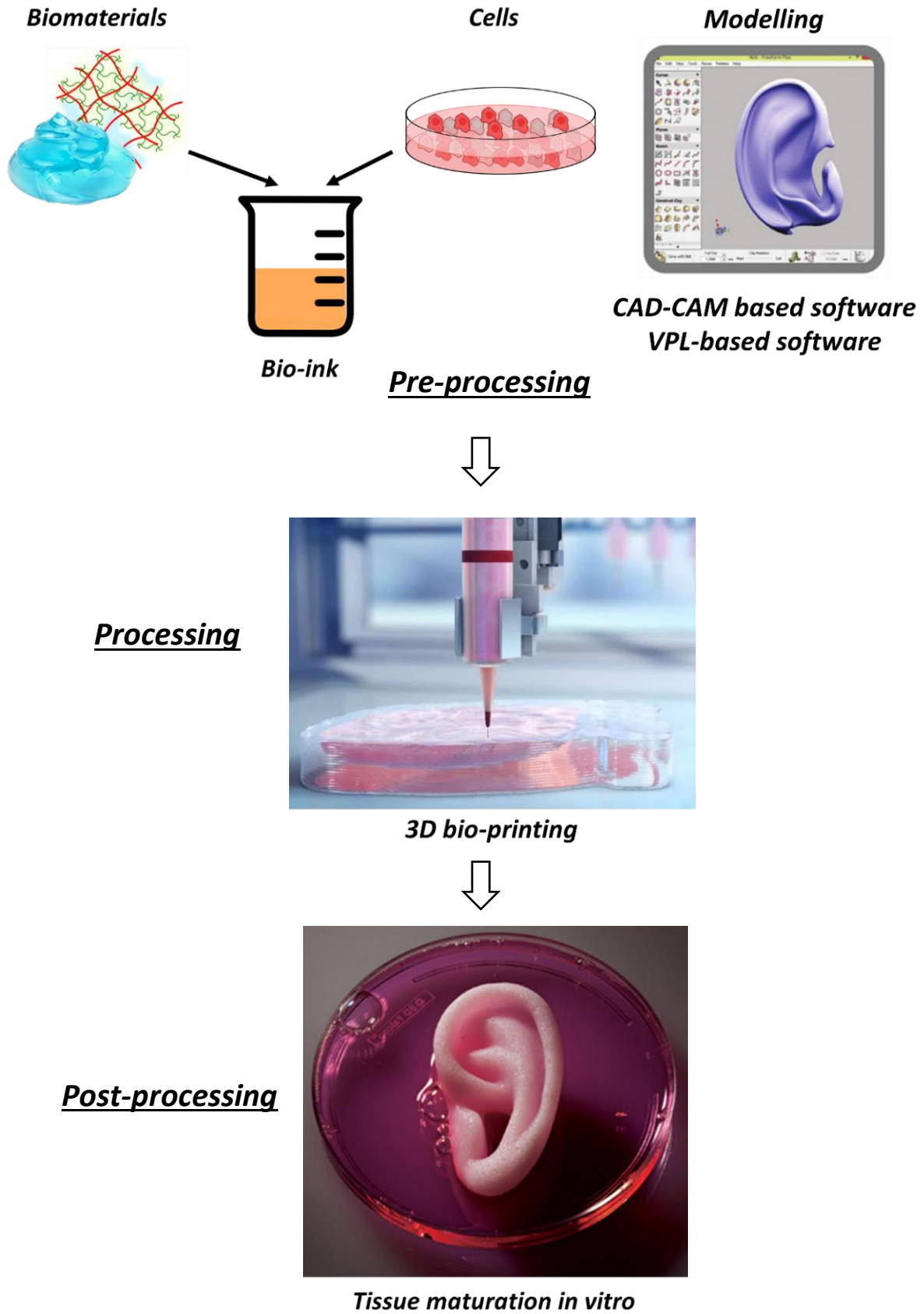


Figure 1.9 3D bio-printing steps

(1) Pre-processing, (2) processing, and (3) post-processing.

The example of a 3D bio-printed ear is shown in this figure. Taken and adapted from (Kyle et al. 2017; Sigaux et al. 2019).

1.3.1.1 Advantages of 3D bio-printing

The advantages of 3D bio-printing stem from its automated approach offering high throughput and adaptability, which overcome limitations of conventional tissue-engineered models. The capacity to precisely dispense multiple cell types, extracellular matrix (ECM) components, soluble factors and hydrogels at precise locations, while preserving high cell viability has great potential in fabricating representative 3D tissue models and organs (Lee et al. 2014; Cubo et al. 2016b; Ng et al. 2016; Zhang et al. 2017; Agarwal et al. 2020). Several laboratories have achieved the bio-printing of tissues which closely mimic the structural and biological properties of their *in vivo* counterparts. For example, Baltazar *et al.* 3D bio-printed a multi-layered vascularized human skin model containing keratinocytes, fibroblasts, pericytes, and endothelial cells, demonstrating a relatively successful recreation of the native skin tissue structure (**Figure 1.10**) (Baltazar et al. 2020). Yang *et al.* were capable of 3D bio-printing cartilage tissue with relevant mechanical properties using a mixture of alginate and collagen (Yang et al. 2018). Cell-containing hydrogels to construct human-scale tissues interspersed with an architecture of microchannels that facilitate local perfusion of nutrients and oxygen within the printed tissue have also been reported (Kolesky et al. 2016; Kim et al. 2018). The development of different 3D bio-printing technologies and strategies has allowed the construction of several anatomically representative tissues and organs including skin, cartilage, cardiac tissue, and bone (Agarwal et al. 2020). This makes 3D bio-printing a productive option for the creation of tissue constructs suitable for therapeutic studies, regenerative medicine, and can potentially be used as platforms for disease research and subsequent translation to the clinic (Gao et al. 2015; Min et al. 2017). Although still in its infancy, 3D bio-printing promises to bridge the gap between 2D/3D *in vitro* models and the *in vivo* native tissue.

● GENERAL INTRODUCTION ●

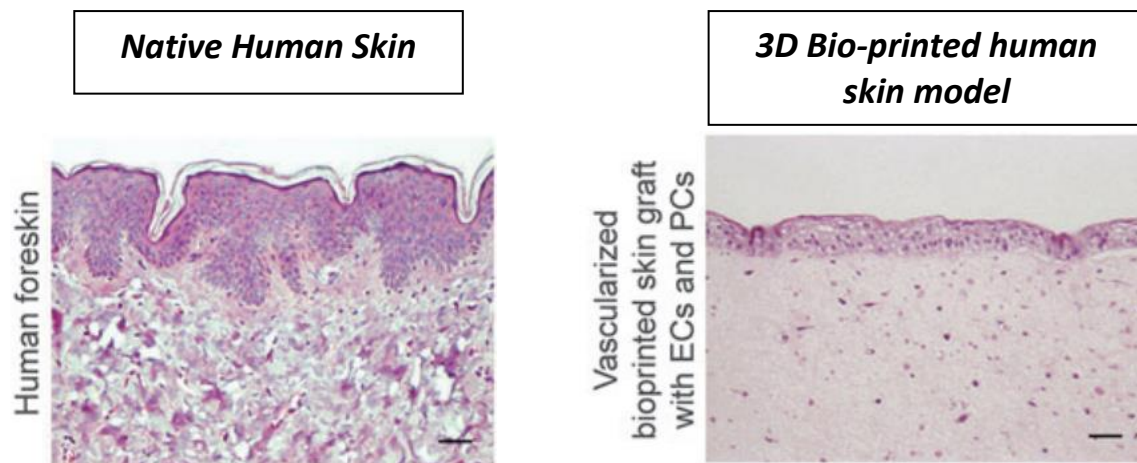


Figure 1.10 A histological comparison of H&E stained native skin with a 3D bio-printed human skin model

The 3D bio-printed human constructs included vascularisation, endothelial cells (ECs), and pericytes (PCs). Scale bar = 50 μ m. Taken from (Baltazar et al. 2020).

1.3.1.2 Limitations of 3D bio-printing

3D bio-printing is emerging as a transformative technology in both academic and industrial R&D, mirrored by an increased demand and availability of commercialised 3D bio-printers in the past few years (Pereira et al. 2018). The development of 3D bio-printing technology holds significant potential in biomedical research and regenerative medicine, making it crucial to increase its accessibility for scientific communities and educational purposes. Despite this, 3D bio-printing is still a relatively novel concept with limited accessibility and acknowledged challenges. A major limiting factor is the high cost of conventional and second-generation commercial 3D bio-printers, currently ranging between ~£2500 to ~£150 000, hindering accessibility, especially for low-resource establishments (Davide Sher, 2015, *The Top 15 Bio-printers*, Accessed on the 08/06/2021) (Pereira et al. 2018; Okubo et al. 2019). Multi-material printing and nozzle clogging due to high bio-material viscosities are also limiting factors in 3D bio-printing (Richard et al. 2020). Although there is some success in generating anatomically-relevant structures, current 3D bio-printing technologies fail to achieve nano-scale bio-printing resolutions and high uniformity arrangements, such as the native thin and highly-ordered corneal collagen fibrils (~30 nm) found in the corneal stroma (Ng et al. 2019). Fabricating complex and heterogenous 3D tissue-like structures with high accuracy requires specialised hardware and software expertise and

● GENERAL INTRODUCTION ●

maintenance. Generally, commercial 3D bio-printers' hardware and software are closed source or propriety-owned, restricting customisation, movement flexibility and modifications to generate more complex user-defined movements and structures (Kahl et al. 2019; Pakhomova et al. 2020). Additionally, conventional, and commercially available 3D bio-printers can often be sizable and cumbersome, hindering movement into a sterile environment. The increasing number and diversity of commercially available 3D bio-printers and tissue-specific bio-inks employed by different laboratories renders standardisation more difficult (Miri et al. 2019). Such limitations have driven a number of research groups to self-engineer bio-printers or modify existing 3D printers to cut costs and gain more flexibility and accessibility (Reid et al. 2016; Roehm and Madihally 2018; Schmieden et al. 2018; Bessler et al. 2019; Idaszek et al. 2019; Kahl et al. 2019; Okubo et al. 2019; Reid et al. 2019; Ioannidis et al. 2020; Sanz-Garcia et al. 2020). However, a 3D bio-printer that is: intuitive to build (hardware) and programmable (software), cost-effective, capable of multi-material bio-printing, globally accessible for parts, and can serve as both educational and scientific research tool is scarce.

1.3.2 Strategies for 3D bio-printing skin

The naturally stratified and layered architecture of the skin makes it an excellent target for 3D bio-printing technology. Furthermore, improved understanding of the skin's morphological, biochemical, and physiological properties *in vivo* over the years, has allowed the development an array of representative 3D bio-printed skin equivalents (Yan et al. 2018). Since 2009, skin bio-printing has considerably developed and demonstrated its superiority to traditional TE methods (Lee et al. 2009). The lack of precise positioning of cells and appendages in traditional HSE and spheroid methods will undoubtedly result in the absence of crucial cell-cell and cell-ECM interactions. The growing body of work involving 3D skin bio-printing presents a tremendous potential in modelling enhanced skin tissue for the study of skin biology disease development. Despite these advances, 3D skin bio-printing is currently encountering two major hurdles: (1) a general lack of accessibility of 3D bio-printer technologies due to high cost and high technical expertise required, (2) lack of standardised methodologies and culture conditions, and (3) slow progress in recapitulating the microarchitectural complexity of the skin (Velasco et al. 2018; Sanz-Garcia et al. 2020).

● GENERAL INTRODUCTION ●

Nonetheless, *in vitro* 3D skin bio-printing has been attempted using all three bio-printing technologies. The general principle of each bio-printing technology will be briefly explained in the next section, with their advantages and limitations. Furthermore, the different approaches for 3D bio-printing skin will be discussed.

1.3.2.1 Droplet-based bio-printing

Droplet-based bio-printing is classified into three technologies: Inkjet, acoustic, and micro-valve bio-printing (Gudapati et al. 2016). In inkjet bio-printing, a volume of cell-hydrogel solution is precisely jetted, in droplet forms, using thermal, piezoelectric, or electrostatic actuators (**Figure 1.8 A & C**) (Gudapati et al. 2016). Micro-valve bio-printing dispenses droplets through an electromechanical valve, using magnetic fields, whilst acoustic bio-printing uses acoustic waves to expel droplets (Gudapati et al. 2016). The main advantages of inkjet bio-printing include: fast printing speed (1 – 10K droplets/s), high resolution ($\geq 20 \mu\text{m}$ / $<1 \text{ pl}$ to $>300 \text{ pl}$ droplets), affordable, and efficient micropatterning (Gudapati et al. 2016; Sears et al. 2016; Pedde et al. 2017; Velasco et al. 2018; Miri et al. 2019). Furthermore, this method has successfully achieved the printing of soft and hard constructs including cartilage, bone, skin and nervous tissue (Pedde et al. 2017). The main limitations of the Inkjet are: limited bio-ink selection due to a narrow range of hydrogel viscosity (3 – 30 mPa.s), low cell density, nozzle clogging recurrence, low throughput rates, heat or mechanical stress induced by the different actuators which adversely affect cell viability, and cross-linking difficulties (Pedde et al. 2017; Velasco et al. 2018; Ng et al. 2019). Although micro-valve bio-printing has lower resolution than inkjet ($\geq 150 \mu\text{m}$), which is also due to a larger nozzle size, it can accommodate a wider range of bio-inks (1 – 70 mPa.s) and is easier to operate and load bio-inks (Gudapati et al. 2016; Ng et al. 2019).

Notable efforts in droplet-based bio-printing have been reported by the group of Bayley et al., using piezo electric droplet ejection for high-resolution patterned of synthetic tissues and cellular constructs (Gabriel Villar, Alexander D. Graham 2013; Graham et al. 2017; Alcinesio et al. 2020). This approach involves producing lipid-coated aqueous cell-laden droplets bio-printed in oil with controlled stage movements for precise spatial control. Droplets can subsequently adhere to one another at their interfaces to form a stable network

● GENERAL INTRODUCTION ●

of bilayers, resulting in an adhesive structure, much like a tissue construct. Despite not having printed skin models yet, Bayley et al.'s research has used a cost-effective strategy to bio-print kidney cells with high viability and proliferation (Graham et al. 2017).

Droplet-based bio-printing, using the micro-valve technology, was the first platform used to bio-print human skin, led by the work of Lee et al. in 2009 (Lee et al. 2009). They demonstrated the potential of bio-printing through precise deposition of keratinocytes and fibroblasts in collagen hydrogels, in an alternating layer-by-layer fashion. In 2014, Lee et al. extended this methodology by further optimising cell seeding density and viability to generate skin models consisting of a dermis and epidermis (Lee et al. 2014). However, this resulted in morphologically and biochemically incomplete models that did not replicate the ordered stratification and terminal differentiation of the native skin, as recognised by the authors (Lee et al. 2014). Technical modifications of the same bio-printing technology with design strategy optimisation and replacement of HaCaT cells with primary normal human epidermal keratinocytes (NHEK) in the following years, resulted in skin models with improved terminal differentiation as evidenced by the formation of a SC (Min et al. 2017). Indeed, immunohistological examination revealed distinct epidermal differentiation biomarkers and patterns that bare similarities to the native human skin (Min et al. 2017). The flexibility in spatial resolution and control of cell numbers of the 3D bio-printer is further exemplified in the work of Min et al. by producing visibly pigmented full-thickness skin models through the precise incorporation of melanocytes within the bio-printed skin constructs (Min et al. 2017).

Despite demonstrating its feasibility in 3D bio-printing skin models, it was speculated that achieving more complex models would require higher resolution patterning, which micro-valve technology lacks. In the hope to increase structural complexity of bio-printed skin models, some studies recently resorted to combining two bio-printer technologies to overcome these limitations. For example, Byoung Soo Kim et al. used a hybrid bio-printing technology termed: Integrated Composite tissue/organ Building System (ICBS), consisting of both an inkjet and extrusion dispensing modules to print a multi-layered skin model (Kim et al. 2017b; Kim et al. 2019). In another recent study, Baltazar et al. extended on the early method developed by Lee et al. using the microvalve bio-printer, and also used commercial extrusion bio-printer, Bio X bio-printer (CELLINK) (Baltazar et al. 2020). For the first time, the

● GENERAL INTRODUCTION ●

resulting bio-printed skin equivalents exhibited full maturation, full-thickness, and included a perfusable/vascularised system (Kim et al. 2019). Furthermore, biomarkers revealed striking structural similarities to native skin, including epidermal thickness, presence of rete ridges, and level of epidermal differentiation. These results indicate the importance of complexifying skin models by incorporating different skin cells with structurally and functionally relevant ECM biomaterial. Equally important is the precise spatial deposition of such materials, which can significantly enhance the microarchitecture of tissues.

Recent developments reveal that diversifying and combining 3D bio-printing platforms presents a promising route to generating enhanced morphologically and structurally complex skin equivalents, which are otherwise currently inaccessible with one platform. However, conventional 3D bio-printers are costly and complex technologies that remain relatively inaccessible (Ioannidis et al. 2020).

1.3.2.2 Laser-assisted bio-printing (LAB)

Laser-based bio-printers (LBB) consist of a laser source that generates a pulsed laser beam; a “ribbon”, which consists of a donor slide (supporting layer), energy absorbing layer, and cell-encapsulated hydrogel bio-ink; and a collector slide whereby bio-materials deposited (**Figure 1.8 D**) (Li et al. 2016b). The pulsed laser beam is absorbed by the energy-absorbing layer causing it to heat and evaporate. This process results in the expelling of the cell-laden hydrogels and precisely depositing them on a substrate. Although less commonly used, LAB supports high cell viability due to the lack of direct applied force (Pedde et al. 2017). It also provides the highest precision and resolution in contrast to other bio-printing technologies (~20 to 80 μm), and high cell densities ($> 10^8$ cells/mL) (Ng et al. 2019). A key advantage of LAB is the nozzle-free printing approach, which circumvents clogging issues. The major challenges reside in the high cost of laser sources and the complexity of the system. More importantly, the heat and pressure generated by the laser can effect cellular behaviour and long-term survival (Sears et al. 2016). Finally, LAB offers limited polymerization methods and so limits the ability to build robust constructs vertically (Gudapati et al. 2014; Sears et al. 2016). LAB has been previously reported in the fabrication of bone stem cells and cardiac tissue (Catros et al. 2011; Gaebel et al. 2011).

● GENERAL INTRODUCTION ●

Skin bio-printing user LAB has not been reported in many studies. To date, only three studies from the same research group reported the use of LAB for skin bio-printing, highlighting its low accessibility, high cost, and complexity (Koch et al. 2010; Koch et al. 2012; Michael et al. 2013). Koch et al. demonstrated the high resolution bio-printing of LAB by producing a grid structure of fibroblasts and keratinocytes at the microscale (Koch et al. 2012). Skin models were produced by bio-printing a bi-layered construct consisting of 20 layers of NIH-3T3 fibroblasts-collagen followed by 20 layers of HaCaT cells-collagen, all deposited onto a Matrigel™ sheet (a porous and permeable acellularized matrix composed of collagen and elastin, used for dermal regeneration or as a dermal substrate for *in vitro* research). The construct was cultured in submerged conditions for 10 days before tissue evaluation. The structure showed that cells retain their initial bio-printed pattern with no intermixing of cell population from the bi-layers. Furthermore, formation of adherens and gap junctions formed between skin cells demonstrated promising recapitulation of important intercellular communication functions and mechanical stability, akin to the native skin environment. This bio-printed structure was further analysed under *in vivo* conditions, when grafted on the back of nude mice using the dorsal skin fold chamber strategy (Michael et al. 2013). Despite resulting in a multi-layered epidermis with a proliferating layer mainly situated in the suprabasal layers, the overall structure was thinner and the differentiation process was incomplete (Michael et al. 2013). However, these discrepancies are most likely attributable to the methodology and materials used. As mentioned previously, immortalised HaCaT cells have consistently shown limitations in generating fully stratified skin models *in vitro* (Schoop et al. 1999). Furthermore, the dorsal skin fold chamber method did not allow enough time for full epidermal differentiation.

LAB has not been sufficiently exploited for skin bio-printing. However, LAB offers higher precision and printing resolution than other bio-printers, which may be advantageous for the printing and patterning of discrete microstructures such as rete ridges.

1.3.2.3 *Extrusion-based bio-printing*

Extrusion-based bio-printing utilizes pressure- or mechanical-based (piston or screw-driven) dispensers to extrude bio-inks in a continuous manner for layer-by-layer deposition (**Figure 1.8 B**) (Sears et al. 2016; Ng et al. 2019). Extrusion-based bio-printing is the most commonly used platform for tissue bio-printing owing to its affordability and practicality. Indeed, it provides higher printing speeds than Inkjet or LAB platforms, which facilitates scalability (Ozbolat and Hospodiuk 2016). Furthermore, it can accommodate hydrogels with a viscosity range of 30 mPa.s - 10⁷ mPa.s, enabling the use of a broad range of biomaterials for hard and soft tissue bio-printing (Ozbolat and Hospodiuk 2016). The main drawback of extrusion-based bio-printing is the low resolution ($\geq 200 \mu\text{m}$), making it much less accurate than the other bio-printers. Additionally, high driving pressures to extrude bio-inks through narrow nozzles can have detrimental effects on cell viability due to nozzle shear forces (Ozbolat and Hospodiuk 2016). Larger nozzles and lower pressure could overcome this limitation, but at the price of resolution and print speed. Extrusion-based bio-printing has been previously reported in several bioengineering applications, including hepatic structures, nervous tissue, skeletal muscle, cartilage, and cardiac tissue (Johnson et al. 2015; Colosi et al. 2016; Kang et al. 2016; Kang et al. 2018).

Like droplet-based bio-printing, extrusion-based bio-printing has made significant progress in skin bio-printing, as mentioned in **Section 1.3.2.1**. However, unlike the reported strategy of droplet-based bio-printing whereby several layers of cellular and acellular collagen-fibroblasts-keratinocytes are bio-printed to produce the bi-layered structure of the skin, extrusion-based bio-printing deposits the dermal layer bio-ink as one element and the epidermal bio-ink on top of it, rendering the design more practical. Pourchet et al. designed a dermal bio-ink consisting of alginate, fibrinogen, gelatine, and human fibroblasts bio-printed using a conventional extrusion-based bio-printer (Pourchet et al. 2017). The bio-printing of keratinocytes on the polymerised dermal bio-ink and subsequent ALI culture resulted in structural similarities and expression of differentiation markers to native skin with a well-formed SC and some rete ridges, demonstrating terminal differentiation and relevant physiological development (Pourchet et al. 2017). Another study reported by Cubo et al., used a custom-built extrusion-based bio-printer adapted from an affordable commercial 3D printer

● GENERAL INTRODUCTION ●

to generate bio-printed skin models based on that design (Cubo et al. 2016a). The printed dermal layer consisted of a fibrin matrix with human fibroblasts, on which human keratinocytes were printed to and allowed to differentiate at the ALI for 17 days. (Cubo et al. 2016a). Similarly, this resulted in structurally relevant skin equivalents that are deemed appropriate for clinical, commercial, and research purposes. In a recent study, Derr et al. also reported the use of an extrusion-based bio-printer adapted from an open-market 3D printer to bio-print skin equivalents structurally validated through IHC marker. Interestingly, the skin equivalents also exhibited proper barrier function (Derr et al. 2019). Achieving this level of architectural relevance with an accessible custom-built 3D bio-printer circumvents the need for costly and complex platforms when developing a bi-layered skin equivalent.

Extrusion-based bio-printers may not offer the level of resolution found in droplet-based or LAB, however, it provides a more readily available and affordable platform that is capable of generating skin models with close resemblance in microanatomy and maturation to native skin tissue.

1.4 Bio-inks for 3D bio-printing

The bio-printable material used in bio-printing is referred to as the “bio-ink”. More specifically, bio-ink is the mixture of cells dispersed in suitable bio-materials, such as hydrogels, which can be bio-printed and polymerised, to provide 3D structural support and ideally mimic the cellular microenvironment to recapitulate *in vivo* structure and function. In 3D bio-printing, bio-polymers must have suitable rheological and crosslinking properties for printing and must offer protection to the cells during the printing process (Fan et al. 2016; Morgan et al. 2016). For nutrient delivery and efficient communication between cells and the environment, bio-polymers must also allow diffusion through scalable pores (Fan and Wang 2017). They should also act as a scaffolding material to maintain structural stability of the bio-printed constructs. Finally, the bio-material should have a controllable degradation rate (Hospodiuk et al. 2017).

● GENERAL INTRODUCTION ●

Common bio-polymers used for bio-printing include synthetic polymers (e.g., poly(vinyl alcohol) (PVA), poly(ϵ -caprolactone) (PCL), or poly(acrylic acid) (PAA)), and naturally derived hydrogels (e.g., alginate, gelatine, collagen, chitosan, and fibrin). Whilst natural bio-polymers offer a more biocompatible and structurally similar architecture to the natural ECM, they are recognised to have weak mechanical properties. Synthetic polymers on the other hand have stable mechanical properties but lack a bioactive environment (Skardal and Atala 2015; Chimene et al. 2016; Gungor-Ozkerim et al. 2018). Hence, bio-ink selection is a pivotal step in the bio-printing process, as tissue fabrication and function rely heavily on the bio-material properties. Furthermore, bio-printers have to adapt to specific bio-ink requirements, such as shear modulus, viscosities, and gelation properties. In a number of studies, researchers have combined the use of several bio-inks to generate both proper mechanical and functional properties. For example, Pourchet et al. used a bio-ink mixture of gelatine, fibrin, and alginate with dispersed skin cells. Whilst gelatine and alginate provided structural support and stability, fibrin provided cellular adhesion properties for keratinocytes differentiation, adhesion, and tissue maturation (Pourchet et al. 2017). This demonstrates the adaptability of 3D bio-printing and the potential strategies that can be utilised.

1.4.1 *Alginate*

Sodium alginate is a widely used bio-material in TE and 3D bio-printing (Anton et al. 2015; Aljohani et al. 2018). It has been specifically reported for the bio-printing of skin equivalents, due its high biocompatibility, ability to support 3D cell growth, controlled gelation, simple degradability, structural similarity to natural ECM, and low cost (Cubo et al. 2016b; Huang et al. 2016; Pourchet et al. 2017). Furthermore, alginate can be polymerised through several strategies and in different patterns, such as encapsulating microspheres, or continuous gelled filaments (Hospodiuk et al. 2017; Pourchet et al. 2017). Therefore, alginate has been selected as an appropriate bio-material in this study, for the encapsulation of keratinocytes and subsequent bio-printing of a skin model.

1.4.1.1 ***General properties***

Sodium alginate is natural polysaccharide typically extracted from brown algae (Ching et al. 2017). Alginate is composed of linear copolymers consisting of (1,4)-linked β -D-mannuronate (M) and α -L-guluronate (G) residues (**Figure 1.11**). The alginate structure can be composed of consecutive M residues, G residues, or alternating M and G residues, with a G/M ratio, molecular weight, and length of each block dependent on the source of extracted alginate (Lee and Mooney 2012; Ching et al. 2017).

Alginate ion cross-linking with divalent cations, such as Ca^{2+} , is believed to be mainly dependant on the participation of the G-blocks. Hence, alginate composition of G/M ratio, G-block length and molecular weight (MW) are important factors that influence physical properties of alginate hydrogel (Lee and Mooney 2012). High MW results in a decreased number of reactive positions available for hydrolysis degradation and greater mechanical properties. Furthermore, an increased in length of G-block and MW results in more robust, stiff, and highly viscous alginate hydrogel (Lee and Mooney 2012). The stability of the hydrogel is dictated by its mechanical properties which subsequently can affect cell phenotype and function. Hence, highly viscous alginate solutions can have detrimental effects on cells during printing due to high shear forces necessary.

Despite alginate being biocompatible, it is composed of inert monomers that lack cell-anchoring bioactive functional ligands (Lee and Mooney 2012). Therefore, cells cannot adhere to cross-linked alginate, which may result in decreased cell viability when working with adhesion-dependent cell populations. To overcome this, a bioactive ligand (e.g., arginine-glycine-aspartic acid (Arg-Gly-Asp, RGD)) sequence is chemically coupled to the alginate, providing cell-anchoring ligands for cells adhesion (RGD-modified alginate) (Lee and Mooney 2012).

● GENERAL INTRODUCTION ●

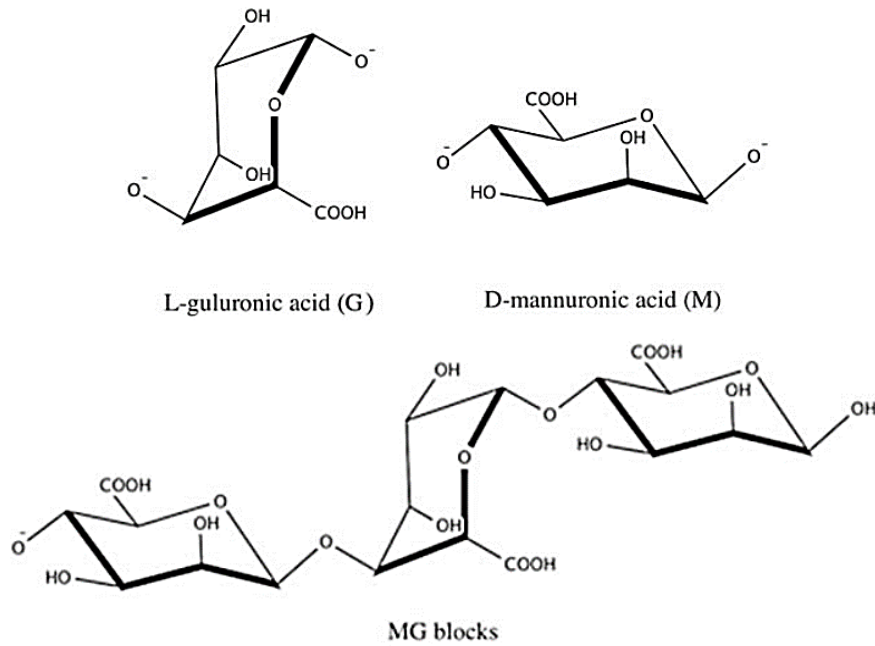


Figure 1.11 Chemical structures of G- and M-residues, and alternating sequence of G- and M-residues of alginate.

Taken from (Ching et al. 2017).

1.4.1.2 Hydrogel crosslinking

A hydrogel is composed of 3-D cross-linked hydrophilic polymers with high water content that are often biocompatible. Cross-linking strategies commonly include chemical and/or physical cross-linking. Furthermore, the physicochemical property of the hydrogel is highly dependent on the cross-linking approach used, MW, and chemical composition of the polymers (Sun and Tan 2013). The reported cross-linking strategies include ionic, covalent, thermal, and cell-cross-linking. In this thesis, only the ionic cell cross-linking approach will be discussed.

● GENERAL INTRODUCTION ●

1.4.1.2.1 Ionic crosslinking

The most common method for alginate polymerisation is ionic crosslinking, which involves combining an alginate aqueous solution with an ionic crosslinking agent, such as divalent cations (Sun and Tan 2013). As mentioned previously, it is speculated that the divalent cations bind exclusively to the G-blocks. Divalent cations allow the binding of two alginate polymer chains by forming junctions between the G-blocks of each polymer chain. This is known as the egg-box structure of cross-linking which results in a polymerised hydrogel (Figure 1.12).

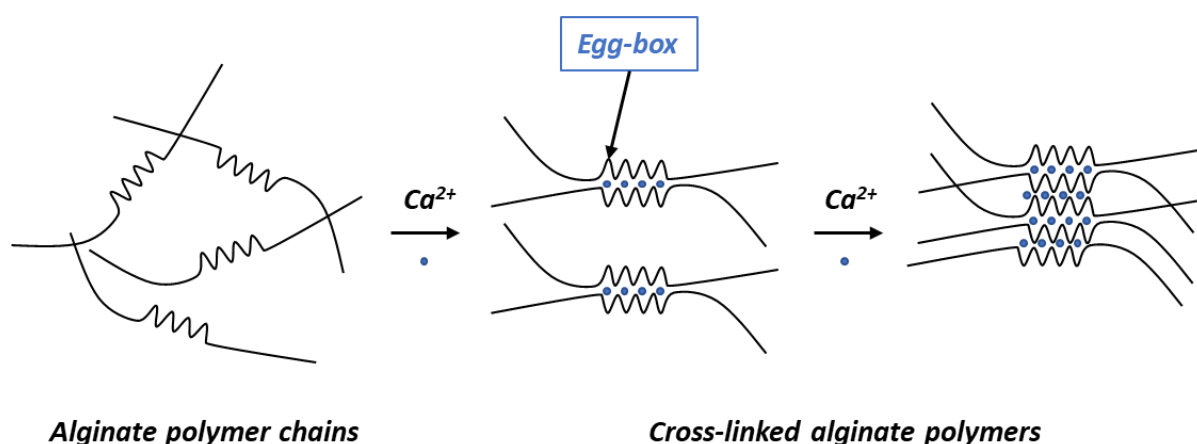


Figure 1.12 Ionic cross-linking of sodium alginate through the formation of egg-box structures.

Ca^{2+} is the most common cross-linking agent used, hence calcium chloride ($CaCl_2$), calcium carbonate ($CaCO_3$), and calcium sulfate ($CaSO_4$) are typically used as calcium salts, although $CaCl_2$ is more commonly found in studies (Sun and Tan 2013). However, the use of $CaCl_2$ generally leads to rapid and uncontrolled gelation due to its high solubility in solutions. For improved control over gelation rate, another approach, known as the internal gelation strategy, is typically used by researchers. In this method, calcium salts with low solubility, such as $CaCO_3$ or $CaSO_4$, are combined with the alginate aqueous solution, and upon pH reduction, Ca^{2+} ions are dissociated from the calcium salt, and induce alginate cross-linking, providing slower and more controlled alginate gelation rates (Lee and Mooney 2012). Slower gelation rates in a controlled manner allows for production of alginate hydrogels with more uniformity and structural stability (Lee and Mooney 2012; Sun and Tan 2013). Low soluble calcium salts, however, can result in heterogenous gelling due to the presence of undissolved salts (Utech

● GENERAL INTRODUCTION ●

et al. 2015). Calcium-chelating agents, such as ethylenediaminetetraacetic acid (EDTA), can form stable chelated complexes of Ca^{2+} -EDTA which are soluble and can be combined with an alginate solution. Using the internal gelation strategy, upon pH decrease, Ca^{2+} is liberated from the EDTA chelating complex and provokes alginate cross-linking (Utech et al. 2015).

The ionic cross-linking strategy results in limited long-term stability in physiological conditions, which occurs as a result of divalent ions release due to exchange reactions with monovalent cations (Lee and Mooney 2012). The effects of alginate gelation and gelation rates are important factors that have been shown to influence cell viability and function using different TE platforms (Gudapati et al. 2014). A study reported that a two-minute partial alginate gelation time results in an increase in cell viability after 24 hour incubation, whilst a 10 minute incubation results in a decreased cell viability due to the forming of thick hydrogels that limit nutrient delivery (Gudapati et al. 2014). Therefore, it is crucial to control these factors in TE *in vitro* models. Reports have shown that cultured alginate hydrogels generated through microfluidic means, demonstrate high stability in culture media for weeks without degradation, allowing cell proliferation and growth (Utech et al. 2015). This demonstrates that alginate hydrogel stability depends on the environment and application. Controlling the levels of Ca^{2+} for cross-linking is also important, as Ca^{2+} ions are known to play a pivotal role in signal transduction in many tissues, influencing cell differentiation (skin) and contraction (muscle cells) (Bikle et al. 2012; Kuo and Ehrlich 2015).

1.4.1.3 Alginate degradation

Alginate is an inherently non-degradable bio-polymer by mammalian cells, due to the absence of the alginase enzyme (Lee and Mooney 2012). In *in vivo*, alginate degradation is a crucial step in drug delivery systems and cell transplantation carriers and require high levels of control to avoid undesirable biological reactions, such as inefficient complete removal from the body, which results from commercial alginates with higher MW than the renal clearance threshold of kidneys (Al-Shamkhani and Duncan 1995). *In vitro* alginate degradation is less stringent and can be easily achieved by incubating polymerised alginate with calcium chelators, such as sodium citrate or EDTA (Chueh et al. 2010; Wu et al. 2016). Also, adjusting the MW of alginate can affect the degradation rate, whereby high MW results in slower degradation and low MW is faster rates (Lee and Mooney 2012). However, it is also important

● GENERAL INTRODUCTION ●

to evaluate the effect of such chelators and MW changes on cell viability and mechanical properties of the bioengineered tissue model. Furthermore, controlling the degradation rate of alginate in order that residual chains do not interfere with the tissue maturation of bioengineered models is desirable. Optimal degradation rate and strategy is strongly dependent on the bio-printed or TE shape, construct volume, and cell and tissue sensitivity to the degradation process (Wu et al. 2016). It has been previously reported that fast alginate degradation rates (~ 12 weeks) *in vivo* resulted in significantly improved bone formation after alginate cell-encapsulated implantation (Alsberg et al. 2003). An alginate-based bio-printed tissue construct containing human corneal epithelial cells was degraded over the course of 8 days using a calcium chelator, resulting in higher cell proliferation and viability in contrast to non-degraded alginate (Wu et al. 2016). Hence, alginate degradation is an important step in both *in vivo* and *in vitro* TE.

1.4.1.4 Alginate applications in 3D bio-printing

Alginate is the most popular and widely used bio-material in 3D bio-printing due to its ability to form biocompatible matrices that closely mimic the natural ECM, good printability, affordability, simple cross-linking mechanisms, structural stability, and good mechanical properties, that all ensure high cell viability, differentiation, proliferation, and tissue maturation (Yang et al. 2018). One of the major advantages of alginate as a bio-material for bio-printing is the wide range of viscosities it can come in. Indeed, as mentioned previously, 3D bio-printers are limited to a specific range of bio-ink viscosities. Alginate has been successfully used in all three major bio-printing platforms, including inkjet, LAB, and extrusion-based bio-printers (Gudapati et al. 2014; Gudapati et al. 2016; Li et al. 2016a; Ng et al. 2019). Alginate bio-printer using extrusion-based bio-printing typically entails printing the alginate solution into a pre-crosslinked form and can be subsequently soaked into a Ca^{2+} -containing solution to strengthen the cross-linking (Li et al. 2016a; Kang et al. 2018). In LAB, alginate beads are projected into CaCl_2 solutions for crosslinking, however, studies have reported that cross-linking should not exceed two minutes, as long exposure to CaCl_2 can lead to excessive stiffness and lack of oxygen and nutrient delivery to cells (Gudapati et al. 2014). Inkjet bio-printing has also utilised alginate as a cell-laden bio-material that is generated in forms of droplets and patterned shapes directly into a CaCl_2 containing pool (Xu et al. 2012).

● GENERAL INTRODUCTION ●

Despite collagen being acknowledged as the optimal ECM material for bioengineering, its poor mechanical properties and narrow range of viscosities, limits its optimisation using 3D bio-printing (Kim et al. 2011). Furthermore, collagen requires pH and temperature variations for polymerisation. For this reason, alginate has been commonly replaced collagen or been used combination with collagen to provide mechanical stability and/or a more representative ECM environment (Kim et al. 2011; Kang et al. 2018). This combination has provided a suitable bio-printing material favouring cell differentiation, proliferation, viability and phenotypic preservation *in vitro* of different cell populations, including chondrocytes, keratinocytes, fibroblasts, and epidermal progenitor cells (Kim et al. 2011; Huang et al. 2016; Yang et al. 2018).

1.5 Microfluidics

1.5.1 Overview

Microfluidics refers to the science of precisely generating, manipulating, and controlling small volumes of fluids using channels with dimensions at the microscale (Sackmann et al. 2014). Microfluidics have emerged as revolutionary technological platforms in many applications, ranging from chemical analysis, to life sciences for bioengineering, tissue engineering, 3D bio-printing, pharmaceuticals, and biomedicine (diagnostic devices and drug detection) (Hosokawa et al. 2004; Günther and Jensen 2006; Hidalgo San Jose et al. 2018; Ortseifen et al. 2020; Richard et al. 2020). Manipulation of fluids on the microscale is widely accessible using microfluidics, which are acknowledged to afford benefits such as being cost-effective, portable/practical, high-throughput, and highly customisable platforms.

The restriction of fluids to flow in micrometre sized channels involves significant changes in the physical properties of fluids, giving rise to unique and advantageous physical phenomena that differs from the macroscale. Hence, some effects become dominant in microfluidics, such as surface tension and viscous forces over gravity and inertia (normally dominant at the macroscale). This phenomenon gives rise to a laminar flow regime for the flow of a single fluid, defined as a passive and smooth movement, as opposed to a turbulent

● GENERAL INTRODUCTION ●

movement observed at the macroscale when gravity and inertia dominate (**Figure 1.13**). Microfluidics exploits this regime for passive flow of single-phase systems or monodisperse droplets in multiphase fluid streams (Sackmann et al. 2014). A laminar flow regime allows the incorporation of two or more streams that join in parallel flow without turbulent mixing, except by diffusion. This can be exploited to generate highly parallel streams of two bio-inks for 3D bio-printing extrusion, or to pattern cell cultures within the microfluidic device (Takayama et al. 1999; Costantini et al. 2017). Diffusion rates at the microscale are very high as a consequence of reduced channel dimensions and therefore diffusion distances are shorter (Damiati et al. 2018). Diffusion is defined as the rate at which molecules move from a high concentration solution to a lower concentration solution. Hence, chemical reactions can occur at a higher rate if otherwise limited by diffusion, allowing for rapid gelation of hydrogels for 3D cell culture or diffusing gradients for nutrient delivery to tissue models *in vitro* (Baker et al. 2013; Zhang et al. 2020). In microfluidics, surface tension also becomes dominant over inertial forces as a consequence of high surface area to volume ratio (SAV). Surface tension arises as a result of liquid intermolecular cohesive forces at the surface of a liquid (liquid/gas interface). In microfluidic systems, liquid/liquid interfaces of immiscible fluid flows (e.g., water and oil) is also dominated by surface tension forces between the liquid molecules, giving rise to the interfacial phenomena. This plays a pivotal role in droplet-based microfluidics.

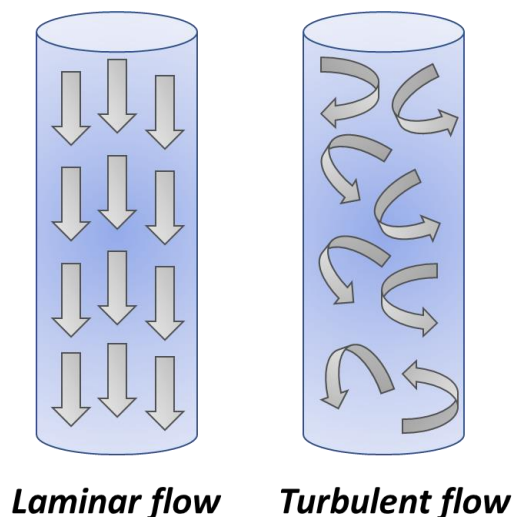


Figure 1.13 Schematics demonstrating the laminar and turbulent flow regimes.
The laminar flow regime is characterised by a passive and smooth movement of fluids, whereas turbulent flow is unpredictable and irregular on the microscale.

1.5.2 Droplet-based microfluidics

1.5.2.1 Overview

Droplet-based microfluidics offers several advantages over continuous-flow systems, whilst benefiting from the inherent advantages of microfluidic systems in general (Suea-Ngam et al. 2019). As opposed to continuous-flow systems, droplet-based microfluidics uses immiscible phases to produce discrete droplets, providing an extra level of miniaturisation. Furthermore, droplet-based microfluidics offers high droplet generation frequencies, control over droplet dimensions, high monodispersity, and the opportunity for high throughput experimentation. The ability to precisely manipulate highly monodisperse droplets with increased throughput and scalability offers an advantage over continuous extrusion. For example, this is also demonstrated by the differences in resolution between extrusion- vs. droplet-/LAB technologies. Indeed, continuous-flow extrusion adopts similar principles as extrusion-based bio-printing, which relies on the deposition of bio-inks in forms of continuous filaments. However, extrusion-based bio-printers have demonstrated low resolution in comparison to droplet-based bio-printing platforms, which rely on the precise deposition of homogenous cell-laden droplets, providing more uniformity in the bio-printed structure (Gudapati et al. 2016). Over the years, droplet-based microfluidics has demonstrated its potency in 3D cell culture, TE, and single cell analysis by encapsulating cells in a biocompatible 3D environment as microculture units (Chou et al. 2015).

Droplet-based microfluidics involves the formation and manipulation of discrete droplets using immiscible phases. Classically, an emulsion is generated by two immiscible fluids (water and oil, for example), producing droplets from one phase, known as the dispersed phase (water), as a result of the shear force applied by the continuous phase (oil) and the interfacial tension at the liquid/liquid interface (Liu et al. 2013), with the hydrophobicity/hydrophilicity of the channel wall usually determining which is the disperse and which is the continuous phase. In addition to interfacial tension, viscosity plays an important role in droplet formation and also becomes dominant at the microscale (Liu and Zhang 2009). Under microfluidic conditions, droplet formation is governed by the competition

● GENERAL INTRODUCTION ●

between the interfacial and viscous forces (Choi et al. 2007). This governs the process of droplet breakup, and heavily relies on the microfluidic device used (Chiarello et al. 2017). Droplet formation is governed by the following equation:

$$Ca = \frac{\mu V}{\sigma}$$

Equation 1.1

whereby Ca is defined as the capillary number (dimensionless quantity), μ is the viscosity, V is the velocity (flow rate), and σ is the interfacial tension between both phases (Tice et al. 2003). Generally, varying the velocity of the continuous or dispersed phase will affect the moment of droplet breakup. Typically, an increased flow rate of the continuous phase will result in a faster droplet breakup resulting in smaller droplets in the dispersed phase (Choi et al. 2007). Generating hydrophilic droplets, such as water-in-oil droplets, requires microfluidic channels with inner hydrophobic walls to avoid adhesion, allow efficient smooth flow and maximise the contact angle between the hydrophilic droplet and the hydrophobic wall surface. For this, different materials used to fabricate the microfluidic device are used, including acrylated urethane, poly(methyl methacrylate) PMMA, Polydimethylsiloxane (PDMS), glass, and Polytetrafluoroethylene (PTFE) (Mazutis et al. 2015; Sohrabi et al. 2020).

1.5.2.2 Strategies in droplet formation

1.5.2.2.1 T-junction

In the t-junction channel geometry, the dispersed and continuous phases flow through two perpendicular channels until they intersect at a junction (**Figure 1.14**) (Sohrabi et al. 2020). At the intersection, the dispersed phase enters the main channel, then shear forces applied by the continuous phase onto the dispersed phase result in the droplet breakup or pinch-off, hence generating dispersed droplets that flow into the main channel. Factors that influence the rate of droplet breakup, droplet size, and pinch-off regime are the flow rates of both dispersed and continuous phases, relative viscosities, and channel widths (Marshall and Walker 2019). For example, when Ca is high, viscous effects become dominant, resulting in

● GENERAL INTRODUCTION ●

droplet deformations, asymmetric droplet shapes, and a tendency for co-flow of both phases (**Figure 1.14 C**). On the contrary, at low Ca , the dominant surface tension minimises the interfacial area giving rise to small spherical droplets and faster droplet breakup (**Figure 1.14 B**).

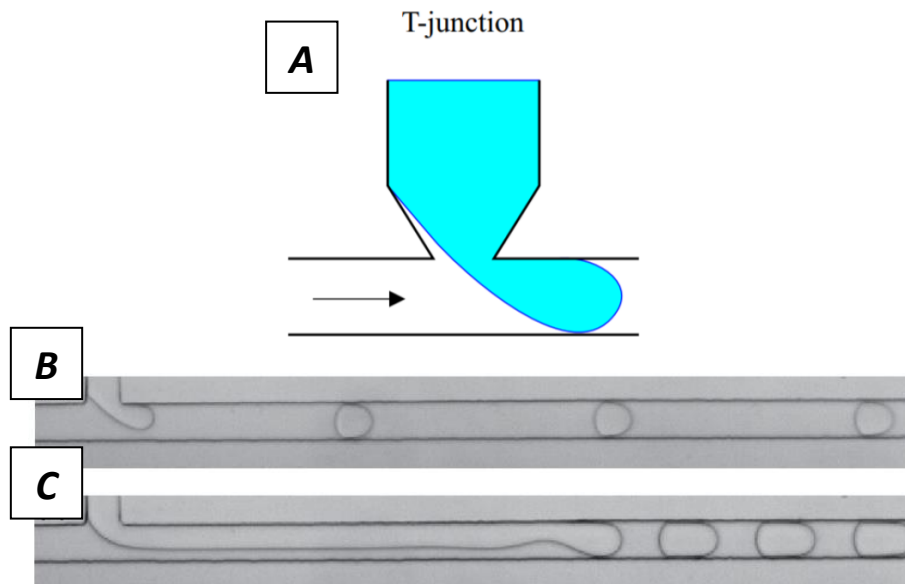


Figure 1.14 Droplet formation with a t-junction

(A) Schematic representation of droplet formation in a t-junction. (B) Example of droplet formation when Ca is low resulting in faster droplet breakup and droplet size, and (C) high Ca , resulting in slower droplet breakup. Taken from (Pit et al. 2015; Chiarello et al. 2017).

1.5.2.2.2 Co-flowing

Co-flow systems consist of an inner capillary within an outer capillary which stream fluids in the same direction in parallel (**Figure 1.15**) (Shah et al. 2008; Damiati et al. 2018). Co-flow occurs when the dispersed phase flows through the inner capillary with the continuous phase flowing in parallel through the outer capillary. This results in a coaxial flow of two fluids (**Figure 1.15**). At the intersection, the continuous phase surrounds the dispersed phase, applying shear force, resulting in the breakup of droplets. Low flow rates of both dispersed and continuous phases results in the formation of spherical droplets at the intersection (**Figure 1.15 B**). When flow rates are high, a thin stream of the dispersed phase forms with droplet breakup occurring farther downstream as smaller droplets (**Figure 1.15 C**).

• GENERAL INTRODUCTION •

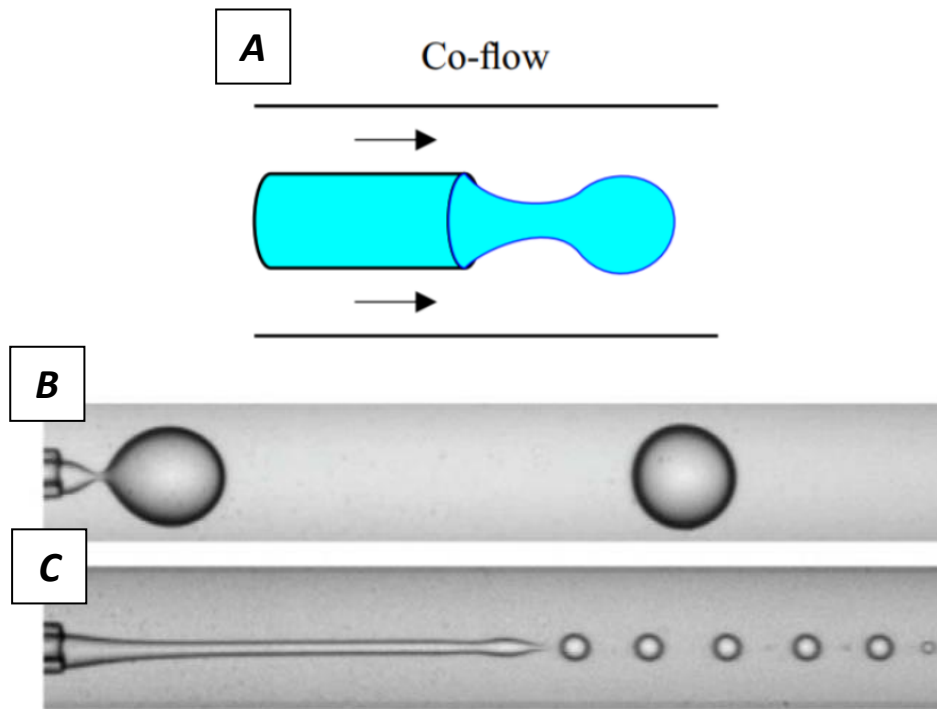


Figure 1.15 Droplet formation in a co-flow system.

(A) Schematic representation of a co-flowing device. (B) Droplet breakup when both continuous and dispersed flow rates are high, and (C) low. Taken from (Shah et al. 2008; Pit et al. 2015).

1.5.2.2.3 Flow focusing

In the flow-focusing design, a symmetrical configuration forces two continuous phases and a dispersed phase through a narrow region at the intersection (**Figure 1.16**). A symmetrical shear exerted by the continuous phases on the dispersed phase, producing droplets with more control, uniformity, and stability compared to t-junction and co-flowing devices (Sullivan and Stone 2008). Indeed, this symmetric shear-focusing creates a maximum shear point at the junction, resulting in more uniform droplets, as compared to the other previously discussed devices. Droplet sizes are affected by flow rates, with droplet size decreasing upon increasing the continuous flow rates, and vice-versa (Ward et al. 2005). As mentioned previously, droplet break-up rates and sizes depend on the interplay of viscosities, flow rates and surface tensions. When the dispersed phase flow rates are higher than continuous flow rates, this results in a long thread of dispersed phase into the main channel, taking longer until droplet breakup (**Figure 1.16 B**). High continuous phase flow rates to

● GENERAL INTRODUCTION ●

dispersed flow rates will generate uniform droplets that breakup after full expansion in the main channel, only through the effect of shear force of the continuous phase (**Figure 1.16 C**).

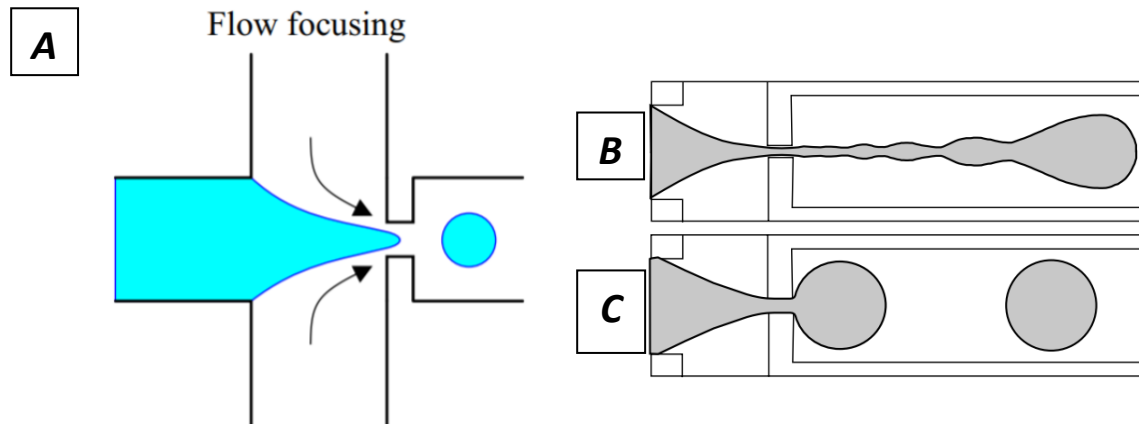


Figure 1.16 Droplet formation in flow-focusing devices.

(A) Schematic representation of droplet formation using a flow-focusing device. (B) Higher dispersed flow rates than continuous flow rates will lead to the formation of extended threads in the main channel. (C) High continuous phase flow rates than dispersed phase flow rates will result in uniform monodisperse droplets that grow fully in the main channel before breakup. Taken from (Sullivan and Stone 2008; Pit et al. 2015)

1.5.2.3 Applications in tissue engineering

Over the past decade, live-cell encapsulation using microfluidics has emerged as a powerful tool for a wide array of potential applications, including transplantation, drug delivery, simulating the mechanisms and physiology of organs on the microscale (e.g. organ-on-a-chip or human-on-a-chip), single-cell analysis, and enabling 3D cell culture (Sugiura et al. 2005; Choi et al. 2007; Clausell-Tormos et al. 2008; Khademhosseini et al. 2008; Köster et al. 2008; Martinez et al. 2012; van Duinen et al. 2015; Utech et al. 2015; Morgan et al. 2016; Headen et al. 2018; Hidalgo San Jose et al. 2018; Suvarnapathaki et al. 2018; Suea-Ngam et al. 2019; Sohrabi et al. 2020). The miniaturisation process for TE and 3D bio-printing offers unique advantages that are difficult to replicate at the macroscale, including low reagent consumption, cost-efficiency, high throughput, rapid prototyping, faster reaction times, efficient nutrient delivery, and increased control over the environment (Dolega et al. 2015; Huang et al. 2017). Furthermore, this allows the integration of an entire organ or tissue models onto a single chip (Stone et al. 2004). The advent of 3D printing has allowed the

● GENERAL INTRODUCTION ●

fabrication of diverse microfluidic systems at low costs, making this technology more accessible (Suvarnapathaki et al. 2018).

A major strength of droplet-based microfluidics lies in its ability to generate reproducible monodisperse droplets with high production rates, with increased control over droplet scalability and diffusional properties that can help control cross-linking properties for liquid/gel based bio-inks in 3D bio-printing (Headen et al. 2018; Suea-Ngam et al. 2019; Sohrabi et al. 2020). Fast diffusion rates may be harnessed to result in *in situ* rapid internal cross-linking of gellable liquid bio-materials, such as alginate, achieved in combination with droplet emulsification of pre-polymer hydrogel solutions, to generate homogenous hydrogel beads for cell-encapsulation (Tan and Takeuchi 2007; Amici et al. 2008; Hidalgo San Jose et al. 2018). This allows for the independent control of single units of cell-laden microgels, acting as 3D culturing units or building blocks, that can be individually manipulated, monitored and analysed (Rossow et al. 2012; Kang et al. 2014; Dolega et al. 2015; Utech et al. 2015). Utech et al. demonstrated the controlled encapsulation of mesenchymal cells (MSCs) in homogenous alginate droplets using a flow-focusing device. Cell-laden droplets were transferred to a culture medium and monitoring of individual droplets revealed cell growth and proliferation via microscopy (Utech et al. 2015). Droplet-based microfluidics offers the possibility to produce multi-layered hydrogel droplets using passive mixing without use of external forces (Carreras et al. 2020). In a recent study, double-layered droplets consisting of an inner layer of alginate and outer layer of puramatrix (synthetic matrix) encapsulating myeloma (bone marrow cancer cells) and MSCs, acting as a 3D scaffold biomimetic model, were generated using droplet-based microfluidics (Carreras et al. 2020). Flow-focusing devices have also been reported for the generation of different sized tumour spheroids (Lee et al. 2020). These models provided a suitable environment for cell culture and a platform for personalised medicine applications and drug testing (Lee et al. 2020). The affordability, simplicity, and high throughput of droplet-based microfluidic makes it a promising tool towards TE and the production of larger tissue structures. Bead-based TE has been previously reported as a promising approach to generating large tissue structures from the moulding of monodisperse cell beads (Matsunaga et al. 2011). Such beads were produced using a flow-focusing device for high droplet monodispersity and uniform seeding of cells per droplet.

● GENERAL INTRODUCTION ●

Integrating microfluidic-based approaches with 3D bio-printing technologies has shown great potential in drug testing and in generating more relevant perfused tissue models (Snyder et al. 2011). A recent report has demonstrated the potential of microfluidics in expanding the capabilities of extrusion-based 3D printers and bio-printers, by integrating a customized microfluidic device capable of high resolution printing of cell-laden constructs with control over dimensionality (Serex et al. 2018). 3D bio-printers can also be combined with a microfluidic chip devices for the extrusion of cell-laden bio-inks to generate multi-material constructs and perfusable systems (Miri et al. 2018; Attalla et al. 2019; Idaszek et al. 2019). Microfluidic-based extrusion systems for multi-material 3D bio-printing with high spatial control is just recently being acknowledged as a cost-effective alternative to conventional 3D bio-printing nozzles, which provide similar bio-printing resolutions (Richard et al. 2020). Indeed, microfluidic systems can accommodate and deliver several bio-inks with controlled gelation and gradients of chemical, mechanical and biological cues with high resolution (Idaszek et al. 2019). To date, there has been very few reports of droplet-based microfluidic systems that have been used as 3D bio-printing nozzle alternatives, with precise deposition of cell-laden droplets for tissue and organ bio-printing (Sharma et al. 2020). The ability to control cell densities, droplet size and spatial deposition of each cell-laden droplet in a cost-effective manner, offers great potential in generating high-resolution functional synthetic tissues.

Aim and objectives

It is hypothesised that generating an anatomically-relevant human skin model through developing a cost-effective, bespoke, widely accessible, and novel 3D bio-printing is feasible. To address this, a 3D bio-printing platform was built using widely available and modular LEGO® pieces which constituted the programmable x/y/z stage. This was subsequently combined with a cost-effective microfluidic t-junction device that allows for cell-laden droplet production. The integration of both devices allowed for the precise spatial deposition of keratinocyte-laden alginate droplets, with the aim to fabricate a 3D human skin equivalent.

The objectives of this thesis were to:

- 1) Establish immortalised keratinocyte cell cultures that can be maintained at different stages of phenotypic differentiation (using different concentrations of Ca^{2+}), to provide candidates for layer-by-layer 3D bio-printing of skin.
- 2) Develop and characterise an alginate bio-ink for bio-printing keratinocyte-laden alginate droplets using a t-junction microfluidic device.
- 3) Build, program and characterise a LEGO® 3D x/y/z stage for a bio-printer that can produce a range of patterned movements designed to bio-print 2D and 3D structures with appropriate resolution and flexibility.
- 4) Couple the microfluidic t-junction (objective 2) with the LEGO® 3D bio-printing stage (objective 3) to create a functional bio-printer and to explore the possibility of creating a fully integrated 3D bio-printing platform constructed using LEGO® alone.
- 5) Explore the printing resolution of the LEGO® based 3D bio-printer (objective 4) on the microscale and strategies for post-printing controllable alginate scaffold degradation.
- 6) Characterise the anatomical structure of the 3D bio-printed human skin in comparison to the native human skin.

● GENERAL INTRODUCTION ●

The interdisciplinary and collaborative nature of this project means that students and researchers from different discipline areas, were able to make important intellectual contributions in specific areas of this study. Some of the data presented in this thesis has therefore included significant contributions from these students and researchers and so their names have been duly acknowledged in the figure captions pertaining to that data set. For clarity, the areas of contribution for each student are also stated below:

Katie Harvey (Engineering student) – Building of the first LEGO® bio-printer prototype and programmes in our lab.

Cameron Pool (Pharmacy student) – Programming of a library of 2D and 3D stage movements for the LEGO® stage.

Katherine Sloan (Pharmacy Student) - Characterisation of alginate droplet production using microfluidics and evaluating the coupling of the microfluidic droplet generation with the movement of the programmed LEGO® stage movements.

Shabbir Moola (Pharmacy student) – Explored the effect of alginate gelation on fibroblast viability and aided in producing bio-printed structures with Cameron Pool and Katherine Sloan.

Grace McDermott (Master's biology student) – Building of the second LEGO® bio-printer prototype and creating a stop motion video of the building progress.

Ameer Al Shukri (Pharmacy student) – Evaluating alginate degradation with calcium chelators and effect of degraded scaffolds on cell viability.

Lluan Evans (Pharmacy Student) – Building of the third LEGO® bio-printer prototype and creation of a second stop motion video of the building progress.

Gabriela Velasquez Diaz (Master's biology student) – Development of fibrin droplets using microfluidics.

Phoebe Crews-Rees (Pharmacy student) – Development of dual nozzle and multi-bio-ink bio-printing.

Danielle Jarvis (Pharmacy Student) – Evaluating droplet production frequency using the LEGO® syringe driver.

Dr Jin Li (Bio-engineering researcher, PhD) – Designing and 3D printing of a microfluidic droplet producing LEGO® compatible brick.

Ahmad Moukachar (PhD Student) – Oversaw entirety of the project and each student's progress. Helped each student in preparing experimental work and data production. Growth and characterisation of keratinocyte cell lines in different Ca^{2+} levels. Optimisation and characterisation of alginate droplet production. Encapsulation of keratinocyte cells in alginate droplets and qualitative/quantitative characterisation of keratinocyte-encapsulated droplets. 3D bio-printing and evaluation 2D and 3D shapes. Multi-bio-ink bio-printing and qualitative assessment of bio-printed structure. Evaluating degradation rates of large bio-printed constructs.

***Chapter 2 Establishing the
optimal culture conditions for 2D and
3D cultures of keratinocytes***

2.1 Introduction

Mammalian primary epidermal keratinocytes (keratinocytes), whether normal human epidermal keratinocytes (NHEK) or mouse keratinocytes, and immortalised keratinocytes cell lines have been widely used as cell culture models to elucidate skin physiology and pathophysiology (Golan et al. 2015; Colombo et al. 2017). The search for the optimal culture system to generate keratinocytes that faithfully mimic *in vivo* keratinocytes functions is still ongoing. Moreover, the choice between NHEK or an immortalized keratinocytes cell line remains a subject of debate. Although primary keratinocytes are directly extracted from the skin tissue, retaining functional characteristics of the tissue, they still present drawbacks that should be considered. Firstly, their limited lifespan does not allow for long-term cell culture (Wilson et al. 2007). More specifically, primary keratinocytes rapidly die when induced for differentiation, limiting long-term investigation. Furthermore, donor-to-donor variability can affect experimental reproducibility and data interpretation. As an alternative, the spontaneously immortalized human keratinocytes cell line, HaCaT, has been widely used owing to its ability to proliferate and adapt to long-term culture (Wilson et al. 2007; Micallef et al. 2008; Colombo et al. 2017). The HaCaT cell line development stems from the long-term primary culture of human adult skin keratinocytes, reported by Boukamp et al. in 1988 (Boukamp et al. 1988). HaCaT cells are a valuable alternative to NHEK, because of their flexibility in culture and ability to stratify in organotypic models (Schoop et al. 1999). However, several studies have reported behavioural and differentiation protein expression deficiencies compared to NHEK when grown in 2D culture and in organotypic 3D models (Boelsma et al. 1999; Houghton et al. 2005; Micallef et al. 2008; Seo et al. 2012; Smits et al. 2017). In contrast, other studies deemed HaCaT cells as a reliable *in vitro* model to elucidate the molecular mechanisms involved in epidermal differentiation and to generate relevant 3D skin models (Boukamp et al. 1988; Garach-Jehoshua et al. 1998; Schoop et al. 1999; Sakaguchi et al. 2003; Lemaître et al. 2004; Wilson et al. 2007; Berning et al. 2015; Colombo et al. 2017). Indeed, *in vitro*, HaCaT cells have been shown to exhibit similar morphogenesis, differentiation characteristics, and functional features to isolated primary keratinocytes (Boukamp et al. 1988; Lemaître et al. 2004; Micallef et al. 2008; Borowiec et al. 2013); HaCaT cells can respond to differentiation-promoting stimuli in a flexible manner. For example, a calcium (Ca^{2+}) switch

● CHAPTER 2 ●

in the medium allows them to revert back and forth between a basal and differentiated state, whilst expressing specific differentiation markers (Garach-Jehoshua et al. 1998; Wilson et al. 2007; Micallef et al. 2008; Borowiec et al. 2013; Colombo et al. 2017).

Ca²⁺ is a major factor that promotes keratinocytes differentiation *in vivo* and *in vitro*. Indeed, Ca²⁺ regulation of keratinocytes differentiation has been extensively studied for the past 5 decades by culturing primary mammalian keratinocytes or immortalised keratinocytes in different extracellular Ca²⁺ concentrations *in vitro* (Hennings et al. 1980; Boyce and Ham 1983; Lemaître et al. 2004; Wilson et al. 2007; Colombo et al. 2017). Although *in vitro* keratinocytes differentiation can also be induced by other factors including cell-density, triterpenes, TGFβ, inhibition of JNK, fibronectin and detachment from the substratum, Ca²⁺ was used as the pro-differentiating agent in this study, due to extensive knowledge found in the literature (Shiple et al. 1986; Adams and Watt 1989; Ura et al. 2004; Gazel et al. 2006; Woelfle et al. 2010; Bikle et al. 2012; Colombo et al. 2017). More specifically, keratinocytes differentiate upon addition of high Ca²⁺ concentrations (>0.1 mM) or revert to a basal-like proliferative phenotype when cultured in low Ca²⁺ levels. Each stage of differentiation is accompanied by phenotypic shifts in cell growth, morphology, and expression of specific biochemical markers. Thus, distinct stages of keratinocytes differentiation can be monitored *in vitro* on the molecular and cellular levels. Furthermore, they can form a stratified epidermis when used in organotypic skin models or after transplantation *in vivo* (Boukamp et al. 1988; Schoop et al. 1999; Berning et al. 2015; Ramadan and Ting 2016). Finally, HaCaT cells require fewer supplementary growth factors and overall, less stringent conditions for culture. Thus, the HaCaT cell line offers an appealing *in vitro* model to potentially generate 3D skin models.

Ideally, precisely positioning keratinocytes in a controlled manner could recapitulate the 3D epidermal architecture, like 3D bio-printing for example, and in turn enable physiologically relevant biological functions (Randall et al. 2018; Yan et al. 2018). This requires a keratinocytes population that can be cultured *in vitro* for long periods of time whilst retaining the functional properties of *in vivo* keratinocytes. For these reasons, HaCaT cells have been identified as an appropriate keratinocytes population for the aforementioned studies. Reproducing the epidermis using the HaCaT cell line in optimal culture conditions *in vitro* provides an accessible and easy route to dissect epidermal differentiation and associated

● CHAPTER 2 ●

skin diseases (Boelsma et al. 1999). Hence, the HaCaT cell line can be potentially used as proof of concept when developing the 3D bio-printing technology in this study. In traditional cell culture methods, keratinocytes are typically maintained in a medium containing a defined concentration of Ca^{2+} , thus resulting in one specific differentiated phenotype. This approach results in a well stratified epidermal model that requires 14 days to 1 month of culture to reach maturity (Lee et al. 2009; Pourchet et al. 2017). However, most of these models consist of epidermal layers containing a single keratinocytes population and rarely recapture the multi-layered complexity and function of the epidermis. The pursuit of more relevant epidermal models necessitates an incremental increase in both the structural complexity of the tissue and diversity of cell populations therein. Recent attempts have been made to incorporate melanocytes and immune cells in printed epidermal structures (Min et al. 2017; Vidal Yucha et al. 2019). Despite these advances, major limitations persist in generating a more complex epidermal architecture.

The first step was to establish the optimal cell culture conditions to generate and maintain keratinocytes cell populations in proliferative and differentiated states *in vitro*. Understanding the cellular behaviour in 2D monolayers serves as baseline comparative results for subsequent integration into the 3D bio-printer; the ability to control the differentiated state of HaCaT cells *in vitro* can potentially provide a route to spatial control in 3D bio-printed tissue akin to that in the epidermis. To this end, HaCaT cells have been grown and maintained in different Ca^{2+} concentrations mimicking the *in vivo* calcium gradient in the epidermis (Menon et al. 1985; Menon and Elias 1991; Proksch et al. 2008; Bikle et al. 2012). Furthermore, this allows to demonstrate the advantages and limitations of the HaCaT cell line as a versatile *in vitro* epidermal model. Cells exposed to low Ca^{2+} conditions were expected to mimic the proliferative layers of the epidermis while those exposed to higher Ca^{2+} concentrations should mimic the upper differentiated layers (Wilson et al. 2007; Micallef et al. 2008; Borowiec et al. 2013; Colombo et al. 2017). 3D bio-printing multi-layered populations of keratinocytes at pre-determined levels of differentiation is an intriguing concept which has not yet been explored. It is therefore hypothesised, that this may result in more realistic epidermal models which could require less time to stratify.

● CHAPTER 2 ●

Physiologically, keratinocytes differentiation induced by Ca^{2+} -level switch is associated with the expression of distinctive protein markers (Bikle et al. 2012; Elsholz et al. 2014). In this study, the expression of four proteins was investigated: Keratin 5 (K5), Keratin 10 (K10), E-cadherin and Involucrin (INV). *In vivo*, K5 is predominantly expressed in the undifferentiated keratinocytes of the basal layer, whilst K10 is found in more differentiating keratinocytes of the stratum spinosum (Moll et al. 1982; Woodcock-Mitchell et al. 1982; Eichner et al. 1986; Moll et al. 2008; Bikle et al. 2012; Elsholz et al. 2014). INV expression is restricted to the uppermost layers of the spinosum and found in the granular layer where keratinocytes undergo terminal differentiation (Rice and Green 1979; Warhol et al. 1985; Elaine Fuchs 1990; Bikle et al. 2012). E-cadherin has been previously detected in all epidermal layers of human healthy skin and skin equivalents with reduced or no expression in the basal and uppermost superficial layers (Maretzky et al. 2008; Vaughan et al. 2009).

2.2 Aim and objectives

It is hypothesized that bio-printing HaCaT cell populations exposed to different Ca^{2+} levels and representing varying degrees of phenotypic differentiation, in a layer-by-layer fashion would result in a stratified epidermal model, akin to the native epidermis. The aim of this chapter was to develop and establish the optimum culture conditions for 2D and 3D cultures of keratinocytes using the HaCaT cell line.

The objectives of this chapter were to:

1. Maintain HaCaT cells under different Ca^{2+} concentrations.
2. Characterise HaCaT cell phenotypical changes in morphology, growth rate, and expression of biochemical markers of differentiation and proliferation, as a result of Ca^{2+} variations in the culture medium.

2.3 Materials and Methods

2.3.1 Cell culture

All cell culture procedures were performed in a class 2 biosafety cabinet (BSL-II) using 70% ethanol as a disinfectant to maintain aseptic conditions. Cells are maintained in an incubator at 37°C containing 5% CO₂ (Thermo Scientific – MSC-ADVANTAGE).

2.3.1.1 HaCaT cell culture

HaCaT cell lines (passages 62, 71 and 75) were cultured in Dulbecco's modified Eagle medium (DMEM)- GlutaMAX (high glucose supplement) supplemented with 10% foetal bovine serum (FBS) (Biowest #S1810-500) and 1% Penicillin-Streptomycin. DMEM-GlutaMAX contains 4 mM of L-glutamine and 1.8 mM of Ca²⁺ by default. In this study, the culture condition will be termed as "Normal Calcium" (NC).

2.3.1.2 Low/high-calcium media and cell culture

Cell culture media containing two different Ca²⁺ concentrations (excluding the NC condition) were prepared as described in a previous study (Wilson et al. 2007): Very Low Calcium (VLC) (0.03 mM) and High Calcium (HC) (2.8 mM). A third condition of Low Calcium (LC) (0.3 mM) was included as described in previous studies (Boyce and Ham 1983; Borowiec et al. 2013). HaCaT cells were maintained in VLC, LC and HC for at least 3 weeks prior to experimentation to ensure that Ca²⁺ concentration changes in the medium have had the appropriate effect on the state of cell proliferation and differentiation (Wilson et al. 2007). Calcium chloride (CaCl₂) (Fisher Scientific) stock solutions were prepared with sterilised distilled water (dH₂O) and filter sterilised into 50 mL conical tubes using 0.2 µm pore syringe filters (Sartorius – Ministart®). Endogenous Ca²⁺ in the FBS is removed by treating it with Chelex 100 Resin (BIORAD). Chelex 100 Resin is used as a chelating agent to selectively bind polyvalent metal ions such as Ca²⁺. An amount of 0.38 g of Chelex 100 Resin was added into sterile 50 mL aliquots of FBS and incubated for 1 hour at 4°C on a tube rotator. Calcium-free DMEM was then supplemented with 10% chelexed FBS, 1% Penicillin-Streptomycin-

• CHAPTER 2 •

Glutamine 100x (200 mM of L-glutamine bringing the final concentration to 4 mM) and CaCl_2 solutions to final Ca^{2+} concentrations of 0.03 mM (VLC), 3.0 mM (LC) and 2.8 mM (HC). The media was then filter sterilised using 0.2 μm pore syringe filters to remove the Chelex resin and ensure sterility. The media was stored at 4°C. HaCaT cells were cultured and maintained in VLC, LC, NC, and HC conditions similarly. Cell culture medium was changed every 2 – 3 days until they reached 70 – 80 % confluence.

To establish different cell populations of keratinocytes *in vitro* that potentially mimic the different viable layers of the epidermis, HaCaT cells have been grown in extracellular Ca^{2+} concentrations shown in **Figure 2.1**. based on previous studies.

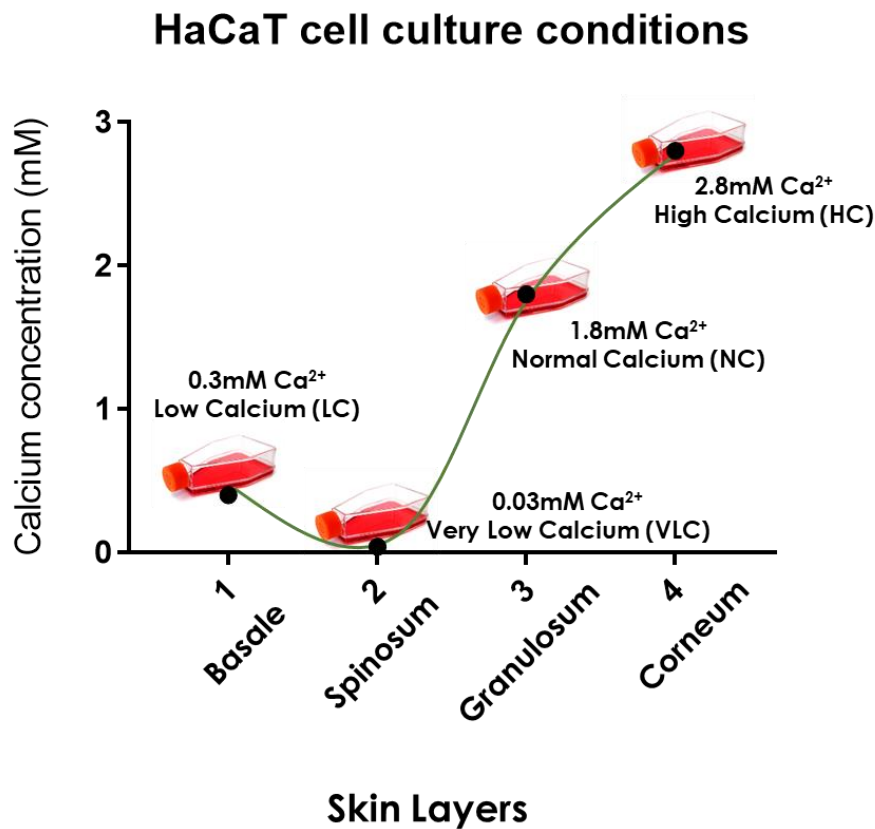


Figure 2.1 *In vitro* extracellular Ca^{2+} conditions for HaCaT cell culture mimicking the physiological non-linear Ca^{2+} gradient in the epidermis.

2.3.1.3 *Routine subculture*

Upon reaching confluence, cell culture medium was aspirated, and cells were washed twice with sterile phosphate buffer saline (PBS). Cells were detached from the flask by adding 0.25% trypsin-EDTA and incubating at 37°C for 5 – 10 minutes. The cell culture flask was then lightly tapped with the palm of the hand until they became rounded and fully detached. The cell suspension was transferred into a 15 mL tube containing fresh cell culture medium with FBS, which neutralises the enzymatic activity of trypsin. The cells were then centrifuged at 300 x g for 5 minutes. After discarding the supernatant, the cell pellet was re-suspended in fresh cell culture medium and re-seeded with adequate cell densities on new flasks. Subcultivation ratios ranged between 1/5 to 1/10 for routine cell culture or other desired ratios as per experimental requirements. Cell culture medium was renewed every 2 – 3 days. The volumes of reagents used were scaled according to the tissue culture flask size.

2.3.1.4 *Cryopreservation and cell culture from frozen stock*

HaCaT cells were routinely frozen to maintain stock. They were preserved as 1 mL aliquot vials containing FBS, 10% Dimethyl Sulfoxide (DMSO) and stored at -130°C in cryogenic storage tanks until use. Following cell detachment as described in **Section 2.3.1.3**, cells were re-suspended in FBS and 10% DMSO at a cell density of 10⁶ cells per mL. A volume of 1 mL of cell suspension was transferred into each cryogenic vial (Corning) then frozen at -80°C. The frozen vials were transferred to liquid nitrogen cryogenic storage units 24 hours later for optimal preservation.

The frozen cells were rapidly thawed by gentle agitation at 37°C in a water bath and then slowly transferred to pre-warmed 5 mL cell culture medium to dilute the DMSO. The cells were centrifuged (Thermo Scientific – MEGAFUGE 8) at 150 x g for 5 minutes at room temperature (RT). Traces of DMSO were removed by discarding the supernatant and the cells were re-suspended in fresh medium and seeded in 25 cm² tissue culture flask (T-25). Cells were incubated to allow adherence and proliferation until they reached 70 – 80% confluence before subculture (**Section 2.3.1.3**). Upon reaching confluence, the cells were transferred into a 75 cm² tissue culture flask (T-75) to allow more space for cells to proliferate.

2.3.1.5 Determination of cell count

The number of cells was counted using a Neubauer improved haemocytometer (Marienfeld Superior) and trypan blue solution (Sigma® Life Science). Trypan blue solution is a cell stain that enables quantification of “live cells” by counterstaining those “dead cells” a blue dye. The impermeable membrane of live cells excludes penetration of the blue dye in the cell, therefore enabling visual differentiation between “live” and “dead”. After detaching cells from the flask as described in **Section 2.3.1.3**, a 20 μL sample of cells was taken and diluted in trypan blue solution at a 1:1 ratio. A volume of 10 μL of the trypan blue diluted cell suspension was then loaded into each counting chamber of the haemocytometer and counted under a phase contrast microscope (IX50 Olympus). Only cells that were not stained blue were counted.

2.3.1.6 Cell growth curves

HaCaT cells grown in VLC, LC, NC, and HC were seeded at different passages on Day 0 in 6 well plates (Sigma-Aldrich) at 5×10^4 cells per well. 8 wells were prepared for each condition corresponding to one well per day. The cells were detached, and only viable cells were counted as described in **Sections 2.3.1.3** and **2.3.1.5** every 24 hours for 8 days using trypan blue. Cell culture medium was changed every 2 – 3 days.

2.3.2 Imaging of cells and time-lapse acquisition

Cell morphology and viability were regularly observed using phase contrast and bright field optics on an inverted microscope (IX50 Olympus). Images were taken using the Olympus software “analysis getIT” (Olympus Soft Imaging Solutions GmbH).

Time-lapse recording of cell proliferation was carried out using the LS420 Microscope (Lumascop) and Lumaview software (etaluma). HaCaT cells were seeded at 1.5×10^5 per well and allowed to attach and adhere for 24 hours before time-lapse acquisition. Live-cell imaging was observed by placing the microscope and the cell culture plate inside an incubator to maintain optimal cell growth conditions. Serial images focusing on a region of interest (ROI)

of the well plate were programmed to be taken at a 30-minute interval for 48 hours. The images were then compiled into a time-lapse video using the Fiji (ImageJ) software.

2.3.3 Human skin sample preparation and cryo-sectioning

Human skin samples were obtained from female patients who underwent breast reduction or mastectomy surgery, with informed consent and under appropriate ethical approval (South East Wales Research Ethics Committee, Reference: 08/WSE03/55). Following surgical procedure, the skin tissue was immediately placed in DMEM supplemented with 2% penicillin-streptomycin and transported to the laboratory at 4°C. The skin samples were either used directly or frozen at -20°C upon arrival at the laboratory until further use.

Subcutaneous adipose fat was removed using curved surgical scissors, then the skin was stretched by pinning the edges on two stacked corkboards, with the epidermis facing up. Small sections of the skin sample, including the dermis, were obtained using a 5 mm biopsy punch (KAI medical, Japan) and each section was placed in a plastic mould containing Optimal cutting temperature (OCT) compound. The skin section was completely covered with OCT compound and the mould was placed on a bed of dry ice for rapid freezing, before storing at -80°C.

Frozen skin samples were cryo-sectioned at 10 µm thickness on the Cryostar NX50 Cryostat and sections were collected on glass slides and stored at -20°C.

2.3.4 Evaluating expression of epidermal markers in HaCaT cells

Protein levels of several epidermal markers in HaCaT cells grown in different calcium concentrations were either semi-quantified by western blotting or qualitatively assessed by immunofluorescence.

2.3.4.1 Western blot

2.3.4.1.1 Cell preparation for protein extraction

Cells were counted, detached from the culture flask upon reaching 70 – 80% confluence, centrifuged and the supernatant discarded leaving a cell pellet in the tube as described in **Sections 2.3.1.3.** and **2.3.1.5.** The cell pellet was washed 3 times with ice-cold sterile PBS with a centrifugation at 300 x g at 4°C for 5 minutes between each wash then transferred into a 1.5 mL microcentrifuge tube. After the last wash, the PBS was carefully discarded to ensure the cell pellet was dry. The samples were labelled and stored at -80°C for subsequent protein extraction.

2.3.4.1.2 Preparation of lysate from cells

The frozen cell samples were slowly thawed and kept on ice during the entire process. Proteins were extracted from the cells by lysing the cells with lysis buffer+ (RIPA Buffer+) (**Table 2.1**). Lysis buffer was prepared, aliquoted in 10 mL falcon tubes and stored at -20°C. Before use, it was thawed to 4°C and kept on ice, then lysis buffer+ was prepared by dissolving 1 tablet of the cOmplete™, Mini Protease Inhibitor Cocktail (Sigma-Aldrich Merck) in 10 mL lysis buffer. 50 µL of lysis buffer+ was added per 1 million cells in each tube of cell pellets and vortexed for 2 – 3 seconds, then kept on ice for 30 minutes. The samples were centrifuged at 9500 x g at 4°C for 15 minutes and the supernatant was transferred into a new tube and the pellet discarded. The samples were kept on ice for direct use or frozen at -20°C for long-term storage.

Table 2.1 Lysis Buffer Recipe (100 mL) (RIPA Buffer)

Reagents	Volume	Final Concentration
1 M NaCl	15 mL	150 mM
0.5 M EDTA, pH 8.0	1 mL	5 mM
1 M Tris-HCl, pH 8.0	5 mL	50 mM
1% Triton-X	1 mL	10%
10% Sodium deoxycholate	5 mL	0.5%
10% SDS	1 mL	0.1%
D ₂ H ₂ O	72 mL	
RIPA Buffer+ = RIPA Buffer + Protease Inhibitor		

2.3.4.1.3 Bradford assay

The Bradford assay was performed to quantify total protein concentrations in the prepared lysates. Protein concentrations were estimated by reference to known diluted Bovine Serum Albumin (BSA) concentrations, assayed alongside the unknown samples following the instructions of the Coomassie Plus (Bradford) Assay Kit. The diluted protein standards (BSA) were prepared as described in **Table 2.2** with 3 custom standards to increase standard curve efficiency (highlighted in red). Serial dilutions of BSA were prepared from a BSA stock of 2000 µg/mL and diluted in PBS generating a range of standard concentrations from 25 µg/mL to 2000 µg/mL. 5 µL of each prepared standard and unknown protein sample lysate (**Section 2.3.4.1.2**) was added to a well in a 96 well plate in triplicates. To each well containing BSA standards and the unknown protein samples, 250 µL of Coomassie reagent was added and mixed by placing on a shaker for 30 seconds. The plate was incubated at RT for 10 minutes and the absorbance reading was determined at 620 nm using the Infinite® F50 Tecan plate reader and Magellan™ software (Tecan). A standard curve and linear equation were generated from the BSA standards allowing to determine the absorbance, and therefore the concentration of the unknown protein samples (**Figure 2.2**). Different ranges of standard curves were used depending on amount of protein generated from the samples. The protein samples were kept at -20°C for future use or kept at 4°C for direct use.

• CHAPTER 2 •

Table 2.2 Preparation of Diluted Albumin (BSA) Standards

Vial	Volume of PBS (μL)	Volume and Source of BSA (μL)	Final BSA Concentration (μg/mL)
A	0	300 of Stock	2000
B	125	375 of Stock	1500
C	325	325 of Stock	1000
D	175	175 of vial B dilution	750
E	198	102 of vial A dilution	680
F	180	120 of vial B dilution	600
G	325	325 of vial C dilution	500
H	75	225 of vial G dilution	375
I	325	325 of vial E dilution	250
J	325	325 of vial F dilution	125
K	400	100 of vial G dilution	25
L	400	0	0 = Blank

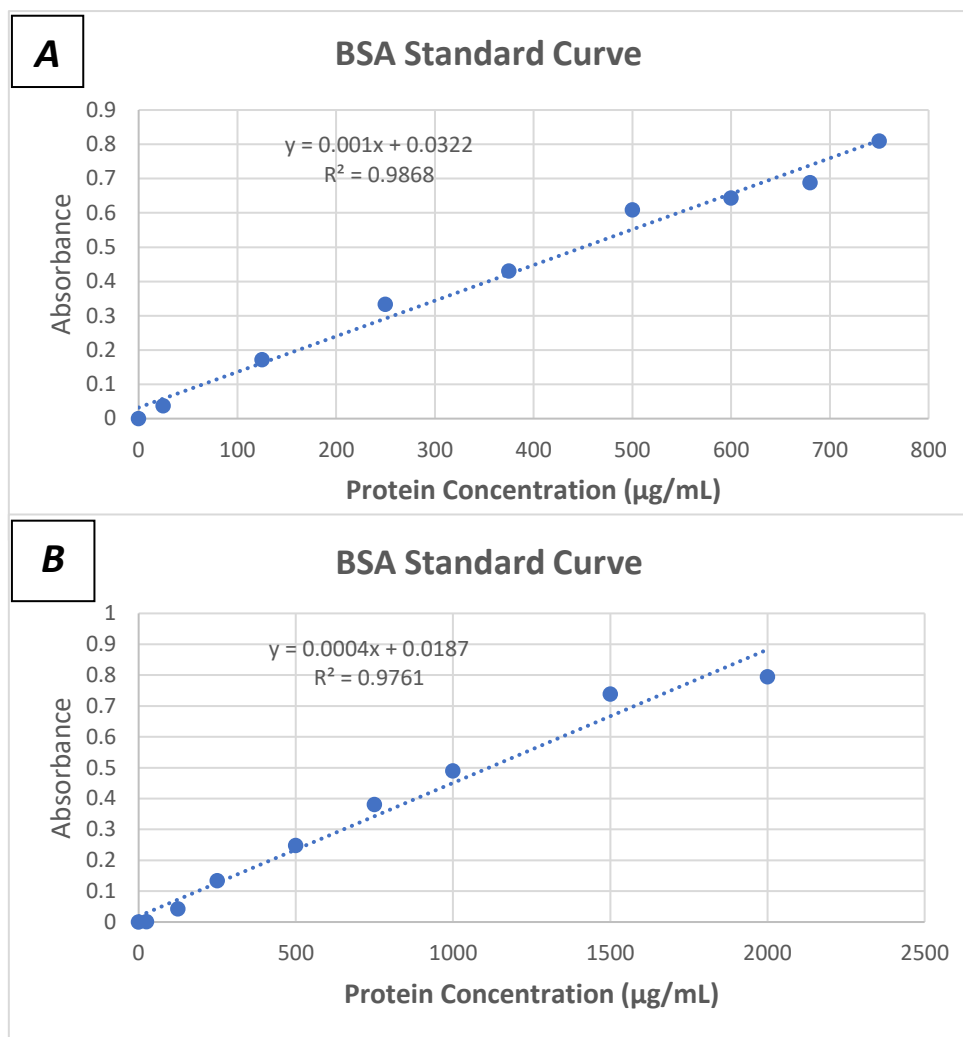


Figure 2.2 Examples of Bovine Albumin Serum (BSA) Standard Curves.
 Linear equations were generated with a range of standard concentrations from (A) 25 to 750 µg/mL and (B) 25 to 2000 µg/mL.

2.3.4.1.4 SDS-PAGE

The proteins from the prepared samples were separated by molecular weight or size using the sodium dodecyl sulphate polyacrylamide gel electrophoresis (SDS-PAGE) procedure. Protein samples were prepared by adding 10 µg to 20 µg of the previously prepared protein in lysis buffer, to loading buffer for a total volume of 40 µL. Loading buffer is composed of 1X diluted Sample Buffer containing lithium dodecyl sulfate (4X Bolt™ LDS Sample Buffer), 1X diluted sample reducing agent containing 500 mM of dithiothreitol (DTT) (10X NuPAGE™ Sample Reducing Agent) and deionised water (dH₂O). The samples were heated in a heating plate at 100°C for 3 minutes to denature the proteins and linearize the chains. Novex™

● CHAPTER 2 ●

WedgeWell™ 10%, Precast Mini Protein Gels, 10-well were prepared by removing the gel comb and placing them in an assembled Mini Running Gel Tank filled with 1X diluted Novex™ Tris-Glycine SDS Running Buffer (10X) making sure the sample wells are filled with the running buffer. Colour Prestained Protein Standard, Broad Range (11 – 245 kDa) (NEW ENGLAND BioLabs) was constantly loaded in the first well of the gel to help distinguish the size of proteins and the protein samples were loaded in the remaining wells making sure the same amount of protein was loaded between wells; this is important as it enables appropriate semi-quantitative comparison. A voltage of 100 V was applied to the gel for 60 minutes allowing the proteins to migrate and separate by molecular weight.

2.3.4.1.5 Protein transfer and blocking

Once the proteins migrated through the gel and were separated by electrophoresis, they were transferred from the gel onto a 0.45 µm pore sized nitrocellulose membrane. After the allotted time for the SDS-PAGE, the gel was removed from the tank, soaked in 1X diluted Novex™ Tris-Glycine Transfer Buffer (25X) and left for 10 minutes to allow the gel to equilibrate. The top-section of the gel containing the wells was then removed and the remaining gel was placed in the transfer cassette between pre-soaked sponges, filter papers and one nitrocellulose membrane in the order described in **Figure 2.3**; this is known as the transfer sandwich setup. The gel is oriented nearest to the cathode (-) electrode whilst the nitrocellulose membrane to the anode (+) electrode ensuring transfer of the proteins from the gel to the membrane upon voltage application. The transfer cassette was loaded in the transfer tank chamber filled with transfer buffer and an ice block. The whole unit was sitting in an ice water-bath. A voltage of 25 V was applied for 60 minutes which was performed using the Mini Trans-Blot® Cell system (Bio-Rad).

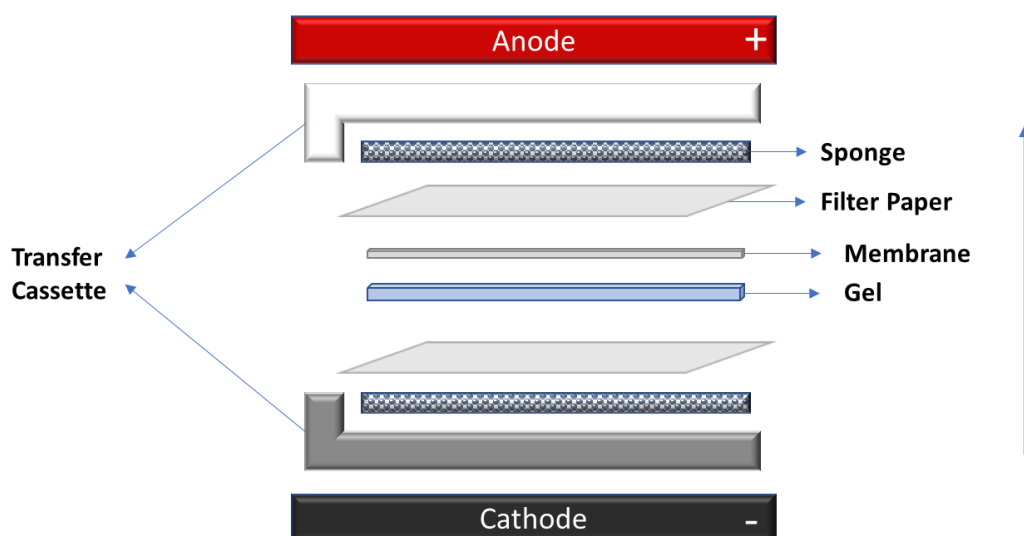


Figure 2.3 Representative scheme of the transfer sandwich setup.

To ensure the successful and efficient transfer of proteins from the gel to the nitrocellulose membrane, the membrane was soaked in Ponceau S solution (Sigma-Aldrich) and then removed and washed with PBS until the Ponceau S was completely removed.

After the protein transfer, the nitrocellulose was retrieved and washed once with PBS, 0.05% Tween® 20 (Sigma-Aldrich) (PBS-T). The membrane was blocked in a blocking buffer consisting of PBS containing 5% w/v skimmed milk for 1 hour at RT or overnight at 4°C. The blocking buffer was prepared by adding 2.5 g of dried skimmed milk (Tesco) to 50 mL of PBS.

2.3.4.1.6 Antibody staining

After the blocking process, the membrane was blotted with antibodies against the target protein and loading control. Prior to this, the membrane was cut at the desired molecular markers to allow incubation of different antibodies on separate areas of the membrane. Then, the membrane was washed with PBS-T 3 times for 10 minutes each. Primary antibodies were diluted in PBS-T at the optimised working concentrations shown in **Table 2.3**. The membranes were then incubated with the diluted primary antibodies with constant rocking for 2 hours at RT or overnight at 4°C.

Table 2.3 List of primary antibodies used for Western Blot

Target protein	Source species	Species reactivity	Working dilutions	Cat. No.	Manufacturer
Involucrin	Mouse	Human	1:1000	ab68	abcam
B-actin	Mouse	Human	1:500	ab8226	abcam

Next, the membrane was washed 3 times with PBS-T for 10 minutes each time, then incubated with a rabbit anti-mouse HRP-conjugated secondary antibody (ab6728, abcam) diluted at 1:2000 in PBS-T for 2 hours at RT. Similarly, the membrane was washed with PBS-T 3 times for 10 minutes each.

2.3.4.1.7 Protein detection

Pierce Enhanced chemiluminescence (ECL) western blotting substrate was used to detect HRP enzyme activity. The luminol and enhancer solutions were mixed at a 1:1 ratio in a 15 mL falcon tube. The nitrocellulose membrane was then soaked in this ECL solution for 1 minute. Excess ECL solution was removed, and the membrane was placed inside a transparent pre-washed plastic wrap (polly pocket). The membrane was finally placed in the Gel imaging G:Box Chemi XX6 system (SYNGENE, AlphaMetrix Biotech) equipped with Charge-coupled device (CCD) cameras allowing for automated detection of chemiluminescence emitted by the HRP and ECL substrate chemical reaction. Exposure times and image acquisition were carried out using the GeneSys control software (SYNGENE).

2.3.4.1.8 Blot analysis

Protein band intensities were analysed and quantified to obtain a normalized signal intensity in numerical values using Image-J software. The area of interest (AOI) or full protein bands were highlighted and plotted as histograms indicating the intensity of each band. A tangent was drawn from where the histogram first starts to where it levels out. When the inside of the histogram is selected using the “wand tool”, a numerical value appears indicating the intensity of each band. This was repeated for the target protein and the loading control in each lane. The next step was to normalize the data using the loading control proteins. To do this, the normalization factor for each lane was calculated by dividing the value of the

● CHAPTER 2 ●

loading control signal of that lane by the highest value of the loading control of the blot as follows:

$$\text{Lane normalization factor} = \frac{\text{Signal value of loading protein for each lane}}{\text{Highest signal value of loading protein of the blot}}$$

Equation 2.1

Following this step, the raw signal intensity value of the target protein from each lane was divided by its lane normalization factor to obtain normalized signal intensity:

$$\text{Normalized signal intensity} = \frac{\text{Raw signal intensity value from each lane}}{\text{Lane normalization factor from each lane}}$$

Equation 2.2

2.3.4.2 Immunofluorescence staining

2.3.4.2.1 Immunohistochemistry on skin samples

Skin samples were obtained as described in **Section 2.3.3**. Histological skin sections of 10 μm thickness prepared as described in **Section 2.3.3**, were initially equilibrated at RT for 15 minutes. Circles were drawn around each skin section using a liquid blocker PAP pen (ab2601, abcam) to maintain local distribution of the staining solution on the tissue. The sections were hydrated by submerging them 3 times in PBS for 5 minutes each time. Blocking solution was prepared by adding 500 μL of goat serum and 150 μL of Tween-20 in 50 mL of PBS (1% goat serum & 0.3% Tween-20). The sections were blocked in a blocking solution at RT in a humid chamber for 1 hour. Primary antibodies were diluted in the blocking solution at the optimised working dilutions shown in **Table 2.4**. A few drops of the diluted primary antibody were added on the skin sections within the drawn circles of the PAP pen and the slides were incubated at 4°C overnight in a humidity chamber.

Table 2.4 List of primary antibodies used for immunofluorescence

Target protein	Source species	Species reactivity	Working dilutions (skin tissue)	Working dilutions (fixed cells)	Cat. No.	Manufacturer
Cytokeratin 5	Rabbit	Human	1:200	1:100	ab52635	abcam
Cytokeratin 10	Rabbit	Human	1:200	1:150	ab76318	abcam
E-Cadherin	Mouse	Human	1:200	1:200	ab1416	abcam
Involucrin	Mouse	Human	1:200	-	ab68	abcam

The next day, the sections were washed 3 times in PBS for 5 minutes each. Secondary antibodies conjugated to fluorescent dyes were diluted in blocking solution at the optimised working dilutions (**Table 2.5**). The sections were incubated with the diluted secondary antibody at RT for 2 hours in a humid chamber. A third washing step was carried out before incubating the sections with a diluted DAPI nuclear stain (1:100 in dH₂O) for 10 minutes at RT. The DAPI stain was kindly provided by the laboratory of Professor Arwyn Jones. The sections were washed 5 times for 30 seconds each time, then a 14 mm round cover slip (VWR) was mounted using the ProLong[®] Diamond Antifade Mountant and stored at 4°C until imaging.

Table 2.5 List of secondary antibodies used for immunofluorescence

Target protein	Source species	Species reactivity	Working dilutions	Cat. No.	Manufacturer
Anti-rabbit (AlexaFluor [®] 488)	Goat	Rabbit	1:500	ab150077	Abcam
Anti-mouse (AlexaFluor [®] 594)	Goat	Mouse	1:500	ab150116	abcam

2.3.4.2.2 Cell preparation and fixation

HaCaT cells grown in LC, VLC, NC, and HC were seeded in 35 mm MatTek glass bottom dishes at a cell density of 2.5 x10⁵ per dish. Upon reaching 70% confluence, the medium was discarded and 2.5 mL of cold BD Cytifix™ Fixation Buffer (BD Biosciences) containing 3 - <5% formaldehyde was added to the MatTek dish for 20 minutes at RT to fix the cells. The cells

● CHAPTER 2 ●

were then washed 3 times for 5 minutes each on a rocker. Occasionally, the cells were stored at 4°C after the fixation step for subsequent blocking.

2.3.4.2.3 Cell blocking, permeabilization and antibody incubation

Fixed cells in MatTek dishes were incubated with 2.5 mL of the BLOCK+ solution (**Table 2.6**) for 1 hour at RT. All reagents except PBS were kindly provided by Dr James Burston. Briefly, fish gelatine and BSA minimize non-specific antibody binding while Triton X-100 is used to permeabilize membranes of cells allowing antibody penetration. The BLOCK+ solution was discarded, and fixed cells were incubated with primary antibodies diluted at the optimal working dilutions in BLOCK+ as described in **Table 2.4**, and left for 16 hours at 4°C.

On the second day, a washing solution consisting of 45 mL of PBS and 0.1 mL of Tween-20 (0.2%) named PBS+ was prepared. The primary antibody was removed, and the fixed cells were washed 5 times for 10 minutes each with PBS+ while on a rocker. During that time, the secondary antibody was diluted in BLOCK+ at the optimised dilutions shown in **Table 2.6**. Fixed cells were incubated with the diluted secondary antibody for 2 hours at RT. All steps were carried out in the dark from this point. The secondary antibody was discarded, and the fixed cells were washed 5 times for 10 minutes with PBS+. DAPI was diluted in dH₂O at a 1:100 ratio and added on the fixed cells for 20 minutes at RT. The diluted DAPI was removed, and the fixed cells were rapidly rinsed 5 times with dH₂O before allowing the cells to dry for 5 hours or overnight. Once completely dry, a 14 mm round cover slip (VWR) was mounted on the glass portion of the MatTek dish using a drop of ProLong[®] Diamond Antifade Mountant. The fixed cells were stored at 4°C until confocal imaging. To examine antibody specificity (negative controls), HaCaT cells (NC) were incubated in secondary antibodies without primary antibodies (**Appendix A-1**).

Table 2.6 BLOCK+ Solution Recipe

Reagents	Volume (mL)	Quantity (mg)
PBS	45	-
Fish Gelatin	-	50
Bovine Serum Albumin powder (BSA)	-	500
Triton X-100	0.3	-

2.3.4.3 Confocal imaging

Immunofluorescent images of stained fixed human skin and fixed HaCaT cells were visualized and captured using the Leica DMI6000B inverted confocal microscope (Leica Microsystems) with the LAS AF software (Leica Microsystems). Both HeNe and Argon lasers were switched on to provide excitation wavelengths of 488 nm and 594 nm for both AlexaFluor® secondary antibodies. Optical sectioning of fixed/stained cells were taken. The images were then analysed and processed using the Image-J software ([ImageJ \(nih.gov\)](http://imagej.nih.gov)).

2.3.5 Statistics

Data are represented as mean \pm SD. Statistical significance was determined by the independent samples Student t-test, whereby $p < 0.05$ was considered statistically significant. Statistical significance was determined only when three independent biological repeats ($n=3$) have been conducted, with three technical repeats per biological repeat. Statistical significance was reached when the p value (probability value that an observed difference has occurred by chance) is equal or less than 0.05 (*), meaning that there is at least a 95% probability that the observed difference has not occurred by chance. Different levels of significance were used: p value < 0.01 (**), p value < 0.001 (***)

2.4 Results

2.4.1 Effect of extracellular Ca^{2+} changes on cell morphology

It has been previously reported that the effects of changes in extracellular Ca^{2+} concentration is observed through morphological changes in keratinocytes *in vitro* (Wilson et al. 2007; Micallef et al. 2008). HaCaT cells were first monitored for visible differences in morphological changes following a calcium switch. After at least 3 weeks in lower Ca^{2+} conditions (VLC and LC), cells became predominantly elongated and spindle shaped whereas cells grown in higher Ca^{2+} concentrations (NC and HC) exhibited a more cuboidal or cobblestone shape (**Figure 2.4**). NC (1.8 mM Ca^{2+}) conditions are conventionally what HaCaT cells are grown in and demonstrate the standard HaCaT morphology whereby a combination of shapes is observed between round, spindle and cuboidal. The tight packing of cells between the conditions was also fundamentally distinct; a loose and disorganised packing of cells is observed when grown in lower Ca^{2+} concentrations in contrast to a tightly packed structure in higher Ca^{2+} (**Figure 2.4**). As a result of lower cell-cell contact, the cells appear larger in size taking up more area surface in the plate. Furthermore, HaCaT cells in HC grew in an ordered fashion in “clusters”, resulting in unevenly spread patches of cells in contrast to the other conditions. The packing of cells and morphological differences observed remained stable even at lower confluency and throughout numerous routine sub-culturing and experiments (**Figure 2.5**).

These preliminary results indicate that an extracellular Ca^{2+} switch in the growth media can alter the morphological phenotype of HaCaT cells.

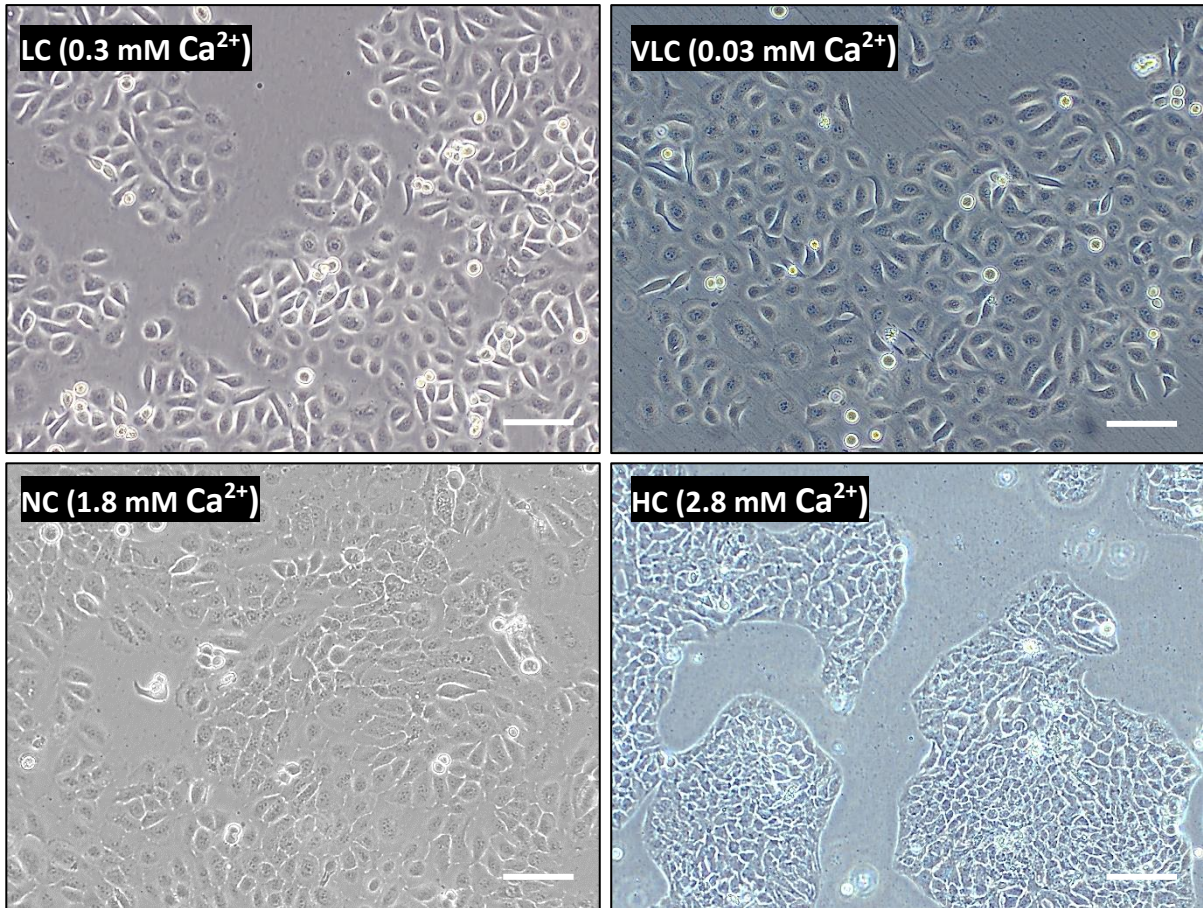


Figure 2.4 Morphological changes of HaCaT cells cultured in different calcium concentrations shown by phase-contrast microscopy.

HaCaT cells were grown in their respective Ca^{2+} levels for 3 weeks before morphological observation. Elongated and spindle shaped cells were mostly observed in HaCaT cells grown in lower Ca^{2+} levels (LC/VLC) as opposed to cuboidal shaped cells in higher Ca^{2+} levels (NC/HC). LC = Low Calcium, VLC = Very Low Calcium, NC = Normal Calcium, and HC = High Calcium. Images were taken at a 70 – 80% confluency. All images were taken at a 10X magnification. Scale bar = 100 μm .

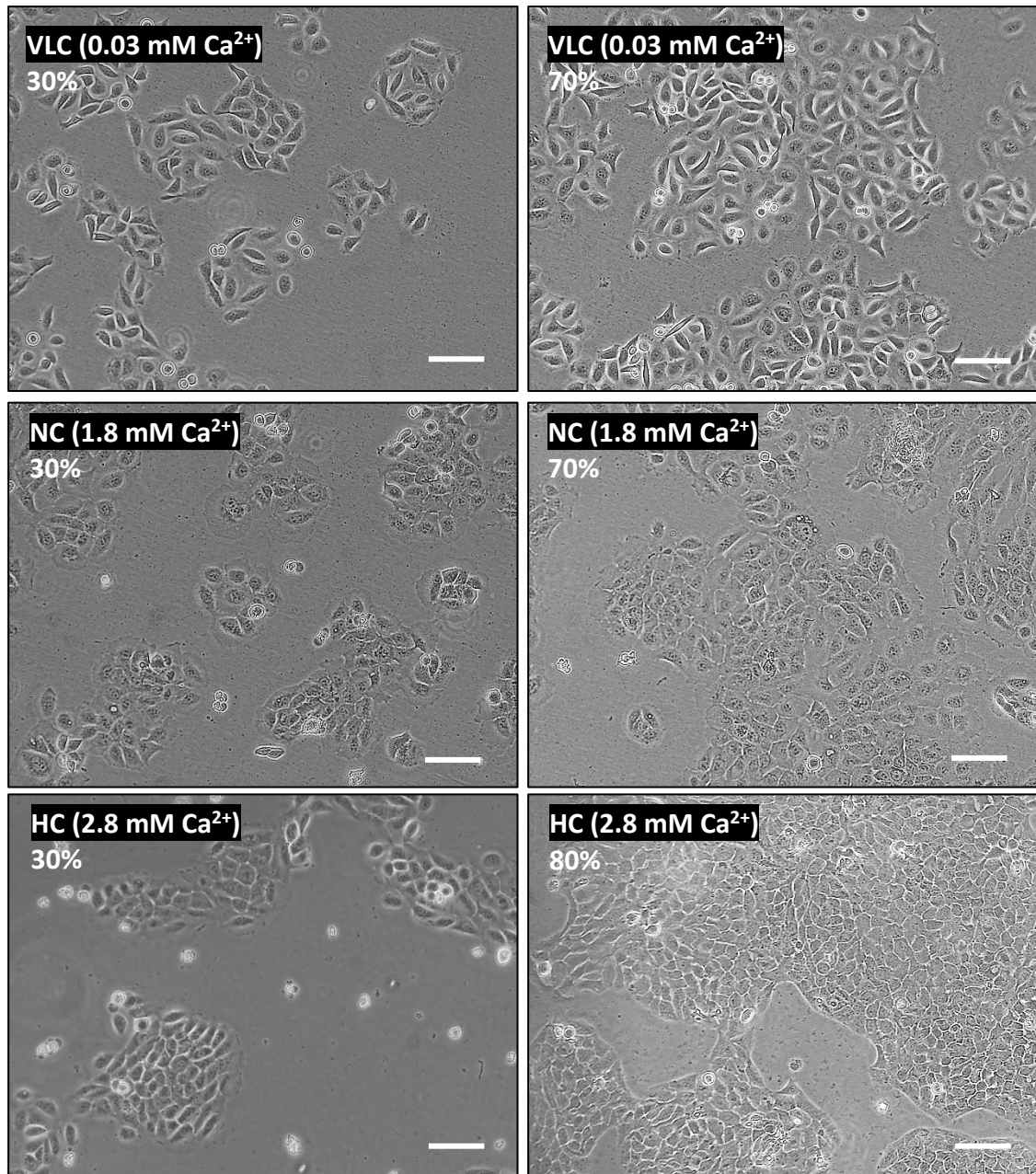


Figure 2.5 Morphological changes of HaCaT cells at different confluence percentages following the extracellular Ca²⁺ switch.

HaCaT cells grown to low and high confluency levels maintained their morphological characteristics following extracellular Ca²⁺ switch. All images were taken at a 10X magnification. Scale bar = 100 μ m

2.4.2 Effect of extracellular Ca^{2+} change on cell growth rate

Basal keratinocytes in the epidermis have a higher mitotic activity compared to keratinocytes in the upper layers exposed to higher calcium concentrations (Wysocki 1999; Fuchs and Raghavan 2002; Tobin 2006; McGrath and Uitto 2010; Kolarsick et al. 2011). To validate this *in vitro*, the growth rate of HaCaT cells in different Ca^{2+} conditions was compared over a period of 8 days with viable cell counts every 24 hours.

A steady increase of cell numbers was observed in all conditions, with a notably slower growth rate in the HC condition (**Figure 2.6 A**). The proliferation rate of HaCaT cells in all Ca^{2+} conditions showed no significant difference until day 4 where a significant decrease of 57%, 40% and 31% was shown in the HC, VLC, and NC, respectively, compared to the LC condition only. At day 5, a 50% decrease in cell numbers was observed in cells grown in HC compared to the VLC and NC, but not the LC condition. Cells grown in HC medium exhibited a marked decrease in cell proliferation of 60% at day 6 compared to the NC condition. The slower proliferation rate of HaCaT cells in HC medium follows the same trend throughout the 8 days, with a significant decrease of 52% compared to the LC condition at day 7 and a non-significant decrease at 53% and 54% compared to the other VLC and HC conditions. Slower proliferation of HaCaT cells in HC medium over time results in significantly lower cell numbers at day 8 with decreases of 54%, 43% and 46% compared to the VLC, LC, and NC conditions, respectively.

The variability in growth rates observed between cells cultured in the different Ca^{2+} conditions owes to different proliferation profiles presented in **Figure 2.6 B**. A graph depicting the typical cell growth curve is shown in **Figure 2.6 C** as a reference representing the four phases: lag phase where cells attach to the plate and start growing, exponential growth (log) phase where cells actively proliferate with exponential increase in cell density, stationary phase (plateau) where cells reach confluence with growth arrest and finally the death phase where cells gradually die. HaCaT cells grown in LC have a shorter lag phase entering their exponential phase earlier, at day 3, compared to cells grown in VLC, NC, and HC medium, which enter their exponential phase one day later, with a longer lag phase (**Figure 2.6 B**).

● CHAPTER 2 ●

HaCaT cells in HC exhibit a more gradual and slower increase in proliferation rates with a less prominent exponential phase lasting from day 3 to day 6. Under NC levels, cells reach a plateau one day (day 6) earlier than cells grown in LC (day 7), whereas a steady increase is observed under VLC levels without reaching a plateau. Under HC levels, a subtle and slow decrease in cell proliferation is observed from day 6 potentially leading to a plateau beyond day 8. The total cell count in LC, VLC and NC conditions does not differ throughout the 8 days despite the shift in the proliferation profile whereas it results in a markedly lower cell count in HC levels (**Figure 2.6**).

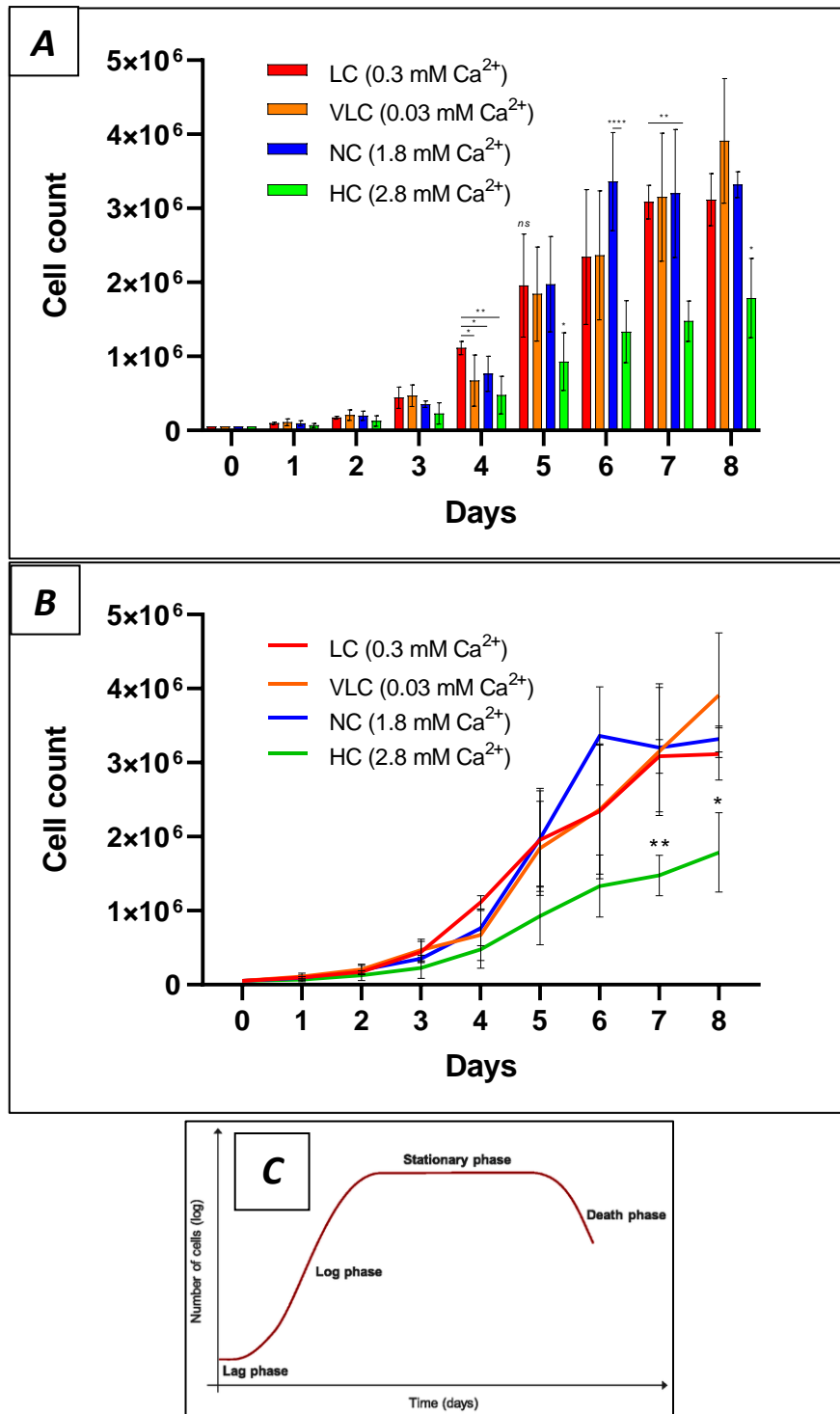


Figure 2.6 Proliferation rate of HaCaT cells grown in very low (VLC), low (LC), normal (NC), and high (HC) calcium-containing medium.

(A) Graph depicting the growth rate of HaCaT cells over a period of 8 days. Cells were seeded at the same cell density (5×10^4 cells per well) and trypan blue dye was used to count viable cells (Independent experimental repeats: VLC: $n=5$, LC: $n=2$, NC: $n=5$, HC: $n=4$). (B) Proliferation profile represented with connected lines. (C) A typical cell growth curve profile made up of four phases. Data are represented as mean \pm SD and significance was reached when p value < 0.05 : *, $p < 0.05$, **, $p < 0.01$, ***, $p < 0.001$. Independent Samples t -test.

● CHAPTER 2 ●

The growth rate of HaCaT cells grown in different concentrations of extracellular Ca^{2+} was monitored in real time by time-lapse microscopy imaging (**Figure 2.7**). When in low Ca^{2+} concentrations (LC), cells reach confluence first, as shown in the image taken at 48h. Cells cultured in VLC and NC reached 70% and 50% confluence, respectively, after 48h. In higher Ca^{2+} levels (HC) cells grow considerably slower reaching 20% only.

Consistent with the previous set of results shown in **Figure 2.6**, cells in LC (0.3 mM) levels enter their exponential phase first whereas high Ca^{2+} (2.8 mM) levels decrease the rate of cell proliferation overtime. A gradual shift in proliferation profiles seems to correlate with the non-linear Ca^{2+} gradient imposed on the cells. LC conditions drives cells to a more proliferative phenotype, whereas cells grown in HC tend to exhibit a more differentiated phenotype. Changes in concentrations of extracellular Ca^{2+} ranging from 0.03 mM to 1.8 mM (VLC – LC – NC) does not seem to affect the proliferation rate of HaCaT cells but generates a shift in the proliferation profile resulting in time-dependent growth rates. Under high extracellular Ca^{2+} concentrations at 2.8 mM (HC) the rate of proliferation is significantly lower resulting in a lower cell count over time leading associated with a more differentiated phenotype.

• CHAPTER 2 •

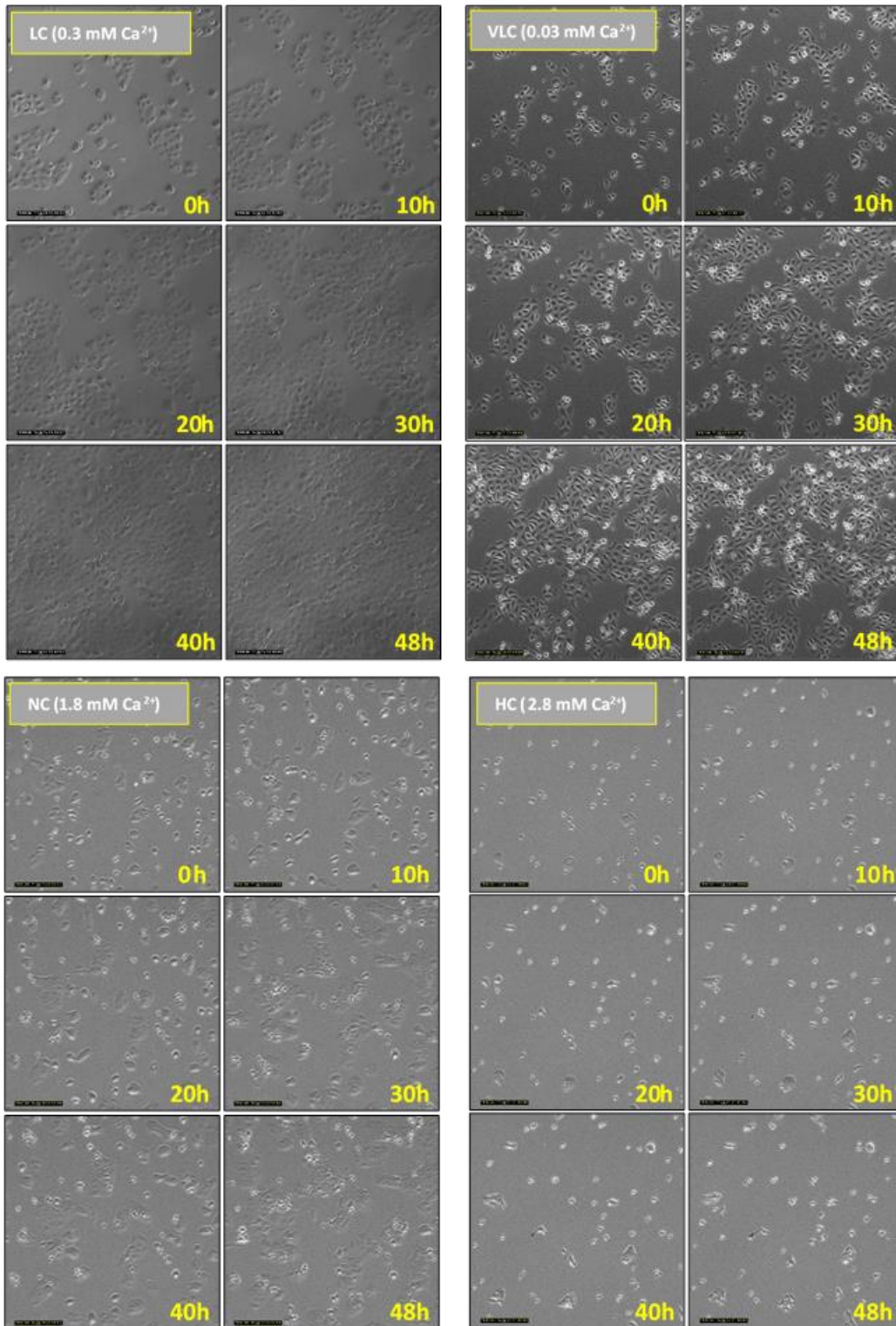


Figure 2.7 Time-lapse micrographs of HaCaT cell proliferation in different Ca²⁺ conditions. Cells were seeded at 1.5×10^5 per well and images were taken every 30 minutes for a total time of 48h. Images taken every 10h (8h for the final image) are shown in this Figure for representation. “0h” represents the moment image acquisition began. (One biological repeat for each condition: $n=1$).

2.4.3 Effect of extracellular Ca²⁺ changes on the biochemical properties of HaCaT cells

The expression of the four protein markers in response to changes in extracellular Ca²⁺ was investigated in HaCaT cells by immunofluorescence and western blot analysis. This allowed assessment of whether they express specific proteins associated with their proliferative/differentiated phenotype.

Antibody specificity was tested by immunofluorescence in human skin samples as shown in **Figure 2.8 A**. Furthermore, skin samples served as a positive control as expression levels and localisation of each marker is well established in the literature. A representative histological H&E image of the human skin with the different layers of the epidermis is shown in **figure 2.8 B**, providing a reference to assess biomarker localisation within the epidermis. As expected, the expression of the proliferation marker K5 was more prominent in the basal layer while the differentiation marker K10 showed a stronger signal intensity in the supra-basal levels (**Figure 2.8 A**). E-Cadherin, considered as a differentiation marker, showed reduced expression in the basal layer and equal levels in the rest of the epidermis (**Figure 2.8 A**). INV expression was almost exclusively localized in the upper granular layer, as expected (**Figure 2.9 A**).

Expression levels of the protein markers showed a dependency on the extracellular Ca²⁺ conditions the HaCaT cells were grown in. The expression of K5 was significantly higher in HaCaT cells grown in lower Ca²⁺ levels (LC/VLC) compared to higher Ca²⁺ conditions (NC/HC), with 100% and 60% K5⁺ (K5 positive) cells in LC and VLC, respectively, confirming a more proliferative phenotype of HaCaT cells when grown in low Ca²⁺ concentrations (**Figure 2.8 C**). Although K5⁺ cells in NC conditions was 100%, a weaker expression was detected in comparison to LC and VLC conditions. The lowest detection was observed in HC conditions with less than 50% K5⁺ cells. In contrast, K10 expression increased significantly in cells grown in the HC condition with approximately 50% of cells being positive, pointing to a more differentiated phenotype under high Ca²⁺ conditions. In NC, very few cells were K10⁺ (K10 positive) but the signal intensity was higher compared to cells in VLC and LC where K10

● CHAPTER 2 ●

detection was very weak. E-cadherin expression showed a similar trend to K10 with increased levels under higher Ca^{2+} concentrations (NC/HC) with almost 80% of positive cells. The strongest signal was noticed in HC conditions and the lowest in VLC. The expression of the late marker of differentiation, INV, was assessed by western blot analysis in HaCaT cells. As shown in **Figure 2.9 B & C**, INV levels were lowest in cells under LC conditions with a significant decrease compared to NC and HC. Moreover, a significant decrease was noticed in VLC compared to HC indicating highest levels of INV under the HC condition.

This data demonstrates that an extracellular Ca^{2+} switch *in vitro* can modulate the level of differentiation of HaCaT cells on the biochemical level by inducing the expression of several proteins of differentiation or proliferation. HaCaT cells can be easily maintained in different extracellular Ca^{2+} concentrations allowing cells to conserve distinct characteristics of a proliferative or differentiated phenotype, potentially mimicking the different layers of the epidermis employable in 3D printing.

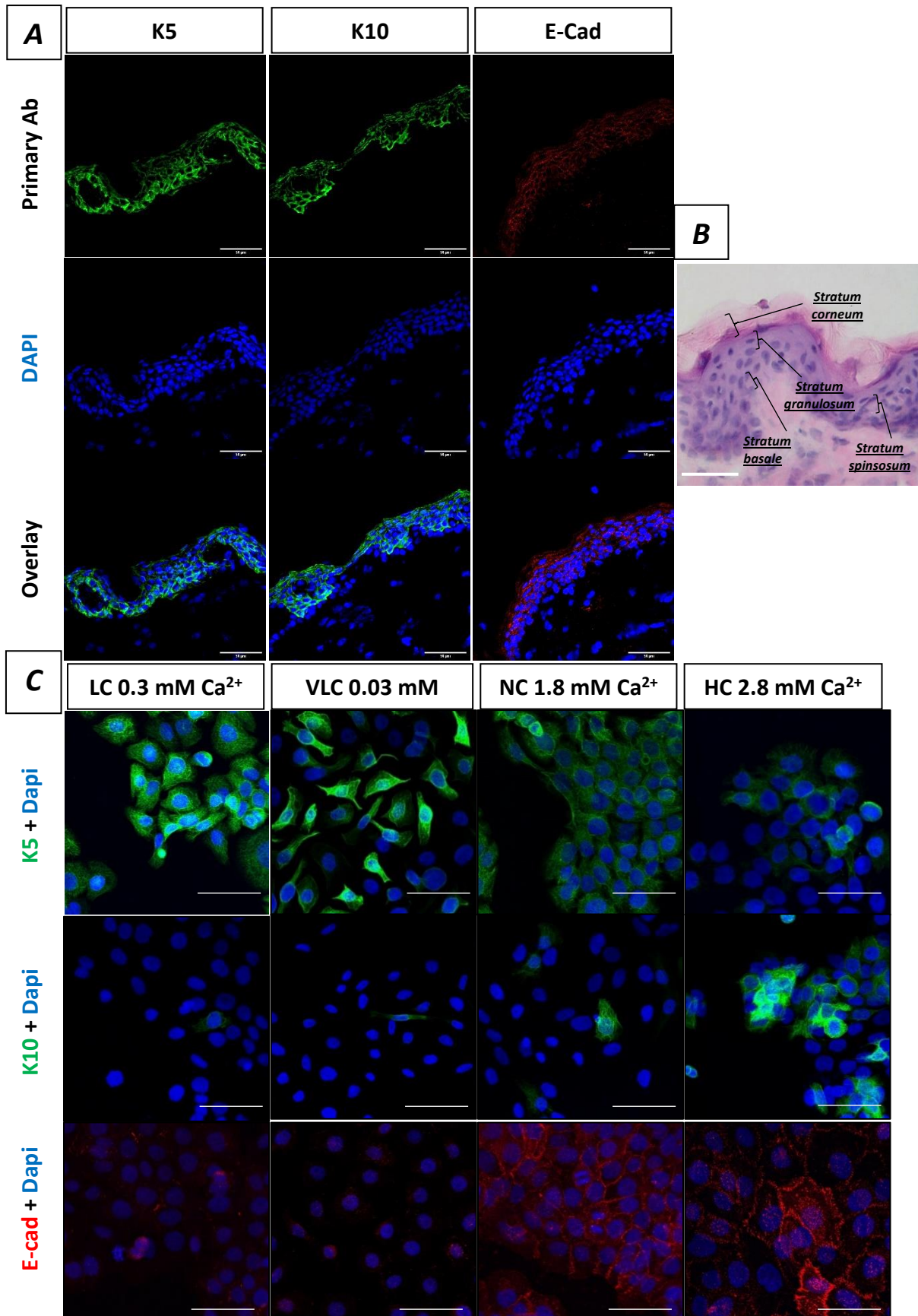


Figure 2.8 Expression of epidermal molecular markers of proliferation and differentiation in *in vitro* cultured KC and in human skin.

Immunofluorescence staining of (A) human skin samples and (C) HaCaT cells, with anti-K5, anti-K10 and anti-E-cadherin antibodies ($n=3$) (Magnification: $\times 60$) Scale bar = $50 \mu\text{m}$. (B) Histological H&E image of a human skin sample showing the different layers of the epidermis. Scale bar = $50 \mu\text{m}$.

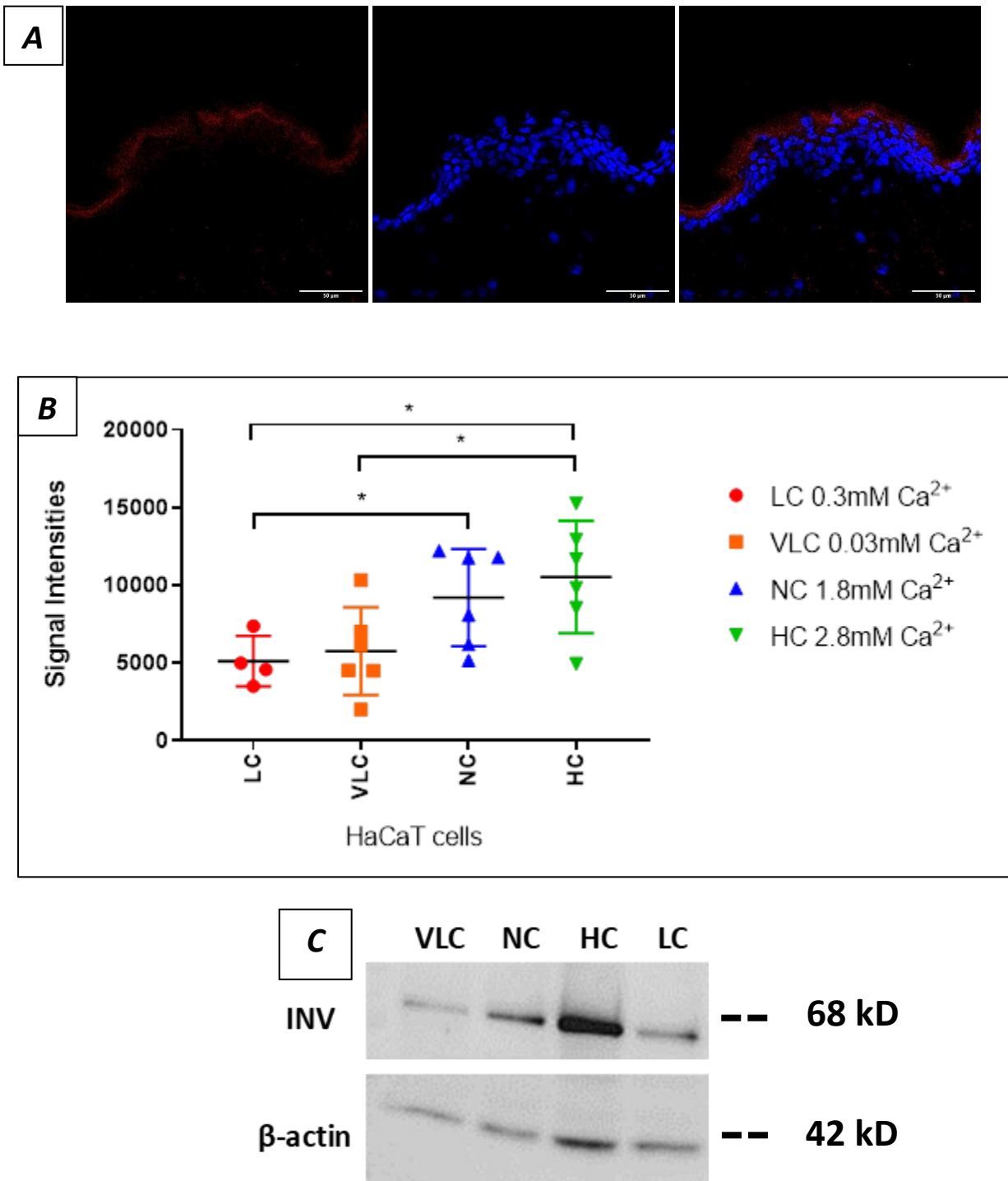


Figure 2.9 Expression levels of Involucrin in human skin and in HaCaT cells grown in different Ca²⁺ concentrations.

(A) Immunofluorescence staining of a human skin sample with an anti-Involucrin antibody (magnification: x60). (B) Signal intensities of Involucrin from repeated immunoblots. Independent experimental repeats: LC: n=4, VLC: n=6, NC: n=6, HC: n=6. (See Section 2.3.4.1.8 for a more detailed description of “Signal intensity” definition) (C) Detection of Involucrin and β-actin by immunoblotting. Data are represented as mean ± SD and significance was reached when p value < 0.05: *, p < 0.05, **, p < 0.01, ***, p < 0.001, Independent samples t test. Scale bar = 50 µm.

2.5 Discussion

The optimal culture conditions to generate keratinocytes populations associated with varying degrees of phenotypic differentiation was evaluated in this chapter. HaCaT cells were cultured and maintained in media containing different Ca^{2+} concentrations akin to the epidermal Ca^{2+} gradient. Lower Ca^{2+} levels (≤ 0.3 mM) promoted the growth of cells with a basal-like phenotype whereas higher Ca^{2+} (≥ 1.8 mM) induced differentiation phenotypes. Four phenotypically different keratinocytes populations were therefore cultured, potentially recapitulating the viable layers of the epidermis. Assessing the reliability of a 3D epidermal skin model requires a fundamental understanding of its biology and microanatomy. It is typically evaluated in morphology and functional molecular markers representing each region of the epidermis, in comparison to a human skin section (Roger et al. 2019). It can also be compared to established differentiated keratinocytes grown in 2D to assess major differences observed between 2D and 3D models. However, this has rarely been explored previously due to the limitations of conventional 2D cell culture.

The Ca^{2+} gradient variability observed in the intact epidermis along with the general knowledge extrapolated from *in vitro* studies helped in selecting the four extracellular Ca^{2+} concentrations in this project (**Figure 2.1**). Previous studies have extensively shown that at low levels of Ca^{2+} (0.03 – 0.1 mM), keratinocytes remain in a basal-like state, whereas in higher levels (>0.1 mM), are induced to differentiate (Bikle et al. 2012). This simplified model has been extended in this project by taking into consideration the non-linear gradient found in the intact epidermis. Therefore, keratinocytes that could potentially mimic the basal layer, were exposed to higher Ca^{2+} levels (0.3 mM) than conventional studies. This could allow the cells to start differentiating all whilst conserving a basal-like phenotype. Indeed, an initial study reported 0.3 mM of Ca^{2+} as the optimal rate for keratinocytes multiplication *in vitro*, which is a major characteristic of basal keratinocytes in the epidermis (Boyce and Ham 1983). keratinocytes exposed to 0.03 mM represent the early spinosum layers with the lowest Ca^{2+} levels as described previously (Malmqvist et al. 1983; Menon et al. 1985; Leinonen et al. 2009; Borowiec et al. 2013). The increasing Ca^{2+} gradient from the viable inner granular layer to the upper one was represented by exposing keratinocytes to 1.8 mM and 2.8 mM, respectively.

HaCaT cells are routinely cultured in 1.8 mM Ca²⁺, however, several studies described it as a high Ca²⁺ environment which induces cells to differentiate (Lemaître et al. 2004; Colombo et al. 2017). The highest concentration chosen was 2.8 mM Ca²⁺ following the work of Deyrieux and Wilson, who demonstrated a rapid shift to a differentiated phenotype under these conditions (Wilson et al. 2007). High cell-density is another well-established pro-differentiating factor *in vitro* (Ura et al. 2004). Indeed, several studies used a combination of a Ca²⁺ switch and cell-density as differentiation stimuli to establish *in vitro* keratinocytes differentiation models (Lemaître et al. 2004; Colombo et al. 2017). Wilson et al. reported a rapid up-regulation of differentiation proteins when HaCaT cells were cultured above 85% confluence in low Ca²⁺ (Wilson et al. 2007). Thus, HaCaT cells were consistently maintained at 70-80% confluence in this study to minimize cell-density effect on the state of differentiation (**Figure 2.4**). If cells reached high densities, it was carefully noted and was considered during result analysis.

The effect of a long-term Ca²⁺ switch on HaCaT cells was first assessed through cellular morphological changes (**Figure 2.4**). When NHEK were grown in high Ca²⁺ (2 mM), an increase in intercellular adhesion was reported with higher E-cadherin formation (Tu et al. 2008); in presence of low Ca²⁺ (0.1 mM), wider spaces between cells with fewer desmosome formation was reported (Watt et al. 1984). With this in mind, similar results were observed in this study, as expected, whereby under lower Ca²⁺ levels (0.3 & 0.03 mM) HaCaT cells were loosely packed and spindle shaped, suggesting loss of intercellular junctions. In contrast, cells grown in higher Ca²⁺ concentrations showed compacted, square shaped cells indicating formation of cell-cell junctions. This confirms the previous reports of Ca²⁺-dependant intercellular adhesion such as desmosomes and e-cadherins, in NHEK (Hennings et al. 1980; Watt et al. 1984; Tu et al. 2008). Micallef et al. demonstrated a similar effect of Ca²⁺ switch on NHEK and HaCaT cell morphology whereas Colombo et al. did not notice any differences in HaCaT cells at ≤80% confluence (Micallef et al. 2008; Colombo et al. 2017). However, Colombo et al. did observe tight cell-cell packing and cuboidal shapes in overconfluent cells at day 14 regardless of the Ca²⁺ concentration, highlighting the effect of cell-density-induced differentiation. The differences may be due to the Ca²⁺ concentration used whereby one used 0.09 mM and 1.2 mM (Micallef et al. 2008) and the other 0.07 mM and 1.8 mM (Colombo et al. 2017) for low and high Ca²⁺-containing medium, respectively. Furthermore, Micallef et al. cultured HaCaT

● CHAPTER 2 ●

cells in keratinocytes Serum Free Media (KSFM) supplemented with epidermal growth factor (EGF) whereas Colombo et al. used the conventional DMEM medium. A previous study has reported that EGF can influence keratinocytes morphology by inducing cell contraction (Haase et al. 2003). Here, DMEM without EGF supplement was used demonstrating a discrepancy with Colombo et al.'s work. Firstly, the Ca^{2+} concentrations used here for the low conditions were different (0.3 mM/0.03 mM vs. 0.07 mM). Moreover, HaCaT cells were given at least 3 weeks in their respective medium before initial characterization in this study, whereas Colombo et al. cultured cells for 6 and 14 days directly after the Ca^{2+} switch before analysis. Indeed, the absence of intercellular adhesion in HaCaT cells was observed after 3 weeks in a low Ca^{2+} environment (Wilson et al. 2007). High cell-density (>90%) resulted in similar intercellular adhesion and shapes as cells maintained in higher Ca^{2+} levels (**Appendix A-2**). Overall, the morphological changes observed in HaCaT cells cultured under different Ca^{2+} levels confirmed previous reports, but also demonstrated how differing culture conditions can affect morphology.

In vitro, an increased proliferative capacity in presence of low extracellular Ca^{2+} was reported in mammalian keratinocytes nearly 40 years ago, whereas exposure to high Ca^{2+} significantly reduces proliferation (Hennings et al. 1980; Boyce and Ham 1983). The effect of Ca^{2+} on the proliferation rate can be evaluated to determine levels of keratinocytes phenotypic differentiation. In fact, low Ca^{2+} levels in the basal layer of the epidermis keeps keratinocytes proliferative, whereas keratinocytes of the suprabasal layers differentiate in presence of higher Ca^{2+} (Bikle et al. 2012; Elsholz et al. 2014). However, the lack of standardised culture conditions has resulted in a poorly understood role of the Ca^{2+} switch on HaCaT proliferation. Here, a significant reduction in HaCaT cell numbers was detected when exposed to the high Ca^{2+} condition (2.8 mM) after 8 days (**Figure 2.6**). A similar trend was previously reported when HaCaT cells were cultured in 1.8 mM compared to cells grown in 0.07 mM (Colombo et al. 2017). Contradictory results were reported by Micallef et al., demonstrating a hyperproliferative response to high Ca^{2+} concentrations (Micallef et al. 2008). However, a Ca^{2+} concentration of 1.2 mM was used in the latter study, lower than 1.8 mM in Colombo et al.'s study, and 2.8 mM in this project. Moreover, EGF was supplemented in the culture medium which has previously been associated with keratinocytes proliferation (Haase et al. 2003). It has been previously reported that decreased proliferation in HaCaT cells is only

● CHAPTER 2 ●

observed in Ca^{2+} concentrations greater than 1.5 mM, demonstrating the degree of insensitivity to extracellular Ca^{2+} (Sakaguchi et al. 2003). Indeed, Sakaguchi et al. exposed NHEK and HaCaT cells to increasing extracellular Ca^{2+} concentrations of 0.03 to 1.5 mM and 1.5 to 10 mM, respectively, and reported a 40% intracellular increase in both cell types (Sakaguchi et al. 2003). These disparities may be due to differences in culture conditions, Ca^{2+} concentrations used in the media, and to the reduced sensitivity of HaCaT cells to environmental factors, in contrast to NHEK (Sakaguchi et al. 2003). Only one approach to this date has provided approximate measurements of Ca^{2+} in the intact epidermis, using the phasor representation of Fluorescent Lifetime Imaging (FLIM) (Celli et al. 2010; Behne et al. 2011). The limited sensitivity range of the Ca^{2+} -dye however, could not detect concentrations below 0.5 μM and above 20 μM (Celli et al. 2010), suggesting a higher Ca^{2+} -sensing ability of keratinocytes *in vivo* compared to *in vitro*, which is reported to initiate at $\sim \geq 100 \mu\text{M}$ (0.1 mM). This discrepancy highlights the limitations of 2D monolayer culture models and how it can affect cellular functions and responses to stimuli. It furthermore emphasizes the need to generate more structurally relevant 3D skin models. Indeed, the immortalized nature and serial passages of a cell line could cause genotypic and phenotypic alterations with time.

Whether HaCaT cells present an appropriate substitute model is questionable and seems to depend generally on the main interest of the study. Nonetheless, it remains widely used due to its ability to retain characteristics and functional properties of normal human keratinocytes differentiation. Despite the differences between studies, exposure to high Ca^{2+} levels is associated with decreased proliferation (**Figure 2.6**); these differences can be explained by variations in experimental procedures and study aims. Here, a significant decrease in cell count in VLC, NC, and HC (0.03, 1.8, and 2.8 mM) conditions was observed compared to the LC condition (0.3 mM) at day 4; however, no difference in cell numbers was seen after 8 days between the LC, VLC, and NC conditions. Interestingly, an original paper described 0.3 mM Ca^{2+} as the optimal level for efficient keratinocytes proliferation (Boyce and Ham 1983). Whilst there was no significant difference in cell count between LC, VLC, and NC conditions after 8 days, it could be noteworthy to extend the incubation period to 14 days, for example, to further evaluate potential variations in cell proliferation. However, this may result in high cell-density, which may be an additional pro-differentiating factor. Further confirmation of the proliferative capacity may be assessed through colorimetric assays, DNA

● CHAPTER 2 ●

synthesis monitoring and cell cycle analysis. HaCaT cells grown in HC show a time-dependant cell number increase suggesting a constant mitotic activity, yet keratinocytes of the upper granular layer have been shown to cease cell division. Raising the Ca^{2+} level to the point of growth arrest or very slow growth may be explored but results in significantly lower throughput of the cell culture process. This concomitantly demonstrates the flexibility and limitations of immortalized cell lines as a 2D *in vitro* model to study keratinocytes differentiation.

Ca^{2+} -induced keratinocytes differentiation is associated with the expression of specific biochemical markers (**Figures 2.8 & 2.9**). The prolonged effect of a Ca^{2+} switch on HaCaT cells *in vitro* was investigated by evaluating the expression levels of four differentiation markers: K5, predominantly expressed in the basal layer, E-Cadherin, mostly present in the supra-basal layers, K10, and INV, mostly restricted to the upper differentiated layers. The data obtained in this study generally coincides with previous observations of Ca^{2+} and cell-density-induced keratinocytes differentiation (Kimutai et al. 2002; Lemaître et al. 2004; Wilson et al. 2007; Micallef et al. 2008; Tu et al. 2008; Borowiec et al. 2013; Colombo et al. 2017). However, the effect of a long term Ca^{2+} switch on K5 expression in keratinocytes has been rarely investigated. In this study, HaCaT cells maintained in lower Ca^{2+} -containing media (LC/VLC) retained a basal-like phenotype expressing high levels of K5. It is worth noting that K5 is an intermediate filament (IF) which dimerizes with Keratin 14 (K14) in the stratified epithelia and are expressed as a pair. Moreover, depleting K14 results in a significant decrease in K5 in HaCaT cells (Alam et al. 2011). With this in mind, a substantial decrease in K14 expression in HaCaT cells was previously reported as a result of high cell-density, regardless of a Ca^{2+} change (Colombo et al. 2017). In contrast, a Ca^{2+} switch from 0.1 mM to 1.8 mM was accompanied with a decreased K5 mRNA and protein expression in NHEK independently of their confluence state (Borowiec et al. 2013). Here, a more or less differentiated phenotype is observed in non-confluent HaCaT cells only. Interestingly, HaCaT cells in higher Ca^{2+} medium showed a progressively weaker expression from NC to HC demonstrating a possible Ca^{2+} -dependant expression of K5 and exhibiting a more differentiated phenotype. However, K5 is supposedly restricted to the basal layer which emphasises the limitations of *in vitro* culture models to study keratinocytes differentiation. In agreement with previous studies, a switch to high Ca^{2+} stimulates an increase in the early and late differentiation markers K10, E-Cadherin and INV

● CHAPTER 2 ●

(Yuspa et al. 1989; Su et al. 1994; Kimutai et al. 2002; Wilson et al. 2007; Micallef et al. 2008; Tu et al. 2008; Borowiec et al. 2013). An early study demonstrated that loss of Ca^{2+} following acute barrier disruption was accompanied with a decreased expression of several differentiation markers *in vivo*, including Loricrin, Filaggrin, and INV (Kimutai et al. 2002). The expression of the markers was restored when the perturbed skin was exposed to high levels of extracellular Ca^{2+} (1.8 mM) and in contrast remained low when exposed to low Ca^{2+} (0.03 mM) (Kimutai et al. 2002). Of note, K10 expression was also investigated by western blot, but the experimental band size observed was smaller than the predicted one, requiring additional interpretations. Moreover, due to technical difficulties, INV was non-detectable by immunofluorescence, which may need further experimental optimisation. Other findings observed no significant effect of a Ca^{2+} change on keratinocytes differentiation, but rather a cell density-dependant effect or even a combination of both (Lemaître et al. 2004; Colombo et al. 2017). Lemaître et al. reported a similar differentiation expression profile of proteins and transcripts between HaCaT cells and NHEK cultured in high Ca^{2+} (Lemaître et al. 2004). In another study, HaCaT cells showed a delayed expression of differentiation markers (Keratin 1 (K1), K10 and INV) when exposed to high Ca^{2+} (1.2 mM), compared to NHEK, under similar culture conditions (Micallef et al. 2008).

The lack of standardized culture conditions makes it difficult to draw comparisons between findings. Furthermore, the underlying mechanisms of Ca^{2+} -induced differentiation are diverse and involve genomic and non-genomic pathways (Bikle et al. 2012). Although the keratinocytes differentiation process is known to be triggered by extracellular Ca^{2+} , studies have shown that it is the increase and sustained release of intracellular Ca^{2+} , mediated by the calcium receptor (CaR), that is vital for differentiation (Bikle et al. 2012; Tu and Bikle 2013; Elsholz et al. 2014). This implies, that the process of tissue maturation of 3D bioengineered skin models relies not only on the addition of external Ca^{2+} as a trigger, but also on the intrinsic expression levels of CaR in the keratinocyte populations and internal Ca^{2+} -mediated pathways. This is demonstrated in 3D organotypic culture models which conventionally use only one keratinocytes population and are grown in static Ca^{2+} concentration levels, resulting in fully stratified epidermal structures and full-thickness human skin models (Reijnders et al. 2015). Indeed, the shift from liquid-liquid to air-liquid-interface (ALI) allows the external Ca^{2+} source to diffuse from the bottom to top layers, triggering the differentiation of keratinocytes

● CHAPTER 2 ●

and epidermal stratification (Sütterlin et al. 2017; Roger et al. 2019). However, as mentioned in **Section 1.2.3**, such skin tissue models still lack in structural and functional complexity, which may be due to the oversimplified culture conditions, fixed Ca^{2+} concentrations, and cell populations used. Indeed, a study revealed that reconstructed human epidermal models demonstrated distinct epidermal morphologies depending on the Ca^{2+} concentration they have been cultured in (Malak et al. 2020). Hence, the model developed in this chapter may not be sufficient in generating more relevant epidermal structures alone and may require a controlled external Ca^{2+} source that can replicate the natural non-linear gradient found in the epidermis (Sütterlin et al. 2017). The presence of Ca^{2+} results in higher intercellular adhesion through an increased formation of tight junctions, desmosomes and adherens junctions (Bikle et al. 2012). This in turn, could trigger a signalling pathway to release Ca^{2+} from the intracellular stores required for differentiation. Indeed, studies reported that deletion of E-cadherin in keratinocytes, a component of adherens junctions, leads to loss of cell-cell adhesion and a concomitant impairment of Ca^{2+} -induced keratinocytes differentiation (Xie and Bikle 2007; Tu et al. 2008; Bikle et al. 2012). Specifically, extracellular Ca^{2+} promotes the formation of the E-cadherin-catenin complex which increases intercellular adhesion; this allows the increased stimulation of CaRs which promote intracellular Ca^{2+} release through the phospholipase C (PLC) signalling pathway. Interestingly, this process provides the epidermis with mechanical strength whilst stimulating keratinocytes differentiation. The critical role intracellular Ca^{2+} plays in keratinocytes differentiation was confirmed by Celli and Behne et al., who revealed that Ca^{2+} is indeed predominantly located in the intracellular stores with very low amounts of extracellular Ca^{2+} throughout the intact epidermis (Celli et al. 2010; Behne et al. 2011). In contrast, Ca^{2+} -regulated differentiation in 2D monolayer culture requires high variations of extracellular Ca^{2+} to induce phenotypic and genotypic changes. This may be explained by the lack of 3D cell-cell interactions and an oversimplified microenvironment in 2D. Taken together, these results imply that different keratinocytes culture conditions can affect Ca^{2+} -sensing properties, resulting in discrepancies between studies. Hence, optimising tissue engineered skin models could benefit from generating keratinocytes at specific phenotypes that respond physiologically to Ca^{2+} variations beforehand. Bio-printing these different keratinocytes populations in defined spatial locations akin to the epidermis, has the potential to recapture essential cellular functions required for efficient tissue maturation. Furthermore, controlling the external Ca^{2+} levels

● CHAPTER 2 ●

could provide a more physiological environment. To this date, very few studies explored the expression of both proliferation and differentiation markers simultaneously in keratinocytes when induced to differentiate. Here, HaCaT cells that have retained a proliferative phenotype still show a weak expression of K10, E-Cadherin, and INV. Equally, differentiated HaCaT cells still retain weak K5 expression. This observation suggests that Ca^{2+} alone is not sufficient to maintain HaCaT cells in a complete proliferative or differentiated phenotype, highlighting potential drawbacks of 2D monolayer culture. Nonetheless, under meticulously optimized and monitored *in vitro* culture conditions, HaCaT cells can be used as a reliable differentiation model. Borowiec et al. emphasized on this by demonstrating that cell culture times, Ca^{2+} concentrations, confluence status, media supplements, presence of absence of serum, or incubation temperatures are variables which influence keratinocytes differentiation *in vitro* (Borowiec et al. 2013). It is clear from these studies that the differentiation process *in vivo* relies on multiple factors which are difficult to control and replicate *in vitro*.

In conclusion, by eliminating the confluence factor and simply switching Ca^{2+} concentrations, HaCaT cells are shown to retain specific differentiation features for long-term experimentation. These characteristics could potentially reflect the functional traits of each layer of the epidermis. Phenotypically proliferative/differentiated HaCaT cells can subsequently be used as a cell-based bio-ink to generate a layered 3D-bio-printed epidermal human skin model. In fact, most epidermal skin models are generated using keratinocytes pre-grown in conventional cell medium (Roger et al. 2019). It would therefore be of interest to investigate how several different phenotypically pre-established keratinocytes populations would behave under 3D conditions in comparison to only one.

Following attendance at the GRC (Gordon Research Conference) on “Barrier Function of Mammalian Skin” in August 2019, an alternative keratinocytes cell source for 2D and 3D human skin models was suggested, known as the immortalized N/TERT keratinocytes (Smits et al. 2017). Developed in 2000 by Rheinwald et al., N/TERT cells are generated by concomitantly introducing a telomerase catalytic subunit (hTERT) and inhibiting the pRB/p16^{INK4a} cell cycle control mechanism in primary neonatal foreskin keratinocytes (Hahn et al. 2000). This resulted in an immortalized keratinocytes cell line that exhibited a normal keratinocytes differentiation pattern and functionality in 2D and 3D organotypic cultures.

● CHAPTER 2 ●

(Smits et al. 2017). The similarities in differentiation characteristics to NHEK proved the superior attributes of N/TERTs over HaCaT cells. One of the major drawbacks of using HaCaT cells in HaCaT-derived skin tissue models is the absence of a stratum corneum as a result of abnormal epidermal stratification and irregular terminal differentiation expression (Boelsma et al. 1999; Schoop et al. 1999). Smits et al. characterised N/TERT keratinocytes in comparison to NHEK and found that N/TERT keratinocytes retain a normal terminal differentiation expression pattern when cultured in 2D. Furthermore, N/TERT-derived skin models showed terminal differentiation and the establishment of a stratum corneum, which is essential to form a functional barrier (Reijnders et al. 2015; Smits et al. 2017). Therefore, N/TERT keratinocytes can potentially result in a more physiologically relevant bio-printed skin model, recapitulating all epidermal layers and retaining more functional characteristics in contrast the HaCaT cell line. Therefore, previous studies investigated that N/TERT keratinocytes should be a more appropriate alternative to HaCaT cells. Hence, HaCaT cells were substituted with the hTERT/Ker-CT (ATCC® CRL-4048™) (hTERT-immortalised human neonatal foreskin keratinocytes), which is immortalized by hTERT and mouse cyclin-dependent kinase 4 (CDK4), for the remainder of the project. The hTERT/Ker-CT line differs to the N/TERT keratinocytes only by the overexpression of CDK4, however, it retains all the aforementioned advantages of the N/TERT keratinocytes cell line as a 2D and 3D skin model (Reijnders et al. 2015; Briley and Shapiro 2016; Beckert et al. 2019). Efforts to phenotypically characterise them in different Ca^{2+} concentrations, replicating the work carried out on HaCaT cells, is still in progress, and should ideally provide a more relevant cell model.

***Chapter 3 Optimisation of
alginate droplet production for
keratinocyte encapsulation –
Development of the bio-ink***

3.1 Introduction

Cell encapsulation in discrete droplets provides a route to 3D bio-printing larger structures from multiple bio-ink droplets (Graham et al. 2017; Richard et al. 2020). Numerous *in situ* cell-encapsulation strategies exist and have been previously reported (Zhang et al. 2020). Generating discrete gelled droplets using microfluidics allows for the encapsulation, compartmentalisation and manipulation of cell populations on the microscale (Sohrabi et al. 2020). Furthermore, such gelled hydrogel droplets can be used as incubators for cell culture or/and as microcarrier systems for the precise deposition of cell-laden droplets (Utech et al. 2015; Graham et al. 2017). Due to its biocompatibility, simple gelation methods and biodegradability, alginate is a common hydrogel choice for cell-encapsulation (Choi et al. 2007). Hence, alginate droplets, can be used as bio-material for the encapsulation of skin cells and subsequently the spatial control over precise deposition of droplets for the fabrication of 3D tissue structures (Richard et al. 2020). Ensuring optimal cell viability and encapsulation relies on the method of encapsulation and alginate hydrogel properties which should provide: (1) low toxicity, (2) minimal external manipulation, (3) sterility, (4) sufficient nutrient delivery and (5) and secure entrapment. One route for uniform microgel droplet production involves the emulsion of two immiscible fluids using T-junction, co-flowing or flow-focusing microfluidic devices, and a subsequent ionic crosslinking method, resulting in internally gelled droplets (Tan and Takeuchi 2007; Zhang et al. 2007; Utech et al. 2015; Morgan et al. 2016). As described in **Chapter 1**, ionic cross-linking involves the formation of hydrogels by coupling ionisable polymers with charged divalent ions. Whilst alginate can be gelled via ionic cross-linking, not all bio-polymers can. Alginate droplet production has been successfully achieved in previous reports by forming emulsions of a sodium-alginate and CaCO_3 solution in an oil phase containing acetic acid (Zhang et al. 2007). Upon contact between both phases, the pH reduction results in the liberation of Ca^{2+} ions, allowing the crosslinking of the alginate hydrogel. The partitioning of acetic acid from the continuous oil phase to the aqueous alginate phase provokes this reduction in pH, which in turn liberates the Ca^{2+} ions. The Ca^{2+} ions then diffuse into the droplet to initiate gelation. In this study, a t-junction microfluidic device was used in combination with the alginate internal gelling method, to produce monodisperse microgels.

● CHAPTER 3 ●

Two main strategies in the production of gelled Ca^{2+} -alginate droplets for cell-encapsulation using droplet-based microfluidics, including external and internal gelation, have been extensively described for the past 15 years (Sugiura et al. 2005; Liu et al. 2006; Tan and Takeuchi 2007; Zhang et al. 2007; Akbari and Pirbodaghi 2014; Chou et al. 2015; Hidalgo San Jose et al. 2018). Whilst internal gelling is achieved through the cross-linking of alginate droplets within the microfluidic device before extrusion, as described in the previous paragraph, external gelling involves the deposition of non-polymerised alginate-in-oil emulsions into oil baths containing Ca^{2+} , which then induces gelation externally (Tan and Takeuchi 2007; Akbari and Pirbodaghi 2014; Ching et al. 2017). A figure recapitulating both strategies is shown in **figure 3.1**. Studies have shown that the internal approach generally provides improved control over droplet gelation, resulting in higher monodispersity, better droplet solidification, and more defined spherical structures (Poncelet 2006; Akbari and Pirbodaghi 2014). One example of an external gelling method is described in Nakajima et al.'s work, whereby two separate microfluidic streams to produce alginate emulsions and CaCl_2 emulsions. Calcium alginate beads were then formed and gelled through coalescence of both droplets. The external method used in this study however, resulted in relatively low monodispersity, low sphericity, and ill-defined beads (Sugiura et al. 2005). Alternatively, Martinez et al. used a different external gelation approach, whereby a double emulsion template consisting of an aqueous alginate core in a mineral oil shell was formed in a coaxial microfluidic device. Alginate droplets were then collected in a CaCl_2 solution and slowly gelled, as they self-separated from the oil shell (Martinez et al. 2012). Despite the efforts to precisely control droplet formation in this study, the gelled Ca^{2+} -alginate beads resulted in non-spherical teardrop shapes which formed in approximately 4 minutes. In contrast, the work of Zhang et al. in 2007 suggested that external gelation provides improved gelation and control over droplet morphology (Zhang et al. 2007).

Droplet-based bio-printing (DBB) has been shown to be versatile, agile, practical, and more importantly, provides efficient precision over bio-material deposition patterning (Gudapati et al. 2016; Jian et al. 2018). Despite these advances, DBB has met several challenges, particularly associated with its printhead design, which restricts control over droplet volume, cell density per droplet, droplet deposition precision, and the use of a wide range of bio-inks (Dababneh and Ozbolat 2014; Gudapati et al. 2016). Due to its ability to

produce scalable monodisperse droplets at high throughput, microfluidic-based microdroplet production is an inexpensive and appealing alternative to overcome some of these limitations. (Huang et al. 2017; Sohrabi et al. 2020). This stems from the user's ability to precisely control a wide range of microfluidic experimental conditions, such as tubing lengths, channel geometry, diameter of internal tubing size, flow rates, bio-ink viscosities, chemical gelation, etc. (Zhang et al. 2020). Diverse microfluidic fabrication techniques, including soft lithography, microstructure milling, and 3D printing, have allowed to generate devices at high resolutions that can range from ~50 nm to 1000 μm , offering high levels of precision and flexibility of droplet scalability. To this date, very few studies have shown potential in generating multi-material/multi-cellular constructs with high resolution, by integrating a droplet-based microfluidic system to a 3D bio-printer, using a low viscosity bio-ink (Colosi et al. 2016; Graham et al. 2017).

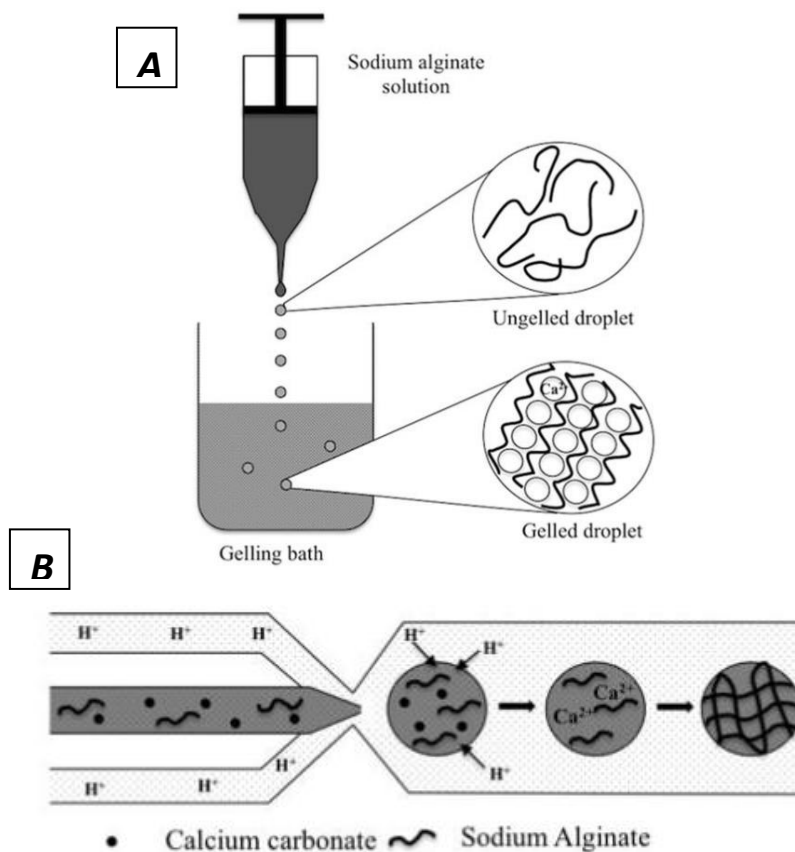


Figure 3.1 Alginate droplet cross-linking strategies.

(A) External gelation is commonly achieved by depositing non-gelled droplets of an alginate solution in an oil bath containing calcium, which allows for droplet cross-linking. (B) Internal gelation is achieved within the microfluidic tubing upon diffusion of acetic acid into the alginate/CaCO₃ emulsion (or other sources of calcium), provoking a pH reduction and liberation of Ca²⁺. The Ca²⁺ then cross-links the alginate polymers to form a hydrogel. Taken from (Ching et al. 2017).

3.2 Aim and objectives

The aim of this chapter was to produce gelled alginate droplets for skin cell encapsulation, using a t-junction microfluidic device. These droplets will serve as the bio-printing bio-material and subsequently the bio-ink upon cell encapsulation, when incorporated in conjunction with the custom-built 3D bio-printer.

The aim was divided into several objectives, including:

1. Characterise alginate droplet formation, gelling properties, droplet morphologies and sizes by exploring different microfluidic parameters, including bio-material flow rates and reagent concentrations.
2. Investigate skin cell encapsulation for cell viability post-encapsulation, cell entrapment efficiency, cell dispersion, and cell density, at the individual droplet scale.

3.3 Materials and Methods

3.3.1 Preparation of microfluidic device and reagents

The oil phase was prepared by diluting 0.5% glacial acetic acid (SIGMA) in mineral oil (SIGMA). For the aqueous phase, 2% low viscosity sodium alginate (SIGMA) was dissolved in deionised water. Nanocrystalline BioUltra precipitated CaCO₃, at a concentration of 75 mg/mL, was added to the alginate solution, then the blend was thoroughly stirred at RT for 2 hours with a magnetic stirrer.

3.3.1.1 Microfluidic device and syringe preparation

The microfluidic device used for all experiments consisted of a Tefzel (ETFE) microfluidic 3 port t-junction with a thru hole size of 0.020" (0.50 mm) and adapted to fit 1/16" (1.5 mm) outer diameter (OD) tubings (Kinesis) (**Figure 3.2 e**). Fluorinated ethylene-propylene (FEP) microfluidic tubings with OD and ID (outer and internal diameter) sizes of 1/16" and 1/32" (~0.8 mm), respectively, were cut using a MicroSolve Technology Clean-Cut90 to generate 2 equal length tubes of 20 cm and one of 9 cm (**Figure 3.2 a & b**). The FEP exit channel of 9 cm in length allowed the extrusion of gelled droplets into a recipient. All tubes were fitted with flangless fittings and ferrules on one end and screwed into the t-junction's internal thread as shown in **Figure 3.2 c, d & e (t-junction end)**. Whilst the longer tubes were fitted in the left and right ports, the exit tube was connected vertically to ensure droplet deposition (**Figure 3.2 h (syringe end)**). The other end of the longer tubes was inserted into a coned fitting which in turn was connected to a Luer Lock Adaptor (**Figure 3.2 f & g**). This allowed for a leak-free connection to 3 mL plastic syringes (**Figure 3.2 i**). The syringe driver injects the liquid phases into the microfluidic tubes allowing water-in-oil droplets to form when both oil and aqueous phases are combined in the t-junction device. A schematic representation of the t-junction microfluidic assembly is demonstrated in **figure 3.2 j**, with an indication of the dimensions.

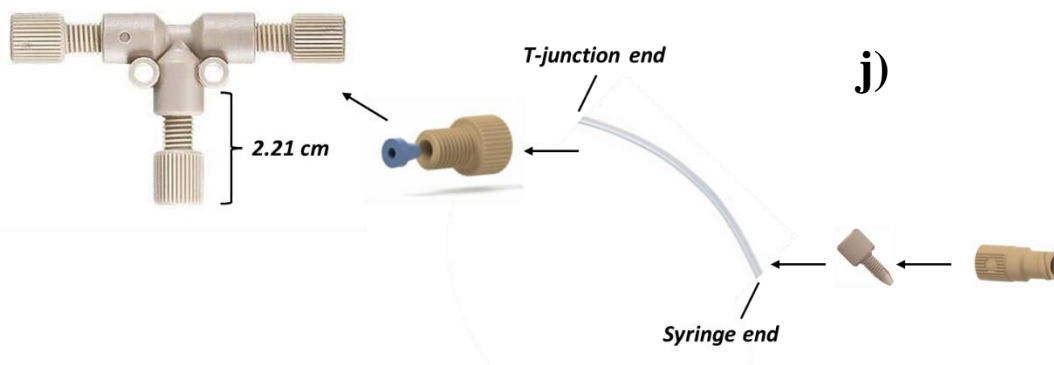
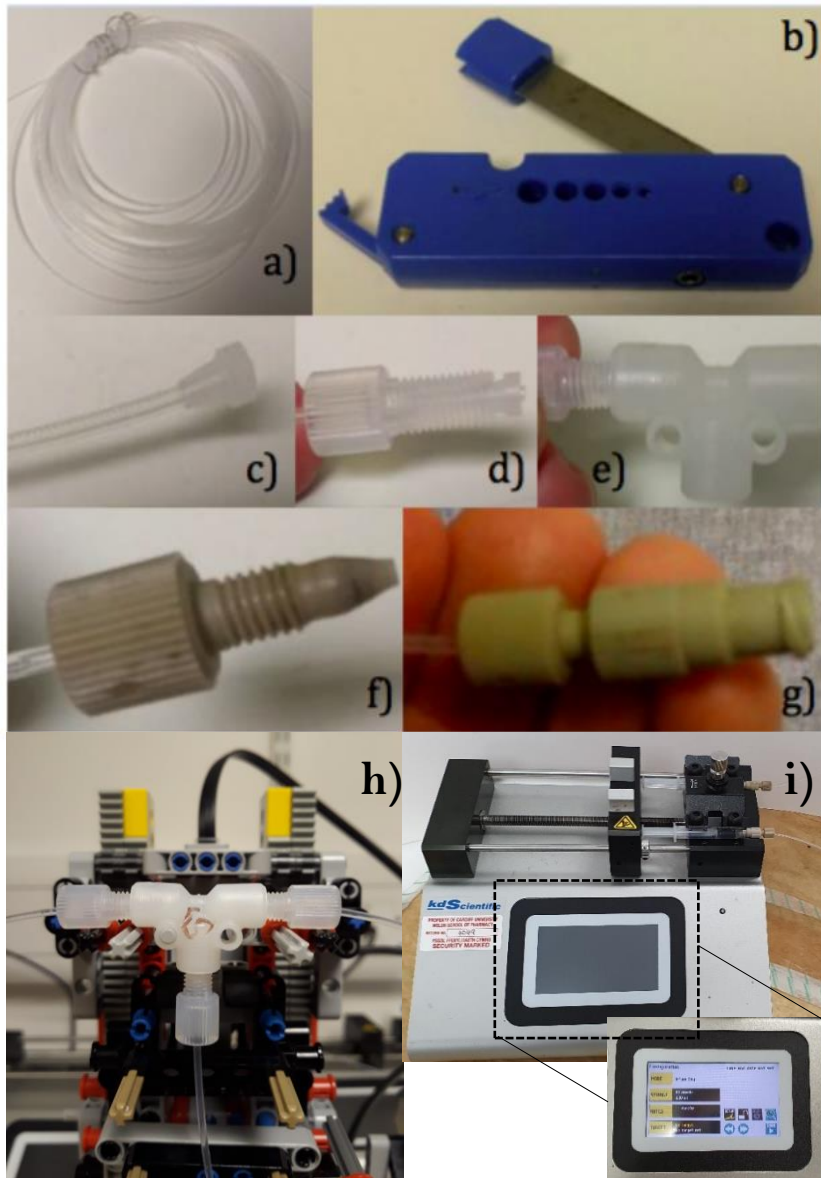


Figure 3.2 Accessories used for the microfluidic device.

a) FEP Tubing, b) MicroSolve Technology Clean-Cut90, c) ferrule attached to the end of the tubing (t-junction end), d) flangless fitting, e) attachment of a tubing to a ETFE t-junction port, f) coned fitting inserted into the tube (syringe end), g) Luer Lock Adaptor attached to the coned fitting, h) attachment of the 3 tubings to the t-junction, and i) 3 mL syringes installed on a syringe driver showing the interactive setup menu. (Co-produced with Katie Harvey & Katherine Sloan). j) Schematic representation of the microfluidic t-junction and tubing assembly procedure.

3.3.1.2 *Alginate droplet generation – Preparation of the bio-material*

Alginate droplets were generated by means of a droplet-based microfluidic t-junction device (Kinesis, SUPELCO) (**Figure 3.2 & 3.3**). Glacial acetic acid in mineral oil (SIGMA) was continuously delivered into one channel as the continuous oil phase (green circle), whereas the aqueous phase or alginate/CaCO₃ solution was delivered into the opposite channel (aqueous phase: blue circle) (**Figure 3.3 A**). Both phases were delivered via 3 mL plastic syringes with a diameter of 8.66 mm. The interfacial tension between the two immiscible phases creates consistent monodisperse water-in-oil emulsions. Subsequently, alginate droplets are gelled downstream of the t-junction via ionic crosslinking with bivalent Ca²⁺, as described in **Section 3.1** (Tan and Takeuchi 2007; Utech et al. 2015; Morgan et al. 2016). The liquid materials are pumped using a dual syringe infusion only pump (KDScientific) at the desired flow rates (mL/hr) (**Figure 3.2, 3.3 B & C**). In the case different flow rates were investigated, 2 dual syringe pumps were used for each syringe. Droplets were deposited either in oil, air, cell medium, or dH₂O, depending on the experimental procedure.

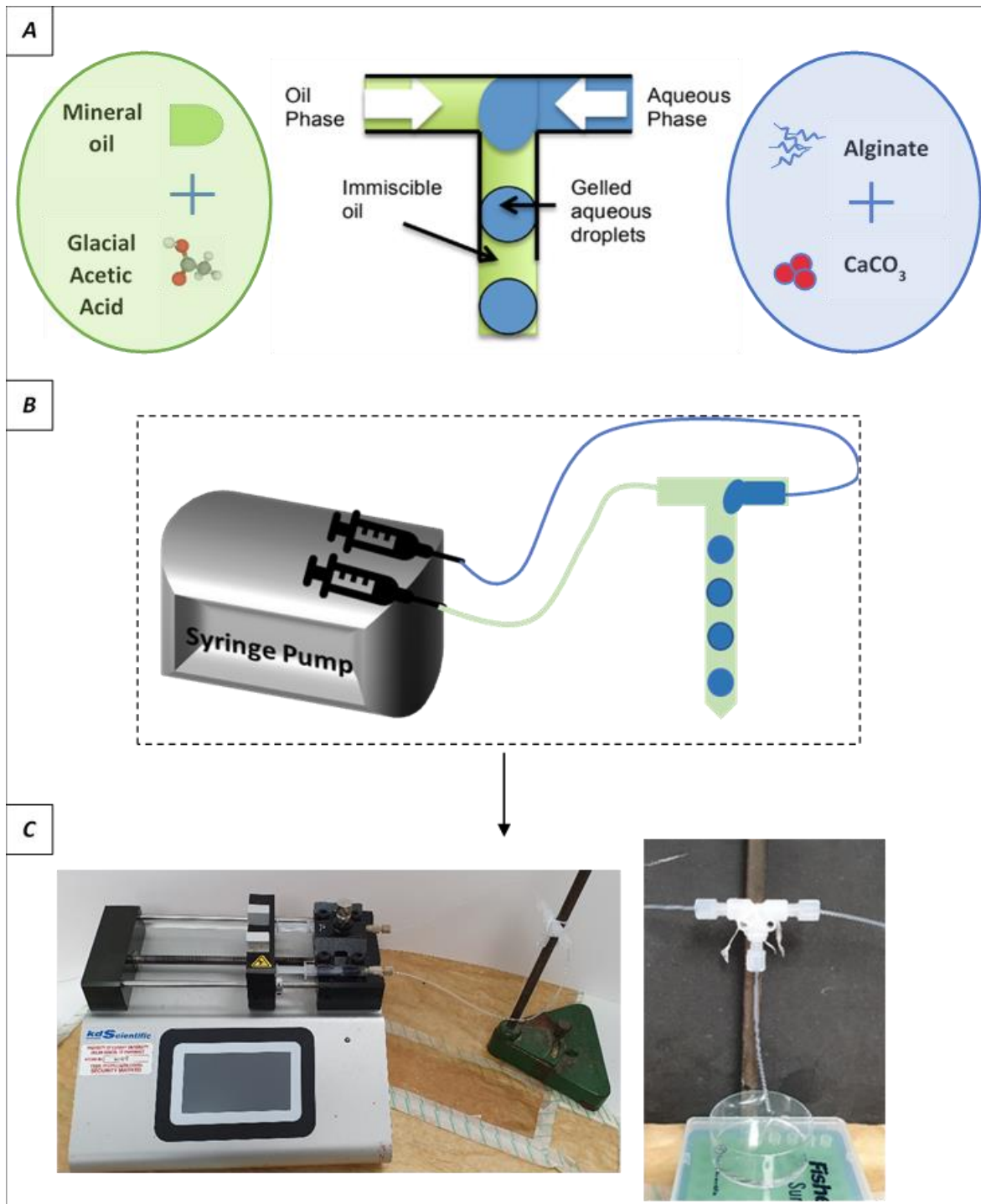


Figure 3.3 Alginate droplet production using a microfluidic t-junction device and infusion-only dual syringe pump.

(A, B) Schematic representations of the t-junction microfluidic method to generate gelled monodisperse alginate droplets, which constitute the bio-material. The t-junction and microfluidic channels are connected to syringes containing the bio-ink (oil phase and alginate phase) which are installed on a syringe pump allowing to drive the contents at defined flow rates (mL/hr). (C) Images of the dual syringe infusion only pump (KDSscientific) used, shown on the left and an enlarged photo of the t-junction device on the right. During optimization, the system was installed on a laboratory stand holder. (Co-produced with Katherine Sloan).

3.3.2 Alginate droplet generation imaging and analysis

To determine droplet length and frequency, the microfluidic system was mounted vertically on a light block next to a reference-measuring tool, with a USB-camera focused on the exit tubing (**Figure 3.4 A**). To ensure efficient fluid flow, the microfluidics system was flushed with ethanol then deionized water with clean syringes between each run. Generated waste was deposited in an empty 50 mm Petri dish (THERMO) and disposed of in an acid waste bottle. Droplets were extruded by submerging the exit tube directly in a clean 50 mm Petri dish containing mineral oil. The exit tubing length, or nozzle, measured 9 cm in length, which provided an adequate distance when installed onto the z-axis unit of the LEGO® 3D bio-printer, which is explained more in detail in **Chapter 5**. Reagents were drawn into separate 3 mL syringes and air bubbles were removed. Syringes were installed on syringe drivers and the desired flow rate in mL/hr along with the syringe diameter size (8.66 mm) were selected on the syringe driver. To ensure full infiltration of the microfluidic channels with the reagents, the fast-forward flow button was pressed. The start button was manually pressed on each syringe driver in unison and the exit tubing was monitored. Droplets flowed for 10-20 seconds before analysis to ensure a consistent flow. For each tested flow rate, a 6 second video was recorded, then flow was paused, and the process repeated to collect 3 videos. The oil phase was run at 10 mL/hr to flush the exit tubing between tested flow rates. Testing began with reagents flowing at equal rates of 2 mL/hr, increasing by increments 2 mL/hr until reaching 20 mL/hr. Additionally, flow rates were tested when 0.5% AA in mineral oil was kept constant (10 mL/hr and 20 mL/hr). At a constant oil or continuous phase of 10 mL/hr, the alginate or aqueous phase was increased by increments of 2 mL/hr, starting with 2 mL/hr until 10 mL/hr. At 20 mL/hr, the aqueous phase was increased by increments of 4 starting at 4 mL/hr until 20 mL/hr.

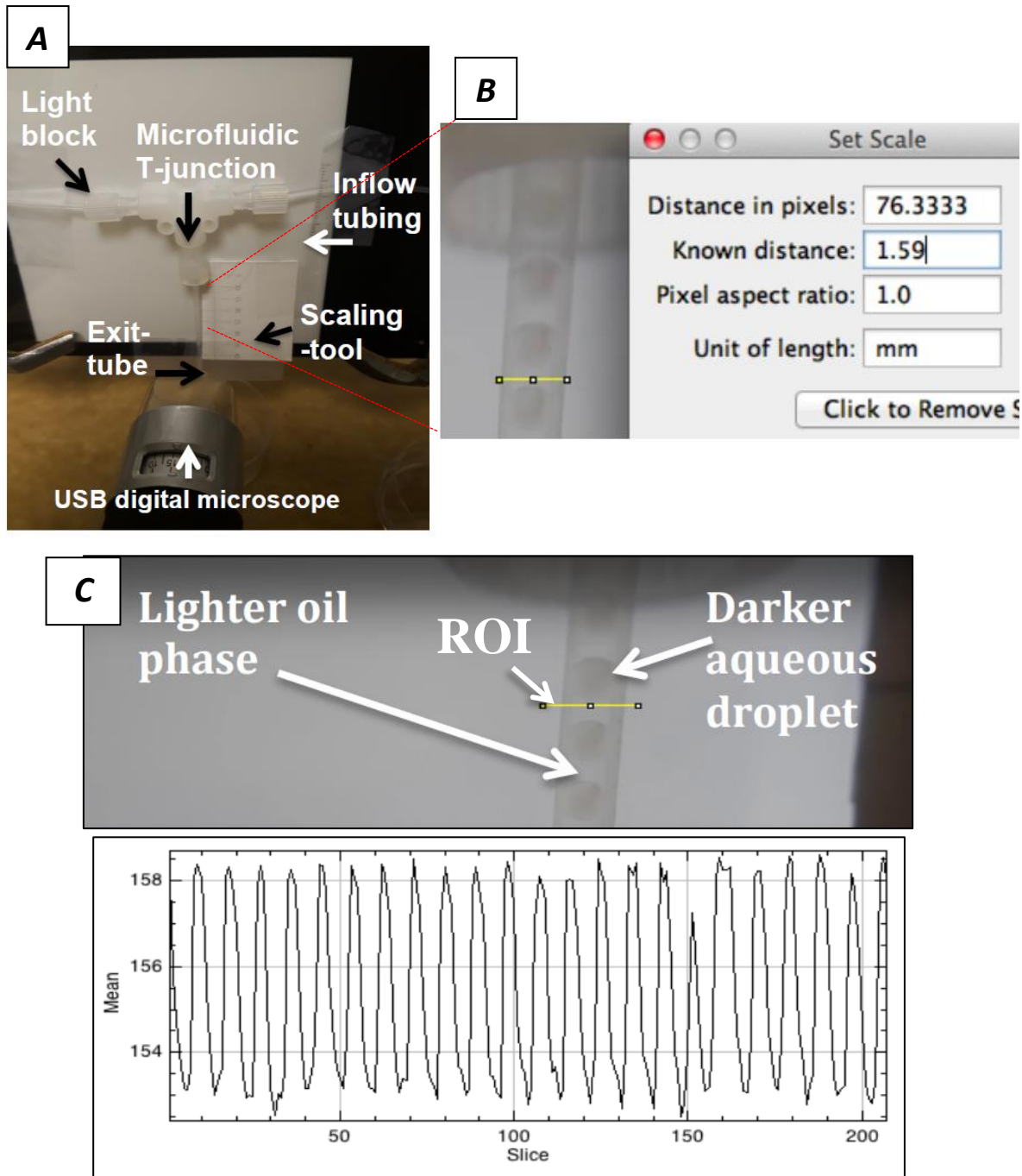


Figure 3.4 Experimental setup and analysis of microfluidic droplet generation.

(A) The microfluidic system was mounted vertically on a light block with a reference scaling tool and a USB-camera focused on the exit-tubing. (B) A screen shot of the scaling-tool used in Image J (Fiji) to measure droplet length, which was scaled to the known tubing diameter (1.59 mm). (C) The microfluidic Z-axis and its profile plot generated in Image J. Pixel values or “peaks” (Y-axis: Mean) are plotted against video frame number (X-axis: Mean), defined by the colour contrast between the droplets and the oil phase. (Produced by Katherine Sloan).

3.3.2.1 *Evaluating alginate droplet frequency production*

To evaluate frequency, the number of droplets passing through the tubing per unit of time was assessed. Similarly, the flow of droplets was recorded, and the video was analysed through Image J (Fiji). A straight line (yellow line), corresponding to the region of interest (ROI) was drawn across the tubing, under one droplet, at a fixed location; as droplets passed the line, a change of contrast between darker droplets and the lighter oil phase was detected and translated to a fluctuation in pixel numbers (**Figure 3.4 C**). A plotted graph of pixel numbers (y-axis) detected by passing through the line at different frames (x-axis) was generated. Thus, each peak represents one droplet that has passed the ROI. The x-coordinates of 10 peaks were recorded and the distance between peaks was analysed (n=9), to determine the average number of frames between two droplets. This was converted to seconds by dividing the number of frames by the video recording frames per second. Droplets per second were calculated by dividing 1 by the number of seconds. Frequency average and standard deviation over three videos were calculated. Real-time image processing through video recording provided a temporal analysis method to efficiently identify and count droplets; this was done by assessing the colour contrast between the aqueous and oil phase over a specific period (per frames) (**Figure 3.4**).

3.3.2.2 *Evaluating alginate droplet length*

The length of droplets was evaluated through analysis of the recorded droplet production. Videos were imported into the Image-J (Fiji) software and scaled by drawing a straight line (straight-line tool shown in yellow) across the known outer tubing diameter (1.59 mm) (**Figure 3.4 B**). Once the scale was set, a straight line was drawn across a droplet's length to assess droplet dimensions. Individual droplets were measured by analysing 3 droplets per video. The inner tubing diameter was fixed at 0.79 mm; therefore, droplets were not measured in width, regardless of the morphology generated in the microfluidic tube. A schematic of the measurements conducted are shown in **Figure 3.5**.

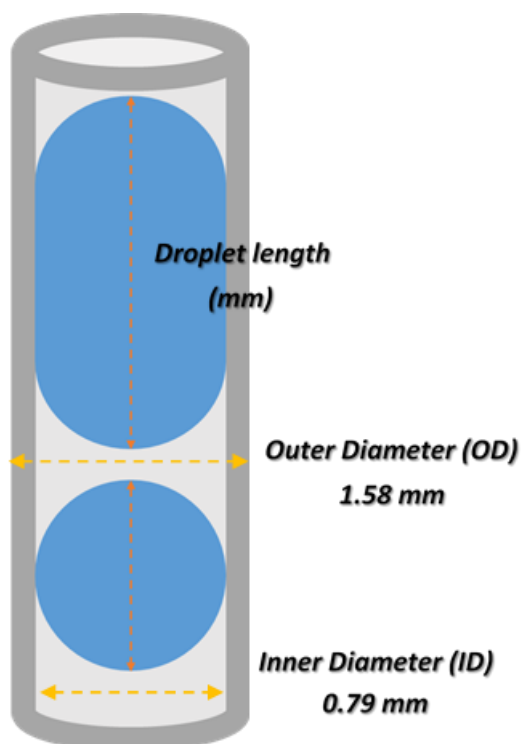


Figure 3.5 Schematic design of alginate droplet measurements inside a microfluidic tube.

3.3.2.3 Evaluating alginate droplet gelling quality

Alginate droplets were generated as described previously, using the same microfluidic device (**Figure 3.4 A**) and exit tube length (9 cm). To determine whether the droplets were gelled within the microfluidic channel upon extrusion, the droplets were directly extruded in dH₂O in 24 well plates at different flow rates and reagent concentrations. The effect of flow rate changes on droplet gelling quality was evaluated using fixed reagent concentrations of 75 mM CaCO₃, 2% alginate, and 0.5% glacial acetic acid, as described in a previous study (Baxani et al. 2016). The effect of reagent concentration variations on droplet gelling quality was investigated at a fixed equal flow rates of 4 mL/hr for both the oil/AA and alginate solution, but with different CaCO₃ concentrations of 0.75 mM, 0.5 mM, and 0.25 mM in 2% alginate were tested in combination with increasing concentrations of glacial acetic acid in mineral oil of 0.1%, 0.2%, 0.3%, 0.4%, and 0.5%.

Each well containing droplets was imaged using a phase contrast microscope (Olympus IX50) coupled with a 9 megapixel (MP) digital camera (AmScope) to evaluate the overall

quality of droplets at a 4x magnification. Images were captured using the ToupView (ToupTek) software. Sufficient alginate droplet gelling was assessed by observing several characteristics including: overall shape (sphericity), size, contact between droplets (fused or individual), and visibility of the droplet perimeter. Contact between droplets was considered the most important factor in evaluating sufficient gelling of individual droplets. For each tested condition, 1 - 2 minutes of continuous droplet extrusion was allowed per well. A minimum of 5 different regions of the well was captured to analyse the variability of droplet formation. Gelling efficiency was evaluated by imaging the overall outer structure of droplets through phase contrast microscopy observation.

3.3.2.4 *Measuring alginate droplet length post-extrusion*

Phase contrast images taken of extruded droplets were analysed using Image J (Fiji). A 1 mm stage graticule slide was used to calibrate image analysis and set the scale bar. Once calibrated, the diameter of individual droplets was measured by drawing a straight line across each one. A numerical value corresponding to the size of droplets in mm was generated by choosing the option “Analyse”, then “Measure”. Non-spherical droplets in “capsule” or oval shapes were measured along the long axis (length) and across (width). The number of droplets measured varies from each condition but was maximized to the amount of visible gelled droplets.

3.3.3 *Generating keratinocyte-laden alginate hydrogels – Preparation of the bio-ink*

For cell encapsulation, an alginate-media (DMEM) solution was prepared as described in **Section 3.3.1.2**, but by using cell culture media (DMEM) instead of dH₂O. Calcium-free DMEM was supplemented with 1% Penicillin-Streptomycin-Glutamine (PSG). The alginate-DMEM solution were stirred for 2 hours at room temperature. The plastic syringes used were sterile and disposable. HaCaT cells were detached, suspended in culture medium, and counted using a haemocytometer, as described in **Section 2.3.1.5**. The cells were centrifuged,

the medium was discarded, then the cells were resuspended at a density of 10 million cells per mL in the alginate-DMEM solution, also known as the bio-ink.

The bio-ink (HaCaT cells + alginate + DMEM solution) was gelled in the form of HaCaT cell-laden alginate droplets as described in **Section 3.3.1.2**. Alginate gelation occurs internally in the forms of droplets, allowing for the encapsulation of cells within individual droplets. Monodisperse alginate droplets containing HaCaT cells were generated using the microfluidic device and extruded in a 50 mm Petri dish containing sterile mineral oil. After bio-printing, the sterile mineral oil was removed, and the cell-laden hydrogel droplets were washed twice with PBS then kept in culture medium at 37° and 5% CO₂ in an incubator.

3.3.4 Determining count and viability of encapsulated keratinocytes

An equal flow rate of oil to alginate phase of 4 mL/hr was used to generate the cell-laden droplets. HaCaT cells were either seeded at a 150,000-cell density per well in a 6 well plate for the control condition in 2D culture, or 3D bio-printed in alginate droplets to yield the same number per well. A cell density of 10⁶ cells/mL was mixed in the alginate/CaCO₃/DMEM solution, and an equal flow rate of 4 mL/hr was used. To generate 150,000 cells per well, a final extrusion volume of 15 µL per well was determined. Therefore, a continuous extrusion time of 13.5 seconds per well was carried out. HaCaT cells were 3D bio-printed in sterile mineral oil which was directly removed after extrusion, and the cell-laden droplets were washed and maintained in culture medium at 37°C and 5% CO₂ in an incubator. Cell-laden alginate droplets were incubated in a filter sterilised solution of 250 mM Ethylenediaminetetraacetic acid (EDTA) and PBS for 15 minutes for complete droplet dissolution and cell liberation (further optimization for alginate droplet dissolution was explored in **Chapter 6**. The cells were transferred to a 15 mL falcon tube with fresh DMEM and centrifuged at 160 x g for 5 minutes. The supernatant was discarded, and the cells were resuspended in 5 mL of fresh DMEM. Cell viability was assessed by counting the number of viable and dead cells using the trypan blue exclusion method as described in **Section 2.3.1.5**.

For the control condition, cells were incubated with trypsin-EDTA (0.9 mM EDTA) (Thermo) for 15 minutes then cell viability was assessed, similarly.

3.3.5 Imaging cell-laden alginate droplets – Bio-ink

3.3.5.1 Phase contrast microscopy

Phase contrast and brightfield images of HaCaT-encapsulated alginate droplets were captured using an IX70 Olympus Inverted Phase Contrast Microscope (Olympus) and the analysis getIT software for image analysis.

3.3.5.2 Confocal microscopy

Prior to encapsulation, HaCaT cells were fluorescently labelled with either the CellMask™ Green plasma membrane stain (Thermo) or a Live/Dead stain (ab115347) for confocal microscopy visualization. The Live/Dead staining solution is a mixture of two fluorescent dyes: The live cell dye which labels viable cells green and the dead cell dye labelling dead cells red. The green, fluorescent dye is membrane permeant and produces green fluorescence only following enzymatic activity in viable cells. The red dye only penetrates dead cells with compromised plasma membranes and produces red fluorescence upon binding to the DNA.

Once detached with trypsin from the flask, HaCaT cells were washed with PBS and DMEM (to neutralize any remaining trypsin), counted and centrifuged at 160 x g. The supernatant was discarded, and the cells were incubated with the Live/Dead stain in the dark at a working solution of 10x in sterile PBS for 10 minutes. Then, HaCaT cells were washed 3 times by centrifuging, discarding the supernatant and adding sterile PBS. After the final wash, the PBS was discarded, and the cells were resuspended in a sterile alginate/CaCO₃/DMEM solution at a final cell density of 10⁷ cells/mL. The cell solution was transferred to a sterile 3 mL syringe for subsequent cell encapsulation with the microfluidic device and syringe driver.

Fluorescently encapsulated HaCaT cells for viable and dead cells were visualized using the Confocal Zeiss LSM (Laser Scanning Microscopy) 880 with a 10x objective. The excitation wavelengths used for the Live and Dead dyes were 495 nm and 528 nm, respectively. Optical slices of 10 μm thickness in the Z-axis were taken using the full Z-penetration distance of the confocal microscope lasers. Images were captured on the Zeiss ZEN software and further analysed using Image J (Fiji) for 3D reconstitution and grouped Z projection.

3.3.5.3 *Light sheet microscopy*

As described in the previous section, HaCaT cells were stained with the Live/Dead dye before encapsulation and resuspended in the alginate/ CaCO_3 /DMEM solution, producing the bio-ink, at a cell density of 10^7 cells/mL. LSFM (Light Sheet Fluorescent Microscopy) (Zeiss Lightsheet z. 1) is an optical method that requires samples to be either embedded in a transparent polymer or suspended in a capillary with a refractive index of 1 (i.e., FEP (Fluorinated Ethylene Propylene) tubes) (Bennett and Ahrens 2016). The sample is then suspended in a liquid filled chamber (PBS or dH_2O) with two illumination objectives exciting a focal plane from the sides. The fluorescent emission is detected by a separated detection objective. To prepare the polymer, a solution of 1% low melting point agarose (Thermo) was prepared in deionised water. Cell-encapsulated droplets were printed and maintained at 37°C in culture medium. When it reached 37°C , a few cell-encapsulated droplets were mixed in the agarose solution. A small volume of melted agarose and cell-laden droplets were subsequently aspirated using a piston into a glass capillary of 1.5 mm diameter. Once completely solidified within the tube, the embedded droplets are pushed into the light sheet chamber for image acquisition. A magnification of 5x was used with excitation wavelengths for the Live and Dead dyes at 495 nm and 528 nm, respectively. Optical slices of 10 μm were taken for the full length of the glass capillary. The Zeiss ZEN software was utilized to visualize the cell-laden droplets and 3D reconstitution/grouped Z projection was carried out using Image J (Fiji).

3.4 Results

3.4.1 Preparation of the bio-material: Characterising alginate droplet formation using microfluidics

The aim of this thesis is to develop a bio-printer consisting of a microfluidic nozzle, capable of generating alginate droplets for skin cell encapsulation. Alginate serves as the bio-material in this study, and upon incorporation of living cells and cell culture solution, becomes the bio-ink. Alginate droplet production was generated by merging two immiscible phases through a t-junction microfluidic device, as described in **Section 3.3.1.2**. Characterising droplet formation, which includes droplet production speed, i.e., droplet frequency, and droplet size, is a vital step in anticipating and optimising bio-printing resolution. By investigation these parameters, the programmable x/y/z stage movements (explored in **Chapters 4 & 5**) can then be programmed to move in unison with droplet frequency and size to allow the patterning of high-resolution 2D and 3D structures. Overall, evaluating these characteristics would be valuable in generating patterns with high resolution droplet spacing and printability.

3.4.1.1 Investigating the relationship between alginate droplet production frequency and flow rates

An increase in droplet production rate, or droplet frequency, is reported to be a result of an increase in flow rates of the dispersed (aqueous) and continuous (oil) phases (Seemann et al. 2012). This in turn, can impact the droplet spacing and overall droplet printability when optimized in combination with the printer's speed. Therefore, adjusting the flow rates and droplet frequency will allow to identify optimal printing speeds required for an optimal bio-printing resolution (**Chapter 5**). Droplet frequency was evaluated through video recordings within the stand-alone Z-axis microfluidic set-up described in **Figure 3.4**, whilst varying flow rate and flow ratio. Increasing the flow rate of both aqueous and oil phases equally or aqueous alone (whilst keeping the oil phase constant at 10 or 20 ml/hr), resulted in an increase of droplet frequency, as expected (**Figure 3.6**). Higher oil to aqueous ratios resulted

in 2-fold and 4 -fold increase in droplet frequency at 10 and 20 ml/hr, respectively, compared to equal flow rates. However, for all conditions, the droplet frequency increase becomes gradually lower as flow rate increases until a plateau is reached. This is specifically observed at 10 ml/hr and 20 ml/hr in all conditions. At equal flow rates, a linear increase in droplet frequency is observed until 10 ml/hr, where the increase gets marginally smaller, then plateaus at 20 ml/hr. At different flow ratios, a decrease in droplet frequency is also observed when the aqueous flow approaches the constant oil phase flow (red and green data sets). Overall, a positive correlation is observed between flow rate and droplet frequency.

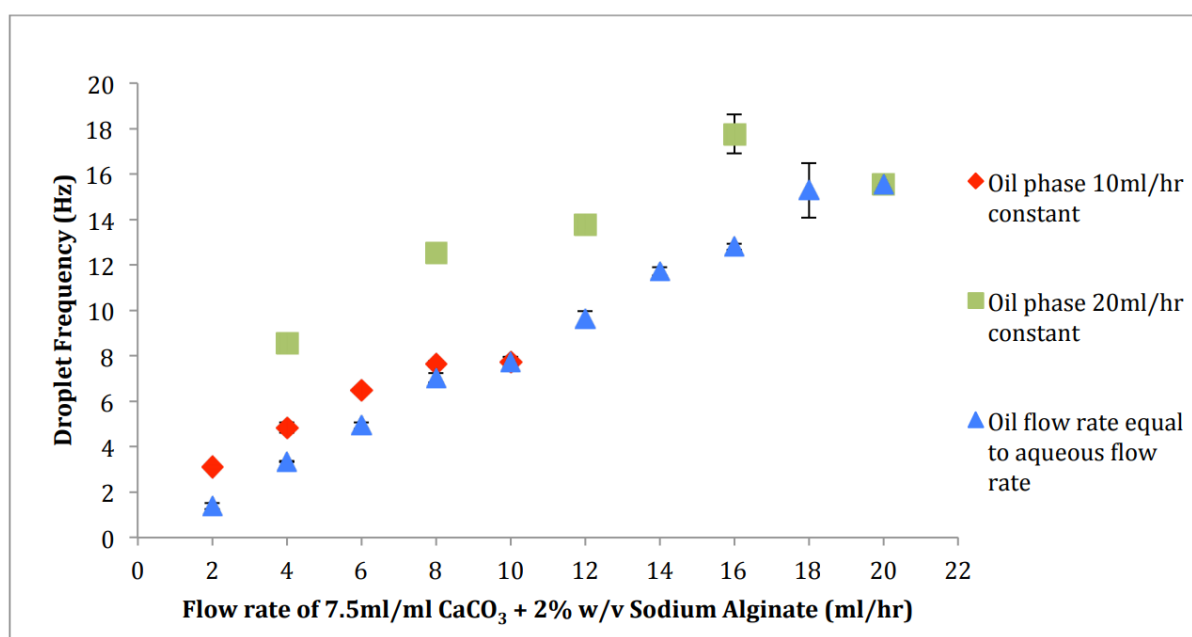


Figure 3.6 Effect of flow rate change on droplet frequency.

Droplet frequency (Hz) produced under different flow rates and flow ratios of reagents (ml/hr). Error bars represent the standard deviation (SD). 10 peaks were evaluated (n=9) for 3 videos (n=27). (Produced by Katherine Sloan).

3.4.1.2 Investigating the relationship between alginate droplet length and flow rates

The next step was to evaluate the relationship between flow rate and droplet length. Control over droplet size is of key importance, as it significantly impacts droplet packing and the overall structural arrangement of bio-printed patterns. Furthermore, the distance between encapsulated cells within a bio-printed structure influences cellular function (Utech

et al. 2015). Droplet packing can be determined through the characterisation of droplet frequency, droplet size, and print-speed. Identifying print speed relies on the numerical values generated from droplet frequency and size results. Increasing the aqueous flow rate when oil is kept constant (red and green data sets) resulted in an increase in droplet lengths, demonstrating a linear relationship between the two variables **Figure 3.7**. Moreover, at constant aqueous flow rates of 4 ml/hr and 8 ml/hr, an increase in oil flow rate is shown to decrease the droplet length significantly. In contrast, a non-linear relationship is observed between flow rate and droplet length at equal flow rates (blue data set), with the largest droplets shown at 2 ml/hr and 20 ml/hr. This is due to the increasing and decreasing droplet lengths under equal flow rates. The length of each droplet was determined within the microfluidic tubing and is used as the parameter which defines droplet volume. In this experimental setup, the droplet length was not assessed after extrusion from the microfluidic tubes and therefore droplets may not have completely gelled. Gelling was a parameter that was evaluated in the following sections of this chapter. Trendlines have been added to demonstrate the correlation between droplet length and flow rate changes. Droplets longer than the inner tubing diameter indicated elongated and non-spherical morphologies overall. Indeed, the fixed inner tubing diameter prevents droplets from expanding in width, whereby only length can be quantified.

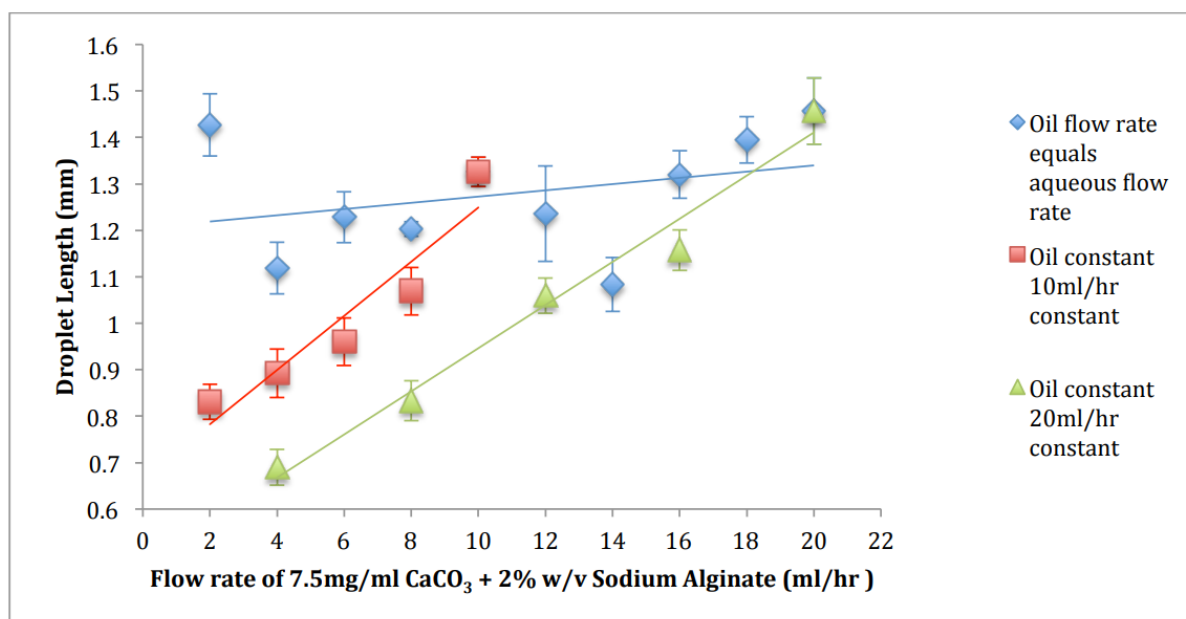


Figure 3.7 Effect of flow rate change on droplet length.

Droplet lengths (mm) were evaluated whilst varying the oil and aqueous phases flow rates (mL/hr). Error bars represent the standard deviation (SD). Gradient lines are added for clarity and to demonstrate trends. $n=9$ for each data point. (Produced by Katherine Sloan).

3.4.2 Preparation of the bio-material: Investigating the relationship between alginate droplet gelling quality, flow rates, and concentration of reagents

Sufficient droplet gelation is an important step in the bio-printing process to ensure efficient cell-encapsulation. Furthermore, the bio-printed resolution and overall structural integrity of the fabricated construct partly depends on the extent of droplet gelation and droplet rigidity. Internal gelling of droplets relies on the manipulation of several parameters, including the residence time (droplet transit time) of the droplets and chemical reaction (Tan and Takeuchi 2007); residence time is defined by how long a droplet remains in the exit tube or how long it takes a droplet to move from the t-junction once formed, to exit the tube, which is determined by the flow rate, length and diameter of the outlet channel, and the chemical reaction depends on the concentration of reagents used (Tan and Takeuchi 2007). Sufficient gelling in this study is observed when droplet-droplet fusing is minor and when the structural integrity of most individual droplets is maintained after extrusion in dH₂O. Furthermore, droplet integrity was considered favourable when the outer perimeter was definable. Droplet lengths and morphology may differ to the measured lengths in the tubing, due to the level of fluidity or rigidity upon extrusion, which rely on several factors including, extent of gelation, reagent concentrations, droplet transit time (residence time) and tubing diameter.

3.4.2.1 Investigating the impact of flow rate changes on alginate droplet gelling quality

The optimal flow rate ratio was determined by evaluating the overall quality of gelled droplets following extrusion from the microfluidic device. At constant oil flow rates of 20 and 10 mL/hr, fusing between droplets was minor when the alginate flow rate was at 2 and 4 mL/hr (**Figure 3.8, 3.9, & 3.10**). Furthermore, integrity was high with a visible outer perimeter highlighting the structure of individual droplets. An increase in the aqueous flow rate resulted in more droplet-droplet fusing, less structural integrity, and more droplet distortion, because of lower residence time in the tubing. As the aqueous flow rate rises, the size in droplet length

increased from 620 μm to 880 μm , when the oil phase was at 10 mL/hr. This increase was more subtle when the oil phase was at 20 mL/hr. As both oil and alginate flow rates approach similar values, droplets result in increased sizes, up to 1 mm in average length (**Figure 3.10**). At equal flow rates of 2 and 4 mL/hr, fusing rarely occurred between droplets, indicating efficient gelling properties and sufficient residence time. However, fractures in droplets were frequent at equal flow rates of 2 mL/hr, indicating high levels of rigidity because of longer residence time. Fusing between droplets occurred more often as equal flow rates increased with indistinguishable outer perimeters, low to no structural integrity, and distorted shapes. Morphological shifts upon flow rate variations were evident. At a constant oil flow rate of 20 mL/hr, low alginate flow rates (2 and 4 mL/hr) produced a majority of spherically shaped droplets, whereas higher flow rates resulted in minor shifts to elongated or capsule shaped droplets accompanied by a small increase in droplet lengths. A similar trend was observed when constant oil flow rate was decreased to 10 mL/hr. As the alginate flow rates approached that of the oil, droplets appeared more elongated and longer. Equal flow rates resulted in a mix of spherical and elongated droplets, all four conditions. However, increasing flow rates equally had little effect on the morphology and size of droplets, in line with the measurement of droplet lengths in the microfluidic tube (**Figure 3.7**). Taken together, when constant oil phase flow rates of 20 and 10 mL/hr are used, an aqueous flow rate of 2 mL/hr was considered favourable, whereas at equal flow rates, 4 mL/hr was the favourable option. This conclusion is drawn solely on the quality of individual droplet gelling, and not on the morphological and size outcome. However, morphology and size remain important characteristics which inform on the extent of gelation upon extrusion.

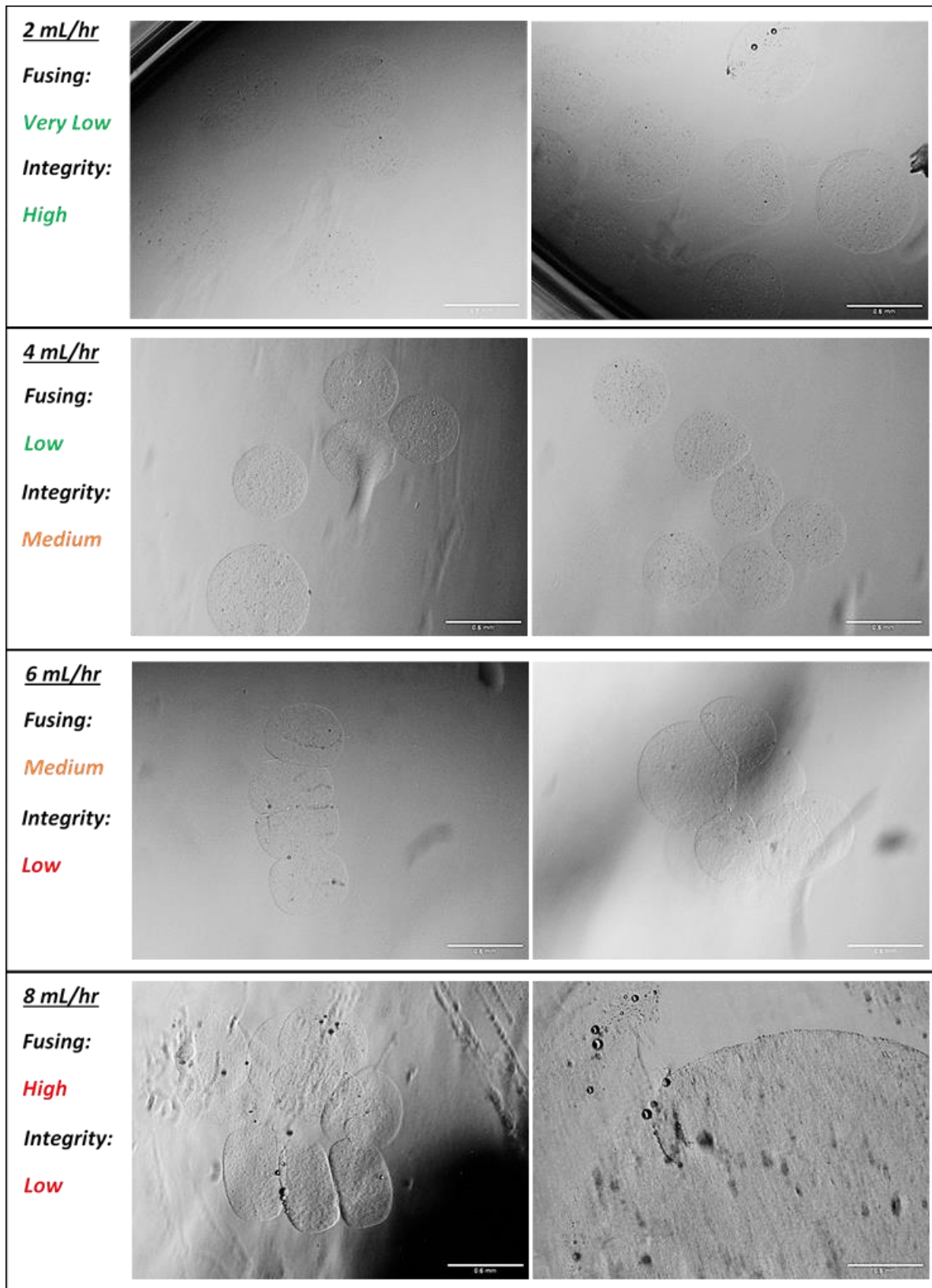


Figure 3.8 Droplet gelling quality assessment at a constant mineral oil flow rate of 20 mL/hr and different alginate flow rates.

Different ROI from each condition (well) were captured using phase contrast microscopy. “Size” represents the length of droplets when measuring non spherical droplets. Experimental repeats were conducted on different days (n=3). Scale bar = 500 μ m.

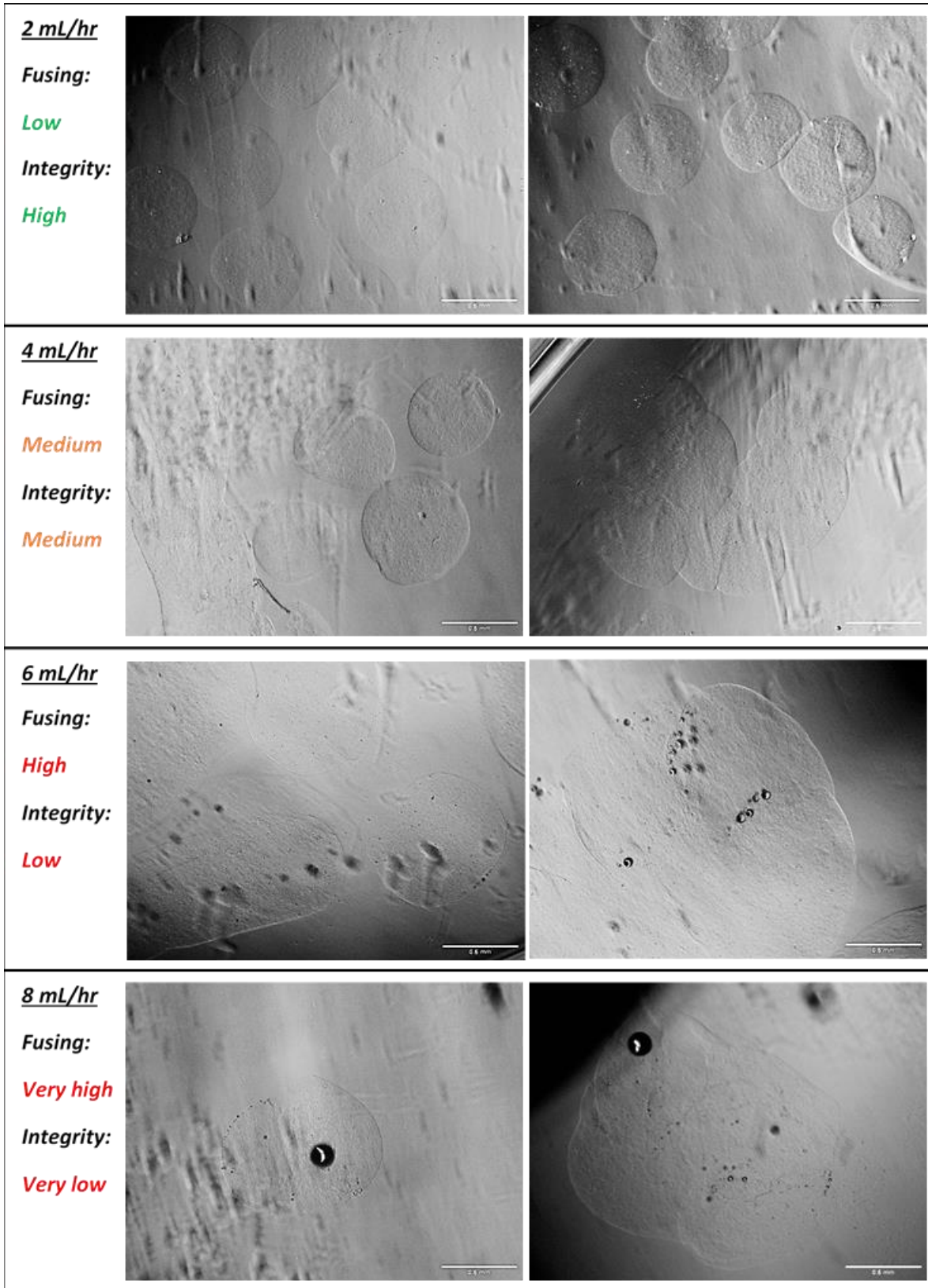


Figure 3.9 Droplet gelling quality assessment at a constant mineral oil flow rate of 10 mL/hr and different alginate flow rates.

Different ROI from each condition (well) were captured using phase contrast microscopy. “Size” represents the length of droplets when measuring non spherical droplets. Experimental repeats were conducted on different days ($n=3$). Scale bar = 500 μm .

● CHAPTER 3 ●

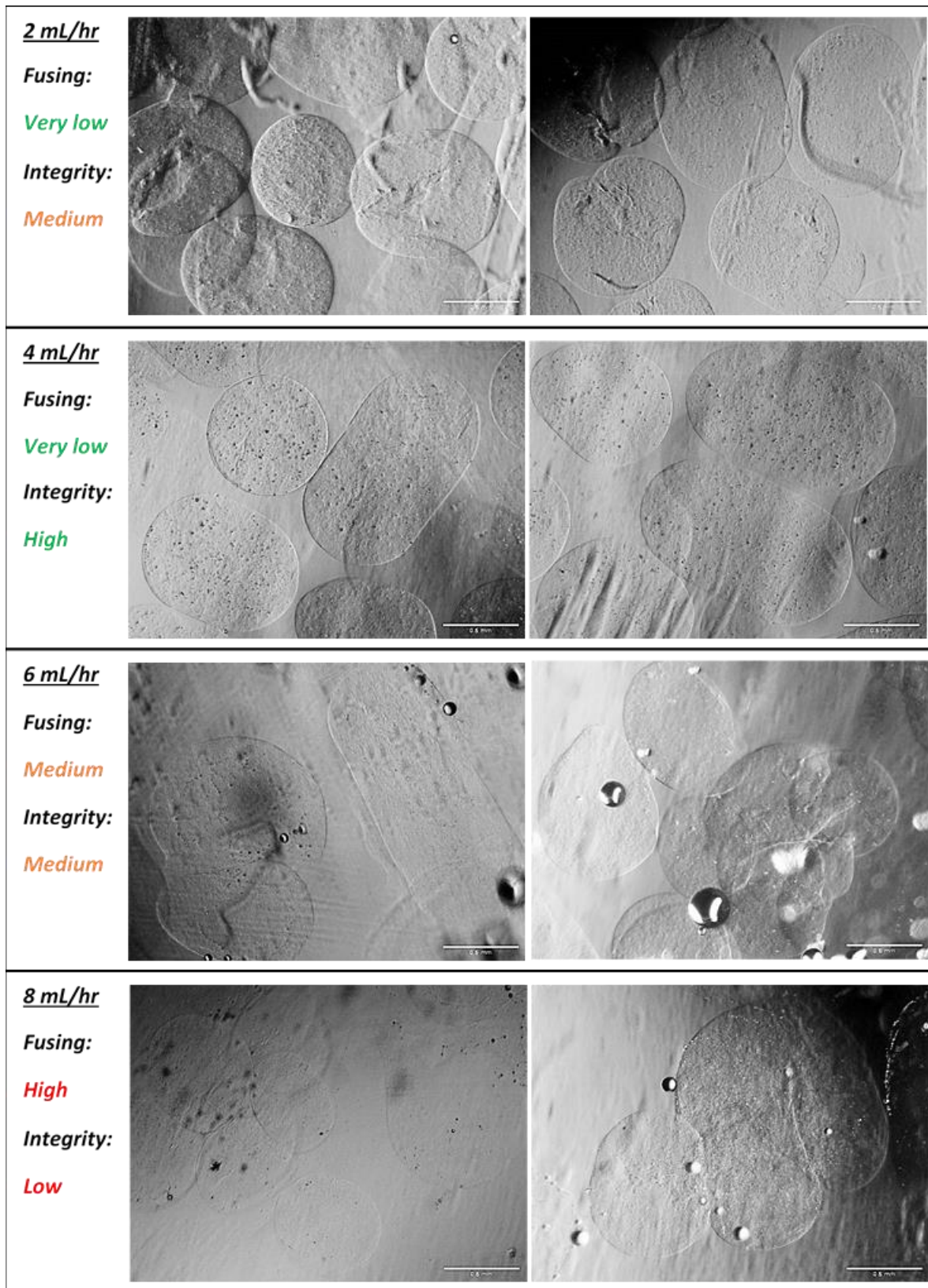


Figure 3.10 Droplet gelling quality assessment at equal flow rates of alginate and mineral oil. Different ROI from each condition (well) were captured using phase contrast microscopy. “Size” represents the length of droplets when measuring non spherical droplets. Experimental repeats were conducted on different days (n=3). Scale bar = 500 μ m.

3.4.2.2 Investigating the impact of reagent concentration changes on alginate droplet gelling quality

The gelling of alginate droplets at a CaCO_3 concentration of 0.25 mM was deemed insufficient, overall, with frequent fusing between droplets and visibly disintegrated shapes (**Figure 3.11**). As the acetic acid concentration increased, gelling was more distinguishable. Nonetheless, the quality of the droplets remains lower than desired at these concentrations. A CaCO_3 concentration below 0.5 mM in combination with acetic acid levels lower than 0.4% resulted in an undesirable droplet quality (**Figure 3.11**). This suggests that with the current microfluidic exit tube length and diameter, a minimum of 0.4% acetic acid and 0.5 mM CaCO_3 are required to generate sufficiently gelled droplets (**Figure 3.12**). Nevertheless, increasing the concentrations to CaCO_3 and acetic acid to 0.75 mM and 0.5%, respectively, had a minor improvement on the droplet integrity (**Figures 3.12 & 3.13**). Indeed, the peripheral outline of each droplet was more pronounced and seemed to indicate a higher structural integrity. Droplet sizes were not significantly affected by the change in reagent concentrations, resulting in droplets around 1.1 mm in average length for all conditions. However, a trend showed that droplets were marginally larger at lower concentrations of CaCO_3 and acetic acid, indicating larger emulsions and coalescence between droplets. Morphologies showed a majority of elongated shaped droplet with few spherical ones. Taken together, these results demonstrate that alginate droplet gelling is optimal when equal flow rates of 4 mL/hr are used and concentrations of CaCO_3 and acetic acid are at 75 mM and 0.5%, respectively. However, this is specific to the microfluidic device setup using a 9 cm long exit nozzle.

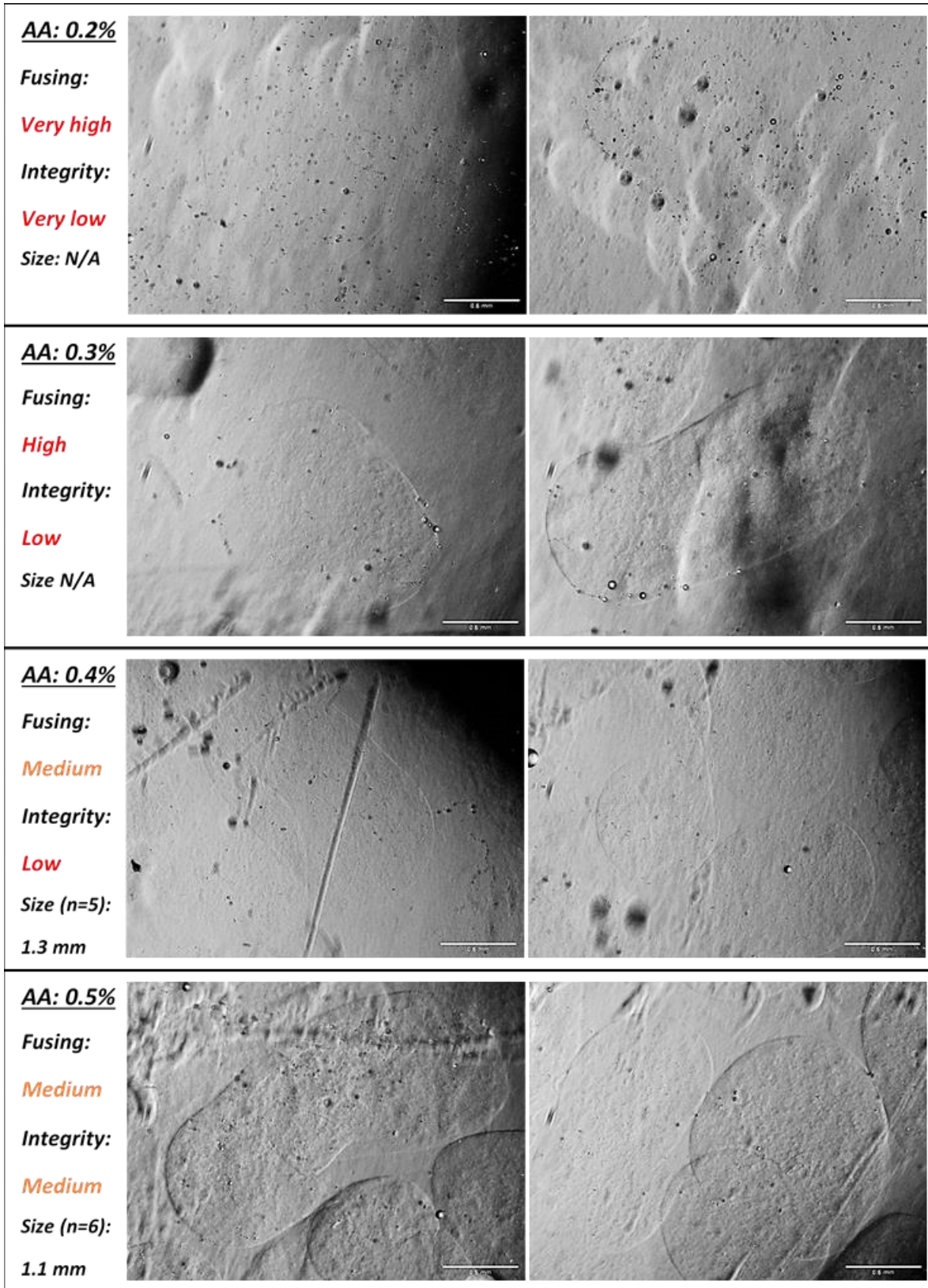


Figure 3.11 Droplet gelling quality assessment using 0.25 mM CaCO₃ and varying levels of acetic acid. Different ROI from each condition (well) were captured using phase contrast microscopy. “Size” represents the length of droplets when measuring non spherical droplets. Experimental repeats were conducted on different days (n=3). Scale bar = 500 µm.

● CHAPTER 3 ●

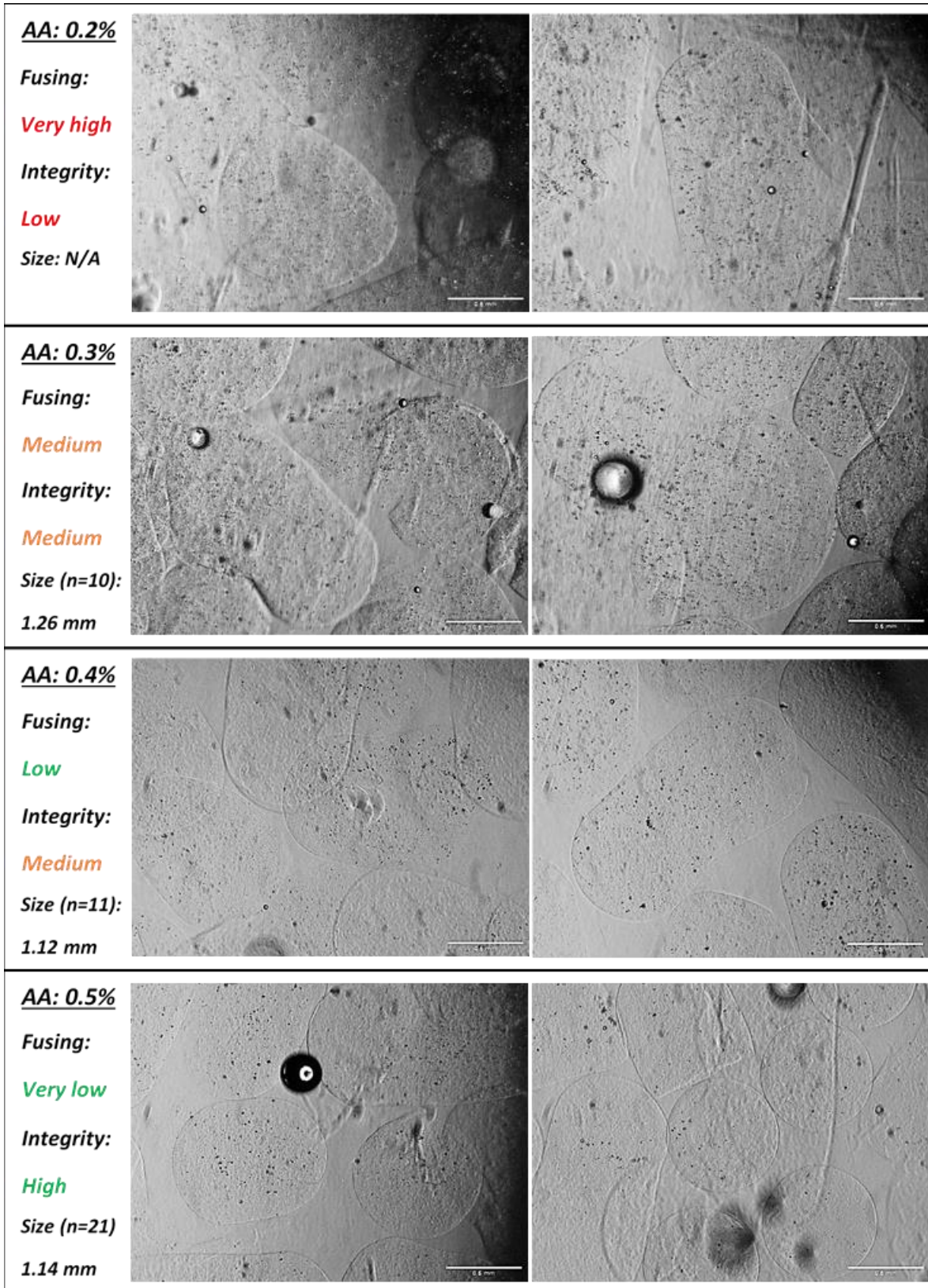


Figure 3.12 Droplet gelling quality assessment using 2% alginate, 0.5 mM CaCO₃, and varying levels of acetic acid.

Different ROI from each condition (well) were captured using phase contrast microscopy. "Size" represents the length of droplets when measuring non spherical droplets. Experimental repeats were conducted on different days (n=3). Scale bar = 500 μm.

● CHAPTER 3 ●

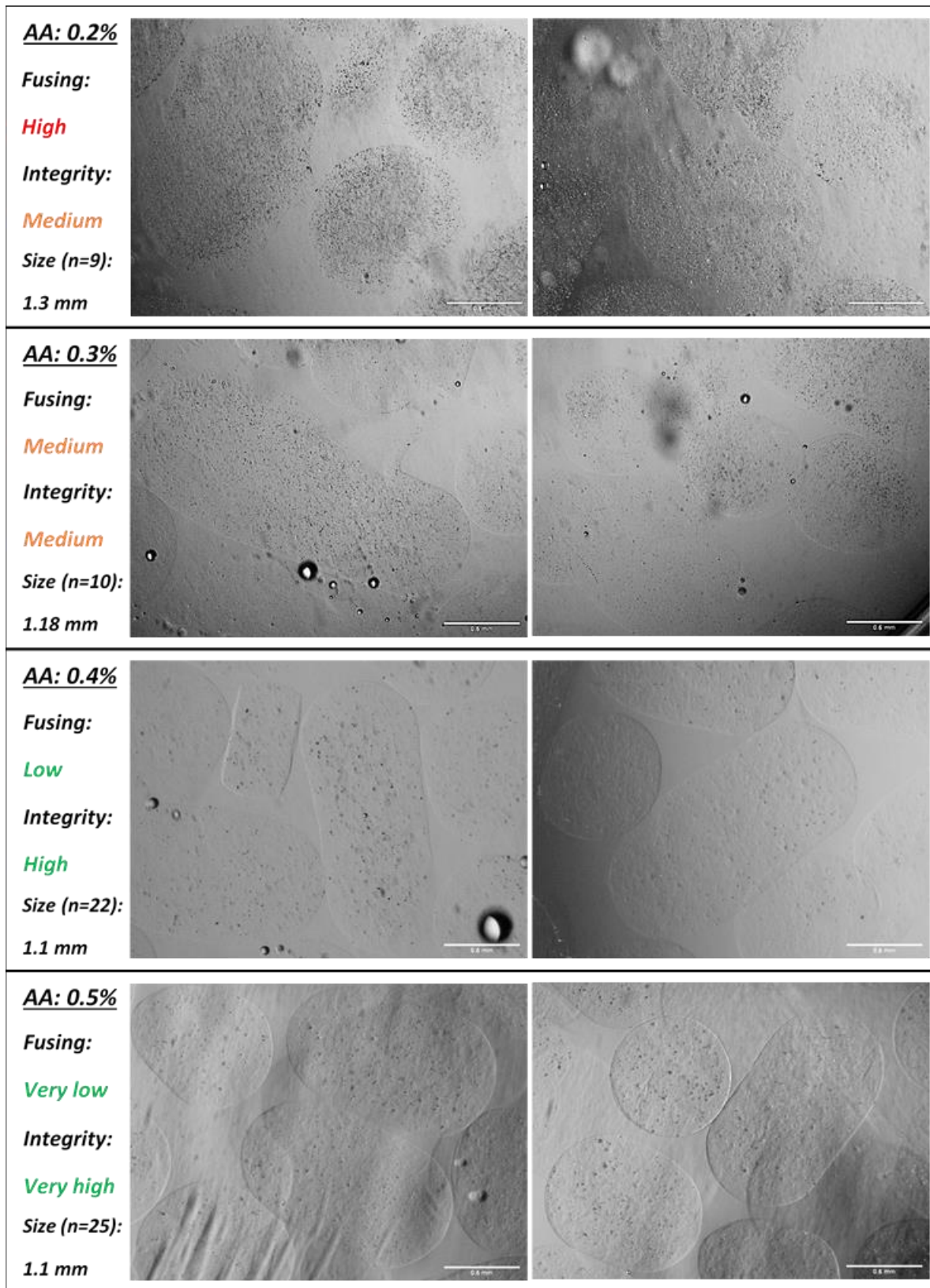


Figure 3.13 Droplet gelling quality assessment using 2% alginate, 0.75 mM CaCO₃, and varying levels of acetic acid.

Different ROI from each condition (well) were captured using phase contrast microscopy. "Size" represents the length of droplets when measuring non spherical droplets. Experimental repeats were conducted on different days (n=3). Scale bar = 500 μm.

3.4.3 Preparation of the bio-material: Characterising the dimensions of droplets produced under optimal microfluidic parameters

Gelled alginate droplets will serve as the bio-material and bio-ink, in the form of discrete cell-laden building blocks for the 3D bio-printing of tissue structure. Hence it is also important to investigate the droplet dimensions on the individual scale, as it would help in optimising the programmable stage movements for the production of patterned constructs.

Alginate droplets produced under the optimal microfluidic parameters were generally capsule shaped or elongated with low spherical morphologies (**Figures 3.13 & 3.14**). The average length and width of individual droplets was evaluated at ± 1.1 and ± 0.8 mm, respectively, particularly for the elongated morphologies. Spherical droplets were smaller in size, resulting in approximately 0.8 – 0.9 mm. These results indicate sufficient gelling upon extrusion.

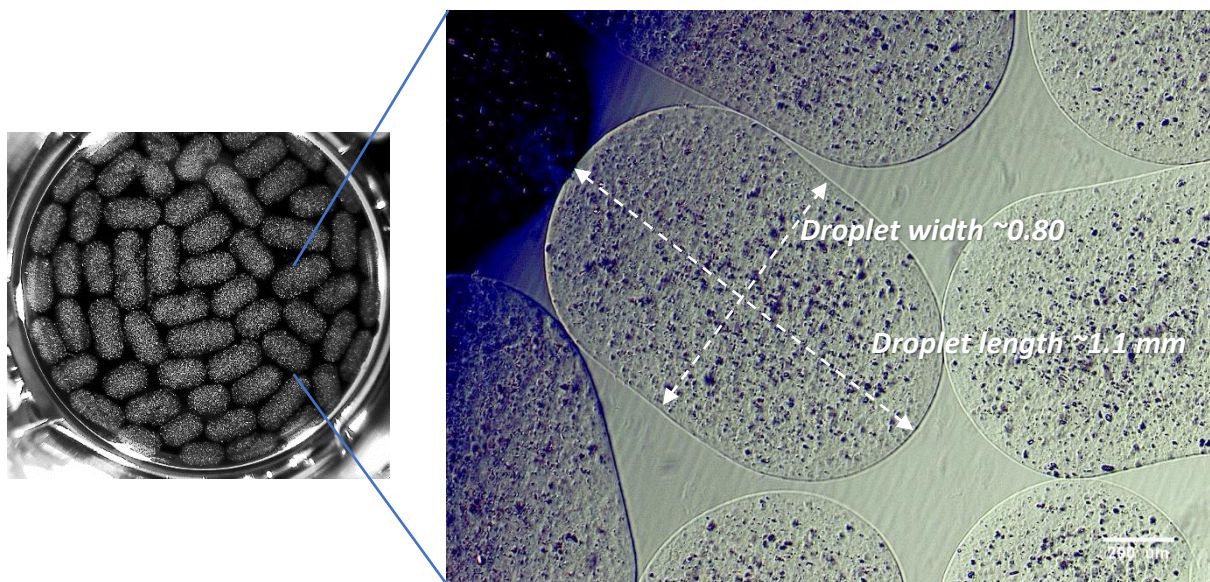


Figure 3.14 Typical droplet morphology produced under the optimal microfluidic parameters.
(A) Macroscopic images of alginate droplets using a stereoscope. (B) x4 magnification of droplets using phase contrast imaging. Scale bar = 200 μm .

● CHAPTER 3 ●

Adequate droplet gelling was obtained through the optimisation of several parameters. One of these parameters is the transit time or residence time of the droplet, which translates to the time required for a droplet to exit the nozzle from the moment of its production. To calculate the transit time, a series of calculations was carried out relying on the tubing inner diameter (ID), total flow rate, and microfluidic tube volume:

- ❖ Tubing ID = **0.79 mm**
- ❖ Radius of ID = **0.395 mm**
- ❖ Total flow rate = 4 mL/hr (continuous phase) + 4 mL/hr (dispersed phase) = **8 mL/hr or (2.2 μ L/s)**
- ❖ Tube volume = 90 mm (tube length) x 0.49 mm² (cross sectional area = π x radius²) = **44.1 mm³**
- ❖ Transit time = Tube volume / Flow rate = **19.85 seconds**

Therefore, with a 9 cm long exit tube of 0.79 mm ID and equal flow rates of 4 mL/hr, a droplet requires 19.85 seconds to traverse the length of the tube before exiting. With concentrations of 75 mM CaCO₃, 0.5% AA, and 2% alginate, the extent of gelation in combination with a residence time of 19.85 seconds, is sufficient for gelled droplet production.

Finally, it was important to identify the volume of the average produced droplet, to allow predictions of encapsulated cell numbers per droplet. To calculate a droplet volume, the aqueous (alginate) flow rate per second was divided by the droplet produced per second, identified in **Figure 3.6** as 3.379 Hz or 3.379 droplet/s:

- ❖ Aqueous (alginate) flow rate = 4 mL/hr or **1.1 μ L/s**
- ❖ Droplet frequency at equal flow rates = 3.379 Hz = **3.379 droplet/s**
- ❖ Droplet volume = 1.1/3.379 = **0.328 μ L**

Therefore, the volume of a droplet is approximately 0.328 μ L in average.

3.4.4 Preparation of the bio-ink: Characterising microfluidic encapsulation of a keratinocyte cell line (HaCaT)

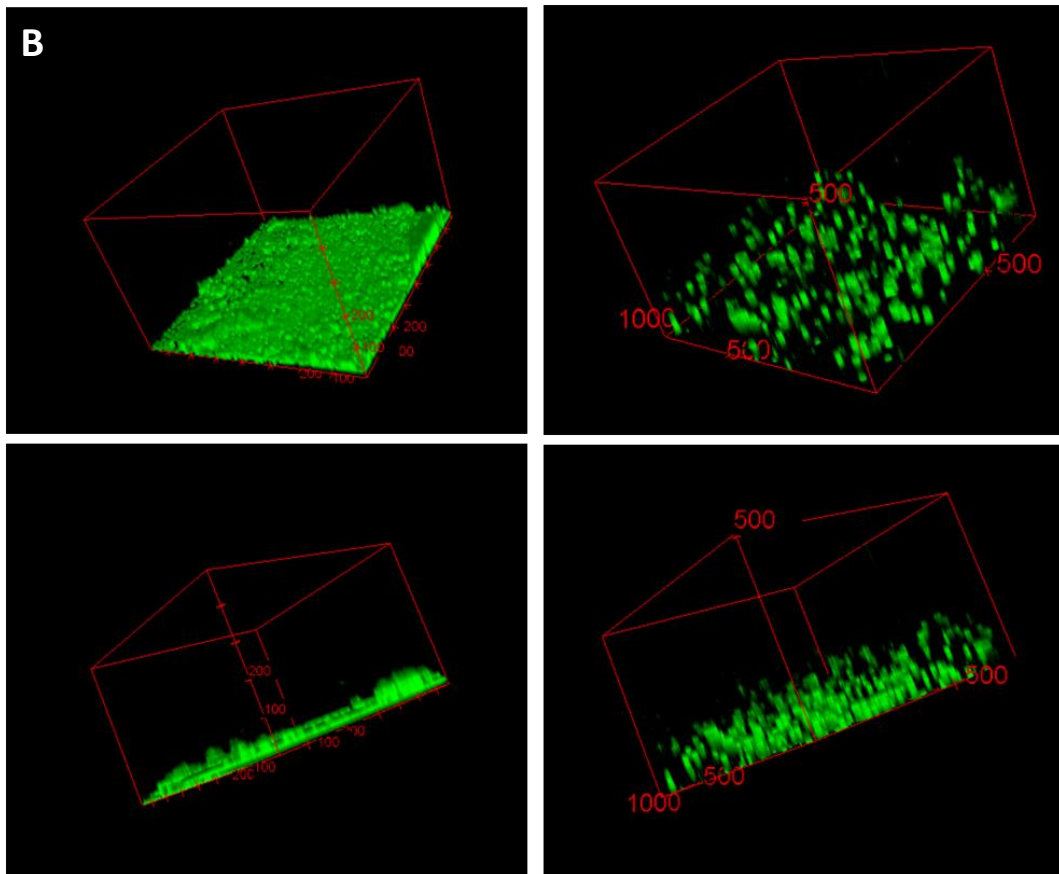
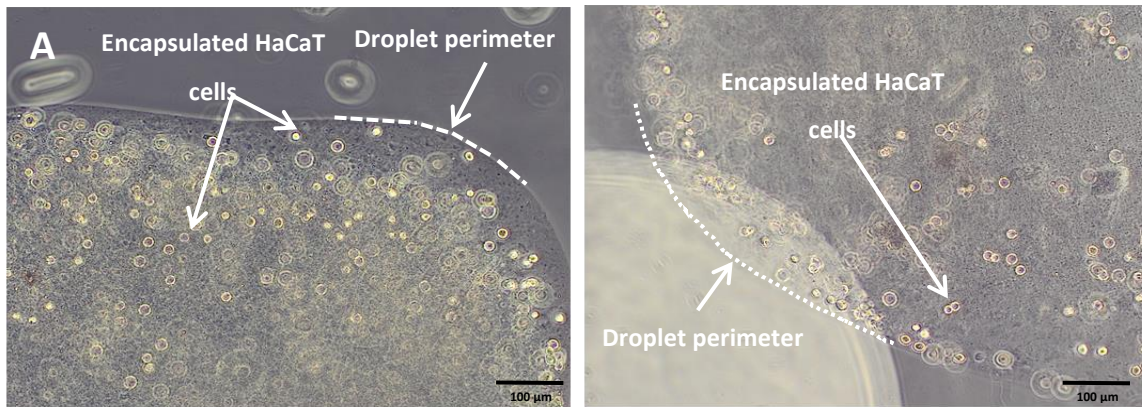
Following the optimisation of alginate droplet production and gelling properties, cell encapsulation was the subsequent parameter to evaluate. Droplet-based 3D bio-printing aims to fabricate relevant synthetic tissue models through high-resolution deposition of live cell-encapsulated bio-material (Gudapati et al. 2016). Importantly, the bio-printing process, should minimally impact cell viability whilst ensuring sufficient cell-encapsulation for patterned deposition. Therefore, printed HaCaT-laden alginate droplets were characterised on the individual scale through various imaging platforms to evaluate the quality of cell dispersion, encapsulation efficiency and cell viability.

3.4.4.1 Qualitative assessment of cell viability, cell dispersion, and encapsulation efficiency in the bio-ink

HaCaT cells were encapsulated in alginate droplets at a density of 2 million cells/mL and printed inside a 35 mm glass bottom MatTek dish (MatTek). Although 2 million cells/mL resulted in a visually low cell count per droplet, phase contrast images showed a successful HaCaT cell encapsulation with few cells found outside the droplet perimeter. Cells also exhibited a viable morphology as assessed by the light emitted around the perimeter of the cells (bright aura surrounding cells), which results from the amplified contrast of the light waves diffracted from the living cells (**Figure 3.15 A**). The visualisation of HaCaT cell dispersion in 3D within individual droplets was limited under phase contrast microscopy but was partially overcome through confocal imaging and the ability for Z-penetrance. For this, the experiment was repeated with the same cell density, including a control which consisted of seeded HaCaT cells conventionally at a density of 2 million cells/mL into the same dish type. Cells were fluorescently labelled with CellMask™ Green plasma membrane stain and observed under a confocal microscope (**Figure 3.15 B**). The results indicate a 3D dispersion of cells up to 200 µm in height when encapsulated in droplets, in contrast to a 2D monolayer flat configuration

● CHAPTER 3 ●

observed when seeded manually. A preliminary attempt at encapsulating HaCaT cells showed positive signs of cell viability and incorporation within each droplet.



2D monolayer seeding

3D bio-printing of cell-laden
alginate droplets

Figure 3.15 3D bio-printing of HaCaT cell-encapsulated biomaterial.
(A) Phase contrast images of single cell-encapsulated droplets and (B) 3D reconstructed confocal images comparing non-printed to 3D bio-printed cells (units in μm). (2 million cells/mL).

● CHAPTER 3 ●

To gain a better insight on the level of dispersion and cell viability post-bio-printing, HaCaT cell density was increased to 10^7 cells/mL of liquid alginate. Phase contrast images showed successful cell encapsulation with very few cells found past the droplet perimeter (**Figure 3.16 A**). A more conclusive analysis on cell dispersion and viability was conducted using confocal and LSM. Live/Dead cell staining with fluorescent imaging 2 hours post-printing revealed a homogeneous dispersion of viable HaCaT cells encapsulated within individually printed droplets (**Figures 3.16 B, C, & 3.17**). The Z-penetration depth distance was a limiting factor on the confocal microscope due to the large size of droplets. A maximum Z-distance of 250 μm was roughly observed, restricting the visualization of full droplets and valuable information on cell dispersion and viability (**Figure 3.16 B & C**). The LSM technology however, allowed to overcome this obstacle and reveal the full depth of individual droplets from a full angle view (**Figure 3.17**). LSM imaging revealed a highly homogeneous dispersion of viable encapsulated HaCaT cells per droplet 2 hours post-encapsulation. Under the optimised printing conditions, the average droplet size was 1.1 mm. With a cell density of 10^7 cells/mL, the number of cells per droplets could be estimated by using the previously calculated volume of a droplet and dividing that by the area in mm^3 that a single cell will be in:

$$\begin{aligned} & \diamond \text{ Average volume of a droplet (V) = } 0.328 \text{ mm}^3 \\ & \diamond \text{ Cell density (Cd) = } 10000000/\text{mL} \text{ or } 1/0.0001 \text{ }\mu\text{L} \text{ (} 1 \text{ }\mu\text{L} = 1 \text{ mm}^3 \text{ or } 0.0001 \text{ }\mu\text{L} = 0.0001} \\ & \qquad \qquad \qquad \text{mm}^3 \text{)} \\ & \diamond \text{ Cells per single droplet = } V/\text{Cd} \\ & \qquad \qquad \qquad = 3280 \\ & \qquad \qquad \qquad = \sim \mathbf{3300 \text{ cells per droplet}} \end{aligned}$$

Therefore, one droplet should potentially contain approximately 3300 cells (**Figure 3.16**). Characterising an individual droplet at this level of resolution promises the ability to pattern several high-cell density structures in more complex shapes, mimicking tissue-like constructs. This qualitative data reveals a high short-term cell viability of HaCaT cells in the alginate droplet bio-ink.

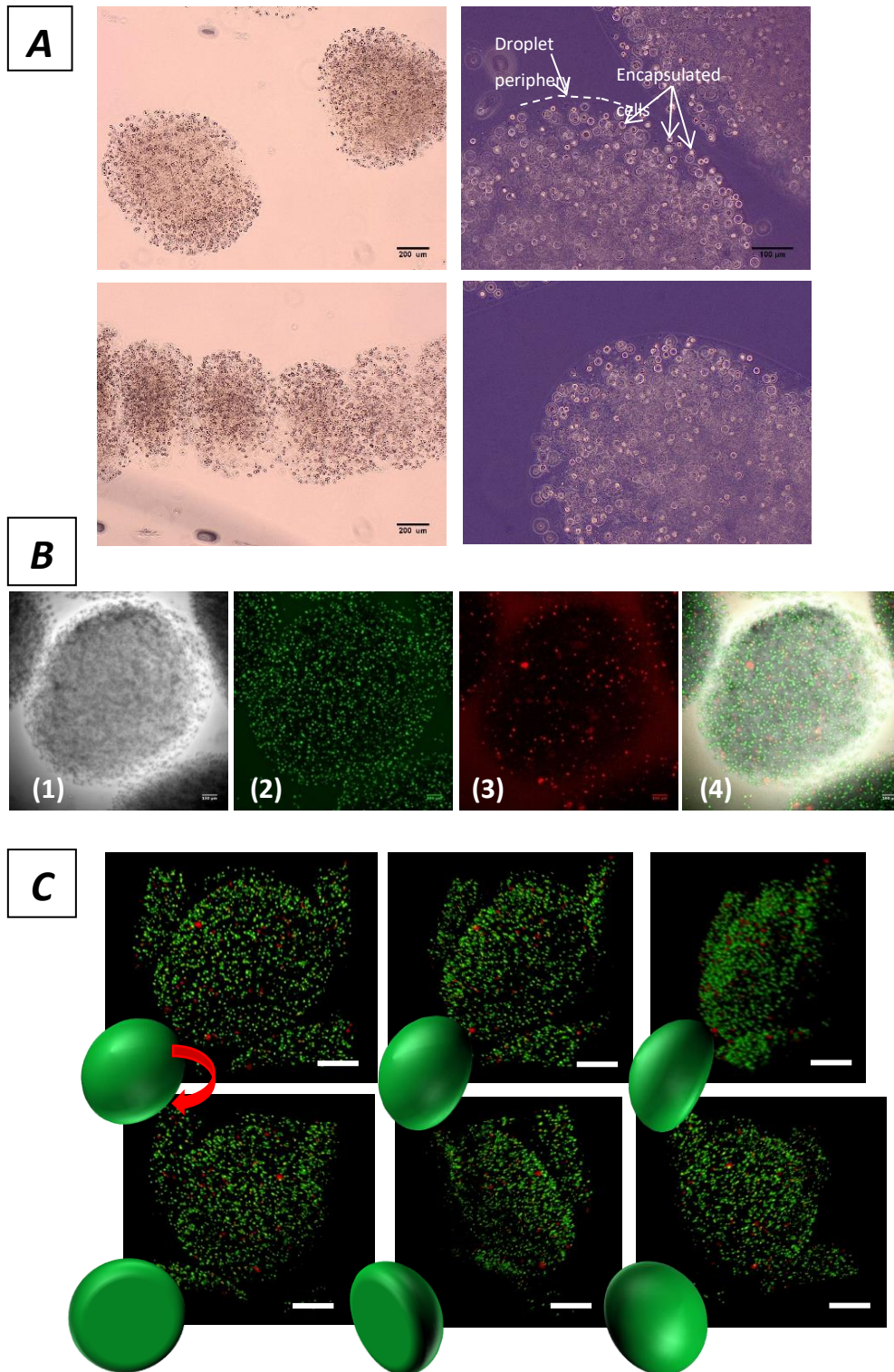


Figure 3.16 Microscopic images of bio-ink units: microfluidic generated alginate droplets with encapsulated HaCaT cells.

(A) Brightfield and phase contrast images of cell-encapsulated droplets at 4x and 10x objectives directly after extrusion. (B-E) LIVE/DEAD fluorescent imaging of cell-encapsulated monodisperse alginate droplets 2 hours post-encapsulation: (B) Confocal fluorescence micrograph of a grouped Z scan projection image (10x) of an individual cell-laden droplet with (1) brightfield, (2) red stain (528 – 617 nm) representing dead cells, (3) green stain (494 -515 nm) representing live cells and (4) a composite image of all filters. Scale bar = 100 μm (C) A 3D projection of the same droplet in an approximate 270° rotation and a schematic 3D model mimicking the rotation movement. (10 million cells/mL) Scale bar = 200 μm.

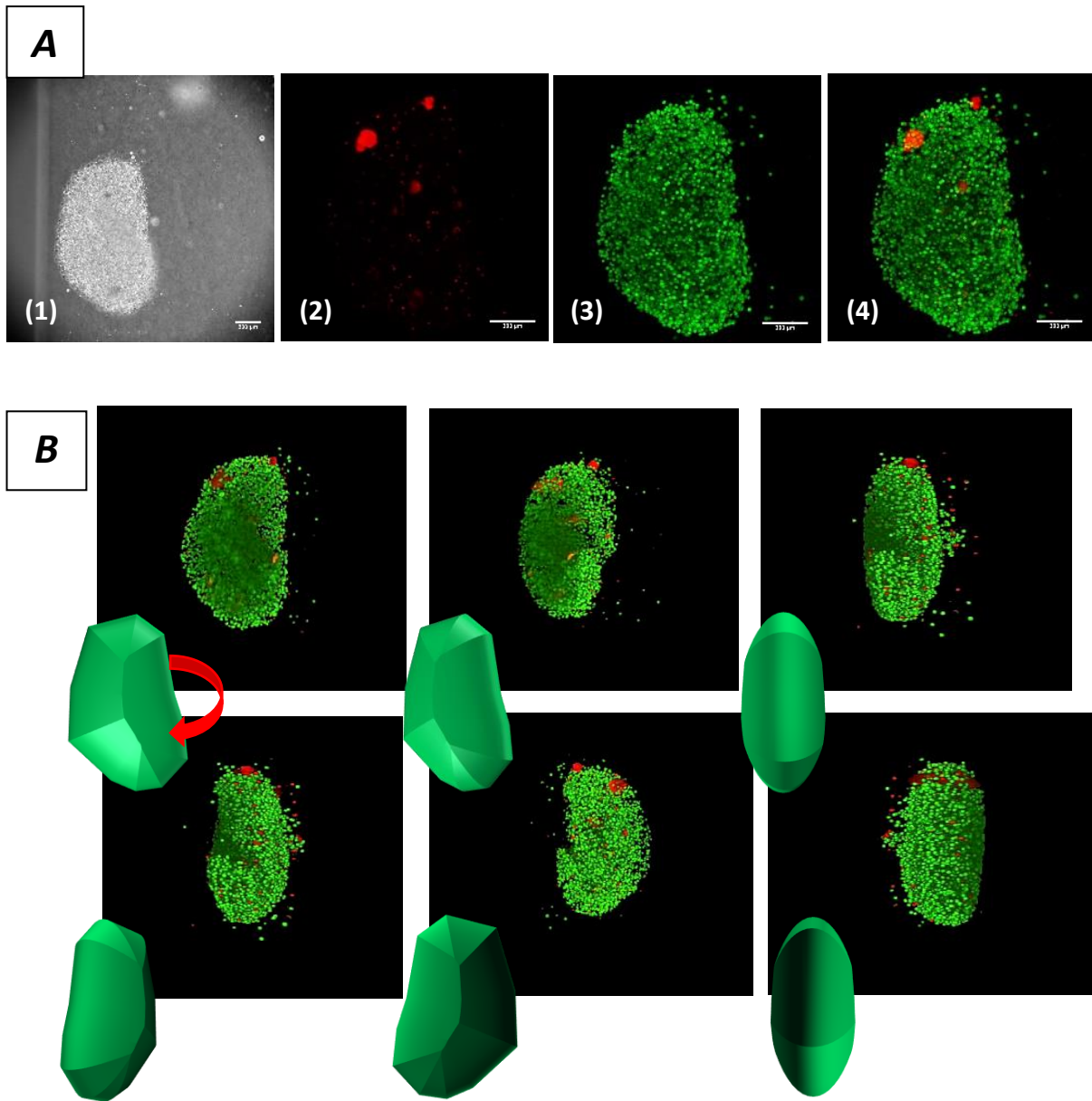


Figure 3.17 Lightsheet microscopic images of the bio-ink units: microfluidic generated alginate droplets with Live/Dead stained encapsulated HaCaT cells.

(A) (1) A transmitted light image and (2, 3, 4) light sheet fluorescent micrograph of an individual droplet embedded in 1% gelled agarose using light sheet fluorescent microscopy (LSFM) (5x). Scale bar = 100 μm (B) A 3D rendered projection of the individual droplet visualized in a 360° rotation showing full cell dispersion. (10 million cells/mL).

3.4.4.2 Quantitative assessment of cell viability upon encapsulation in the bio-ink

Assessing the cell numbers that can be encapsulated per droplet was a crucial step in defining the systems sensitivity and future potential for 3D bio-printing high-resolution tissues. Furthermore, the effect of chemical gelation on cell viability was evaluated by determining the number of encapsulated live and dead cells. The objective was to attempt bio-printing HaCaT-encapsulated alginate droplets at similar number of cells comparable to a conventionally seeded 2D cell monolayer counterpart. By knowing the droplet volume, frequency, and cell density, the number of droplets needed to bio-print, to achieve comparable results was accessible. 2D monolayer seeding was fixed at 150000 cells per well. To reach similar cell numbers under bio-printed conditions, the number of droplets per well was determined at 45 HaCaT-laden droplets per well. This was calculated by dividing the number of cells per well (150000) by the average number of cells per droplet (3300). Once the alginate droplets were dissolved with 250 mM EDTA for 15 minutes, cell numbers were counted and an average of 202,500 cells per well for the bio-printed condition whereas 147,500 cells was counted in the control condition. This demonstrated the ability to achieve reproducible density of cells per droplet. Trypan blue exclusion cell viability assay revealed a HaCaT cell viability of 87.5%, 2 hours post-3D bio-printing (n=3) (**Figure 3.18**). HaCaT cells seeded in a 2D monolayer were detached and equivalently assessed with the trypan blue assay revealing 92% cell viability. These results indicate high cell viability upon encapsulation within the bio-ink and precise control over number of encapsulated cells, resulting in efficient reproducibility of cell density per droplet. The combined ability to precisely control cell densities and flow rates in microfluidics is a key factor for the fine-tuning of more complex cellular structural arrangements.

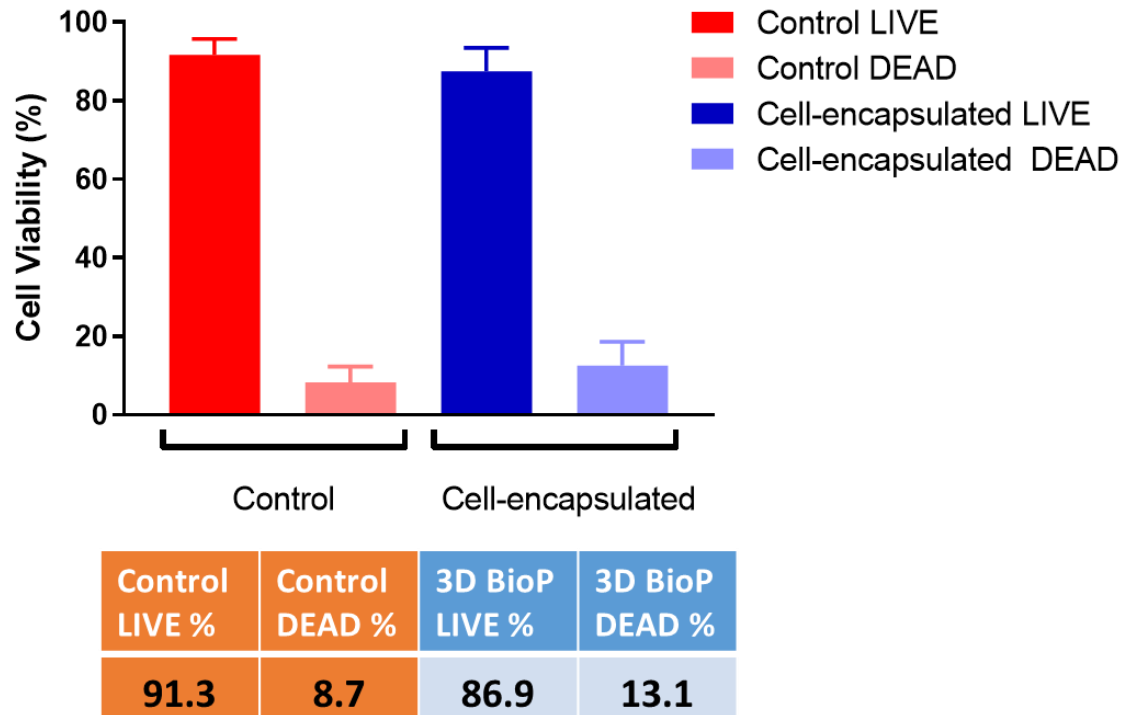


Figure 3.18 Cell viability assessment 2 hours post cell-encapsulation in the bio-ink.

Cell-encapsulated alginate droplets were dissolved with 250 mM of EDTA for 15 minutes and cells were counted using the trypan blue exclusion dye. Cell viability is represented in percentage of live vs. dead cells (n=3). Control condition consisted of 2D seeded cells and detached with trypsin-EDTA (0.25%-0.9 mM) for 15 minutes (n=3).

3.5 Discussion

In this chapter, a t-junction microfluidic device was used to generate gelled alginate droplets by an internal gelation method. The microfluidic parameters and reagent concentrations were optimised to produce sufficiently gelled droplets for the encapsulation of a viable keratinocyte cell line (HaCaT). Droplets were characterised based on their level of gelation, morphology, size, entrapment capacity, and biocompatibility.

Extensive studies revolving around microfluidic-based droplet production, provide a large spectrum of microfluidic concepts and devices suitable for various research and medical applications (Tan and Takeuchi 2007; Seemann et al. 2012; Huang et al. 2017; Sohrabi et al. 2020; Zhang et al. 2020)s. The choice of a t-junction device in this study, stems from its low demands in droplet size or morphology homogeneity, wide use in studies, high droplet frequency, and simplicity (Seemann et al. 2012). Indeed, although tissues are precisely organised complex structures, a natural level of flexibility in cellular and tissular arrangements is evident. Therefore, generating highly homogenous cell-laden droplet morphologies and sizes may not represent the true arrangements of tissue structures. Hence, a “Head on” t-junction geometry, where both dispersed (alginate) and continuous (oil) phases join from opposite sides, was chosen to produce alginate droplets in this study. FEP (fluorinated ethylene-propylene) microfluidic tubing was used in this study as an alternative to PTFE (polytetrafluoroethylene), owing to its cost-effectiveness, ease of sterilizability, greater biocompatibility, and higher tubing transparency for droplet clarity (*FLUOROTHERM™- FEP Tubing*, Accessed on 19/06/2021).

The rate of droplet frequency was investigated in relation to flow rate and flow rate ratio changes. It was predicted that increased flow rates and ratios would result in higher droplet frequency (Seemann et al. 2012; Huang et al. 2017). As expected, the results obtained in this chapter showed faster droplet production per unit time when increasing flow rates (**Figure 3.6**). However, the increase in frequency is attenuated when aqueous flow rates approaches continuous flow rates and when flow rates generally increase, suggesting a direct impact of flow rate on the droplet-breakup dynamic in the t-junction (Chiarello et al. 2017).

● CHAPTER 3 ●

Droplet frequency was evaluated through pixel fluctuation of droplet to oil contrast in the tubing. Therefore, distortion of the droplet size, such as elongation, along with inter-droplet gelling differences, can impact the lighting and subsequently the result of droplet frequency. Indeed, higher aqueous to continuous flow ratios or high equal flow rate ratios have been shown to result in droplet elongation and accumulation of larger droplets before breakup (Chiarello et al. 2017; Marshall and Walker 2019). This may result in a reduced increase in droplet frequency when equal flow rates increase and nearing of aqueous to continuous flow ratio values occurs. The decrease in droplet frequency may not therefore be a reduction in the number of droplets being produced, but merely a shift in size which alters the pixel value readings. Indeed, larger droplets are produced when aqueous flow rates approach continuous phase flow rates (**Figure 3.7**). Repeating the same experiment with higher aqueous to continuous flow rate ratios may inform further on the droplet breakup dynamic and confirm the abovementioned hypotheses. Interestingly, the minor decrease in droplet frequency is consistently observed in all conditions between 8 – 12 mL/hr and then 16 – 20 mL/hr (**Figure 3.6**). This suggests a common technical limitation which can be caused by the geometry of microfluidic channel (t-junction) or even particle blockage due to the insoluble CaCO_3 which can alter droplet formation and breakup (Wang et al. 2011; Seemann et al. 2012; Utech et al. 2015). Several studies demonstrated how the complex interplay of flow ratios, channel contact angle, channel geometry, and bio-material viscosity can influence droplet breakup, shape, size and frequency in t-junctions (Garstecki et al. 2006; Liu and Zhang 2009). Future work can be conducted using different microfluidic devices to assess the extent of channel geometry implications in the break-up regime. Additionally, during long periods of droplet production, frequencies occasionally showed irregularities which may be due to insoluble CaCO_3 particle settling in the tubings and syringes. This may hamper droplet monodispersity and gelling homogeneity (Utech et al. 2015).

Droplet length and size influence droplet patterning, packing arrangements and encapsulated cell function (Utech et al. 2015; Alcinesio et al. 2020). Upon extrusion, the nature of the droplet's orientation when deposited on a glass coverslip will determine the ultimate patterning of the structure. Therefore, determining droplet length would allow to predict optimal bio-printing speeds for compact high-resolution packing. Additionally, comparing droplet lengths pre- vs. post-extrusion informs on the extent of gelation and

droplet rigidity. Previous microfluidic studies have shown that an increase in aqueous to continuous flow rate ratio results in longer droplets, whereas the opposite is observed when continuous flow rate is higher (Garstecki et al. 2006; Chiarello et al. 2017). Indeed, a higher continuous flow rate will result in a faster droplet break-up at the intersecting junction, generating smaller sized droplets (Liu and Zhang 2009). In contrast, when flow rate ratio values are close to equal, droplet length increases but shows little variance in length when flow rates are kept constant, confirming previous findings and predictions (**Figure 3.7**) (Garstecki et al. 2006; Chiarello et al. 2017). Higher continuous to aqueous flow rate ratio results in significantly smaller droplets, which increase the closer the ratio values become. Interestingly, equal flow rates of 10 and 20 mL/hr showed the steepest increase in droplet size (red and green), which may explain the small dip in droplet frequency observed specifically at these conditions in the previous frequency results (**Figures 3.6 & 3.7**). Despite high experimental variance observed between different equal flow rate values (blue), a non-linear trend confirms the smaller effect equal flow rates have on droplet length. Droplets tend to measure between ~1.1 to 1.45 mm in length, demonstrating a standard deviation overlap within a relatively short length range (0.35 mm). Testing a larger sample size could aid in flattening the curve and decrease experimental variability. From the numerous parameters potentially influencing the observed variability in results, the insoluble CaCO_3 may play a detrimental role on droplet monodispersity, mentioned previously (Utech et al. 2015). Although the microfluidic tubings have been carefully flushed with 70% ethanol and dH_2O , and syringes replaced between each condition, deposits of CaCO_3 particles may occur, clogging the system and disturbing droplet formation and break-up. The scaling-tool used to measure droplet lengths was set to measure the outer tubing diameter of 1.59 mm as reference. However, inner diameter readings still exceeded the known inner diameter of 0.79 mm, which may be due to the difference in air to the FEP tubing's refractive index (1 and 1.344, respectively), resulting in droplet magnification and potential distortion. To overcome this, the use of higher magnification stereoscopes may be more beneficial to capture tubing and droplet sizes more realistically. All droplet lengths measured at equal flow rates resulted in lengths exceeding the tubing diameter of 0.79 mm, suggesting the production of elongated or capsule shaped droplets. However, only observations post-extrusion can fully reveal the real length and size of droplets, hence, the extent of gelation.

● CHAPTER 3 ●

In this study, alginate microgels were generated by internal gelation, based on previous reports (Zhang et al. 2007; Akbari and Pirbodaghi 2014; Hidalgo San Jose et al. 2018). Qualitative assessment of alginate droplet gelling relative to flow rate ratio and reagent concentration variations was carried out post-extrusion, in dH₂O-filled dishes. Droplets were assessed based on their structural rigidity, outer perimeter visibility, and observable inter-droplet. Gelling sufficiency is not only dependent on flow rates and reaction rate, but equally on droplet residence time (Tan and Takeuchi 2007). To achieve sufficient *in situ* gelation, the acetic acid diffusion rate to the droplets and Ca²⁺ release need to occur rapidly before droplet extrusion (Tan and Takeuchi 2007; Zhang et al. 2007). Furthermore, reagent concentrations need to be sufficient to ensure rapid reaction times for adequate gelation. Finally, the microfluidic channel length downstream the t-junction, or the exit tube, should be sufficiently long to allow enough time for alginate crosslinking process. Hence, increased flow rates and sub-optimal reagent concentrations, may result in incomplete droplet gelling, especially if the exit tubing length is insufficient. Since the exit tube length is a fixed parameter which relies on the 3D bio-printer build, it was more convenient to evaluate the optimal flow rates and reagent concentrations. Flow rates were assessed in combination to fixed reagent concentrations as described in a previous microfluidic study (Baxani et al. 2016). As expected, higher continuous to aqueous flow rate ratio generated smaller spherical droplets (**Figure 3.7**) (Liu and Zhang 2009; Chiarello et al. 2017). The importance of droplet residence time is confirmed in these results, as they demonstrate that above an aqueous flow rate of 4 mL/hr in combination with a constant continuous flow rate of 10 or 20 mL/hr, droplets are insufficiently gelled when observed post-extrusion. Equal flow rates generate larger elongated droplets, but gelling begins to decrease in quality at 6 mL/hr, again indicating insufficient residence time above this rate. At higher continuous to aqueous flow rates, droplets were smaller in size, whereas equal flow rates showed similar length sizes overall. The implication is that the previously tested measuring method using a USB camera, may have led to overestimations, especially when droplets are smaller than the internal tubing diameter. At equal flow rates, droplet lengths were relatively more consistent with the previous result (**Figure 3.7 & 3.10**), suggesting adequate residence time until 4 mL/hr. However, increased residence time can generate overly rigid droplets that break as observed at equal flow rates of 2 mL/hr. As expected, most droplets were gelled in an elongated configuration when at equal flow rates of 4 mL/hr, indicating sufficient time for droplet cross-

● CHAPTER 3 ●

linking with an exit tube length of 9 cm. Changes in droplet sizes showed low dependency to flow rate changes when increasing aqueous flow rate from 2 to 4 mL/hr in all conditions, contrary to the results found when measured in the tubing. This suggests other factors influencing droplet gelling behaviour, including fluid viscosities, surface tension, tubing diameter, and residence time (Garstecki et al. 2006; Seemann et al. 2012).

Optimal concentrations of the aqueous and continuous phases were investigated at a fixed equal flow rate of 4 mL/hr. An alginate concentration was kept at 2% following previous findings which showed production of highly monodisperse droplets with adequate mechanical properties for cell encapsulation and artificial membrane platform studies (Baxani et al. 2016; Hidalgo San Jose et al. 2018). Results suggested that concentrations at $\geq 0.4\%$ AA and ≥ 50 mM CaCO_3 are required to gel the droplets completely. A CaCO_3 concentration of 0.25 mM resulted in insufficient Ca^{2+} ions to achieve proper droplet gelation, regardless of AA concentrations. Best results were observed when CaCO_3 concentration was at 75 mM in combination with a 0.5% AA concentration, resulting in monodisperse droplets with low to no fusing, and high structural integrity. However, a distribution of non-partitioned CaCO_3 nanoparticles were seen in droplets, owing to excess CaCO_3 particles, resulting in non-homogenous Ca^{2+} distribution in droplets and ultimately, may be detrimental to cell viability on the long term (Cao et al. 2012). Indeed, physiological extracellular Ca^{2+} levels are tightly regulated in the range of 1 – 2 mM and can perturb cell function at excessive levels. This is especially true for keratinocyte differentiation and skin maturation, which heavily rely on Ca^{2+} regulation, as described in **Chapter 2**. Previous studies suggested an ideal pH range of $5.5 < \text{pH} < 6.5$ for Ca^{2+} liberation (Chan et al. 2006; Zhang et al. 2007). Therefore, an additional experiment to determine the amount of AA that diffuses from the oil to the aqueous phase was conducted based on pH level changes, whereby equal volumes of oil/AA, at varying AA concentrations of 0.1%, 0.2%, 0.3%, 0.4%, and 0.5%, and DMEM were added in a tube and thoroughly mixed to mimic the microfluidic mixing process at equal flow rates (**Appendix A-3**). A control experiment consisted of adding AA directly into DMEM. Once the oil was discarded, pH levels of the DMEM were measured at ~ 4.5 at 0.4% and 0.5% and ≥ 5 at 0.3%. Hence, pH levels were used as indicators of how much acetic acid partitioned into the DMEM, whereby lower pH levels indicate more acetic acid partitioning owing to the higher concentrations. However, this method is an approximation and does not indicate specific

● CHAPTER 3 ●

partition coefficients of acetic acid to DMEM. Interestingly, at higher oil to aqueous volume ratios and a fixed AA concentration of 0.1%, pH levels were fell to ~ 4 , suggesting an important influence of flow rate ratios on AA partitioning (**Appendix A-4**). The ideal pH for Ca^{2+} liberation and crosslinking will therefore depend on the oil to aqueous volume ratio. Together, these results indicate that complete gelation of droplets, at equal flow rates, in a 9 cm long exit microfluidic tube of 0.79 mm inner diameter requires at least a pH of 4.5 and 50 mM CaCO_3 . Droplet sphericity and high monodispersity were not specifically sought after in this study. However, homogeneity in morphologies and better Ca^{2+} distribution should be addressed in the future. Utech et al. suggested replacing the insoluble CaCO_3 nanoparticles with a water-soluble calcium-EDTA complex (Utech et al. 2015). The chelation of the Ca^{2+} by the EDTA allows for improved control over Ca^{2+} liberation upon pH reduction. Liberated Ca^{2+} ions react with the emulsified alginate droplets to form droplets with high monodispersity and structural homogeneity.

The optimised microfluidic parameters were used to encapsulate the HaCaT keratinocyte cell line, and assess cell-entrapment quality, cell dispersion, and short-term cell viability. Brightfield, phase contrast, confocal, and light sheet microscopy all revealed successful cell entrapment, viability, and dispersion per droplet when cell density was at 1×10^7 cells/mL (**Figures 3.16 & 3.17**). Although not a major concern at the present stage of the study, droplet size may be problematic on the long term, especially for long term encapsulation and image acquisition. Studies have revealed that the optimal droplet size for efficient cell viability should be $< 200 \mu\text{m}$ (Velasco et al. 2012). Furthermore, that would benefit image acquisition when manipulating smaller droplets, allowing to image a larger field of view, hence droplet numbers. Confocal images testified to this limitation by only acquiring one third of the droplet, due to insufficient laser penetration and optical sectioning. Light sheet microscopy overcame this challenge owing to its superior laser penetration, optical sectioning, rapid imaging and 3D resolving power (Power and Huisken 2017). Previous studies resorted to similar imaging methodologies to investigate cell-encapsulation characteristics (Utech et al. 2015; Hidalgo San Jose et al. 2018). Indeed, Hidalgo et al. recently demonstrated high cell viability ($\sim 100\%$) of encapsulated dental pulp stem cells within alginate-collagen droplets using confocal microscopy at day 1, similar to the observations in this study (Hidalgo San Jose et al. 2018). However, this is the first time the light sheet microscopy technology has

● CHAPTER 3 ●

been utilised to visualise individual cell-encapsulated alginate droplets with high-resolution and multiangle views. Nonetheless, aiming to reduce droplet size is within the future scope of this study. All imaging platforms revealed high short-term cell viability of encapsulated HaCaT cells indicating a biocompatible encapsulation process.

Droplet volume calculations predicted a cell density of ~3300 cells per droplet when preparing 1×10^7 cells/mL of bio-ink. This was calculated relative to the tubing diameter, as cells will be encapsulated within the microfluidic space. The results obtained in the quantitative cell count demonstrated a relatively high level of the experimental feasibility used in this study and confirmed the theoretical cell per droplet count as a function of droplet volume (**Figure 3.18**). It was anticipated that bio-printing 45 droplets, which translates to ~13.5 seconds of extrusion, would generate a total number of 150000 cells per well. However, an average of 202,500 cells was counted resulting in an error margin. This is most likely due to experimental inaccuracies when trying to bio-print an exact number of droplets. Indeed, several parameters can contribute to this error, including inconsistent droplet frequency and microfluidic back pressure when stopping the syringe driver, generating extra droplet deposition. Despite these factors, the error margin remains satisfactory given the elasticity of the project's scope. The mean keratinocyte cell density in bio-printed droplets as a function of the bio-ink cell density can be calculated. This can be achieved by dividing the mean number of cells per droplet (~3300) by the volume of a droplet (0.328 mm^3 or 0.000328 mL), resulting in a cell density of 10^7 cells per mL, similar to cell densities found in physiological tissues (Bianconi et al. 2013). Trypan blue cell count findings showed a cell viability >85% throughout the printing process, confirming previous qualitative results. Interestingly, inkjet and laser-assisted bio-printing technologies have reportedly similar cell viability proportions, whereas extrusion-based techniques showed cell viabilities between 40%-80% (Dai and Lee 2015). Furthermore, HaCaT cells showed tolerance to a short exposure to EDTA, whilst ensuring alginate dissolution. The promising results using the HaCaT cell line should be further extended to using different keratinocyte cells, like the hTERT/Ker-CT keratinocyte cell line or NHEK.

In summary, microfluidic parameter optimisation allowed to generate alginate microgel droplets with control over droplet size and gelling quality, for efficient keratinocyte

● CHAPTER 3 ●

encapsulation. Encapsulated keratinocytes showed high short-term viability and cell dispersion, indicating high tolerance to the bio-printing process. Keratinocyte-encapsulated alginate droplets will serve as the 3D bio-printing bio-ink. The optimised microfluidic parameters and droplet characteristics provide a robust foundation to allow printing speed prediction for the creation of patterned 2D and 3D cell-laden patterns to move closer to skin tissue structure. The preliminary results of this chapter were deemed sufficient to test in parallel with the custom-built 3D bio-printer.

***Chapter 4 Exploring the spatial
capabilities of the custom-built LEGO®
3D bio-printer stage***

4.1 Introduction

To bridge the gap between performance and accessibility, a number of studies have successfully circumvented acknowledged 3D bio-printer limitations by either customising commercially available bio-printers and software, creating custom bio-ink mixtures, converting low-cost off-the-shelf 3D printers into bio-printers, or even resorting to custom-built machines (Arai et al. 2011; Gabriel Villar, Alexander D. Graham 2013; Gao et al. 2015; Homan et al. 2016; Johnson et al. 2016; Ma et al. 2016; Reid et al. 2016; Costantini et al. 2017; Graham et al. 2017; Schmieden et al. 2018; Kahl et al. 2019). Furthermore, this allowed to compensate some limiting features found in each commercial bio-printing technique, including accuracy, printing resolution, printing speed, cell viability, bio-ink viscosity, and clogging, etc., described in **Section 1.3.1.2**. However, the main reason which has contributed to the development of alternative solutions to the use of commercial bio-printers is the high costs leading to limited accessibility to many laboratories. Hence, low-cost 3D bio-printers, ranging between £100 - £250, have been previously developed by converting 3D printers or building them from scratch (mechbio-printer, 2019, *Low Cost Bio-printer*, Accessed 08/06/2021) (Reid et al. 2016; Kahl et al. 2019). One of the earliest reported custom-built 3D bio-printer was a static piezoelectric actuated droplet generator resting on a motorised stage, capable of patterning droplet networks with high resolution (Gabriel Villar, Alexander D. Graham 2013). In 2017, this same low-cost technology led to the high-resolution 3D bio-printing of cellular constructs resulting in high cell viability, cell proliferation and differentiation (Graham et al. 2017). Reid et al. was the first research group that reported the adaptation of a low-cost off the shelf 3D printer (Felix 3.0) into a micro-extrusion-based bioprinting system capable of precise placement of stem cells and their differentiation (Reid et al. 2016). In the same year, Cubo et al. reported the bio-printing of a skin model validated through H&E and immunohistochemistry, using an adapted extrusion-based 3D bio-printer from the original Printrbot (3D printer), being the first study to bio-print tissue from an in-house adapted technology (Cubo et al. 2016a). In the following years, similar strategies were adopted by several laboratories, however, all in-house built bio-printer technologies are currently being evaluated for accuracy and reproducibility, along with validation of cell survivability, proliferation, and differentiation (Kahl et al. 2019; Ioannidis et al. 2020). Despite

● CHAPTER 4 ●

these efforts, adapting and building bio-printers requires prior expertise in custom hardware engineering and software programming.

Automation of LEGO® MINDSTORMS® toy constructs has led to creative and innovative developments of LEGO®- based 3D printers over the past 5 years. In addition to supporting educational and engagement ideas, custom-built LEGO® MINDSTORMS® robotics and LEGO® Technic present a versatile, low-cost, widely available modular construction system that has recently been exploited in a number of scientific research areas. Liquid-handling pipetting robots capable of handling volumes up to 1 mL have been reported in 2017 (Gerber et al. 2017). Moser et al. reported the build of LEGO®-based tensile testers that yielded comparable performance in tension sensing of stretchable electronics to commercial systems (Moser et al. 2016). In another research area, arrays of LEGO® syringe drivers were built for automated fluid handling of reagents to live cells during microscopy imaging (Almada et al. 2019). The visual programming software provided by LEGO® has been demonstrated to provide an ideal programming environment for novice users with minimal prior expertise (Kim and Jeon 2007). The modular nature of LEGO® has also inspired researchers to engineer microfluidic devices based on the brick-on-brick system, creating diverse microfluidic platforms (Morgan et al. 2016; Nie et al. 2018). The open-source format of LEGO® systems provide global accessibility and space for design improvements. Custom-built LEGO® robotics can be easily built, providing automated user-defined movements to carry out tasks that would otherwise require poorly accessible and expensive machinery. Recently, the LEGO® MINDSTORMS® EV3 robotics have been used to build 3D printers, providing an accessible and low-cost 3D printing platform to a wider public (Marc-Andre Bazergui and Thomas Madeya, 2017, *NEW EV3Dprinter: LEGO MINDSTORMS 3D Printer (3rd Generation)*, Accessed on 08/06/2021). This served as an inspiration to adapt a LEGO® 3D printer into a LEGO® 3D bio-printer in this study, by combining a microfluidic system with a LEGO® programmable x/y/z stage. The potential LEGO® tools hold in carrying out sophisticated robotic tasks in previous scientific studies, along with its intuitive building and accessibility can be translated to areas of biological research for laboratories with limited funding resource or extensive engineering and programming expertise.

● CHAPTER 4 ●

As an extension of 3D printing, 3D bio-printing technology similarly uses computer-aided design (CAD)-based software to create digital models, which designate specific paths the nozzle or stage will take in the x, y, and z planes. Simultaneously, bio-material and living cells (bio-ink) are extruded to generate scalable biomimetic tissue structures. Such software tools are currently under-developed compared to 3D bio-printer hardware (Pakhomova et al. 2020). Indeed, the complexity of the 3D bio-printing process requires specialised software tools which are currently not widely available (Pakhomova et al. 2020). Company-owned 3D bio-printer software is generally closed source whereas the software used for LEGO® robotics, LEGO MINDSTORMS EV3, is open source and initially dedicated to a wider public with little to no expertise in mechanical engineering programming, making it readily accessible. Furthermore, this provides the user with the flexibility to create user-defined 3D models.

4.2 Aim and objectives

The aim of this chapter was to build, evaluate, and optimize the capabilities of a bespoke low-cost custom-built LEGO® x, y, z stage to be used in a 3D bio-printer.

The objectives of this chapter are:

1. Build a programmable LEGO® x, y, z stage to which an integrated droplet microfluidic nozzle (Chapter 3) can be integrated to allow controlled spatial deposition of bio-material and cell-encapsulated alginate hydrogel droplets (bio-ink).
2. Explore the spatial and speed limitations of the programmable LEGO® x, y, z stage
3. Develop software programmes using the LEGO® MINDSTORMS® EV3 software to instruct movement of the LEGO® x, y, z stage, including setting the origin.

4.3 Materials and Methods

4.3.1 LEGO® Bio-printer Design

The design of the LEGO® x/y/z stage is adopted from the original build reported by Marc-Andre Bazergui and Thomas Madeya. It was initially designed and built with a polymer extrusion pen, intended as a traditional plastic polymer 3D printer (Marc-Andre Bazergui and Thomas Madeya, 2017, NEW EV3Dprinter: LEGO MINDSTORMS 3D Printer (3rd Generation), Accessed on 08/06/2021) (**Figure 4.1 A**). To replicate the 3D printer, the authors provided a list of LEGO® parts needed and a step-by-step building guide file, which are both accessible to the public. The 3D printer consists of several components:

1. A programmable EV3 brick which is the control hub in which all programs are uploaded and connects to all motors and sensors.
2. The x/y stage on which the polymer is extruded. The stage is connected to motors, sensors, and actuators.
3. The z vertical unit on which the plastic polymer extruding pen rests. This unit is also connected to a motor and sensor, but not an actuator.
4. Motors provide the power and speed for stage movements. Motor units are defined by “power of motor rotation” or “motor speed rotation” (arbitrary units au), degree(s) of rotation (DOR), or number of rotations.
5. Touch sensors allow to detect limits of movements when pressed, therefore determining the position of the stage and pen (z-axis).
6. Actuators are extendable devices that are responsible for the stage movement and control.
7. A plastic polymer extruding pen mounted on the z-axis unit.

A CAD model of the original 3D printer and the labelled main components are shown in **Figure 4.1 B**. In this study, this original design was adopted and replicated with slight modifications of LEGO® pieces to serve as a low-cost three-axis programmable motorised LEGO® stage. To adapt this into a 3D bio-printer, the previously

● CHAPTER 4 ●

optimised microfluidic t-junction droplet generator device connected to a dual syringe infusion (**chapter 3**) would replace the plastic polymer extruding pen, as shown in **Figure 4.2**. Furthermore, the x/y stage will accommodate the substrate for bio-printing (PPetri dish).

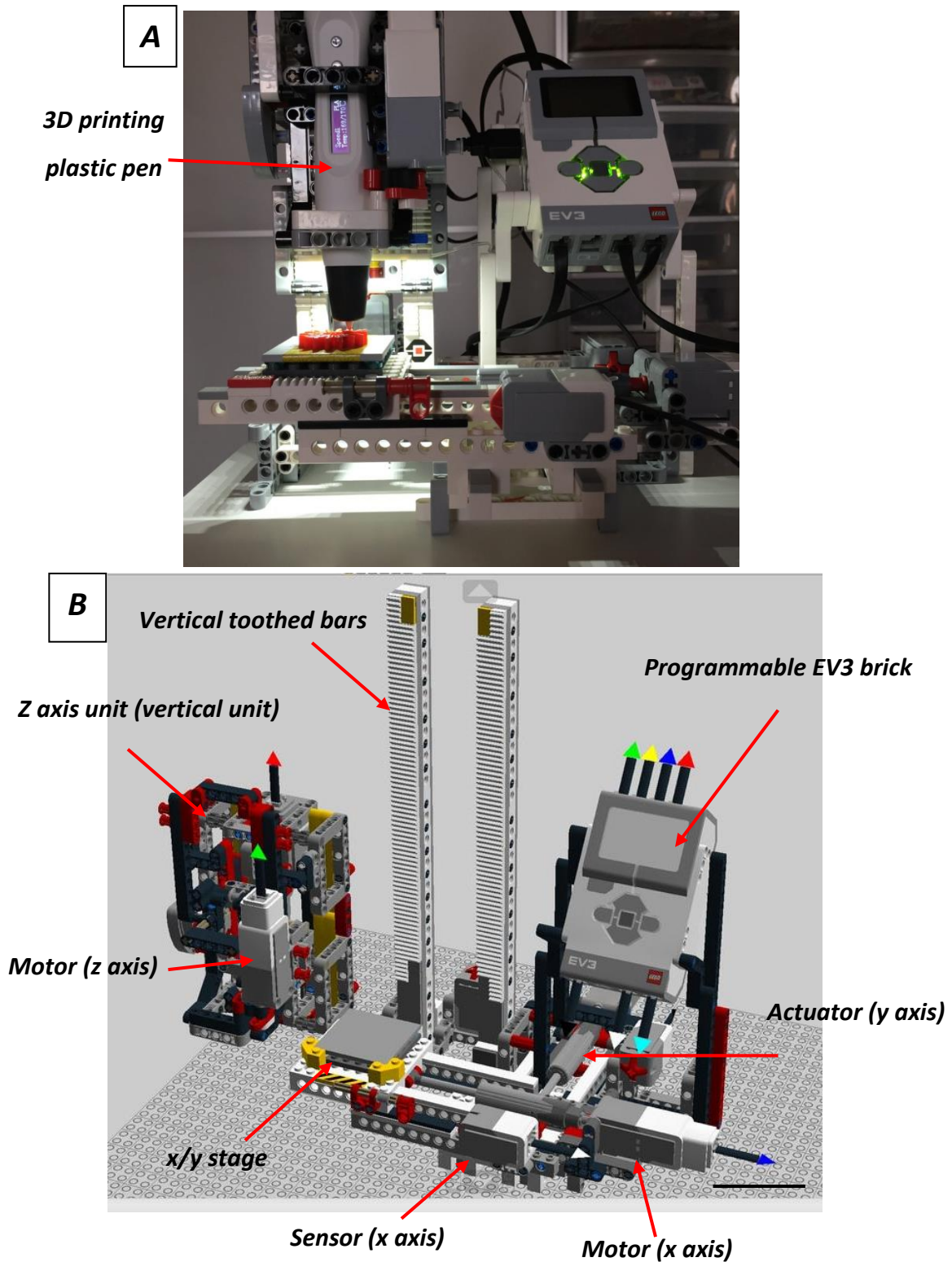


Figure 4.1 The original LEGO® 3D printer: EV3Dprinter.

(A) The 3rd generation LEGO® 3D printer was built from the LEGO® MINDSTORMS EV3 robot. A plastic polymer extruding pen is mounted onto the z unit and designed to 3D print shapes. (B) A CAD image of the LEGO® 3D printer. The Z axis unit has not been mounted on the vertical toothed bars in the design for representative purposes. Scale bar = 50 mm. (Taken & adapted from Marc-Andre Bazergui and Thomas Madeya, 2017, *NEW EV3Dprinter: LEGO MINDSTORMS 3D Printer (3rd Generation)*, Accessed on 08/06/2021).

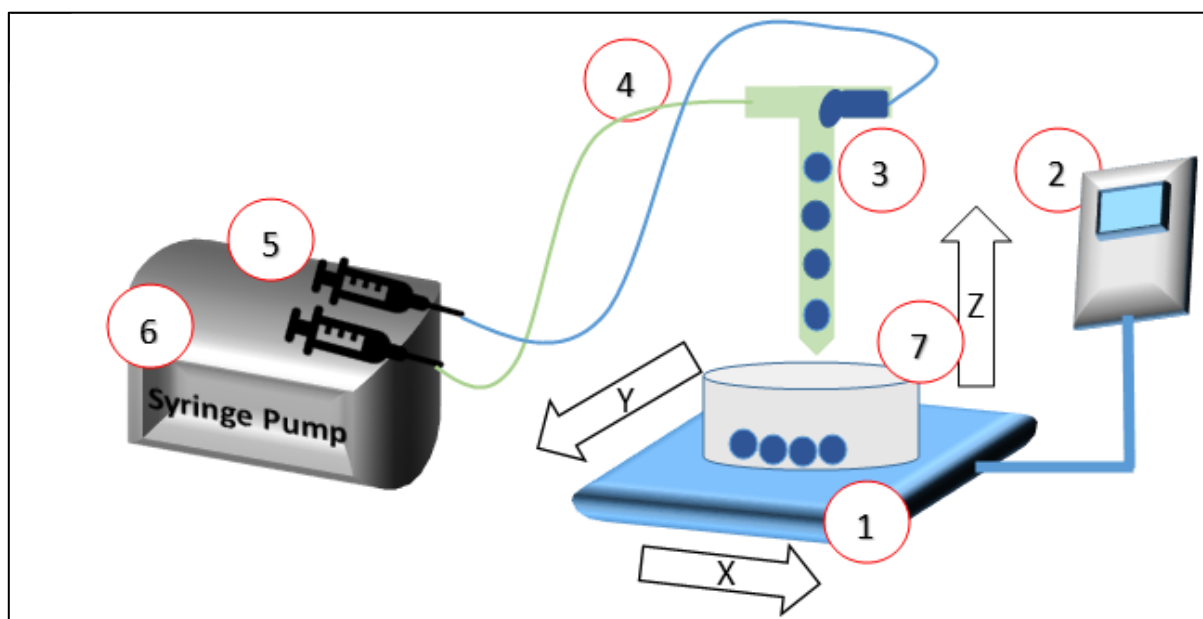


Figure 4.2 The 3D bio-printer concept.

The conceptual 3D bio-printing system would remove the 3D plastic polymer extruding pen and replace it with a t-junction microfluidic system and syringe driver. Furthermore, several LEGO® pieces would be modified and added to adapt to the 3D bio-printing system. The system would contain: (1) LEGO® x/y stage, (2) programmable EV3 brick, (3) t-junction microfluidic device mounted on the z axis unit, (4) microfluidic tubes, (5) bio-ink loaded syringes, (6) syringe pump, and (7) recipient of cell-laden droplets.

4.3.2 LEGO® Bio-printer Build (Hardware)

Katie Harvey, an engineering student, was the first to construct and adapt the first LEGO® bio-printer prototype, as shown in Figure 4.3. This was constructed from a combination of LEGO® Technic and the LEGO® MINDSTORM EV3 following a virtual step-by-step guide to building the LEGO® 3D printer model and the full LEGO® parts required. The step-by-step guide is provided with the LEGO Digital Designer (LDD) software, which is similar to CAD programs, providing a virtual rendering of the 3D printer and individual LEGO® pieces needed to complete the build. The required LEGO® components were purchased from (LEGO® store, John Lewis and Ebay). A full list of used LEGO® parts is found in the appendix (**Appendix A-5**). The complete 3D bio-printer setup with the syringe pump is shown in **Figure 4.3**. The majority of previously reported custom-built bio-printers have been adapted from 3D desktop printers and provide an open-access building guide and parts list (Kahl et al. 2019).

● CHAPTER 4 ●

The x sensor and motor are positioned horizontally on the right side of the stage whilst the y-axis modules are positioned at the rear of the programmable EV3 brick. The x and y medium servo motors were connected to linear large “L” actuators, with an extendable capacity of 4 cm, that were responsible for the stage movement. The z axis sensor is fixed at the rear of the stage and the motor on the moving unit with the microfluidic nozzle. Stage movements are controlled by the x and y-axis motors and sensors. Whilst motors control actuator extension and retraction, i.e., the stage movement, sensors allow to detect the limit of that movement. The z large servo motor is responsible for the printer nozzle height positioned on the vertical track, or perpendicular movement. The programmable EV3 brick supplies power to all the printer pieces using 6 AA rechargeable batteries and communicates the programmed commands to define stage movement speed and orientation. A display screen and buttons located on the brick allow control and display of uploaded programs.

In later stages of the project, two more students, Grace McDermott and Lluan Evans, built one LEGO® bio-printer each, providing the lab with a total of three bio-printers. A timelapse video of the complete LEGO® x/y/z stage build is available in the appendix **(Appendix A-6)**.

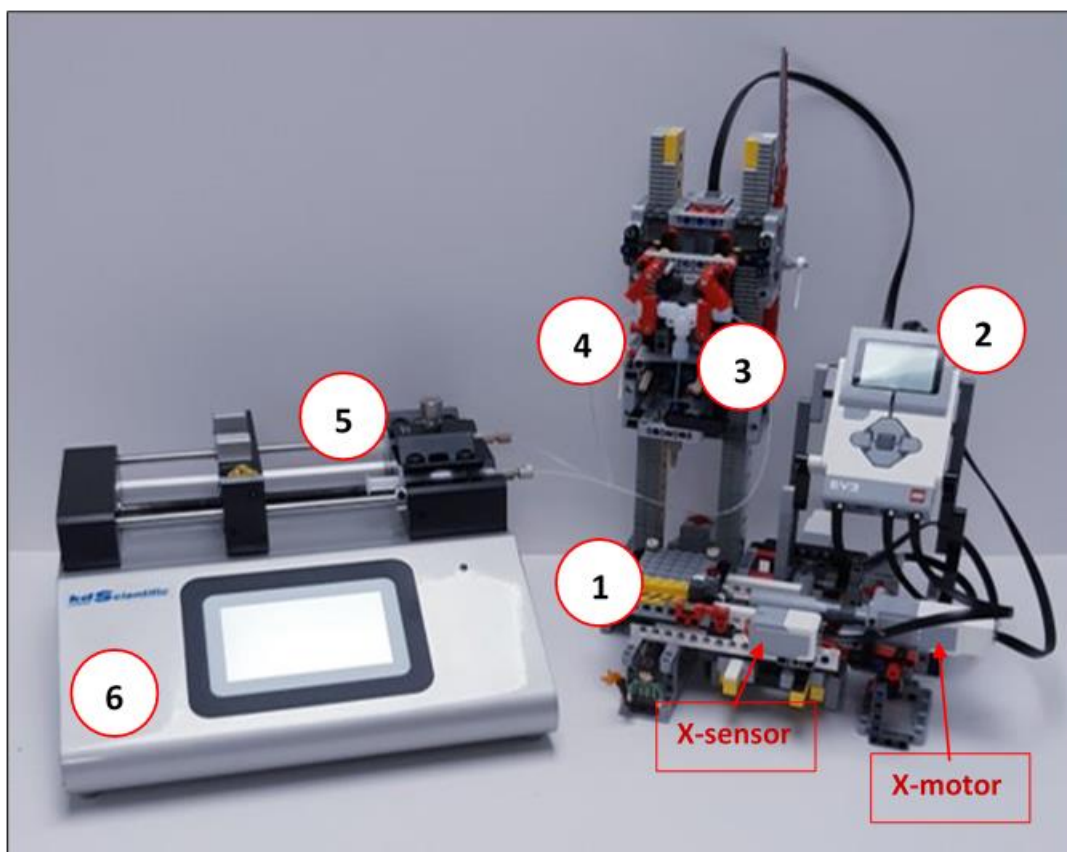


Figure 4.3 The adapted LEGO® 3D bio-printer.

(1) A controlled x/y/z programmable stage was built and adjusted allowing fine movement in the x, y, and z positions at different speeds. Specific programmes dictating the movement of the stage were uploaded and controlled via the (2) control brick or EV3 brick. This was combined with a (3) microfluidic T-junction (4) and microfluidic channels connected to (5) syringes containing the bio-ink (oil phase and alginate phase) placed on a (6) syringe pump allowing to push the contents at defined flow rates (ml/hr). The droplets are extruded in a (7) target substrate mounted on the stage (50 mm petri dish).

4.3.3 Printer Control (Software)

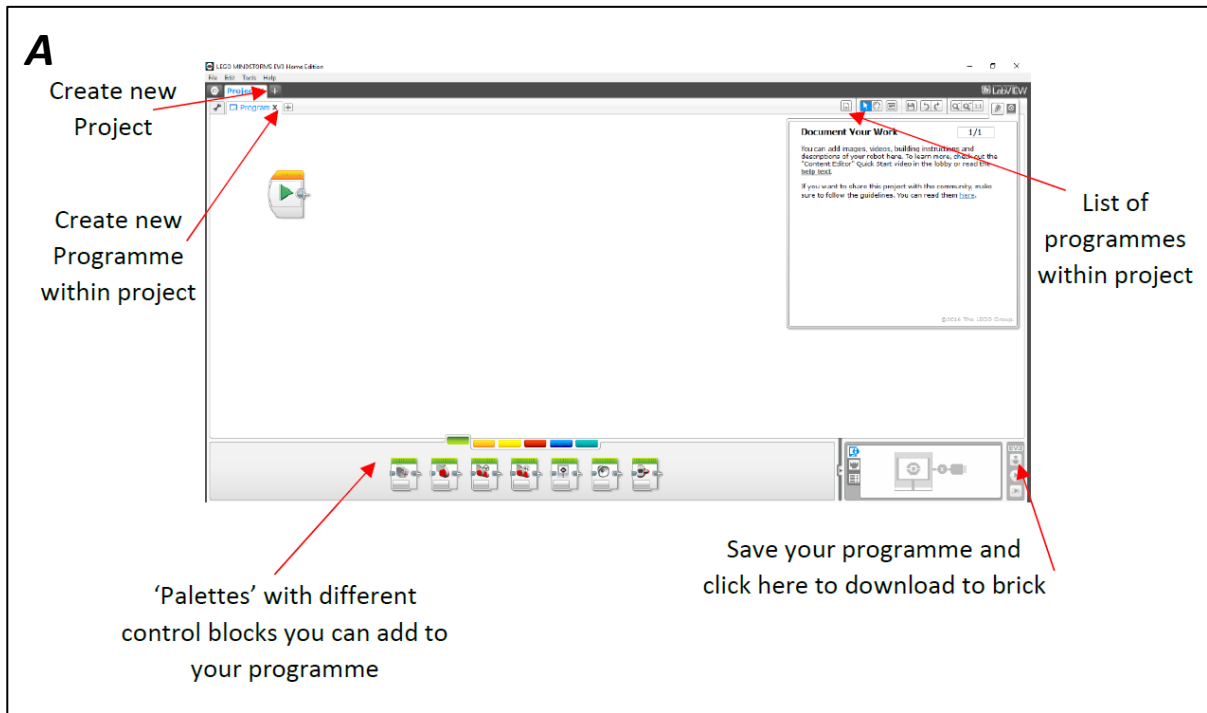
The programming software used to generate orders to the motorized stage uses a visual programming language (VPL) powered by LabVIEW (LEGO® Mindstorms® Programmer) (Figure 4.4 A). The programmes consist of a chain of command blocks (described below) and arrows (or graphic symbols) which are uploaded and executed through the “programmable brick”. These programmes dictate the movements of the stage in the x/y/z plane at defined trajectories and speeds. The stage speed, trajectory and distance are user-definable and programmed to work in unison with the frequency of droplet production. This allows control of printing resolution and dimensionality. Once uploaded, the

● CHAPTER 4 ●

selected program can be located and chosen using the EV3 brick. Alternatively, the programmes can be directly tested via a PC connected to the brick.

Six types of palettes containing different control blocks can be used in the programme marked by different colours: action blocks (green), flow control blocks (orange), sensor blocks (yellow), data operation blocks (red), advanced blocks (blue), and “my blocks” (cyan) (**Figure 4.4 B**). Green action palettes are mainly responsible for powering the motor which is defined in rotation speed, number of rotations and degree of rotations (DOR). This affects stage movement speed and distance travelled in the x/y/z axis. It also allows control over display changes or sound effects. The orange flow palettes determine the execution and flow of the programme including any pauses, delays, or loops. Yellow sensor blocks are used to measure values provided from different types of sensors. This can also set the rotation count to 0 to set a new origin. Red data operation blocks allow the robot to carry out a variety of mathematical calculations logical operations and variables: logic blocks can determine whether a statement is true or false before providing a defined feedback function; maths blocks allow to input formulas, program numbers, or round up/down when required; variable blocks can store data in different forms (numeric, text, or logic) allowing labelling of the data within a program. This data can then be read and used to display different types of information depending on the type of variable used. The advanced blue blocks have not been used in this study. My blocks allow the user to condense a created programme into one block which can then be implemented into other programmes for visual ease. The software allowed the creation of a library of stage movements and trajectories that were saved into one file and uploaded into the EV3 brick.

• CHAPTER 4 •



B

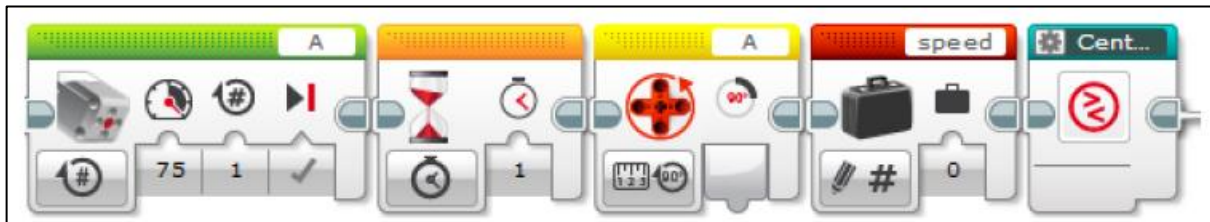


Figure 4.4 Mindstorms visual programming language (VPL).

(A) The software allows the user to input specific sequences of motor and sensor blocks allowing control over motor speed, x/y/z trajectory, and distance. The created programme can be directly output to the programmable EV3 brick and ultimately determines 2D and layer-by-layer 3D print designs. (B) An example of all 5 available palettes. Each palette fulfils a specific type of command and can be dragged and linked to other palettes to create command sequences. (Co-produced with Katie Harvey).

4.3.4 Measuring lateral and perpendicular movements of the LEGO® stage

Stage distances were explored and measured using the DOR of the x and y motors. To determine the ratio relationship between DOR and the stage travel in the x and y planes, using a measurable unit such as millimetres (mm), a pen was mounted onto the z axis unit perpendicularly and a white paper was positioned on the stage in a Petri dish. This enabled lines to be drawn corresponding to a certain value of DOR (**Figure 4.5**). These lines were measured and the relationship between the DOR and distance in mm, in the x and y planes, was established by measuring increments of 1000 DOR. To evaluate the relationship between the large motor DOR of the z-axis unit and z-axis distance movements, increments of 100 DOR were manually measured using a ruler. A ruler was stabilised onto the toothed bar and each 100 DOR distance moved was measured on graduated ruler.

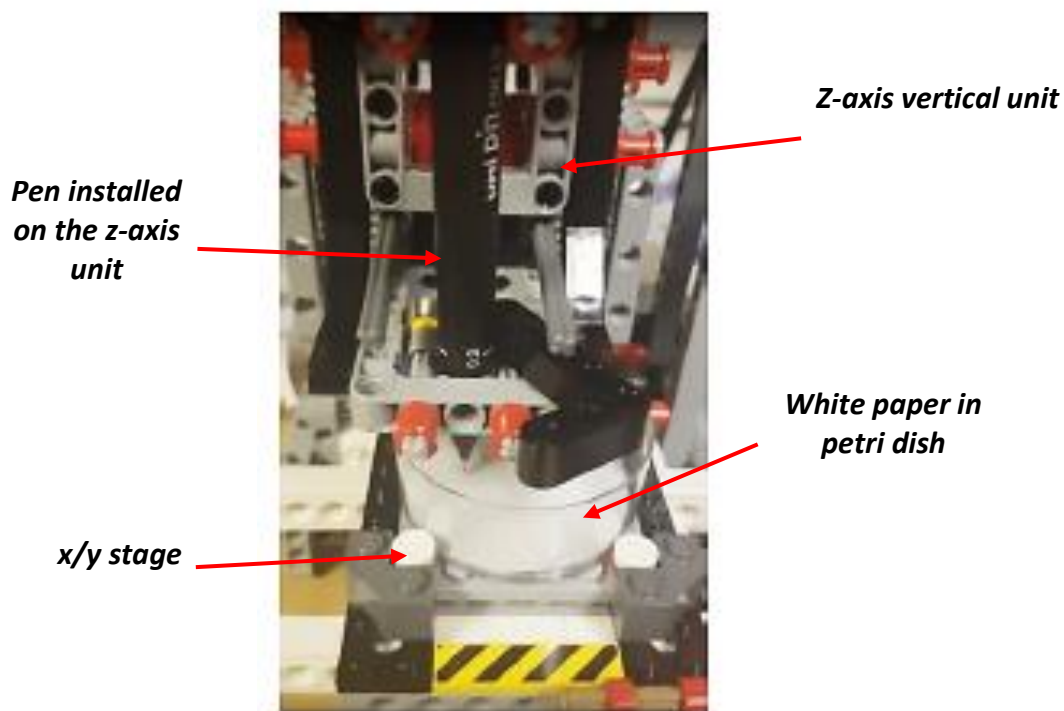


Figure 4.5 Method development for measuring the LEGO® stage lateral distances.
(A) DOR was converted to millimetres (mm) by mounting a pen onto the z-axis unit and drawing a line that was measured. (Produced by Cameron Pool).

4.3.5 Measuring the lateral speeds of the LEGO® stage

Speed limits of the LEGO® stage were explored and measured using the “power of motor rotation”, or motor rotation speed, expressed in arbitrary unit (au). To translate the au to a metric measurement, parallel lines were drawn on a piece of paper in a Petri dish using the same setup shown in **Figure 4.5**. Each drawn line was subsequently measured using a ruler.

4.4 Results

4.4.1 Defining the LEGO® 3D bio-printer hardware dimensions

A LEGO® x/y/z stage weighing 0.55 kg, measuring 225 mm in width, 320 mm in height, and 160 mm in depth (320 x 225 x 160 mm), was successfully built using a range of LEGO® parts, as described in the methods **Section 4.3.2. (Figure 4.6)**. Images of the LEGO® stage were captured with 30 cm rulers as references for dimensions.

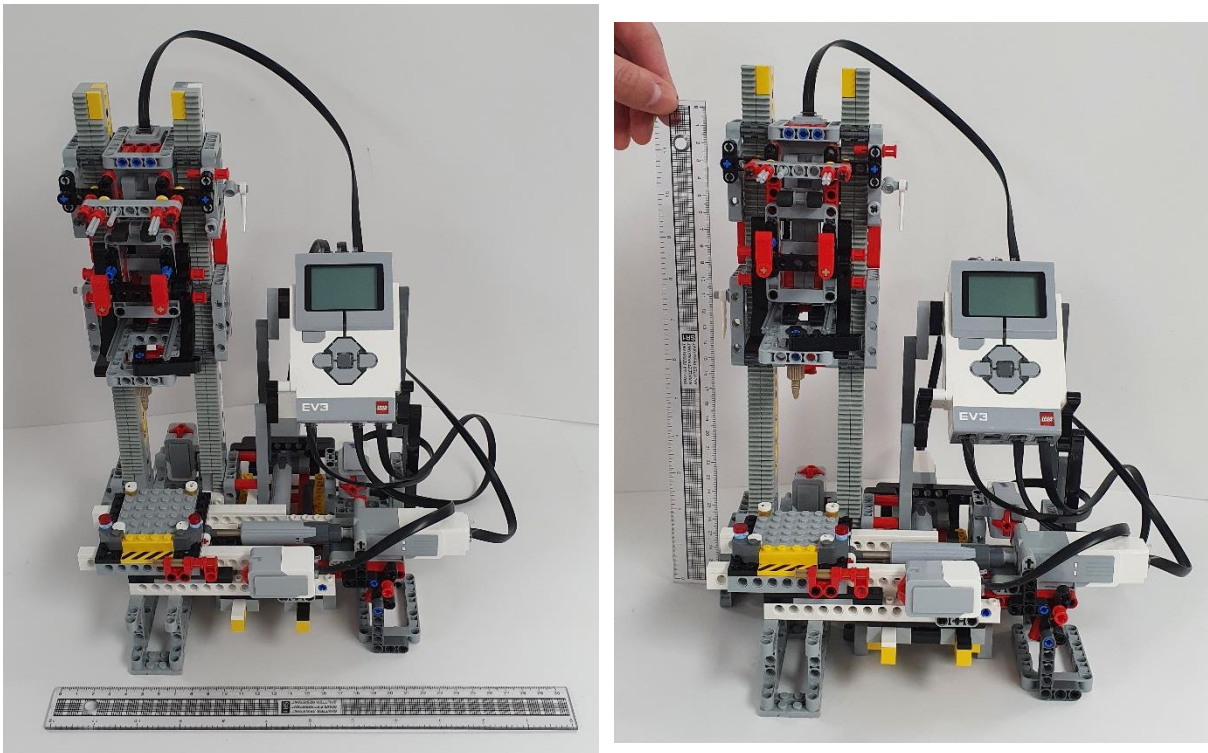


Figure 4.6 The dimensions of the LEGO® x/y/z stage.

4.4.2 Exploring and controlling the movements (distance and speed) of the LEGO® 3D bio-printer stage

Exploring the spatial and speed limitations of the custom-built LEGO® 3D bio-printer stage is crucial to determining its capabilities. Understanding such parameters would aid in: (1) identifying the possible printing area and size limitations in the x, y, and z planes, (2) predicting and testing stage speed movements for optimal droplet deposition, i.e., 3D bio-printing resolution, and (3) programming custom-defined stage movements in 2D and 3D which translate to movements determining the locations of droplet deposition. For this, it was firstly important to convert the programming language into an identifiable measurable format, which means to describe a ratio relationship between the units provided by the programming software and known units of distance and speed. Secondly, to identify the printer's spatial and speed limitations which will subsequently be programmed to work in unison with droplet generation frequency.

4.4.2.1 Measuring and controlling the lateral and perpendicular distances moved by the LEGO® 3D bio-printer stage

Printing in x and y planes is facilitated by lateral movements of the stage, whereas printing in the z direction is controlled by perpendicular movement of the printing nozzle. These are controlled by two different servo motors, which include a rotating wheel that can be programmed to rotate at a set degree of rotation. Control of the servo motors allows the stage to move to a specified length in the x and y planes or the nozzle to be moved to a specific height to control build in the z direction. Programmed motor blocks or palettes determine this distance using arbitrary units set by the LEGO® programming software, including number of motor rotations, number of seconds it rotates, DOR. To achieve the highest level of precision in stage movement, DOR was used to programme the distances of travel. Two servo motors are used in the LEGO® 3D bio-printer stage, a medium servo motor for x and y movements of the stage and a large motor for z movements of the nozzle.

● CHAPTER 4 ●

The first step was to determine the ratio relationship between DOR and the stage travel in the x and y planes in mm. Whilst 360° DOR corresponds to one full motor rotation, the travelled distance in measurable units was unknown. Results demonstrated that 1000 DOR equates to 4.16 mm and therefore 1 mm of movement corresponds to 240.38 DOR (**Figure 4.7 A**). This was repeated in both the x and y axis to confirm a 1:1 relationship. The 3D bio-printer step-size (smallest movement possible provided by the motors and actuators) is therefore theoretically ~4.16 μm, which corresponds to 1 DOR.

The printer has a motion range of 4 cm in the x and y planes, owing to the length of the extendable actuators. However, a restricted area for bio-printing on the circular Petri dish, which has a diameter of 2.56 cm, was required. The print area was therefore restricted to an imaginary square within the circular Petri dish, as shown in **Figure 4.7 B**. To find this, the length of the square vertices was calculated (c) to be 2.82 cm. With a Petri dish radius of 2 cm (rounded down from 2.56 cm for safety) and half the cross-section length of 2 cm (a and b), the use of the Pythagoras theorem ($a^2+b^2=c^2$) allowed to find the square vertices of 2.82 cm in length, making a 2.82 cm by 2.82 cm square a safe printing area. The corresponding DOR (6778.716) was then calculated and programmed in to the software as the limits of movement for all future shapes. However, due to issues related to the adherence of droplets to the plastic substrate (i.e., the Petri dish surface), the printing area for the current iteration of LEGO® bio-printer x/y stage was on a glass cover slip with a length and width of 5 and 2.4 cm, respectively. Hence, the optimal printing area of 2.82 cm in the x axis and 2.4 cm in the y axis is therefore considered more appropriate to ensure efficient droplet adherence to the surface.

The perpendicular z-axis unit is mounted onto two toothed vertical bars with a range of motion of approximately 15 cm. As mentioned previously, the z-axis unit is not controlled by an actuator, but its movements are dictated by the toothed bar, which provides a different relationship between the DOR, and the distance moved. A linear relationship resulted in approximately 14.3 DOR equating to 1 mm of movement or a step-size of 70 μm. The precision of the primer in the z direction is therefore not as refined as the x and y planes.

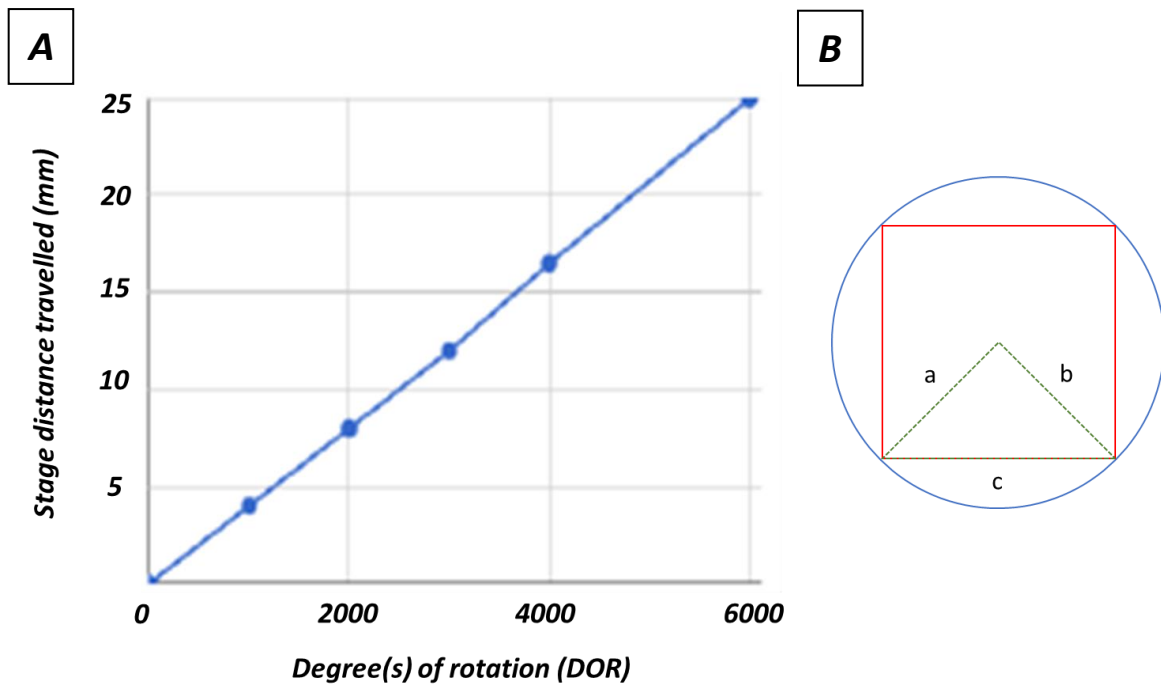


Figure 4.7 Measuring and controlling the lateral movements of the LEGO® stage. (A) A graph showing the ratio relationship between DOR of a medium servo motor and the stage movement in millimetres (mm). (B) The red square corresponds to a safe printing area within the petri dish, identified using the Pythagoras theorem ($a^2+b^2=c^2$). ($n=2$ for both x and y axis). (Co-produced with Cameron Pool).

4.4.2.2 Measuring and controlling the speed of lateral movements of the LEGO® 3D bio-printer stage

The speed of lateral movement of the 3D bio-printer stage in the x and y directions is a key parameter which contributes to bio-printed resolution (packing of droplets or droplet spacing) and is therefore an important step towards efficient 3D bio-printing. The speed at which the stage moves is determined by the “power of motor rotation”, or the speed of motor rotation. This can be specified in the motor block by inputting arbitrary units (au) from -100 to +100, which needed to be converted, as previously described, into measurable units of the distance travelled in a specified time (mm/s). Negative and positive values correspond to the direction of motor rotation. Hence, positive au values were used to extend the stage (extend the actuator) whilst negative values retract the stage (retract the actuator). For example, if the y motor au is positive, the y actuator will extend, moving the stage towards the user laterally.

● CHAPTER 4 ●

Different motor speeds (stage movement speeds) were explored by running the motor for 5 seconds at a “power of motor rotation” (au) starting at 10 au, until a maximum power of 100 au was reached. Maximum motor power was reached at 75 au, and this translated to a 25 mm line in 5 seconds i.e., approximately 5 mm/s (**Figure 4.8**). The smallest increment of 10 au corresponded to a 0.66 mm/s stage speed movement. Hence, the stage speeds ranged from 0.66 mm/s to 5 mm/s, following the explored au. Results demonstrated that increasing the power by 15 au relates to increasing the movement speed by 1 mm/s. With a maximum speed of 5 mm/s and a degree of accuracy <1 mm/s, a range of speeds can be subsequently tested alongside droplet frequency generation to achieve high resolution bio-printing. The speed of the vertical movement (z-axis) was not explored as it was considered irrelevant to the proposed application of the bio-printer.

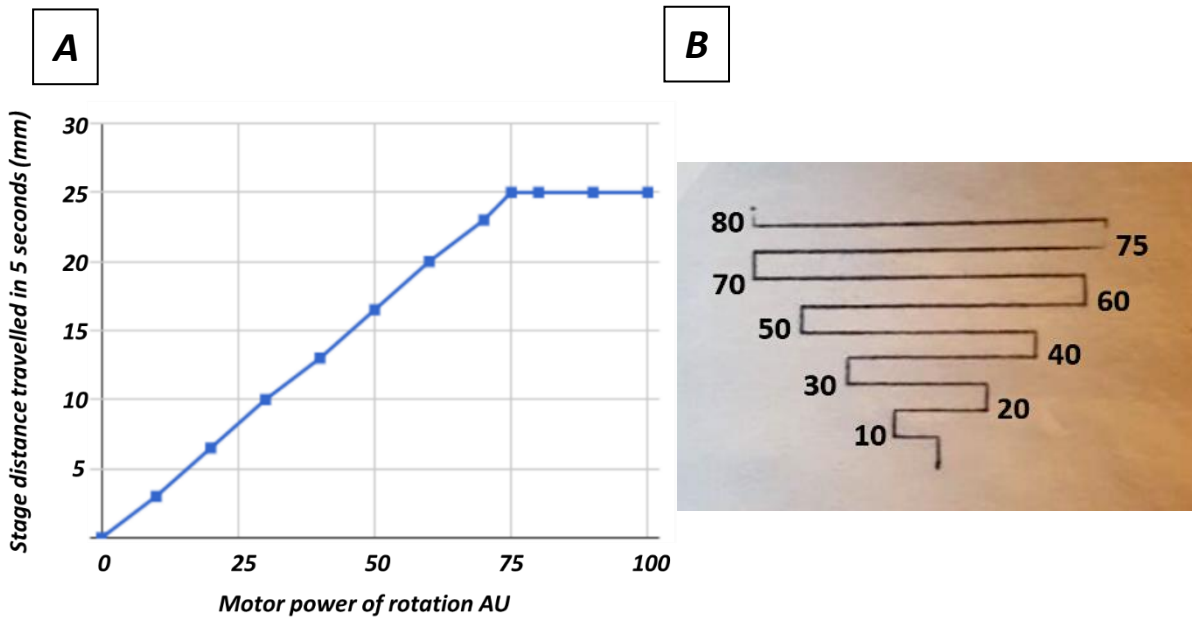


Figure 4.8 Measuring and controlling the lateral stage speed.

(A) The relationship between the power of the motor and the speed of stage travel in millimetres (mm). (B) A visual representation demonstrating the stage’s distances travelled in 5 seconds (mm) in relation to a range of motor power from highest (top) to lowest (bottom) (Co-produced with Cameron Pool).

4.4.3 Defining the default positions and parameters of the LEGO® 3D bio-printer stage

With the tool to efficiently instruct user-defined stage movements and speeds, a software programme known as the “Programme_Run” was created that would instigate a calibration process consisting of moving the stage to a reproducible x/y/z origin position known as the default positions, from which different print patterns would be instigated (**Figure 4.9**). It is crucial to initiate this programme before selecting any other programmes for 3D bio-printing as it allows for spatial calibration. The spatial origin is defined as the position at which the centre of the stage is aligned with the microfluidic exit nozzle in the x/y axis, and the height (z-axis) is set to 7 cm above the stage. This occurs when the stage is driven to both x and y sensors and the z-axis to its z sensor, which when triggered, will lead the stage and nozzle back to its origin. As an example of how it functions, if the position of the stage is not at the origin position, initiating the “Programme_Run” programme would spatially calibrate the stage and nozzle to the pre-defined origin. A video showing the calibration process when selecting “Programme_Run” is shown in **Appendix A-7**.

The default positions are not optimal for droplet deposition, because the nozzle distance to the stage (7 cm) is far. However, the calibration process is simply the initial step to ensure consistent stage and nozzle spatial calibration. Indeed, the calibration process was programmed independently from the droplet characteristics and rate of droplet production. The calibration setup differs from the subsequent programmes intended for bio-printing which were programmed according to the droplets’ approximate geometry and flow rate production (**Chapter 3**). These three parameters include: (1) the control of the height step-size increments (smallest movement increment), which was instructed depending on the droplet average lengths and widths (approximately 1.1 and 0.8 mm, respectively), (2) the x/y step-size instructed depending on droplet width (~0.80 mm), and (3) default motor speed which was programmed proportionally to droplet production rate. (**Figure 4.9 b, c & d**). However, these parameters are defined by the user and can be altered as desired.

● CHAPTER 4 ●

The “Programme_Run” programme not only provided the 3D bio-printer with a calibration setup, but also allowed the user to enter a main menu screen with several choices that would be available upon creating and uploading new programmes. This will be further explored in the following sections.

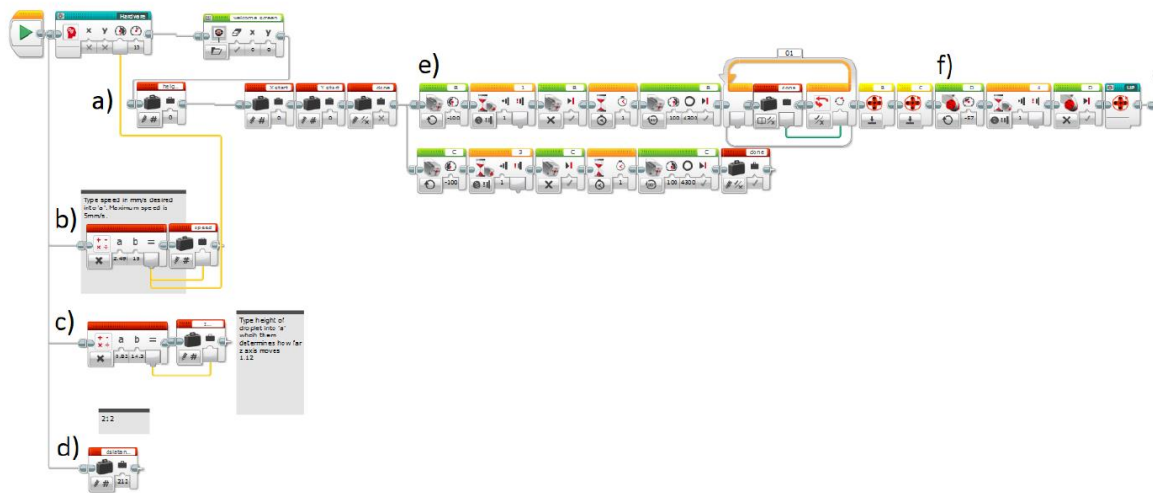


Figure 4.9 “Programme_Run” calibration programme.

(a) Sets all axis to a value of 0. (b) Default motor power input in mm/s controlling the default speed of the stage. (c) Height step-size movement distance. (d) x/y step size movement distance. (e) Motor movement driving the stage to the x and y sensors which triggers it to move back to the origin point or centre. (f) Motor movement driving the z-axis to its sensor which then moves it back to its origin point. (Produced by Cameron Pool.)

4.4.4 Modifying the default print height, starting position and speed for the LEGO® 3D bio-printer stage

Once the 3D bio-printer is calibrated to the origin position, the user will require different parameters depending on the desired prints. Therefore, the incorporation of user-defined parameters post-calibration, is important in enabling more flexibility and print variability. “User-defined parameters” are options implemented in the programme that allow the user to select options that differ from the default set height, starting position, and speed. This allows higher flexibility in the future designed models. To facilitate this choice, three programmes allowing to set a user-defined starting height, centre point, and speed were created and uploaded into the EV3 brick. Once “Programme_Run” programme has been chosen and the 3D bio-printer is calibrated to its default positions, a new menu option named “Parameters” can be selected, in which all three user-definable programmes were uploaded

in as shown **Figure 4.10**. Three options are available: “Height”, “Adjust Centre”, and “Speed”, which allow to change the default starting position of the x/y and height of the z-axis and change the default speed. These options can be selected before selecting a defined patterned movement.

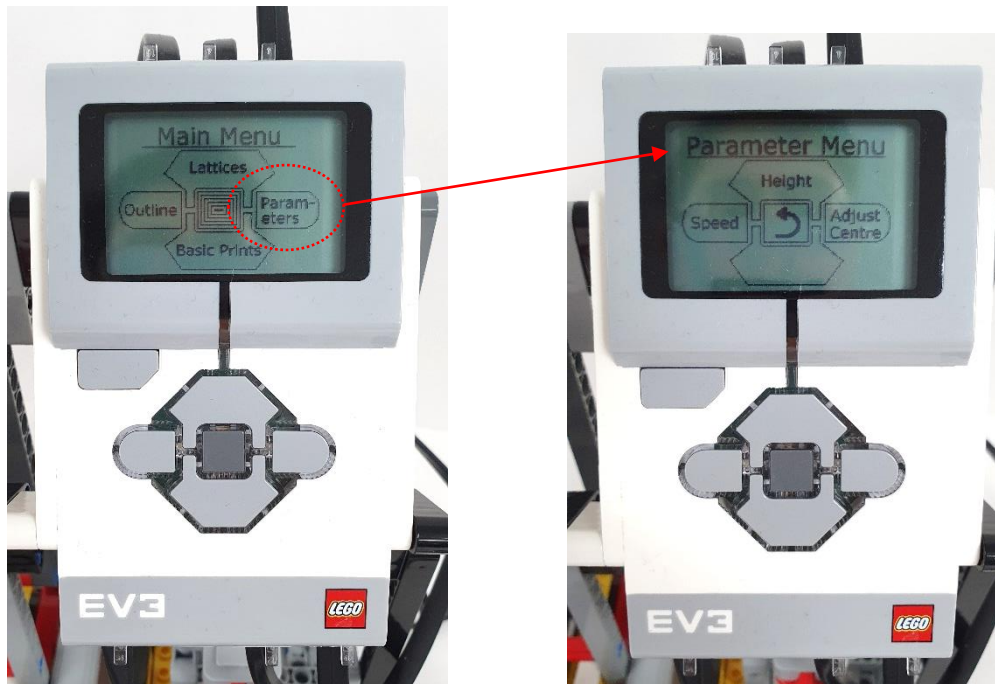


Figure 4.10 Main menu and Parameter menu options.

The parameter menu includes options to change the default starting position (Adjust Centre) and height of the x/y stage and z-axis and change the default speed.

4.4.4.1 Modifying the default print height for the LEGO® 3D bio-printer stage

Setting a desired initial print height, differing from the default height of the extruding nozzle is important in generating a variety of 3D bio-printed structures. Upon selecting “Set Height”, the extruding nozzle will move from its neutral position to a lower position, from which the user can start adjusting a desired starting point on the z-axis. Options include raising or lowering the nozzle in step-sizes instructed depending on the droplet height size (1.1 mm) (**Chapter 3**) or ten times the droplet size for faster vertical movements. The user can then

confirm the choice and the nozzle will commence at the chosen position when bio-printing programmed shapes.

4.4.4.2 Modifying the default starting lateral (x/y) position for the LEGO® 3D bio-printer stage

Although the centred position (origin or default) is programmed into the calibration process, the user can define a custom starting position in the x and y planes within the Petri dish area, permitting flexibility in the patterns that can be bio-printed in 2D and 3D. The user can define a centre position, from which prints can start. The step size in the lateral movement of the x or y is programmed to move at an equal size to a droplet width, determined from **Chapter 3**, (~ 0.80 mm). Once confirmed by pressing on the tick button, the position is recorded and the next shape that will be chosen to bio-print will commence at that chosen x/y position.

4.4.5 Modifying the default starting speed for the LEGO® 3D bio-printer stage

Like previous parameters, the speed of the x/y motors can be altered as desired. Five different speeds, from 1 mm/s to 5 mm/s were programmed and uploaded to the “Parameters” menu option (**Figure 4.10**). The user-defined parameters not only provide movement flexibility and versatility to bio-print a range of shapes, but also offer a range of parameter options that can be directly selected from the menu without altering the programming language.

4.5 Discussion

A custom-built LEGO® 3D bio-printer was developed for the controlled spatial deposition of bio-material and bio-ink to generate tissue-like 3D structures. The 3D bio-printer's capabilities and bio-printing resolution were explored by synchronising the x, y, z stage speed and movements with the droplet production frequency, allowing for the bio-printing of 2D and 3D patterned structures.

Often, the proprietary nature of commercial bio-printers can restrict access to hard- and soft-ware, and subsequently restrict flexibility in generating complex bio-constructs (Pakhomova et al. 2020). To avoid this, laboratories commonly resort to converting open-access low-cost off-the-shelf 3D printers into 3D bio-printers by replacing the printing nozzle with a cell-compatible extruding printhead (Reid et al. 2016; Kahl et al. 2019; Ioannidis et al. 2020; Sanz-Garcia et al. 2020). Whilst most commercial bio-printers consist of complex hardware, designing and building a custom-built bio-printer provides a strong understanding and familiarity of the hardware system. Indeed, the modular nature of LEGO® systems, diversity of parts, low-cost, and high commercial availability makes it easier to modify, adapt, repair, and increase in complexity. Furthermore, the in-house built LEGO® 3D bio-printer stage is lightweight and compact, making it portable for insertion into a sterile culture hood (**Figure 4.6**). Reported custom-built 3D bio-printers are less cumbersome compared to commercial hardware, however, they remain larger and heavier than the LEGO®-built bio-printer (Kahl et al. 2019; Sanz-Garcia et al. 2020). For example, Kahl et al.'s bio-printer, based on the "Anet A8 Desktop 3D Printer" measures ~510 x 400 x 415 mm and weighs 8.5 kg. Earlier studies using droplet-based bio-printing techniques require the entirety of the sterile culturing hood area to install the bio-printing setup (Moon et al. 2010; Xu et al. 2010).

In these studies, bio-constructs are modelled using 3D printing-dedicated open-access computer-aided-design (CAD)-based software, such as FreeCAD or TinkerCAD (Faramarzi et al. 2018; Sanz-Garcia et al. 2020). However, according to Gulyas et al., 3D printing-dedicated software tools are subpar for 3D bio-printing applications, which require unique and specialized motion patterns and nozzle control (Gulyas et al. 2018). A key advantage in using a visual programming language (VPL), such as that created by LEGO®, is the high accessibility

to a wide public, especially for those with little expertise in programming. With an intention to engage younger communities to discover robotics engineering and programming, the EV3 MINDSTORMS software application provides a user-friendly platform for novice and expert programmers in an intuitive graphic environment (Kim and Jeon 2007). Indeed, programming can be considered as a hurdle for those with a non-engineering background. Many tutorial videos dedicated to novice programmers were available and significantly helped in creating the programmes used to move the LEGO® stage. Designing simple lateral movements, implementing a selection of options in the main menu, and calibration movements were accessible and enjoyable tasks for both novice and expert users in this project. As opposed to traditional text programming, VPL uses a simple drag-and-drop of coloured blocks with defined functions in specific sequences to fulfil a command. This provided an intuitive environment when testing different combinations of sequences and palettes. Therefore, line-by-line text command, which requires more expertise, is not required. Furthermore, copying the programme into the EV3 brick can be circumvented by directly connecting a computer which operates the EV3 software to the 3D bio-printer, allowing VPL programmes to be immediately visualised and tested. In the near future, a dedicated laptop will be systematically linked to the 3D bio-printer, for faster editing. Whilst the LEGO® MINDSTORMS EV3 visual programming language (VPL) software provides a good platform to learn programming functions, it is unsuited for the large files with complex programming sequences that may be needed to bio-print tissue. In this study, as the programmes grew more complex and the file became larger, the software encountered several ‘crashes. Generating increasingly complex programmes with unique stage patterns will necessitate a more adequate VPL software and operating system.

In this study, the maximum distance the stage can travel in the x and y planes is approximately 4 cm, which is dependent on the maximum extendable length of the actuator used. This is useful for this project’s current purposes, but LEGO® also provides different sized linear actuators that can extend from 2.4 (small “S”) to 6.4 cm (x-large “XL”), possibly providing a larger working area in the future (Sariel’s Bricks & Pets, October 09, 2019, *NEW LEGO XL Linear Actuator: How Good Is It?* Accessed on 09/06/2021). The working area of other 3D bio-printers varies greatly depending on the hardware used, whether adapted from 3D printers or commercially bought. For example, Byoung Soo Kim et al. developed a combinative

● CHAPTER 4 ●

bio-printing platform accommodating both extrusion- and inkjet-based dispensing modules with a working space of 20 x 20 cm (Kim et al. 2017b). Kahl et al. converted an off-the-shelf desktop 3D printer into a bio-printer and reduced the travel range from 22 x 22 cm (x – y) to 10 x 10 cm (x – y) (Kahl et al. 2019). However, sizes of 3D bio-printed bio-material or tissue typically found in studies are significantly lower, and rarely exceed 25 cm² (5 cm x 5 cm) (Lee et al. 2014; Liu et al. 2016; Kang et al. 2018; Yang et al. 2018; Kahl et al. 2019; Kim et al. 2019). Large working space can however be beneficial when bio-printing large-scale tissues, organs or biomedical devices, as demonstrated by the work of Pourchet et al. who produced an adult sized ear measuring 8 cm (Pourchet et al. 2017). A working space of 2.82 cm and 2.4 in the x and y, respectively, were established in this project and considered an adequate area to 3D bio-print tissue structures at the mm scale (**Figure 4.7 B**). The z-axis range is significantly larger, spanning ~15 cm. This distance is more than required as for structures that are constructed with ≥ 1 mm sized droplets. Nevertheless, a 70 μm step size, due to the toothed bar LEGO® pieces and cogwheels found on the z-axis, could be a potential limitation in the future when aiming to reduce droplet sizes and improve print resolution. In future iterations of the bio-printer, alternative LEGO® pieces could replace this mechanism resulting in finer step-size movements, allowing the deposition of smaller droplets with high resolution.

Stage movements could reach step-sizes of 1 mm ($\sim < 240.38$ DOR) experimentally, demonstrating high accuracy of LEGO® motors and actuators. Accuracy of the LEGO® 3D bio-printer stage in the x and y axis could theoretically reach a step-size of approximately ~ 4.16 μm , corresponding to 1 DOR, similar to bio-printers found in the literature (Kim et al. 2017b). Although this theoretical level of resolution has not been tested experimentally, whilst testing speed parameters the stage proved capable of achieving movements as low as 60 $\mu\text{m}/\text{s}$ (corresponding to 1 au of motor power), thus practically demonstrating potential micrometre length movements. Further fine-tuning of stage movements is therefore feasible and arbitrary units could be implemented into the code to three decimal places. For example, a theoretical DOR of 0.250 can translate to a resolution of 1 μm of stage movement. Reducing droplet sizes to $\sim 150 - 200$ μm , as commonly found in the resolution of extrusion-based bio-printers, whilst reducing stage movement speeds would be preferable, as it would approach the bio-printed model to more relevant dimensions (Ozbolat and Hospodiuk 2016; Graham et al. 2017).

● CHAPTER 4 ●

Stage and bio-ink deposition speed are also determinant parameters for the production of high-resolution tissue-like structures and bio-material (Ding et al. 2019). The maximum stage movement speed, defined by “motor power”, was identified at 5 mm/s, corresponding to +75 motor power au (**Figure 4.8**). The first set of experiments demonstrated a speed plateau at values between 70 and 80 units. Stage travel speeds tested ranged from 0.06 mm/s (60 $\mu\text{m/s}$) – 25 mm/s (5000 $\mu\text{m/s}$), or 1 to 75 au, similar to previous studies using in-house built bio-printers (Ding et al. 2019). This provided a wide range of speeds that can be tested with different microfluidic flow rates. Print speeds of commonly used 3D bio-printers are defined as the speed at which a material is produced, which is determined by a combination of stage movement and bio-ink deposition speed that are coupled (Sears et al. 2016). An advantage of the custom-built LEGO® 3D bio-printer resides in the ability to decouple the stage movement and droplet frequency production, which could provide flexibility in parameter optimisation for finer resolution patterning. Ding et al., printed GelMA (gelatin-methacryloyl) grid structures with varying degrees of resolution, using an in-house built 3D bio-printer (Ding et al. 2019) and by optimising the travel speed of the stage independently from the printing head, the resulting grid structures showed different levels of printing resolution, as defined by the printed line thicknesses and pore sizes (Ding et al. 2019).

Implementing custom initial parameters as opposed to the default programme, such as nozzle height, speed, and starting x/y position, is an important step towards producing a variety of bio-printed shapes and diversifying bio-constructs (**Figure 4.10**). Custom parameters allow the user to explore stage parameters in combination with different microfluidic devices, droplet sizes, and/or flow rates in the future. Custom parameters were directly uploaded into the control brick into the parameter’s menu, which bypasses the need to edit or implement programmes into the VPL sequence. However, options for more refined stage speed and starting x/y coordinate choices would require editing from the programming source.

Together, these results allowed to identify the 3D bio-printer’s spatial and speed capabilities. Identifying the relationships between the arbitrary units instructed to the motors and desired measurable units is an important step in optimizing the 3D bio-printer’s stage movements and speeds. This allows to efficiently dictate a user-defined speed movement and determine

● CHAPTER 4 ●

specific movement locations. Furthermore, the stage movement in the x and y planes can be instructed at the micrometre scale. Although the prototype LEGO® 3D bio-printer stage requires further development, exploration and improvement, preliminary data provided adequate levels of stage movement capabilities that have the potential to be enhanced. Indeed, the vertical toothed bar used in this prototype may result in lower z-axis resolution. Furthermore, the programming software was not intended for sophisticated movements, which may result in frequent programme crashes. However, LEGO® offers the advantage of being modular, hence allowing to change pieces easily to optimize movement and stability. As previously described, EV3 MINDSTORMS software can be replaced by a more professional and optimal software such as LabVIEW. Overall, the first LEGO® 3D bio-printer prototype shows promise as an intended 3D bio-printing platform owing to several characteristics: ability of the stage to move in the x/y/z in 3D, ability to control and improve stage movements and speeds to acceptable bio-printing resolutions at the sub-mm scale, and a sufficient bio-printing area to generate bio-constructs of different sizes.

Chapter 5 Evaluating the bio-printing capabilities of the custom-built LEGO® 3D bio-printer platform

5.1 Introduction

Precise patterning of cell-laden constructs and bio-material is important to fabricate tissues with structural fidelity. This relies partly on the 3D bio-printer's printing resolution capabilities, which generally reside between 20 – 500 μm for commercial bio-printers (Miri et al. 2019). Whilst cell-cell distances and resolution within a tissue widely vary in the human body, current bio-printing resolutions have proven to be sufficient in maintaining high cell viability for several weeks, proliferate, differentiate and even grow into a 3D tissue structure (Murphy and Atala 2014). Depending on the type of 3D bio-printer, the printing resolution is affected by several factors, including nozzle or stage moving speed, bio-ink viscosity, extrusion speed, surface contact angle, crosslinking properties, nozzle diameter, etc. (Miri et al. 2019). Custom-built 3D bio-printers have previously shown similar bio-printing resolutions and accuracy to commercial 3D bio-printers, bridging the gap between accessibility and performance (Reid et al. 2016; Costantini et al. 2017; Kahl et al. 2019).

In the literature, bio-printing resolution by low-cost bio-printers is qualitatively and quantitatively assessed by patterning of various shapes (Sanz-Garcia et al. 2020). The 3D bio-printing of multi-layered (3D) constructs are commonly achieved through the layer-by-layer deposition of single layers (2D). Hence, it is important to characterise and establish the capability of a bio-printer to generate a single layer (2D), prior to producing complex multi-layered (3D) structures (Moon et al. 2010). However, this depends on the type of technology and software used. Bio-printing grid structures with controlled pore sizes and strand widths is conventionally reported (Kahl et al. 2019; Sanz-Garcia et al. 2020). Alternatively, other constructs such as pyramids, inverted pyramids, connected parallel lines, cylinders, localised droplets, helices, multi-layered squared lattices, interlaced filaments, etc, have been previously reported (Arai et al. 2011; Faulkner-Jones et al. 2013; Hinton et al. 2015; Colosi et al. 2016; Reid et al. 2016; Pourchet et al. 2017; Ding et al. 2019; Kahl et al. 2019; Ioannidis et al. 2020). In addition to bio-printing different patterned shapes, bio-printing resolution is quantified by measuring the structures dimensions in contrast to the designed or expected model dimensions (Sanz-Garcia et al. 2020). In droplet-based bio-printing, the characteristics of individual droplets partly dictate the bio-printed resolution (Gudapati et al. 2016). Indeed,

● CHAPTER 5 ●

droplet packing, and patterning are not only influenced by the stage speed, but by the shape of the extruded droplets. Droplet shapes are in part affected by the way a droplet is compressed and positioned amidst other droplets. In droplet-based microfluidics, the extent of a droplet's fluidity and surface tension intra-droplets, defines its overall shape, which depends on the interplay of multiple variables, including tubing size, extent of gelation, residence time, T-junction droplet pinching, microfluidic obstruction, reagent concentrations, flow rates, alginate viscosity, surface tension, etc (Lee et al. 2013; Mazutis et al. 2015; Zhang et al. 2020).

Complex multiscale tissue architecture is essential in recapitulating cell-cell and cell-environment interactions and function (Ng et al. 2016). The performance of a 3D bio-printing platform is not only measured through its ability to deposit cell-laden hydrogels in precise locations, but also relies on its ability to deposit multiple bio-inks, material and cell populations (Peng et al. 2016; Kim et al. 2019). This is commonly achieved through interchangeable multi-nozzle bio-printing systems, each containing a unique bio-ink (Lee et al. 2009; Lee et al. 2017a). Recent studies demonstrated the possibility to implement multiple nozzles into off-the-shelf low-cost 3D printers, promising to build accessible and cheap multi-material bio-printing platforms (Sanz-Garcia et al. 2020). Furthermore, a microfluidic device that has been used as 3D bio-printing nozzles has been recently reported and can accommodate two bio-inks for the fabrication of multi-material/multi-cellular constructs for bone and cartilage regeneration (Idaszek et al. 2019)

In this study, a conventional commercial dual syringe driver, costing ~£1500, is used to drive fluid flow to produce alginate hydrogel droplets. Furthermore, the control of the LEGO® 3D bio-printer stage and microfluidic extrusion through the commercial syringe driver are decoupled. In the aim to develop a bespoke and cost-efficient 3D bio-printer, it is necessary to circumvent the use of a costly syringe driver. Hence, a programmable LEGO® syringe driver was built, based on those reported by Ricardo Henrique's "Pumpy" Nano-J Fluidics, which is an open-source system designed for automated fluid handling for treating, labelling and imaging cells under microscopy (Almada et al. 2019). At ~£50, the LEGO® parts needed are readily accessible and affordable. Additionally, the LEGO® syringe pump's motors can be

● CHAPTER 5 ●

integrated with the 3D bio-printer as one system by adding multiplexers, allowing for simultaneous control of the stage and fluid flow delivery.

5.2 Aim and objectives

The aim of this chapter was to integrate the microfluidic T-junction nozzle (**Chapter 3**) with the LEGO® x, y, z stage (**Chapter 4**) and evaluate its potential as a 3D bio-printer platform.

The objectives of this chapter are:

1. Optimise bio-printing resolution by synchronizing stage movement/speed with droplet production frequency.
2. Control the build of 2D (single layer) and 3D structures (multi-layer), in a pre-determined pattern, using individually deposited hydrogel droplets.

5.3 Materials and Methods

5.3.1 Designing a 2D pattern programme to evaluate the relationship between the LEGO® stage movements and droplet deposition printability quality

The 3D bio-printer bed was levelled with a digital spirit level on a smart phone to ensure the custom-built stage has an adequate horizontal surface. Printing was consistently performed into a 50 mm Petri dish containing 20 mL mineral oil or not, onto a glass coverslip inserted at the bottom of the dish.

Preliminary bio-printing experiments were conducted by programming the initial distance from the nozzle to the printing surface at 1.1 mm which corresponds to the average droplet length (**Chapter 3, Sections 3.4.2 & 3.4.3**). However, repeated experiments revealed this distance as sub-optimal due to droplet orientation shift when deposited onto the glass surface. Therefore, the nozzle height was set to a distance of 0.80 mm to the printing surface. 0.80 mm is the average droplet width (**Chapter 3, Section 3.4.3**).

Optimisation of droplet printability was tested by bio-printing four parallel lines onto the glass cover slip. For this, a programme was explicitly created named “4 parallel lines” and uploaded into the brick. The “4 parallel lines” programme was designed to move the stage in the x/y planes, in the shape of 4 interconnected lines, as shown in **Figure 5.1**. To generate a 4 interconnected parallel line movement, the x and y motors were programmed to move the stage alternately, at distances of 0.5 and 2 cm in the x and y axis, respectively. This resulted in a total of 7 movements that would generate 4 parallel lines in the y axis when printing droplets. An image of the “4 parallel lines” programme demonstrates how the order sequence of the motor blocks (green palettes) can be chained together to generate defined movements. Preparation of the microfluidic device, reagents, syringes, and production of alginate droplets were conducted as described previously (**Chapter 3, Section 3.3.1.2**). The microfluidic t-

junction device was mounted on the z-axis vertical unit and one syringe pump was used to generate equal flow rates of alginate and mineral oil, at 4 mL/hr each.

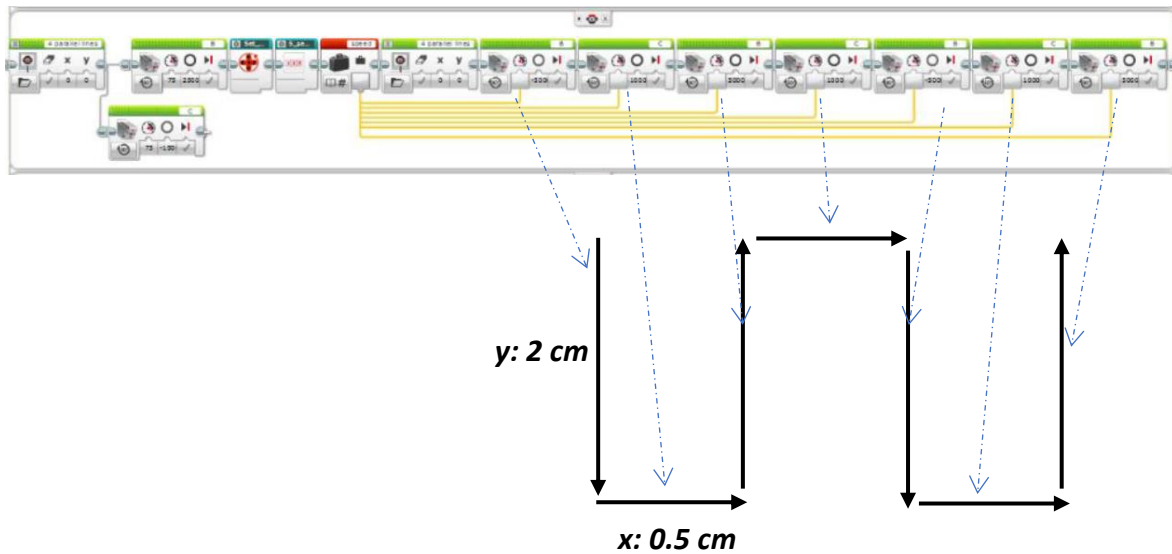


Figure 5.1 The “4 parallel lines” programme sequence and resulting movement concept.
(Produced by Cameron Pool).

5.3.2 Evaluating the relationship between stage movement/speed and droplet printability quality

A range of LEGO® stage speeds were tested in combination with constant alginate and mineral oil flow rates. Tested stage speeds were: 1.75, 2.25, 2.5, 2.75, 2.99, 3.25, 3.75, 4.25, and 4.75 mm/s. The “4 parallel lines” programme was used to evaluate the effect of stage movement on droplet line continuity, packing and spacing. i.e., printability. The quality of adjoined droplets and connecting perpendicular lines were categorised into “printable” or “non-printable” (**Figure 5.2**). Only the two middle parallel lines were evaluated for printability, as shown in **Figure 5.2** by the area marked by the dotted rectangle. Hence, “printable” is defined as: (1) a single adjoined continuous line of droplets, (2) tight droplet-droplet packing with minimal disruption or spacing, and (3) defined connections at two perpendicular angles of the two middle parallel lines (white dotted circles) (**Figure 5.2**). Other flow rates were additionally explored in combination of different stage speeds collectively

demonstrating a range of printable and non-printable lines (**Appendix A-8**). The printed constructs were imaged using a smart phone.

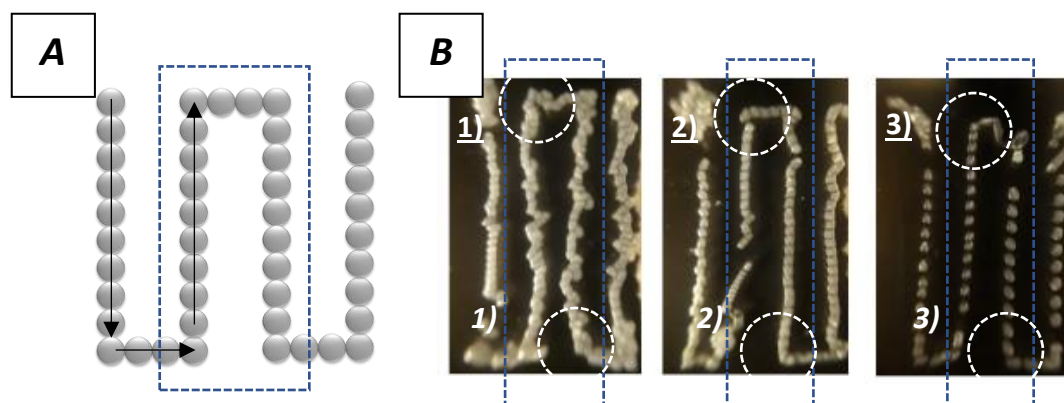


Figure 5.2 A 4 parallel lines programme designed to evaluate the relationship between LEGO® stage movements/speeds and droplet printability.

(A) Schematic concept of the desired “printable” 3D bio-printed structure. (B) Example of “printable” (2) and “non-printable” (1, 3) bio-prints produced at 1.75, 2.75, and 4.75 mm/s, respectively. The dotted rectangle and circles show the evaluated areas for printability, hence the two middle vertical lines and the two connected right angles, respectively. (Co-produced with Katherine Sloan).

5.3.3 Preparation of a visible bio-ink for optimisation of multi-layered bio-printing

Polystyrene fluorescent microspheres of 15 µm size, or FluoSpheres®, were purchased in 4 different colours (carmine, green, yellow and red-orange) from ThermoFisher. FluoSpheres® are polystyrene beads loaded with a specific dye and are originally designed for regional blood flow studies in tissues and organs. FluoSphere® were centrifuged at 160 x g for 5 minutes then mixed with the alginate solution for a final concentration of 5×10^5 beads/mL. The resulting suspension was then drawn into a 3 mL syringe, which was then installed onto the syringe driver. FluoSphere®-encapsulated droplets of different colours were generated by alginate droplet gelation methods mentioned previously (**Chapter 3, Section 3.3.1.2**). An 18-layered cube was bio-printed through the deposition of 18 squared lattices of 16 mm length. The multi-bio-ink cube is comprised of 3 main sections: (1) 8 bottom layers of droplets containing green FluoSphere®-containing, (2) 4 layers of blank droplets, and (3) 6 layers of droplets containing carmine FluoSphere®. To achieve this, the bio-inks

were prepared in advance and interchanged manually between sections. Incorporated FluoSphere® used in this experiment served as cell-sized models (15 µm) to enable visualisation and mimic the potential to incorporate different cell types in the future.

5.3.4 Longitudinal sectioning of bio-printed constructs and macroscale imaging

To visualise the internal patterning and structure of multi-layered and multi-bio-ink constructs, a razor blade scraper was used to cut the structures longitudinally with minimal distribution of the patterning.

Macroscopic images of 3D bio-printed structures containing different coloured FluoSpheres® were taken using the Nikon SMZ 745T (Nikon) stereoscope. The Brunel Eyecam Plus (Brunel Microscopes Ltd) was used to visualise the bio-printed construct and images were saved using the SharpCap capture tool program. Image analysis was carried out using Image J. Images and videos were also taken using Android smart phones.

5.3.5 Dual bio-ink microfluidic setup

Dual bio-ink extrusion was achieved through two strategies: (1) connection of two t-junction microfluidic devices into **one extruding nozzle or single nozzle device (Figure 5.3 A)**, or (2) a **dual parallel nozzle** comprised of two independently controlled t-junction microfluidic devices (**Figure 5.3 B**). The dual parallel nozzle system consisted of two microfluidic t-junction devices with different exit tubing lengths, whilst the single nozzle device had one exit tubing measuring 9 cm. The dual nozzle system consisted of a 9 cm and 14 cm length exit tubes. The 14 cm exit tube was mounted onto the upper section of the LEGO® z-axis vertical unit, whereas the 9 cm exit tubing was mounted onto the original bottom position, as described previously. The bio-inks were prepared as described previously (**Chapter 3, Section 3.3.1.2**), but with the addition of red or blue common food colouring agents (Langdale's Food Colouring). Food colouring agents were diluted at a ratio of 1:5 in dH₂O prior to mixing them with the dispersed alginate phase.

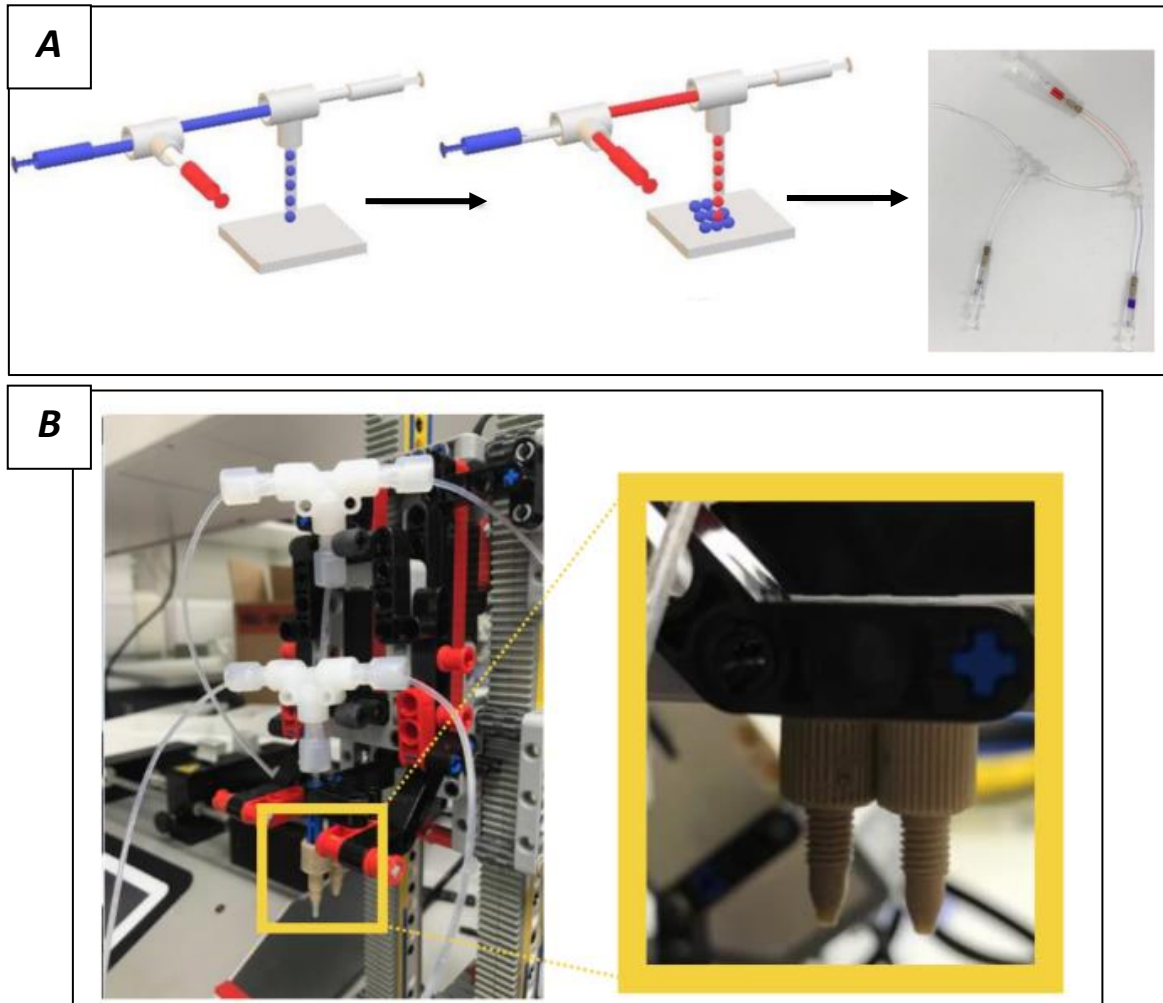


Figure 5.3 Developing strategies for multiple bio-ink bio-printing.

(A) Schematic and experimental images of a multi-setup to allow dual bio-ink printing. Two bio-inks may be sequentially delivered to the microfluidic droplet generating t-junction to print using different bio-inks. (B) Dual parallel nozzle configuration provides an alternative approach to depositing different bio-inks, either sequentially or simultaneously. (Produced by Phoebe Crews-Rees).

5.3.6 LEGO® syringe driver build and droplet production characterisation

A LEGO® syringe driver was built based on designs reported by Ricardo Henriques, who built the NanoJ-Fluidics (Pumpy) multiplexed LEGO® syringe driver arrays designed for liquid additions to microscopy samples (Almada et al. 2019). Similar to the LEGO® stage, the LEGO® syringe driver was built using the LDD software (LEGO®) in a virtual step-by-step environment,

but the design was modified to accommodate a wider range of flow rates (Pedro Almada, May 12, 2018, *NanoJ-Fluidics: open-source fluid exchange un microscopy*, Accessed on 09/06/2021). This was achieved by replacing the medium motor with a large servo motor and changing its position to the rear of the driver instead of placing it in the middle (**Figure 5.4**). A full parts list of LEGO® pieces required to build the LEGO® syringe driver can be found in **Appendix A-9**.

Once the syringe pump was built, the large servo motor calibration was used to predict the relationship between the motor power (speed) in arbitrary units (au) from 0-100, and fluid flow rate (**Figure 5.4 C**). This allowed modification of the gearing and motor positions to determine the optimal range of flow rates required for alginate droplet production. Predictions were compared to experimentally measured flow rates tested using the LEGO® syringe motor speeds. Motor speeds were tested at increments of 10 au, until 100 au, providing a quantitative relationship between motor speed (au) and flow rates in mL/hr. Therefore, working at 30 au translated to a flow rate of 4 mL/hr, which is the previously determined optimal flow rate in this study, is achievable using the LEGO® syringe pump. Droplet production of blue colored alginate bio-ink was evaluated through video captures and a region of interest (ROI) was defined across the tubing using ImageJ (FIJI). Pixel intensity traces corresponding to the passage of each droplet through the ROI were generated using ImageJ (FIJI). The same method was used for commercial KD scientific syringe driver as a comparison.

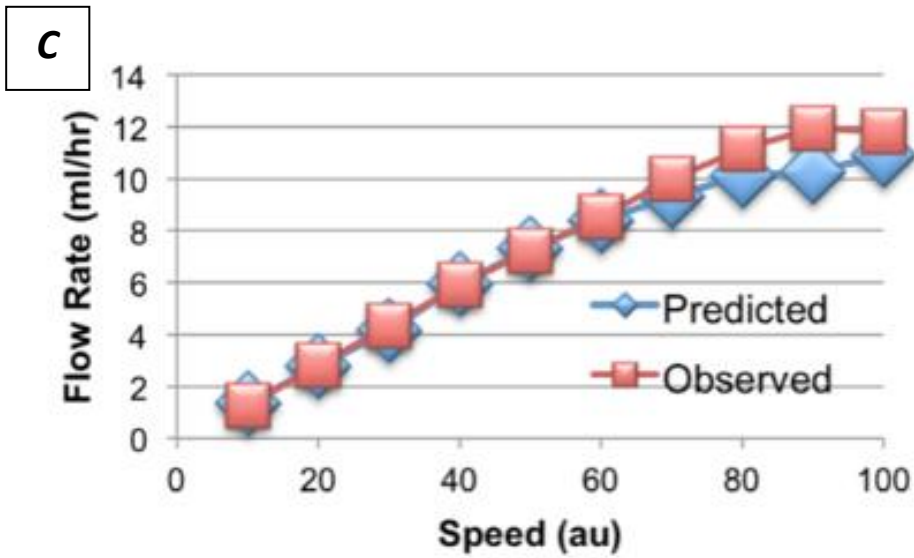
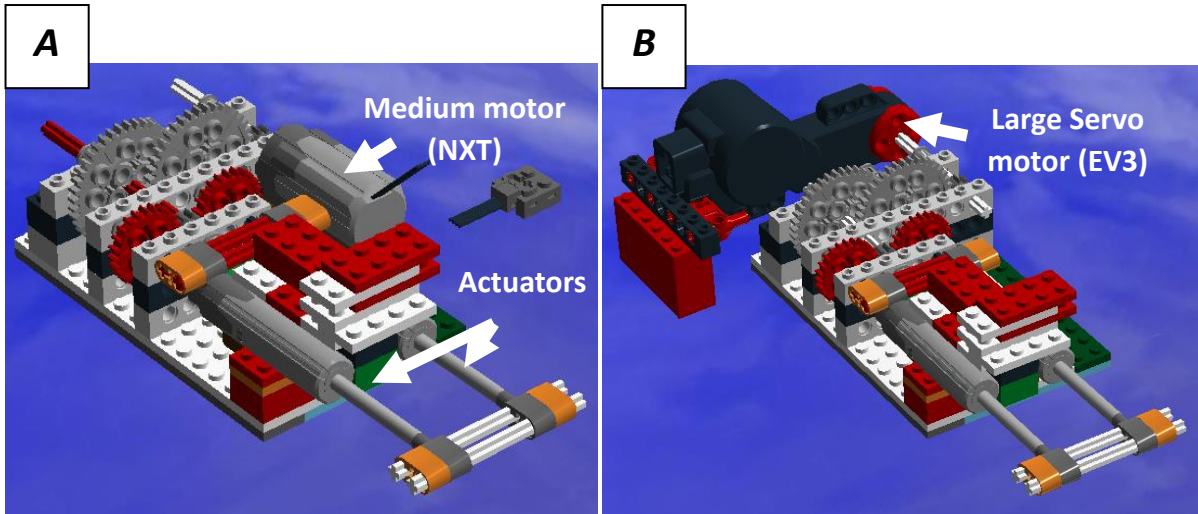


Figure 5.4 Developing strategies for multiple bio-ink bio-printing.

(A) Schematic and experimental images of a multi- setup to allow dual bio-ink printing. Two bio-inks may be sequentially delivered to the microfluidic droplet generating t-junction to print using different bio-inks. (B) Dual parallel nozzle configuration provides an alternative approach to depositing different bio-inks, either sequentially or simultaneously. (C) Establishing the relationship between large servo motor speed (au)/LEGO® gear cog configuration and fluid flow rate. (Co-produced with Danielle Jarvis).

5.4 Results

5.4.1 Combining the LEGO® stage and microfluidic droplet production to explore printability

In this chapter, the stage speed was tested and programmed to move at a rate proportional to the bio-material alginate droplet production rate in order to achieve optimal droplet printability and resolution, when generating 2D and 3D patterned bio-printed structures. This resolution, i.e., droplet packing, spacing and line continuity, is determined by the lateral movement of the stage (speed and direction), the rate of droplet production and individual droplet size and surface tension. Furthermore, sufficient levels of gelation should provide a balance between droplet structure rigidity and fluidity, allowing for tight droplet-to-droplet contact. In **Chapter 3**, different rates of droplet production and reagent concentrations were tested in pursuit of viable parameters to ensure sufficient droplet gelling. The aim in this study was to pattern droplets in a single adjoined droplet packing structure and therefore the speed of stage movement was sequentially increased, at a constant droplet flow rate, to determine its impact on the droplet line continuity, packing, spacing and droplet shape i.e., its printability. Adhesion of the alginate droplets to the glass cover slip is key to maintaining structure. Indeed, glass cover slips provide a hydrophilic base, allowing for increase alginate adhesion and oil repulsion. Initial results indicate that deposited alginate droplets adhere sufficiently to the glass to maintain the intended 4-parallel connected lines shape, irrespective of the stage speed (**Figure 5.2**). Therefore, droplet deposition on a glass cover slip provides a hydrophilic surface to which contacting droplets adhere, ensuring droplets detach from the printer nozzle and are deposited in defined locations.

5.4.1.1 *Evaluating the relationship between the lateral movement of the LEGO® 3D bio-printer stage and droplet line continuity, packing, and spacing quality*

Results indicated that droplet production frequency exceeded stage speed at speeds ≤ 2.25 mm/s, causing over-extrusion of droplets (**Figure 5.5**), which manifests as significant overlapping and clustering at lower stage speeds, distorted lines, and offset packing (significant number of droplets found outside a straight line). Additionally, the connection between the perpendicular lines is poorly defined. In contrast, at speeds ≥ 3.25 mm/s, there were observable gaps between droplets. This droplet spacing effect increases in proportion to an increase in the lateral speed of the LEGO® 3D bio-printer stage. At speeds of ≥ 4.75 mm/s lateral movement significantly exceeded droplet deposition, resulting in clear spacing between every individual droplet. Whilst patterns were not perfectly formed (evidence of breakage or discontinuity) at a stage movement of 2.75 mm/s, it produced a single line of closely packed droplets with defined connections between the parallel lines as shown by the white dashed circles (**Figure 5.5 A**). Therefore 2.5, 2.75 and 2.99 mm/s were tested. Line continuity and droplet packing was better at 2.75 and 2.99 mm/s compared to 2.5 mm/s (**Figure 5.5 B**), where droplets were more clustered and resulted in frequent discontinuous lines and offset packing. However, the perpendicular connections between parallel lines were better at 2.75 mm/s than 2.99 mm/s. Therefore 2.75 mm/s was determined to be the more desirable stage speed, producing better resolution when printing straight lines and right angles. Unfortunately, the absence of a scale bar renders it difficult to evaluate the dimensions of the printer structures. However, because all pictures were taken from the exact same distance, all structures demonstrate close resemblance to each other in terms of dimensions. This shows a promising level of consistency in preserving printed dimensions despite increasing stage speeds.

Differences in colours of bio-printed constructs and droplets are observed. Indeed, whilst some droplets seem more translucent, others exhibit the presence of white dense colouring. This may indicate heterogeneous droplet gelling as a result of heterogeneous Ca^{2+} partitioning in individual droplets and constructs. This was similarly observed through

microscopic imaging in **Chapter 3**, revealing the presence of black dense spots of CaCO_3 undissolved particles.

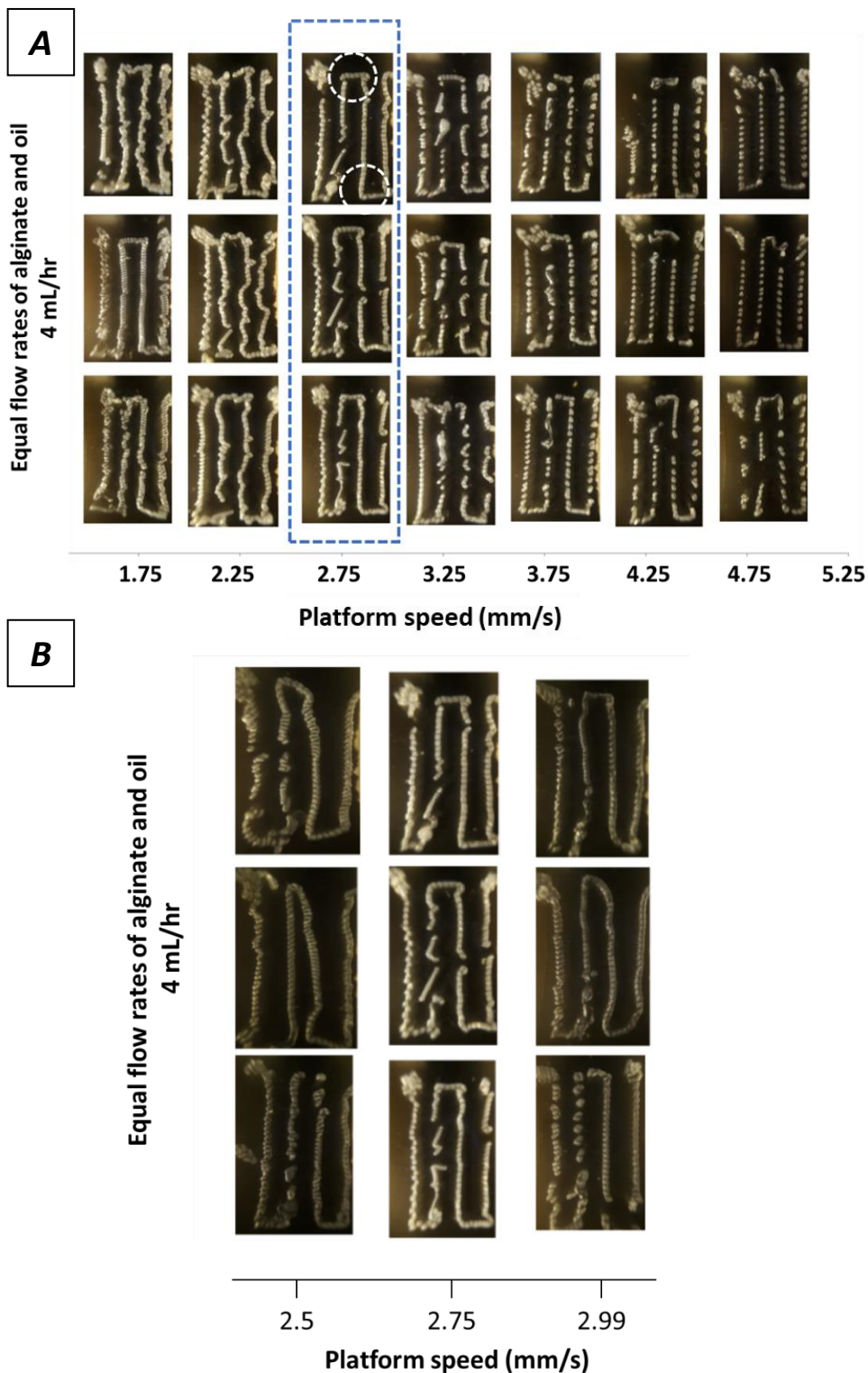


Figure 5.5 Testing the printability at a constant bio-material flow rate of 4 mL/hr when altering the speed of the lateral movements of the LEGO® stage (mm/s).

(A) A region of adequate printability was identified at a stage speed of 2.75 mm/s by assessing the overall quality of the bio-print. The white dashed circles highlight the right-angle section of the bio-print ($n=3$). (B) Intermittent speeds around 2.75 mm/s were tested. (Produced by Katherine Sloan).

5.4.1.2 *Evaluating the relationship between the lateral movement of the LEGO® 3D bio-printer stage and printed droplet shapes*

Magnification of the printed parallel lines in **Figure 5.5** illustrates how stage speed can also impact on the shape of deposited droplets (**Figure 5.6**). Four categories of shapes were observed. At a low stage speed (1.75 mm/s) resulted in a mix of round, angular and elongated shapes whereas stage speeds from 2 -3.25 mm/s generated rounded square shapes. As speeds increased, droplets became more elongated and stretched. At the optimal speed of 2.75 mm/s, droplets were rounded square shaped. Droplet shapes were also characterised at different flow rates and stage speeds resulting in a wider range of shape categories (**Appendix A-10**). For example, at constant mineral oil flow rate of 10 mL/hr and alginate flow rates of 2 or 4 mL/hr, the produced droplets were predominantly round, at stage movements speeds of 1 to 4 mm/s. In another example, droplets were packed in teardrop shapes at stage speeds of 2.5, 3, and 3.5 mm/s when mineral oil and alginate flow rates were both at 10 mL/hr. Droplets showed different levels of distortion when tightly packed, ultimately affecting the overall patterning of bio-printed structures. From this point, all other 2D and 3D bio-prints were carried out using the combination of optimised parameters from **Chapters 3 and 4**: (1) equal bio-ink flow rates of 4 mL/hr resulting in droplet production frequency of ~3.4 droplets per second, (2) an exit nozzle length of 9 cm resulting in droplet transit time of 19.9 seconds, (3) 75 mM CaCO₃, 2% alginate, and 0.5% acetic acid reagent concentrations, (3) stage speed of 2.75 mm/s, and (4) nozzle set to 0.80 mm from the printing surface (droplet width).

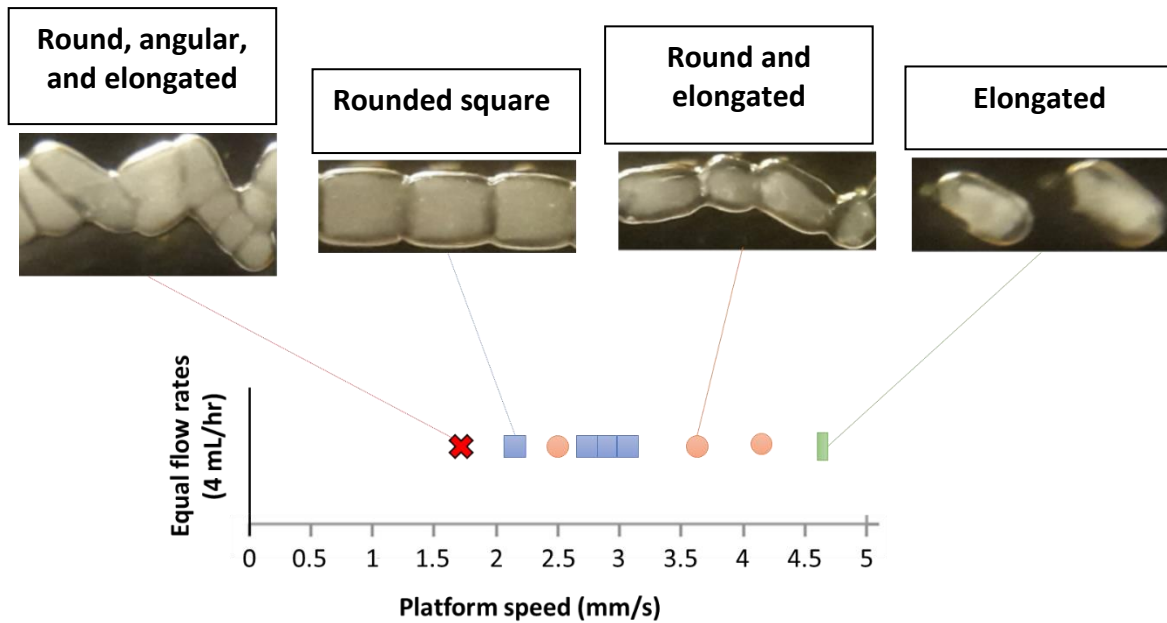


Figure 5.6 Effect of the stage speeds on printed droplet shapes extruded at equal flow rates of 4 mL/hr.

Four categories of shapes were observed at different stage speeds. (Co-produced with Katherine Sloan).

5.4.2 Programming and evaluating different 2D and 3D print patterns and shapes using the LEGO® custom-built 3D bio-printer

The ability to synchronise the LEGO® stage movements with the droplet frequency of the microfluidics allowed to generate printable lines and right angles at sub-mm resolutions. However, more complex 2D and 3D structures are critical to mimicking the complex architecture and function of living tissues (Xia et al. 2018; Alcinesio et al. 2020). Thus, the layer-by-layer deposition of closely packed malleable alginate droplets into larger structures is vital for producing relevant engineered tissues. The LEGO® custom-built 3D bio-printer should, therefore, provide a variety of custom-spatial movements in the x, y, and z planes, enabling the deposition of droplets in custom-defined arrangements.

As mentioned previously, the EV3 brick provides a main menu screen with several options which the user can chose from (**Figure 5.7**). A library of 2D and 3D movements were programmed and uploaded into the brick, providing a variety of shape choices that can be

● CHAPTER 5 ●

used (Figure 5.7). All the shapes were programmed to move in the x/y plane at the optimal speed of 2.75 mm/s and z-axis increments of 0.80 mm by default when bio-printing 3D shapes, unless specified otherwise by the user.



Figure 5.7 Main menu interface of the LEGO® x/y/z stage as shown on the EV3 programmable brick.

The main menu consists of four different options, including “Lattices”, “Parameters”, “Basic Prints”, “Outline”, and “Concentric shapes” (represented as a concentric squared shape in the middle). Selecting one of the options opens up a new menu with more selectable choices of 2D and 3D patterned movements.

5.4.2.1 *Programming and evaluating 2D print patterns using the LEGO® 3D bio-printer*

Amongst the earliest programmes uploaded into the 3D bio-printer brick was “Basic Prints”, which was intended for droplet printability development. Featured options include simple prints consisting of minimal stage movements, 3D layering and customisable options. They include straight line movements in the x and y planes, a right angle, 4 parallel lines, which was previously used to develop droplet printability (**Sections 5.3.2 & 5.4.1**), and a two layered square lattice at a fixed size. The “Basic Prints” programme is represented in **Figure 5.8** with the available options and a screenshot of what can be found in the menu (**Figure 5.8**). Furthermore, the 4 parallel lines is demonstrated schematically and 3D bio-printed (**Figure 5.8 B**)

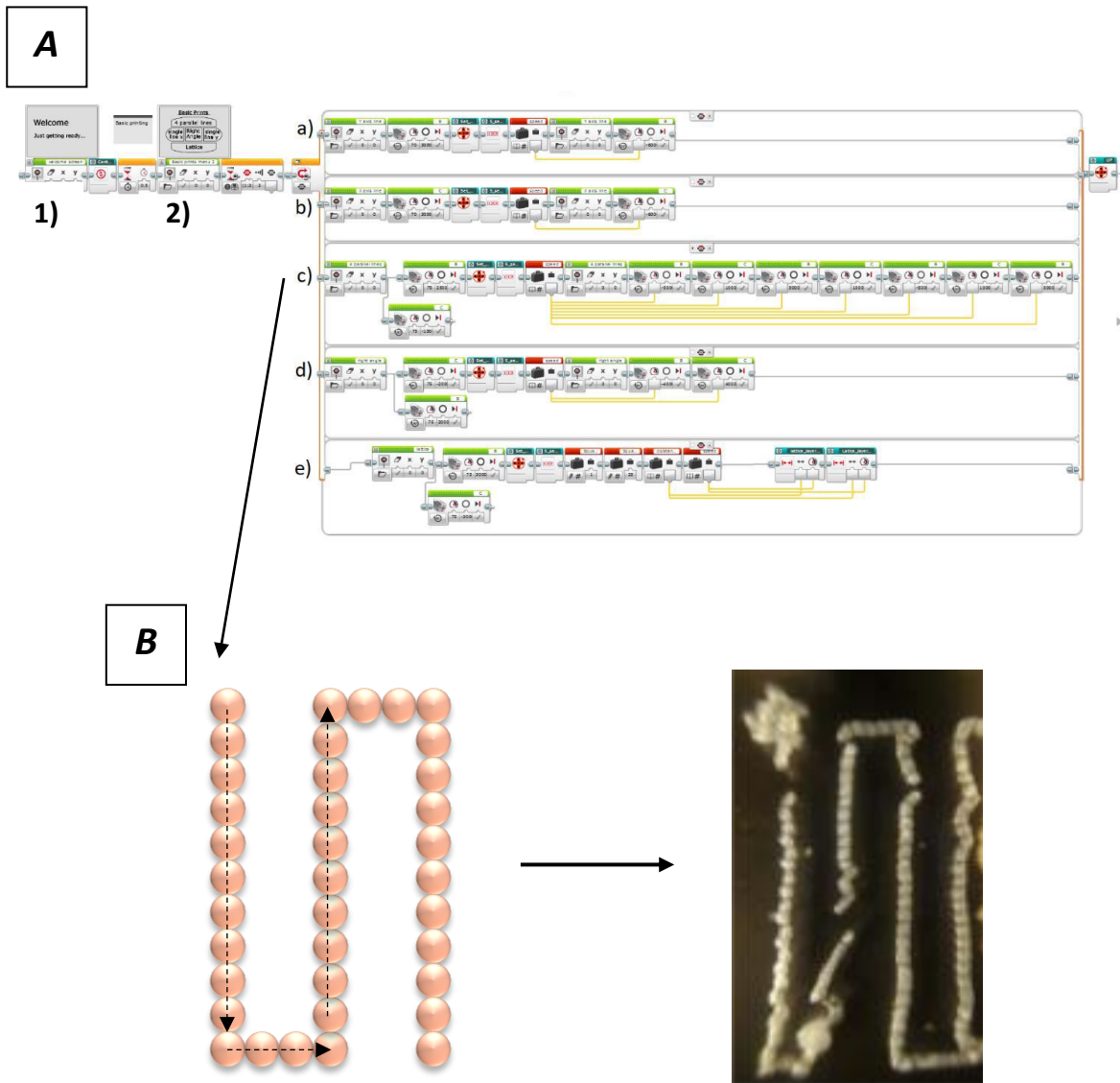


Figure 5.8 Programming sequence of the “Basic Prints”, available shapes, and a 4 parallel lines bio-print.

(A) (1) The “Programme_Run” programme, and (2) the “Basic Prints” menu with available options. The “Basic Prints” enables the 3D bio-printer to produce: (a) single straight line in the x and (b) y plane, (c) 4 parallel lines connected by right angles, (d) a right angle connecting two straight lines from the x and y planes, and (e) a two layered square lattice with a fixed size. (B) A schematic and 3D bio-print of 4 parallel lines indicating the movement direction of the stage enabling the deposition of droplets in a custom-defined space. (Produced by Cameron Pool and Katherine Sloan).

5.4.2.2 *Programming and evaluating 3D print patterns using the LEGO® 3D bio-printer*

3D structures are generated through sequential layering deposition of 2D patterned droplet arrangements. Following the deposition of a layer, the nozzle is automatically programmed to rise by 0.80 mm increments (droplet width) to ensure tight droplet-droplet packing in the z-plane and prevent disruption of previously laid layers. Lattice structures are produced by sequential interlaced parallel lines (**Figure 5.9**). Lateral stage movements in the x plane were defined to move the size of a droplet width between each bio-printed line, allowing for close packing of parallel lines. 3D structures can be built by layering several sequential 2D droplet arrangements, with sufficiently gelled droplets and solid foundations. The user can choose the “Lattice” option from the main menu, which provides several printable lattice shapes, including, a square lattice, triangle lattice, or a square pyramid lattice. Moreover, produced lattices can be custom-defined in size and height prior to initiating the bio-print. The size is defined as the length of shapes, i.e., distance moved by the stage, and the height defined as number of layers required, i.e., number of times the nozzle will escalate after depositing one full layer. A two-layered squared lattice with a length size of 25 mm was printed to demonstrate the 3D bio-printer printability (**Figure 5.9**). The resulting bio-print clearly shows how droplets were deposited in an interlaced pattern configuration. The intended dimension of 25 mm length is achieved with reasonable resolution. Whilst the left and right printed lines of the first layer were relatively straight, the top and bottom lines revealed some distortion that can be associated to a dragging effect of the nozzle, low droplet adhesion, or/and the pattern used to generate a square (interlaced parallel lines). At first glance, the first layer showed printing inconsistencies, gaps, and breaks. However, some of these gaps started to close upon deposition of the second layer of droplets, generating a more complete structure. Overall, a reasonable-resolution patterning of tightly packed droplets in a single line produced a defined squared lattice of approximately 25 mm length.

Two types of square pyramid lattice structures were also implemented and can be found in the “Lattice” menu, under the titles “Pyramid Lattice 1” and “Pyramid Lattice 2”. Pyramid lattice 1 is produced by creating incrementally smaller squared lattices for every two

● CHAPTER 5 ●

lattices created, as shown in **Figure 5.10**. Once two layers are deposited, the nozzle moves closer to the centre of the stage by 2 mm, thus reducing the square size, and the stage commences the movement for a smaller sized squared lattice. This specific printed pattern outcome is defined within the software as a “loop”, as described in **Figure 5.11**, and this allows repeated stage and nozzle movements once a specific task has been fulfilled. The red palettes or maths blocks present within the software loop, allow input of numerical variables and equations that determine the pyramid size, stage speed and distance movements, and calculate motor movements inwards (towards the centre) between each two layers. Despite the user’s ability to define the number of layers, the loop automatically ceases any movements when the nozzle arrives at the centre, ending the print. Images of the printed pyramid, taken from different angles, are shown in **Figure 5.10**. and demonstrate a multi-layered pyramid structure with four sloping slides. Pyramid lattice 2 differs in the number of base squared lattices produced before decreasing the lattice size for the following layer. Pyramid lattice 2 produces only one squared lattice whereas pyramid lattice 1 produces two.

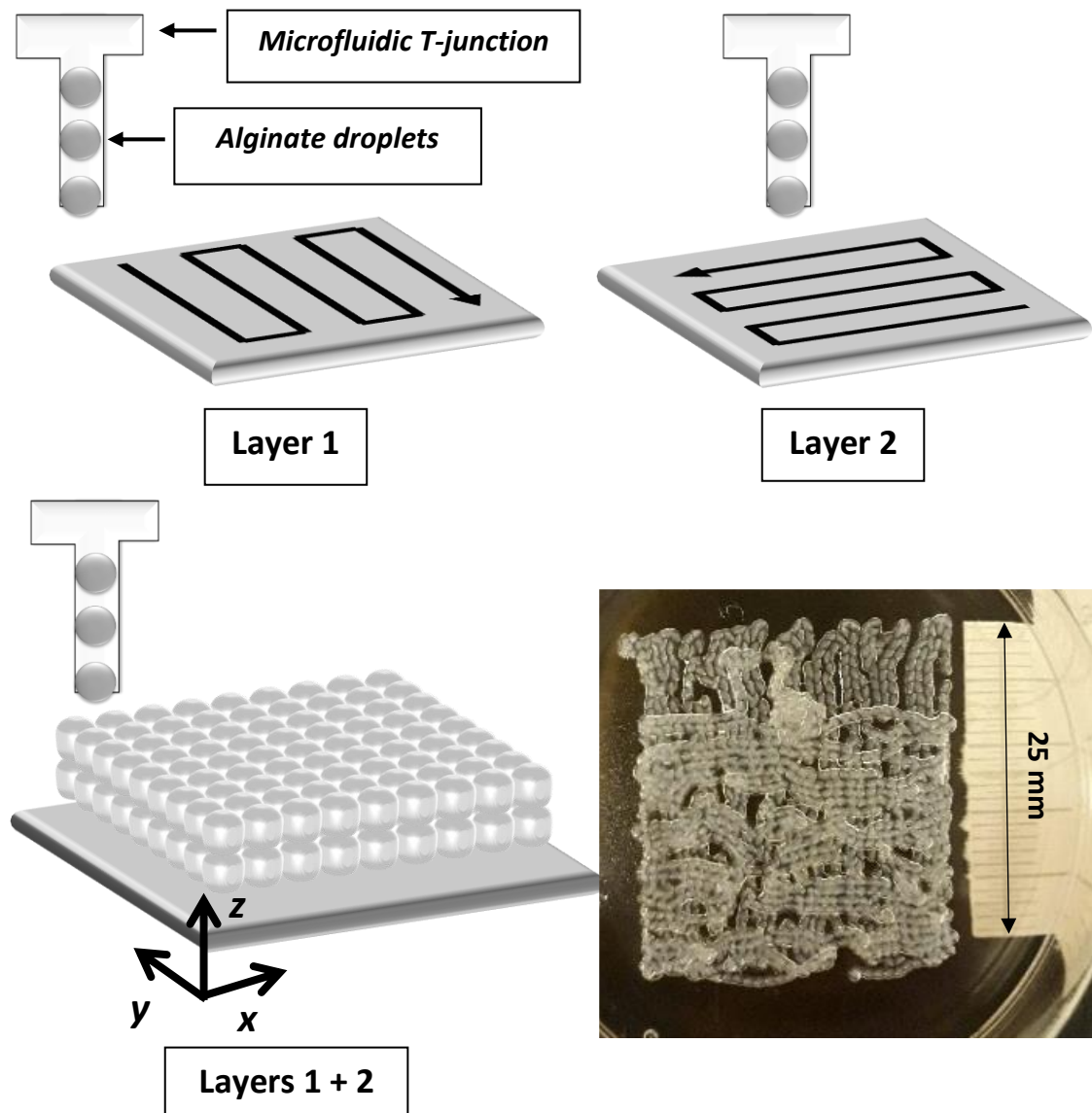


Figure 5.9 Schematics of the two-layered square lattice printing process and the resulting print. A 25 mm two-layered square lattice can be printed using the custom-built LEGO® 3D bio-printer. This is achieved by selecting the “Lattice” option in the printer’s main menu. Square lattice structures, like others, can be user-defined in terms of diameter and number of layers. (Co-produced with Cameron Pool).

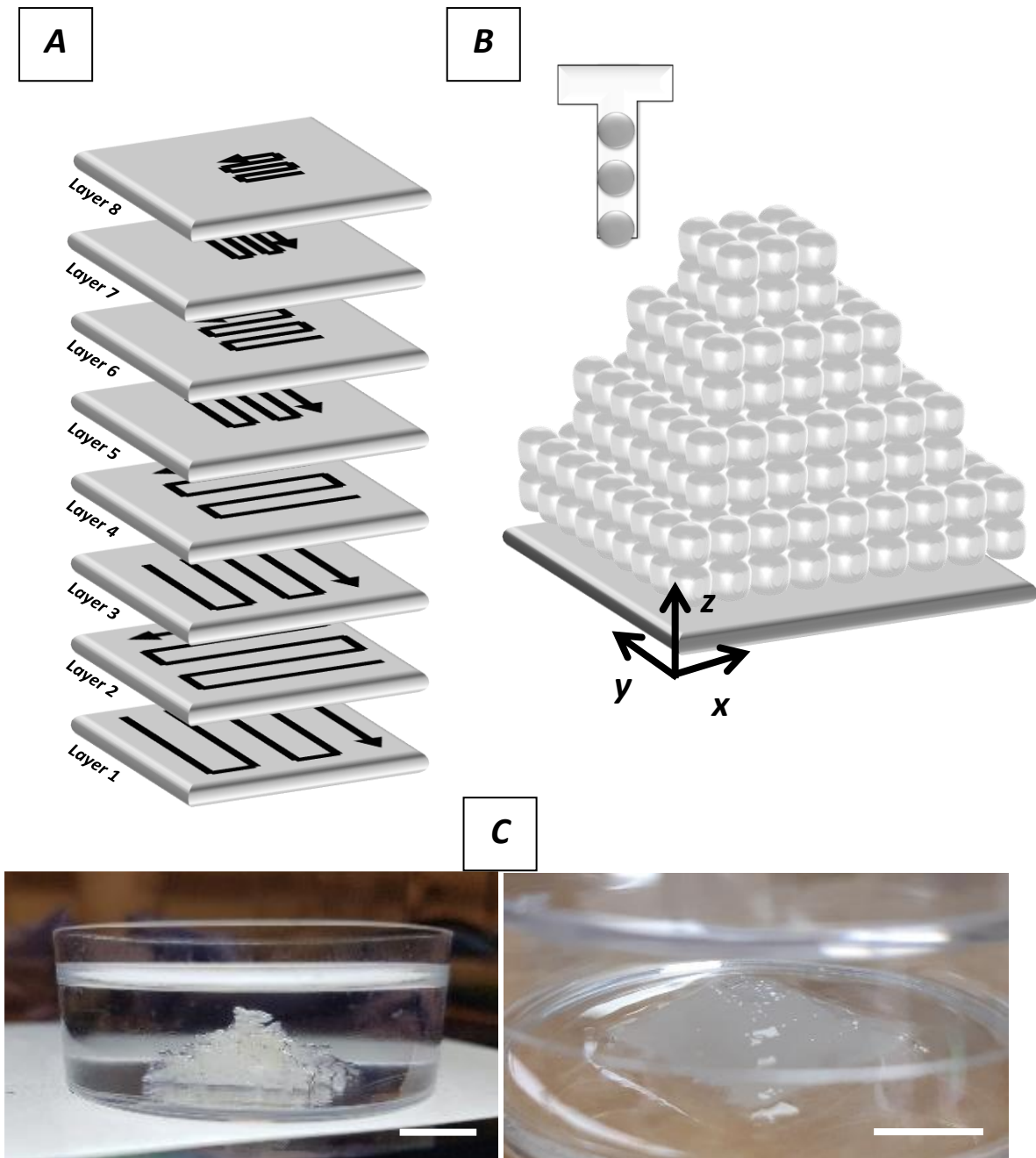


Figure 5.10 The printing process of an 8-layered “Pyramid Lattice 1”.

(A) Defined movements of the custom-built 3D bio-printer allow production of incrementally smaller squared lattices, resulting in a multi-layered pyramid. (B) A schematic representation of a pyramid lattice produced through deposition of spatially organised alginate droplets. (C) A 3D bio-printed pyramid lattice comprised of alginate droplets. Scale bar = 10 mm

● CHAPTER 5 ●

structure showed a stable and defined cylindrical structure, resulting from the sequential layering of 15 2D concentric circles (**Figure 5.12 C**). Custom-shape outline allows the user to select a desired number of sides to produce different shapes. When selected, a display function will generate a drawing of that shape on the EV3 brick screen.

Taken together, the versatility of the LEGO® custom-built 3D bio-printer is exemplified through the synchronisation of gelled alginate droplet production with shape-defined stage movements, resulting in the production various 3D patterned shapes at a mm scale. Furthermore, different strategies are programmed to generate similar shapes, emphasising the printer's flexibility in defining spatial organisation.

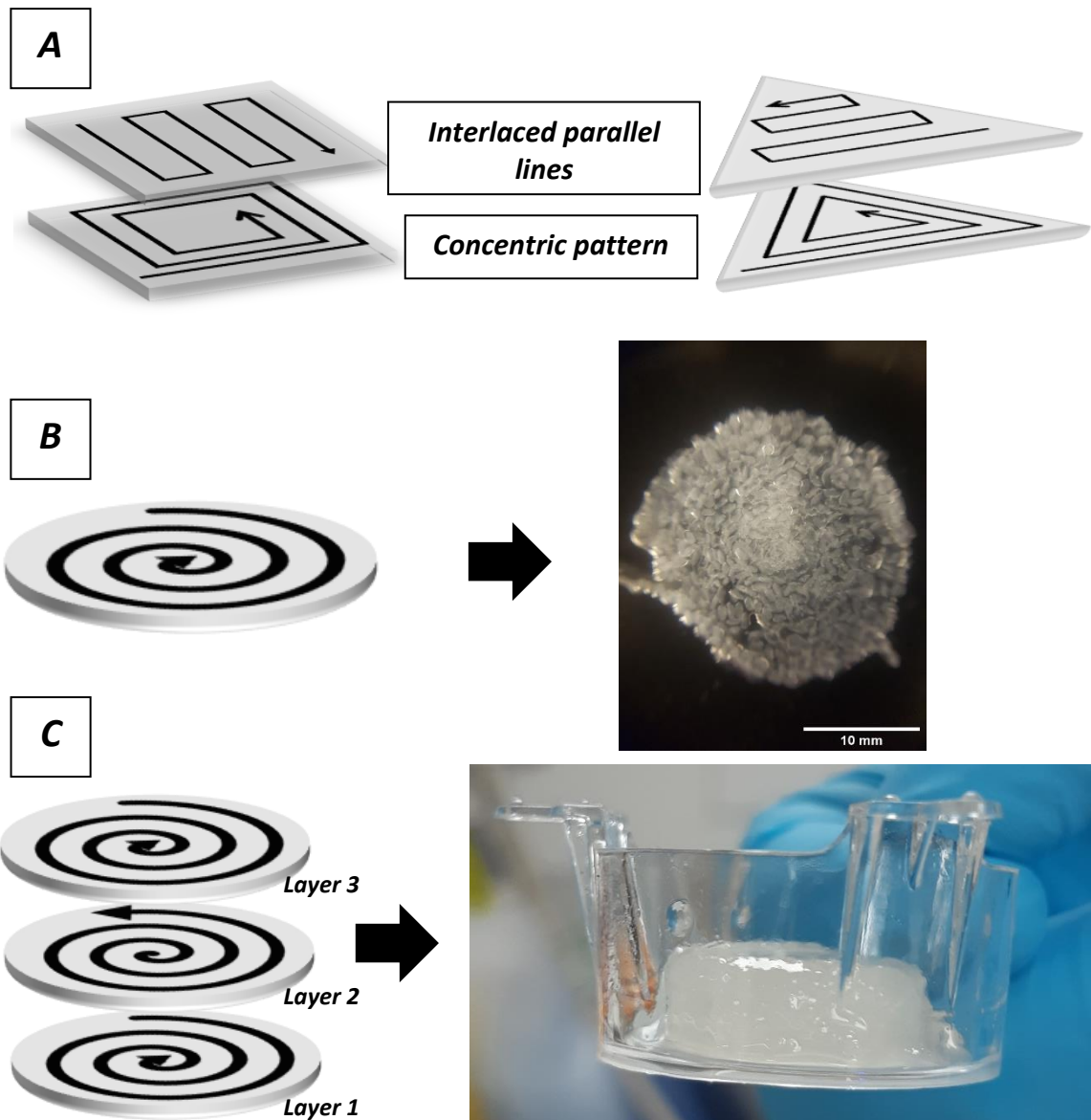


Figure 5.12 Generating 3D lattices of different shapes using the concentric function.

(A) Squared and triangle lattices can be produced via two stage movement strategies: interlaced parallel lines or concentric movements. (B) A 2D concentric circle was produced when gelled alginate droplet production was synchronised with the stage movements in a circular manner. (C) The layer-by-layer deposition of droplets in sequential 2D layers resulted in a 15 layered 3D cylindrical solid fill.

5.4.3 Investigating the sequential print of multiple bio-inks using the LEGO® 3D bio-printer

The ability to control spatial deposition of gelled alginate droplets has been previously demonstrated by bio-printing 2D and 3D patterned structures. This was achieved through the synchronisation of blank alginate droplet extrusion with the 3D bio-printer stage movements. Increasing the potential relevance of a 3D tissue model will require the integration of different cell types and biomaterials in one structure. Multi-bio-ink bio-printing was tested by printing three different bio-inks within a single 3D structure, thus demonstrating the ability to synchronise stage-movement and syringe pump control. Furthermore, different stage-movement patterns were used to produce a multi-material 3D lattice, emphasising the 3D bio-printer's adaptability. The first example of multi-material bio-printing was achieved by bio-printing an 18 layered cube through the deposition of 18 2D squared lattices of 16 mm length, as illustrated in **Figure 5.13 A & B**. The multi-material cube is comprised of 3 main sections: (1) 8 bottom layers of droplets containing green FluoSpheres®, (2) 4 layers of blank droplets, and (3) 6 layers of droplets containing carmine FluoSpheres® (**Figure 5.13**). To achieve this, each bio-ink was prepared in advance, loaded in a syringe, and loaded onto the syringe driver once an instructed section was complete. Incorporated FluoSpheres® used in this experiment served as cell-sized models (15 µm) to enable visualisation but mimic the potential to incorporate different cell types in the future. A longitudinal section of the 3D bio-printed structure demonstrates efficient retention of the patterned sections and FluoSpheres® within droplets (**Figure 5.13 D & E**). Furthermore, the dimensions of the 3D structure showed high precision of droplet deposition, demonstrating a width that approximates 14 mm, whereas the intended diameter of each layer was set at 16 mm. However, this depends on the measured area, and may differ due to a lack of structural uniformity between layers and sections. The length of the structure measured approximately 9.5 mm. Theoretically, with an average droplet width of 0.8 mm, printing an 18 layered structure should result with a 14.4 mm length. However, a flattening of the structure is observed at the bottom layer. Furthermore, the inconsistencies and gaps observed in the previous result (**Figure 5.9**) can lead to droplet sinking between different layers, contributing to a smaller experimental length. Indeed, this is also observed in the upper layer, showing a

● CHAPTER 5 ●

sinking-like structure as compared to the outer rims of the construct. Macroscopic fluorescent imaging of the longitudinal section demonstrated successful retention of each layer of bio-ink in its respective section and FluoSphere® encapsulation (**Figure 5.13 E**). Furthermore, the intended number of each layer is reflected accurately in the layer thicknesses observed in the bio-printed structure. For example, the blank droplet layer exhibited a smaller thickness in contrast to the upper and lower sections, as intended. Overall, the structure showed good fidelity to the designed model in terms of layering and dimensionality. This was repeated three times by using different coloured FluoSpheres® (**Appendix A-11**).

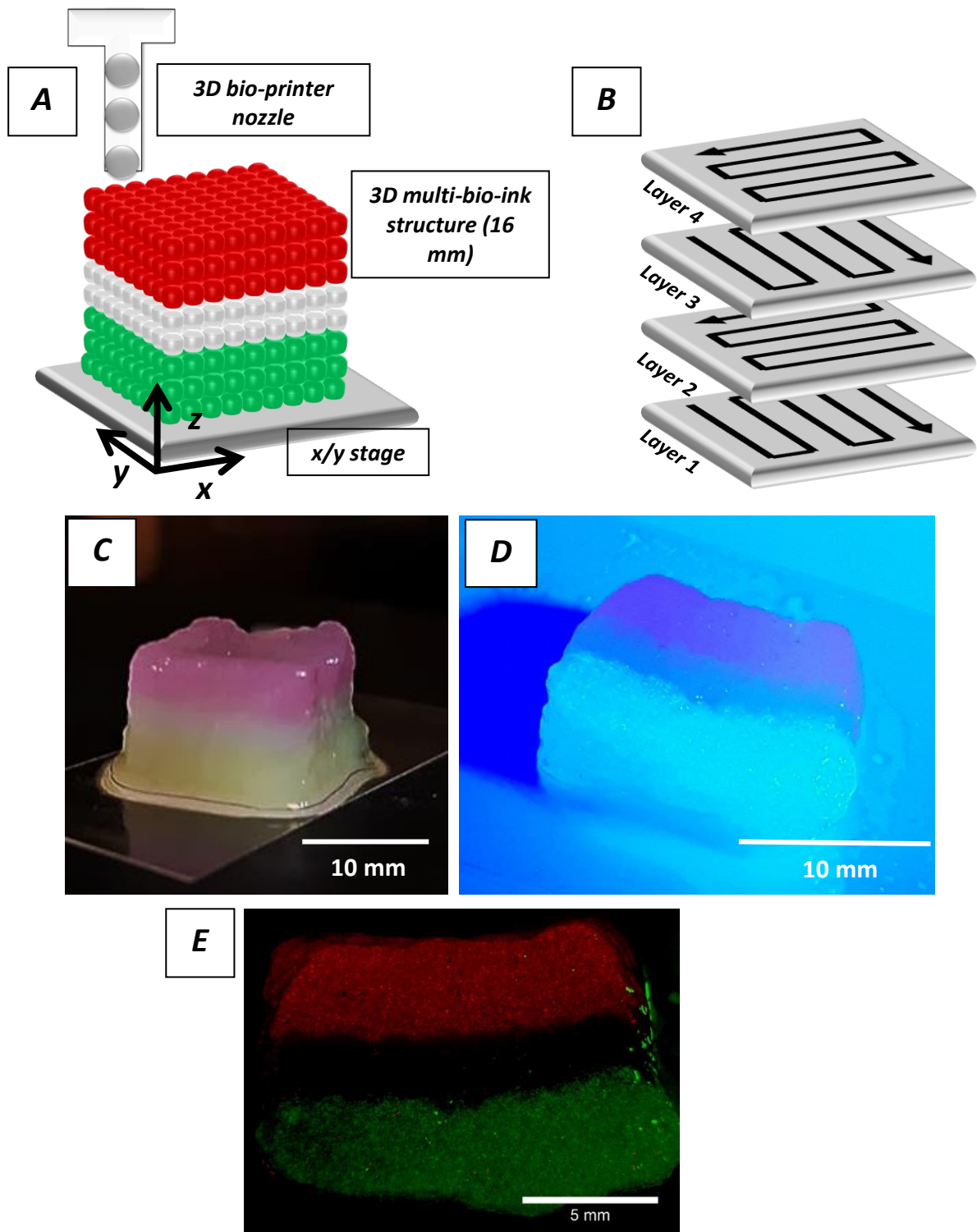


Figure 5.13 Multi-bio-ink bio-printing: Example of a three-bio-ink multi-layered cube lattice. (A) Schematic representation of a 16 mm three-bio-ink multi-layer cube lattice print, consisting of 8 bottom layers of encapsulated green cell-sized FluoSpheres®, 4 layer of blank droplets, and 6 layers of carmine FluoSpheres®. (B) Representation of stage and print nozzle movements resulting in a multi-layered lattice through the interlaced parallel-line patterning strategy. (C) Macroscopic image of a completed three-bio-ink multi-layered cube lattice print. (D) A longitudinal section of the cube print showing the inner patterning and successful retention of the three-bio-ink sections. (E) Macroscopic fluorescent imaging of the longitudinal section showing FluoSpheres®-encapsulation within each section.

● CHAPTER 5 ●

To further demonstrate the 3D bio-printer's flexibility, a more complex structure was generated, in which more than one patterned stage movement was used. An inner cube containing encapsulated carmine FluoSpheres® was deposited within an outer structure of blank droplets (**Figure 5.14 A**). This structure was produced by printing 4 sections: (1) 8 layers of blank droplets with a 20 mm diameter in an interlaced parallel pattern, (2) 8 layers of carmine FluoSphere® encapsulated droplets in the middle of the previous layer, at a size of 8 mm diameter, (3) 10 layers of blank droplets in a concentric square revolving around the smaller carmine coloured section measuring 20 mm in diameter, and finally (4) 5 layers of blank droplets deposited in an interlaced parallel pattern to cover the carmine structure (**Figure 5.14 A, B & C**). A longitudinal section of the print demonstrated the retention of the smaller carmine coloured structure within a larger outer structure (**Figure 5.14 D**). This structure illustrates the LEGO® custom-built 3D bio-printer's ability to produce 3D patterned structures from multiple 2D deposited layers. Furthermore, it emphasises the ability of the 3D bio-printer to use various printing patterns and strategies to construct complex 3D shapes. The ability to overlayer different bio-inks or strategically enclose distinct bio-inks into larger ones also provides promise for mimicking the 3D tissue microarchitecture.

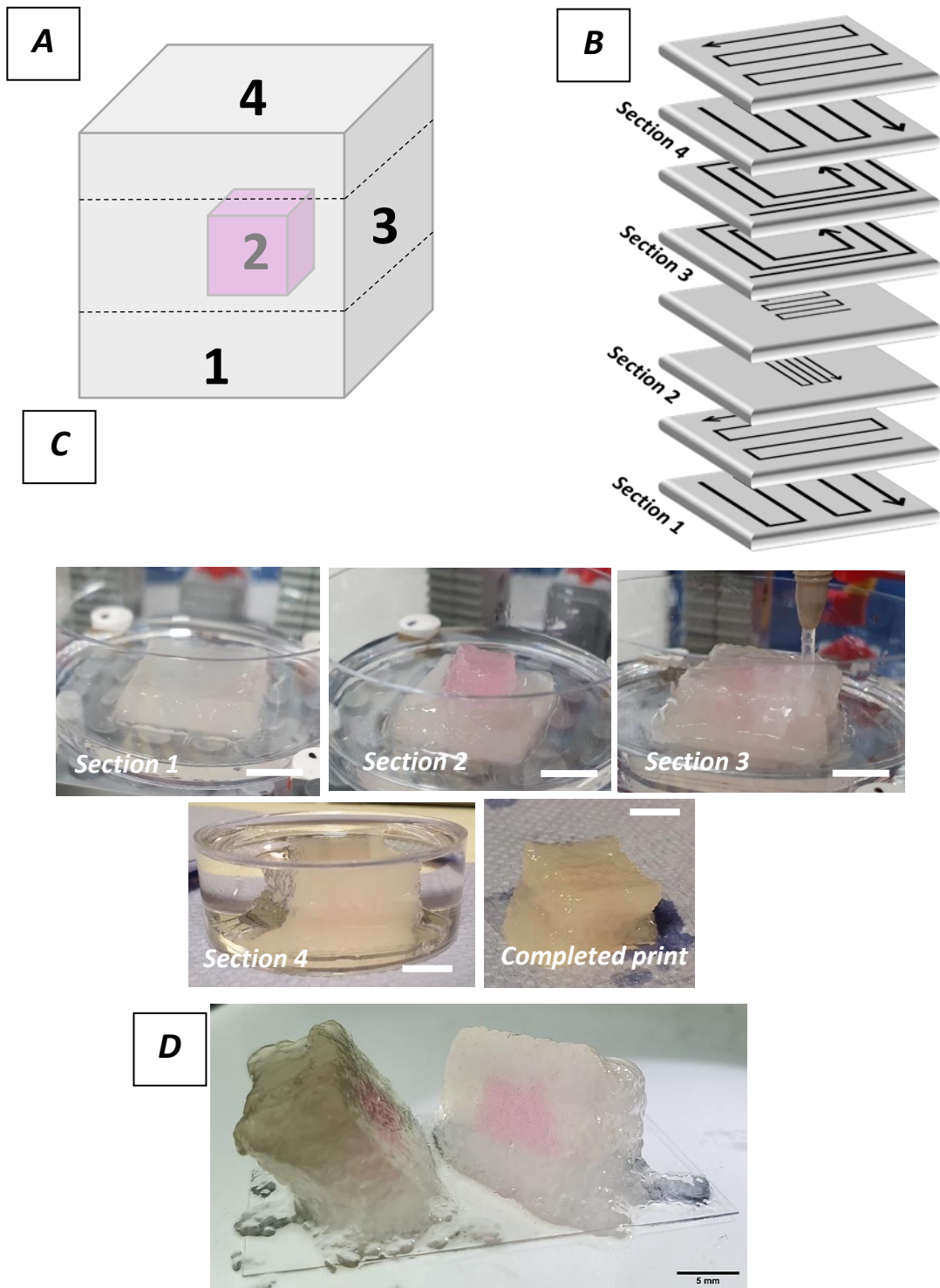


Figure 5.14 Multi-bio-ink bio-printing: Example of a dual bio-ink cube encased within a larger cube. (A) Schematic representation of a two-bio-ink design of a smaller cube encased within a larger cube, made up for 4 different sections. The smaller cube consists of carmine FluoSphere® encapsulated cell-sized beads whereas the outer structure is composed of blank alginate droplets. (B) Layer-by-layer stage movement instructions, utilising different patterned movement strategies, to generate the two-bio-ink design. A total of 23 layers with 4 distinct layering sections. (C) Resulting prints from the 4 sections and a completed print of the whole structure. Scale bar = 10 mm. (D) Longitudinal section of the structure showing the encased cube within the larger one. Scale bar = 5 mm.

5.4.4 Developing multiple nozzles for extrusion and a LEGO® syringe driver for future iterations of the LEGO® 3D bio-printer prototype

5.4.4.1 Developing multiple nozzle prototypes for multiple bio-ink printing using the LEGO® 3D bio-printer

To facilitate multi-bio-ink bio-printing in the future, two setups using different extrusion strategies were proposed: (1) a single nozzle/dual microfluidic t-junction system and (2) a dual parallel nozzle/dual microfluidic t-junction system. Both setups are capable of dual bio-ink bio-printing and can be easily accommodated within the LEGO® 3D bio-printer (**Figure 5.3**). The single nozzle system is limited to sequential extrusion with two bio-inks and microfluidic t-junction, whilst the dual parallel nozzle system allows delivery of two different bio-inks simultaneously or sequentially. The dual parallel nozzle system was tested by bio-printing a multi-layered square lattice consisting of three bio-inks. The multi-bio-ink structure was achieved by bio-printing a few layers of blue-coloured alginate, followed by several layers of blank alginate, and finally a few layers of a red-coloured bio-ink (**Figure 5.15**). The bio-printed structure exemplified successful layering of multiple bio-inks using the dual parallel nozzle system. Initial offset positioning of the dual nozzles was determined through the programming software to ensure identical spatial alignment when commencing bio-printing. This data is in the early stages of development and requires further studies for optimisation. The development of multiple bio-ink dispensing in a layer-by-layer configuration can aid in generating anatomically relevant tissues which have a highly compartmentalized zonal microarchitecture, such as the osteochondral tissue (Idaszek et al. 2019). Applying this concept to the fabrication of a skin model can potentially generate relevant microarchitectures *in vitro*.

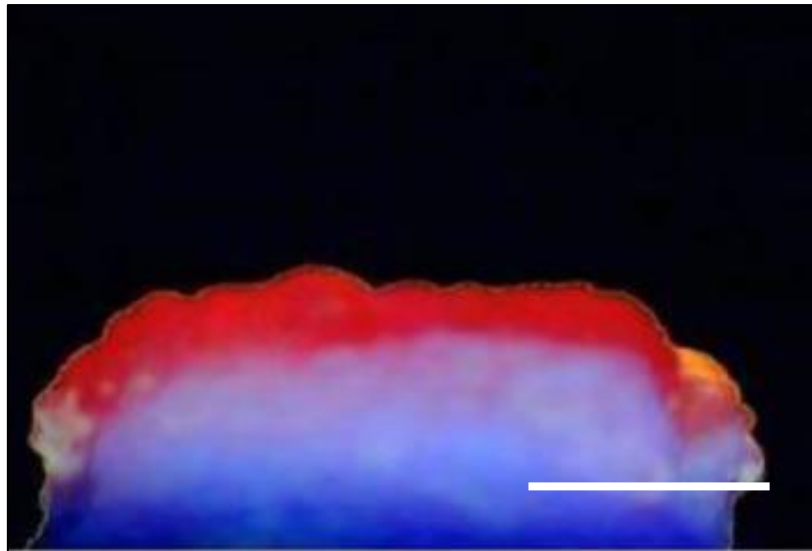


Figure 5.15 Preliminary data showing a multi-bio-ink construct bio-printed using the dual parallel nozzle device.

The construct consists of a few bottom layers of blue coloured alginate droplets, followed by a larger layer with blank droplets, and finally a few layers of red coloured alginate droplets. A macroscopic side view image was taken to show the different coloured layers. (Produced by Phoebe Reese). Scale bar = 5 mm.

5.4.4.2 Developing a LEGO® syringe driver prototype to create a fully integrated LEGO® 3D bio-printer

The syringe pump has been slightly modified from the original setup to allow the incorporation of a large Servo motor and the EV3 brick instead of a medium motor and NXT brick (Almada et al. 2019) (**Figure 5.4**). The main setup consists of a dual LEGO® syringe pump, with t-junction microfluidics, that is connected to an EV3 programmable brick (**Figure 5.16 A**). Blue-coloured alginate droplets were successfully produced using the LEGO®-built syringe driver as demonstrated by macroscopic images and the presence of peaks representing an increase in pixel intensity or a passing droplet through the region of interest (ROI) (**Figure 5.16 B**). Furthermore, a similar droplet frequency signature trace is observed when comparing the commercial syringe driver (KD scientific) and the LEGO®-built syringe driver, suggesting high droplet generation reproducibility in the low-cost LEGO® syringe driver (**Figure 5.16 C**). A fully integrated LEGO®-built 3D bio-printer using LEGO® syringe drivers and a LEGO® programmable robotic 3D stage is shown in **Figure 5.17**.

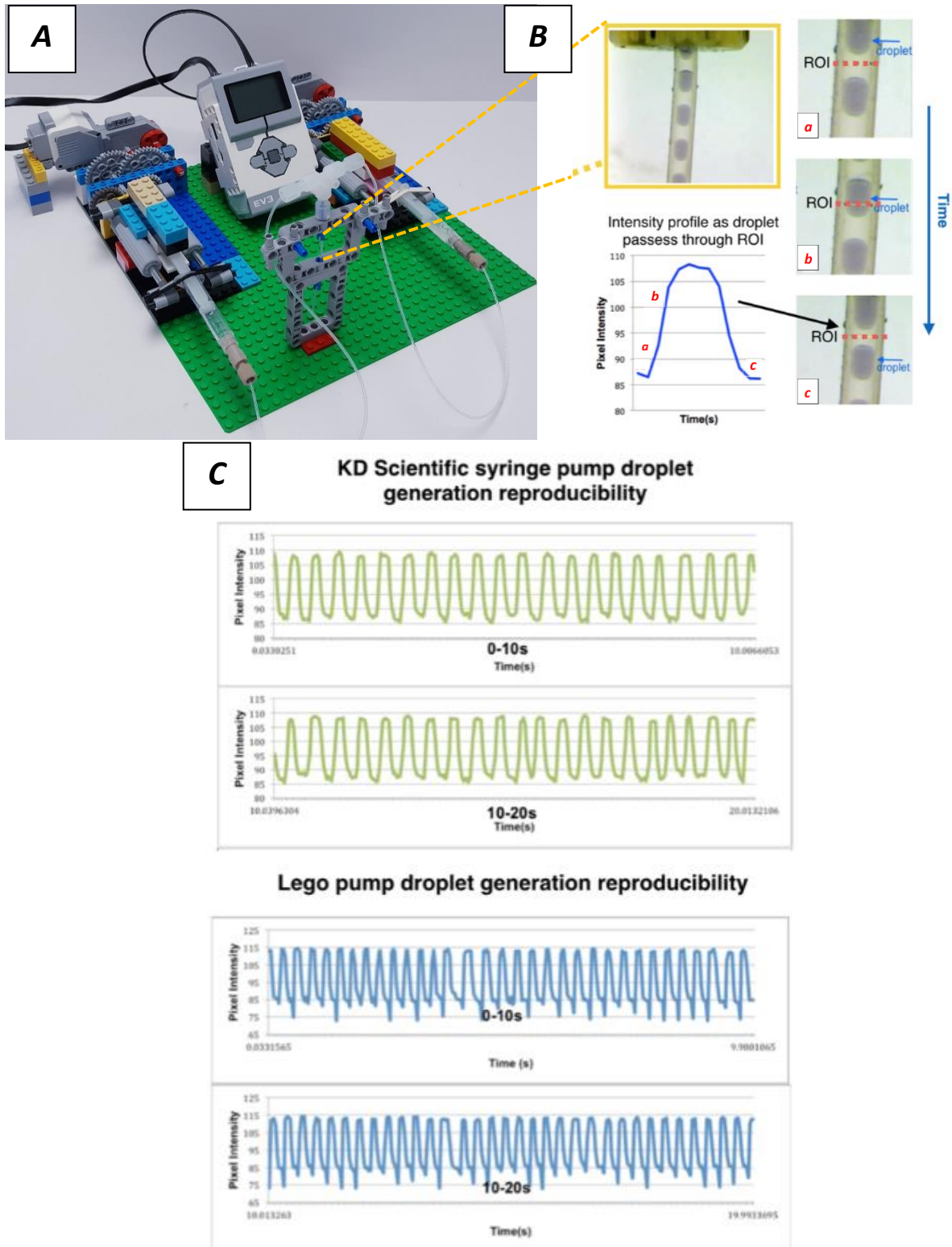


Figure 5.16 Developing LEGO® syringe drivers for alginate droplet production.

(A) Setup of a dual LEGO® syringe driver with a microfluidic t-junction sitting in a LEGO® stand. (B) Image capture of blue-colored alginate droplet production (yellow box) using the LEGO® built syringe drivers. A region of interest (ROI) line crossing the imaged tubing was set using ImageJ (Fiji). The pixel intensity at the ROI, represented as a peak, is seen to change as droplets flow and pass the set line (a-c) (Produced by Danielle Jarvis). (C) Droplet reproducibility was compared between a commercial KD Scientific syringe driver and the LEGO® syringe driver, by characterizing the droplet frequency over a period of time. Each peak represents a droplet passing through the ROI (Produced by Danielle Jarvis).

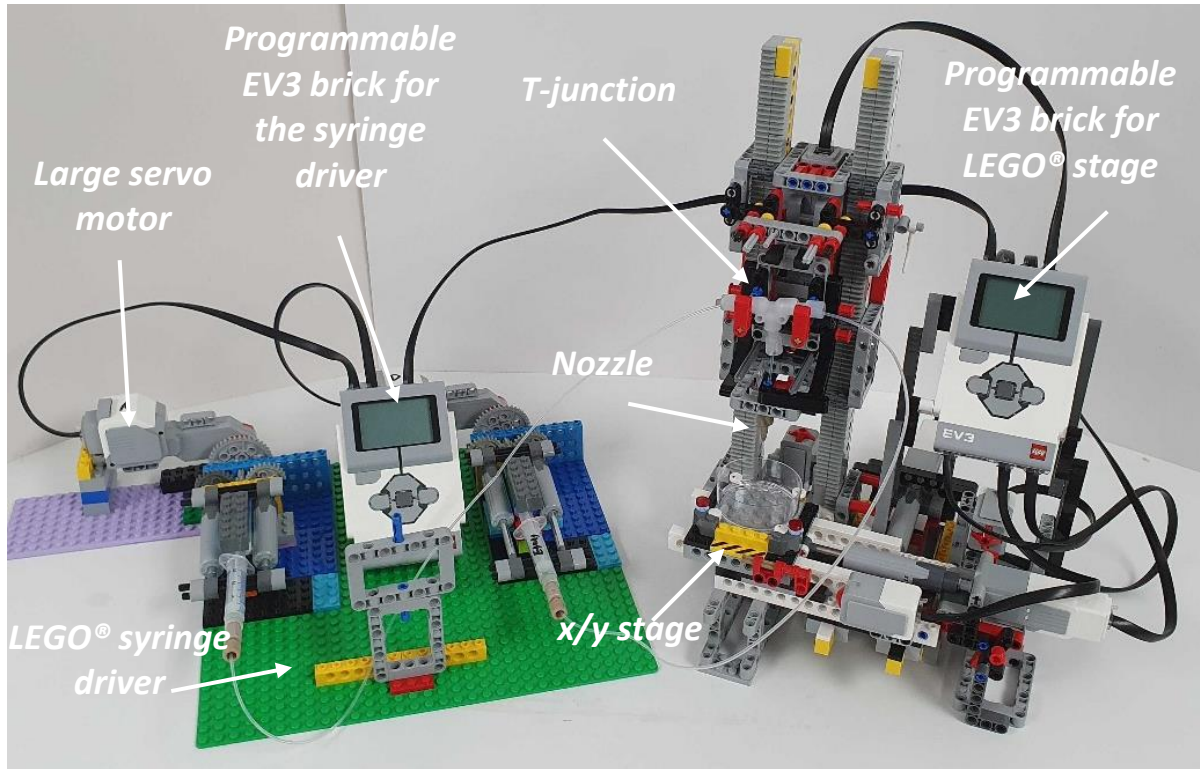


Figure 5.17 Fully integrated setup of a LEGO® 3D bio-printer connected to a dual LEGO® syringe driver.

5.5 Discussion

3D structures were generated through the layer-by-layer deposition of sequential pre-defined 2D shapes using the custom-built LEGO® 3D bio-printer. This was achieved through “loops” or repeated coding sequences using VPL programming to generate repeated 2D patterned x/y/z locations, with an increase in nozzle height after the deposition of each layer. Bio-printing of multi-bio-ink/multi-layered structure with high resolution at the macroscale was achieved in this chapter.

In this study, the categories of “printable” and “non-printable” have been subjectively defined to help assess the optimal printing resolution and reproducibility of results. Hence, printability is characterised by the precision of droplet deposition in the x/y/z planes and subsequently by the ability to pattern tightly packed droplets in single lines with minimal gaps. Moroni et al., characterises 3D bio-printing resolution as the “minimum feature dimension” or the “best spatial resolution that can be achieved” by the bio-printer (Moroni et al. 2018). Depending on the bio-printing strategy, the approach to achieve sufficient printability and high-resolution patterning can differ. For example, Moon et al., took a similar approach in assessing their droplet-based bio-printer printability. They did so by characterising the overlapping and layering of cell-laden collagen droplets, measuring ~650 µm, into patterned line structures, in the aim to generate 3D tissue structures with spatial control of cell seeding (Moon et al. 2010). In another strategy, cell-laden aqueous droplets of 130 µm, were ejected and sank into a lipid-in-oil bath with a motorised x/y/z stage, packing the droplets into a hexagonal array and forming droplet-droplet interface bilayers (Graham et al. 2017). Whilst droplet-based bio-printing resolution is partly dictated by individual droplet dimensions, extrusion-based bio-printing printability is generally characterised by the extruded hydrogel’s line width and spreading ratio (Ioannidis et al. 2020; Sanz-Garcia et al. 2020). Despite these different strategies, all 3D bio-printing studies aim to achieve high-resolution hydrogel patterning with spatial control and cell-seeding uniformity. This would directly influence cell-cell distances and subsequently cell-cell communication, which are key in replicating tissue structure and function.

● CHAPTER 5 ●

The 4 parallel-line programme was designed specifically to test droplet printability and resolution, allowing characterisation of droplet packing in single lines and right-angle connection quality (**Figure 5.2**). Although dimensions of the bio-printed line were not quantitatively evaluated, the line width was approximately 1 mm and was dictated by the individual droplet diameters. This is currently higher than resolutions found in Inkjet printers ($\sim 100 \mu\text{m}$), extrusion bio-printers ($\sim 200 \mu\text{m}$), and laser-assisted bio-printers ($< 20 \mu\text{m}$) (Li et al. 2016b; Moroni et al. 2018). However, the LEGO[®] 3D bio-printer is a prototype that is being iteratively developed and further characterisation with a wide range of microfluidic devices, which can generate different sized droplets, could improve this resolution. With the stage's potential range of speeds and fine accuracy, as demonstrated in this chapter, it is anticipated that microscale resolutions could be achieved.

The two middle vertical lines and two right angles only were considered, to avoid the effect of over- or under-extrusion at the beginning and end of prints (**Figure 5.2**). Over- or under-extrusion of droplets occurs when droplet frequency exceeds or falls behind the lateral stage movement speed, respectively. This occurs as a result of controlling the LEGO[®] stage movement independently from the droplet frequency, making it a notable limitation. Whilst the decoupling of droplet deposition from stage movements can be useful for increased optimisation flexibility, it would be beneficial to integrate both systems to allow simultaneous initiation and communication during the print (Ding et al. 2019). This has been explored further in this chapter by building a LEGO[®] syringe driver unit to replace the commercial syringe driver.

Optimal printability was defined at a stage speed of 2.75 mm/s with equal flow rates of 4 mL/hr. However, there were observable breaks in the first printed lines which may have occurred due to a poor droplet-to-glass adhesion, infrequent droplet flow and/or the distance between the nozzle (z-axis) and substrate, which was originally set to 1.1 mm (droplet average length). A lack in droplet size uniformity could lead to droplet-droplet or droplet-substrate (glass cover slip) adhesion loss. The droplet distance to the substrate is key for precise positioning and adequate adhesion, hence if droplets are smaller than average ($< 1.1 \text{ mm}$) this may disrupt precise positioning whilst larger than average droplets ($> 1.1 \text{ mm}$) could induce a

dragging effect on other droplets. Nozzle-substrate distance was therefore set to a starting height of 0.80 mm in subsequent experiments to improve adhesion.

Another explanation for poor droplet adhesion in some places could be the effect of the mineral oil bath. The majority of bio-printed structures produced in the early stages of the study were generated directly in oil-immersed Petri dishes and the viscosity of the oil therefore provided some structural support (Graham et al. 2017). However, repeated experiments confirmed improved adhesion of alginate droplets onto glass coverslips when printed in air rather than oil. This may be due to an increase in droplet-droplet and droplet-glass interfacial tension when oil is minimised, thus providing the structural support and stabilisation onto the substrate that is needed. Future studies of side-by-side experiments of 3D bio-printed 4-parallel lines in oil and in air would be helpful in assessing adhesion differences between both strategies. To date however, there is very limited research on alginate hydrogel droplet-to-glass adhesion properties. Printing directly in oil may decrease droplet-droplet adhesion as a result of diluting the acetic acid, allowing for droplet gelation to resume in parallel to droplet deposition. This may result in improved gelation, thus improving the overall resolution of the print. Despite the known cytotoxicity of acetic acid on mammalian cells, results obtained in the previous section showed high short-term cell viability of keratinocytes when bio-printing using 0.5% acetic acid (**Chapter 3**) (Okabe et al. 2014). In summary, infrequent droplet production can generate gaps or over-extrusion if combined with insufficient adherence to the glass which can disrupt the overall structure. Whilst eventual gaps may seem problematic when printing simple 2D patterns, the layer-by-layer deposition into larger scaled 3D structures can compensate such gaps making them unnoticeable (**Figure 5.13**). The LEGO® 3D bio-printer's printability was further tested with a combination of different flow rates and speeds demonstrating other "printable" regions that may be exploited in future experiments (**Appendix A-8**). The variation in speed increments as little as 0.25 mm/s resulted in significant differences in printability, which demonstrates both the LEGO® motors' precision as well as the bio-printer's sensitivity (**Figure 5.5**).

A limitation of the gelling strategy used in this study is the insoluble Ca²⁺ particles used for alginate crosslinking (Utech et al. 2015). This is observed by differences in colour between droplets due to different gelling efficiencies (**Figure 5.5**) (Baxani et al. 2016). White dense

aggregations found in droplets likely indicates insoluble CaCO_3 which have not yet reacted or partitioned. More opaque droplets could indicate weaker gelling. Indeed, the insoluble nature of CaCO_3 makes it difficult to constantly ensure gelling homogeneity owing to eventual particle sinking in the syringe and tubings (Utech et al. 2015). Furthermore, eventual clogging can produce heterogenous dispersion of Ca^{2+} ions between droplets. However, precautions were taken whereby the syringe was thoroughly mixed before each bio-print, and assessment was systematically carried out immediately after each print.

Four categories of droplet shapes were identified when printing at equal flow rates (4 mL/hr) and at a stage speed of 2.75 mm/s (**Figure 5.6**). A more diverse range was found when varying flow rates and speeds, such as round, teardrop, pinched, or angular (**Appendix A-10**). This demonstrates the LEGO® 3D bio-printer's sensitivity to various parameters feeding into droplet formation and shape. Parameters that may influence droplet shape include: (1) gelling time, (2) bio-ink composition, (3) flow rates, (4) tubing dimensions, (5) microfluidic geometry, (6) droplet-droplet packing, and (7) droplet-substrate adhesion (Xu et al. 2005; Liu et al. 2006; Liu and Zhang 2009; Baxani et al. 2016; Chiarello et al. 2017; Graham et al. 2017). Results obtained in **Chapter 3** indicated that droplets produced at equal alginate and mineral oil flow rates of 4 mL/hr resulted in a mix of round, elongated capsule shaped droplets, when printed directly in water (**Chapter 3, Section 3.4.2**). Droplets deposited during stage movement in droplet-droplet packed configuration shows a wider range of different shapes when, demonstrating a significant impact of droplet-droplet packing and speed on resulting droplet shapes. Droplet shapes are rarely investigated in the literature, despite having a significant effect on droplet-based printing resolution. However, most droplet-based bio-printing platforms and droplet-based microfluidic studies resort to improved droplet-generating strategies resulting in more homogenous droplet shapes (Faulkner-Jones et al. 2013; Utech et al. 2015). In the future, it is necessary to improve droplet shape homogeneity with alternative microfluidic systems. Qualitative assessment of droplet shapes was attempted in this study, although it is acknowledged to be a subjective process. Furthermore, a single print can contain more than one shape, making it difficult to categorise. This can be associated to inconsistent droplet production and the system's sensitivity to the interplay of multiple variables, requiring increased repeats to gain more confidence. To this date, there have been very few studies combining the capabilities of both droplet-based microfluidics and

programmable x/y/z stages, making this a promising prototype for future iterations (Ma et al. 2018; Richard et al. 2020).

Under the optimised parameters tested in **Chapters 3 and 4**, precise spatial positioning of individual droplets was achieved with reasonable printing resolution. This first LEGO® bio-printer prototype has not yet reached resolutions comparable to the commercial bio-printers, however, it is still capable of depositing droplets at the sub-mm resolution and has the potential to improve due to its iterative nature. Despite the system's sensitivity to parameter variations, its adaptability to accommodate a wide range of movements and speeds, allowed synchronisation of stage movements with droplet frequency production, resulting in the deposition of droplets in tightly packed single line configurations.

The first 3D bio-printed structure comprised a two-layered squared lattice programmed to measure 25 mm in length (**Figure 5.9**). Dimensions slightly exceeded 25 mm due to possible loss of droplet-glass/droplet-droplet adhesion when printed in oil. However, the overall structure and retention of shape was a promising outcome from the early LEGO® bio-printer prototype. Experimental repeats were conducted showing similar results (**Appendix A-12**). Whilst results are promising, the dimensions of the bio-printed structure were not accurately measured and therefore future studies should compare the programmed and print dimensions to determine the error to provide more robust quantitative data similar to a study carried out by Sanz-Garcia et al. whereby dimensional error is calculated as the different of the CAD model vs. the extruded bio-printed model (Sanz-Garcia et al. 2020). Observable inconsistencies in the lower layers may be considered a limitation due to a lower resolution bio-printing platform compared to other low-cost 3D bio-printers (Reid et al. 2016; Kahl et al. 2019; Ioannidis et al. 2020) and therefore improvements may be required in future iterations of the printer. However, in more complex structures, such as the 18 layered lattice or pyramid structures in **Figures 5.10 and 5.13**, deposition of more layers was shown to significantly improve the overall structure and resolution. Whilst relevant biological functions emerge from the defined locations of cells and appendages, there is a realistic and unique flexibility in biological architectures and tissues that remains difficult to replicate using automated hardware systems like 3D bio-printers (Ng et al. 2019). In this study however, the presence of gaps and breaks between layers and droplets can potentially exemplify this flexibility and the

non-uniformity of tissue architectures more realistically, as shown by the preliminary two-layered lattice in **Figure 5.9**. An example of this can be seen in the skin's basement membrane, which is naturally formed in an undulating pattern of rete ridges as opposed to *in vitro* 3D bio-printed skin models, which are a flat membrane (Baltazar et al. 2020). However, a mathematical modelling of the epidermis predicted that this unique pattern beneath the epidermis is key in generating more physiologically relevant and realistic epidermal thickness, as opposed to current skin *in vitro* models (Kumamoto et al. 2018). Nonetheless, the early stage of the project makes it difficult to predict such outcomes and further optimisation of the bio-printer is required.

The LEGO® 3D bio-printer's capabilities were therefore tested by implementing a library of 2D, 3D shapes and user-defined parameters into the EV3 programmable brick allowing precise printing locations in the x/y/z planes. Whilst a grid-like structure is achievable using the LEGO® 3D bio-printer, this pattern has not been created in this study. This should be possible by creating increased spacing between interlaced parallel lines. However, a full 8-layered pyramid structure with minor breaks and defined slopes was bio-printed (**Figure 5.10**). Whilst the pyramid's dimensionality was not measured to determine the bio-printer's accuracy of print, macroscopic imaging indicates a shape retention that resembles the designed pyramidal shape. A similar construct, consisting of 13 layers and measuring 9 x 9 mm in size and 5 mm in height, was also reported in Arai et al.'s study using a commercial Inkjet printer (Arai et al. 2011). However, the software used in Arai et al.'s study required 95 separate input images, with each image instructing the bio-printer to produce one individual layer of the pyramid, in contrast to the single VPL pyramid programme sequence used for the LEGO® bio-printer.

Studies have revealed that increasing architectural complexity of a 3D bio-printed tissue model through deposition of multi-material/multi-cellular components can recapitulate the microanatomy and function of that tissue (Johnson et al. 2016; Kim et al. 2019). Achieving the bio-printing of multiple distinct hydrogel cell-laden populations in defined patterns promises to replicate the natural structural fidelity found in healthy or diseased tissue, subsequently providing a platform to study cell-cell or cell-microenvironment functional interactions in a 3D environment. Hence, multi bio-ink 3D bio-printing was tested in this study by

encapsulating and bio-printing cell-sized FluoSpheres® of different colours in a multi-layered fashion (**Figure 5.13**). Reasonable-resolution bio-printing was achieved as demonstrated by the structure's dimensionality and layer-by-layer demarcation (**Figure 5.13**). The ability to deposit multiple materials in a layer-by-layer configuration represents a first promising step to producing skin *in vitro* models, due to the skin's layer-by-layer structure. Indeed, the 3D bio-printing of skin tissue is conventionally achieved through the layer-by-layer deposition of collagen, fibroblasts and keratinocytes, and this is translated to the dermal and epidermal layers once matured, as described by Lee et al. (Lee et al. 2014). In the three-layered structure that was printed in **Figure 5.13**, macroscopic visualisation showed efficient entrapment of FluoSpheres® in layers 1 and 3 but some were also present within the second printed layer, which was programmed to consist of droplets that do not contain FluoSpheres®. This could be due to residues in the microfluidic tube and device when changing bio-inks between prints, although diffusion between the layers cannot be discounted.

Creating a variety of strategies to produce fill-patterned structures or empty outlines improved on the prototype bio-printer capabilities. Combining different stage movement strategies enabled generation of even more complex models, such as a small cube within a larger cube structure at resolutions close to $\leq 1000 \mu\text{m}$ (**Figure 5.14**). 3D patterning of different cell populations with precise locations is an appealing concept which is currently being explored in several studies and has been explored in this chapter by incorporating encapsulated cell-sized FluoSpheres® in precise patterned structures. Graham et al., was capable of patterning different cell populations in Y-shaped, cruciform or arborised patterns within a cuboidal structure with $< 200 \mu\text{m}$ resolutions. Resolutions of $< 250 \mu\text{m}$ were also achieved in earlier studies using laser-assisted bio-printing to micropattern alternating grid structure layers of fibroblasts and keratinocytes to generate a 3D skin model (Koch et al. 2012; Michael et al. 2013). Although the LEGO® 3D bio-printing prototype has not yet achieved features lower than $1000 \mu\text{m}$, it is anticipated that decreasing droplet sizes will allow an increase in printing resolution. Further developments are required to optimise the multi-bio-ink extrusion of the custom-built LEGO® 3D bio-printer, which can be translated in the future to delivering different cell types, extracellular matrix, or scaffolds simultaneously or sequentially in a spatially controlled fashion. Furthermore, both setups are scalable providing

the opportunity to increase the bio-printer's complexity, hence the number of possible bio-inks used.

Challenges to multi-bio-ink bio-printing were encountered in this study. Firstly, flushing of microfluidic tubes was necessary between use of each bio-ink to avoid cross-contamination. However, this still may have resulted in the presence of some FluoSpheres® 'bleeding' in to other layers. This may be avoided if more thoroughly flushed with solvents, such as ethanol or by use of microfluidic parts that are dedicated to a single bio-ink. Furthermore, flushing the microfluidic tubing and cleaning the nozzle also required removal of the Petri dish containing the bio-printed structure. This potentially compromised the precise repositioning of the structure due to human error in manual positioning and may have resulted in the offset alignment between each layer. Indeed, each layer was deposited independently and required programme reset, whereby it was necessary to re-establish the number of layers, the spatial starting position and printing pattern. This is the reason for the imperfect cuboidal shape observed in the bio-printed structures in **Figure 5.13**. Future work is therefore needed to optimise the programming language to allow easier control of nozzle positioning and direct coordinate selection. Additionally, a specific software programme to facilitate nozzle movement to a location convenient for a flushing step is also desirable in future iterations of the printer.

Replacing syringes containing a different bio-ink was also time consuming and had to be done quickly to avoid CaCO₃ and FluoSpheres® sedimentation. Multiple nozzle bio-printers can compensate for this limitation and is now being investigated as demonstrated in **Figure 5.3 & 5.15**. Integrating multiple printing heads in a custom-built 3D bio-printer was reported 8 years ago by Faulkner-Jones et al., to print stem cell spheroid aggregates (Faulkner-Jones et al. 2013). In 2017, Lee et al., integrated four bio-ink dispensers into a low-cost desktop 3D printer allowing for multi-material bio-printing (Lee et al. 2017a). Lee et al.'s method was still considered complex and expensive, and similar results were achieved in Sanz-Garcia et al.'s study at a lower cost and was more accessible (Sanz-Garcia et al. 2020). However, microfluidics offers a more accessible device for multi-material bio-printing owing to its low-cost and modular nature (Baxani et al. 2016; Morgan et al. 2016). The custom fabrication of microfluidic devices to accommodate multiple inlets has great potential for multi-material

● CHAPTER 5 ●

bio-printing and can eventually replace conventional 3D bio-printing nozzles. For example, Costantini et al. reported the bio-printing of two distinct bio-inks containing two cell types using one microfluidic printing head (Costantini et al. 2017). The same research group fabricated a microfluidic 3D bio-printing nozzle which accommodates two bio-inks and can bio-print alginate-based multi-material/multi-cellular structures with high resolution (Idaszek et al. 2019). These studies have used microfluidic devices for extrusion-based bio-printing. However, there are very limited studies that have explored the use of microfluidic devices as 3D bio-printer nozzle alternatives, and to date, no reports of droplet-based microfluidic devices have been used for 3D bio-printing.

Two strategies for dual bio-ink extrusion were developed. Whilst the single nozzle strategy may be a slower alternative compared to the dual parallel nozzle device, it is predicted to produce more homogeneously gelled alginate droplets owing to the single length exit tubing used. In contrast, the dual parallel system is comprised of exit tubings measuring different sizes (9 cm and 14 cm). These sizes were optimised to allow optimal positioning onto the LEGO® z-axis vertical unit. Using the same flow rates, studies have shown that longer tubing, or longer resident times of droplets may significantly impact gelling properties (Sohrabi et al. 2020). The single nozzle would require syringe replacements between each layer or printed section. Despite these differences, it is possible to tune many of these parameters to adapt for optimal multi bio-ink deposition. For example, Lee et al., previously built a low-cost rotary table installed with four printheads allowing for programmable multi bio-ink dispensing system (Lee et al. 2017a). The modular nature of LEGO® and microfluidic devices is well suited to incremental improvements and an increase in the complexity of the bio-printer to build multiple programmable nozzles. This flexibility is portrayed in several recent studies whereby modular microfluidic droplet generator devices were 3D printed and assembled into user-defined shapes (Morgan et al. 2016; Nie et al. 2018). A bio-engineering researcher in Cardiff University, Dr Jin Li, recently 3D printed a microfluidic t-junction droplet generator in a LEGO® compatible brick design that was successfully integrated into the LEGO® bio-printer build (**Appendix A-13**). This would provide a more integrated LEGO® platform and a more structurally stable t-junction alternative device in contrast to the conventional t-junction.

● CHAPTER 5 ●

The LEGO® platform is low cost, although not the cheapest 3D bio-printing hardware; the cost of the prototype is approximately £500, in contrast to custom-built 3D bio-printers found at ~£150 (Kahl et al. 2019). Nonetheless, it provides arguably the most accessible route to building and programming for experts and beginners alike. This is considered as a small price to pay to gain coding experience and scientific knowledge in microfluidics. A major limitation to the cost of the bio-printer that has been developed in this study was use of a commercial syringe driver costing ~£1500, bringing the whole system to ~£2000. Recently, Almada et al., built low-cost LEGO® syringe drivers allowing for controlled reagent delivery to cells during microscopy imaging (Almada et al. 2019). Therefore, a LEGO® syringe pump based on Almada et al.'s. concept was built and characterised in terms of its droplet frequency and generation (Almada et al. 2019). Ultimately, this system could be integrated with the LEGO® platform to build a fully integrated LEGO® bio-printing platform with simultaneous control of droplet production and stage movements. The LEGO® syringe pump does not exceed £50 and so the estimated cost of an integrated LEGO® 3D bio-printing platform is ~£550. Therefore, with further optimisations, the LEGO® syringe driver prototype is anticipated to replace the commercial syringe driver. Whilst two EV3 programmable bricks are used to control the stage and syringe drivers, future direction aims at using commercially available EV3 motor multiplexers which would allow to simultaneously control several motors.

The modular and reconfigurable nature of LEGO® parts and robotics makes it an attractive construction kit to invent, create, and build complex yet accessible laboratory hardware (Kim and Jeon 2007; Almada et al. 2019). This chapter evaluates the bio-printing capabilities of a low-cost bespoke LEGO® 3D bio-printing platform in producing 2D and 3D patterned shapes with multiple bio-inks. The stage speed and movements, along with microfluidic gelling methods and droplet production frequency are collectively tunable parameters that have been developed and evaluated to produce reasonable-resolution patterned constructs. However, the LEGO® 3D bio-printer is in its early stages of development and there is still space for improvement of the prototype. Despite not achieving similar levels of resolutions to previously reported 3D bio-printers, the modular nature of the stage and flexibility of microfluidics promise to build on the platform's complexity, thus enhancing its performance. The LEGO® 3D bio-printer was capable of producing multiple bio-ink structures

● CHAPTER 5 ●

with structural integrity and good patterning resolutions, comparable to previously reported custom-built 3D bio-printers. Increasing the platform's complexity by adding multiple nozzles is in the optimisation stages but shows promising results. Finally, bio-ink delivery can be achieved through a LEGO® syringe driver with high droplet production reproducibility in contrast to the commercial syringe driver. Taken together, the LEGO® 3D bio-printing platform promises to be an accessible and affordable platform for tissue 3D bio-printing, opening opportunities for laboratories to explore 3D cell culture and 3D tissue engineering.

***Chapter 6 Towards bio-printing a
human skin model: processing and
post-processing***

6.1 Introduction

A 3D bio-printer's performance partly resides in its ability to precisely pattern different cell-laden bio-inks (i.e., resolution) with high repeatability and flexibility (Graham et al. 2017). Ensuring high resolution patterning of a bio-printer is a crucial step in validating a 3D bio-printer's performance, and is generally achieved through microscale imaging of fluorescently labelled cells or bio-material embedded in a hydrogel (Koch et al. 2012; Graham et al. 2017). Next, a 3D bio-printer's performance is evaluated from its ability to produce tissue structures with both microanatomical and physiological relevance, i.e., that can replicate the native tissue biology (Murphy and Atala 2014). This requires tissue maturation, where cells are allowed to proliferate and/or differentiate, known as the post-processing stage (Murphy and Atala 2014; Yan et al. 2018). The final phase involves evaluating the 3D bio-printed tissue equivalent in comparison to the native tissue, achieved through characterisation of microanatomical structuration and functional features. In skin 3D bio-printing, the post-processing stage is described as the maturation phase whereby the extruded cells, such as keratinocytes, melanocytes, fibroblasts, pericytes, or endothelial cells, proliferate and/or differentiate in culture to produce a functionally relevant biomimetic skin (Min et al. 2017; Yan et al. 2018; Baltazar et al. 2020). This is commonly achieved using the air-liquid interface (ALI) method in conventional skin tissue-engineering, necessary for epidermal differentiation and maturation (Roger et al. 2019). For example, Baltazar et al., bio-printed a multi-layered construct composed of collagen, fibroblasts, keratinocytes, pericytes, and endothelial cells, cultured under submerged conditions for 4 days, and then lifted to the ALI for another 20-30 days (Baltazar et al. 2020). Microanatomical and biochemical analysis of the 3D bio-printed skin grafts showed promising resemblance to the native human skin, revealing relevant epidermal thickness, maturation and the expression of CD31⁺ vessel-like structures when compared to an *in vivo* skin model (Baltazar et al. 2020).

Bio-ink properties can significantly affect several cellular functions including, adhesion, proliferation, differentiation, and migration (Chimene et al. 2016; Gungor-Ozkerim et al. 2018; Yang et al. 2018). Since *in vitro* maturation of 3D bio-printed tissue models relies on these functions, selection of the appropriate bio-ink is crucial. Indeed, bio-inks for 3D bio-

● CHAPTER 6 ●

printing are required to have high biocompatibility, controllable gelation/degradation, provide structural support, and promote cell proliferation and differentiation (Gungor-Ozkerim et al. 2018). For example, Pourchet et al., 3D bio-printed a skin model using a combination of 3 hydrogels composed of gelatine, alginate, and fibrinogen. In their study, each hydrogel provided a unique purpose allowing to simultaneously maintain appropriate rheology during extrusion bio-printing, consolidate the structure post-printing, and provide cellular adhesion promoting skin maturation (Pourchet et al. 2017). Alginate is the most widely used bio-ink in bio-printing owing to its high biocompatibility and fast gelling properties (Gungor-Ozkerim et al. 2018). However, alginate is a largely inert material therefore not possessing cell-adhesive properties, which may result in apoptosis of encapsulated cells (Derby 2008; Hong et al. 2015). Furthermore, alginate is inherently non-degradable by mammalian cells due to the lack of the alginase enzyme, meaning that cell-encapsulated hydrogels remain static post-printing, limiting cell migration, proliferation, and differentiation (Pati et al. 2014). Thus, exploring the process of alginate degradation and timescales is a pivotal step in optimising maturation of the bio-printed structure (Wu et al. 2016). In this study, alginate droplets are essentially used as carriers or transport building units of keratinocytes, which are ultimately sacrificial once precise spatial cell deposition is achieved. Hence, alginate droplets act as a sacrificial scaffold that require degradation post-bio-printing. Alginate degradation is commonly achieved by using calcium chelating agents, such as sodium citrate or Ethylenediaminetetraacetic acid (EDTA) (Bonaventure et al. 1994; Masuda et al. 2003; Wu et al. 2016; Fan and Wang 2017). However, the degradation rate of alginate should be controllable, whilst providing a biocompatible environment for keratinocytes. Indeed, subjecting keratinocytes to high levels of calcium chelator agents may be detrimental to cell viability, proliferation, adherence, and skin maturation (Li et al. 1995).

In the previous chapters, a bespoke 3D bio-printer was built and evaluated for its ability to bio-print 2D and 3D patterned structures with reasonable printability and resolution, using a bio-ink which consists of an alginate scaffold made up of discrete droplets. In this study, the alginate droplets act as a transportation means for cell deposition and are ultimately sacrificial once deposited with in a spatially controlled manner. Hence, prior to bio-printing cell-laden structures for tissue maturation (part of the post-processing step), it is vital to explore the degradation process of alginate in terms of rate of degradation and its effect on

● CHAPTER 6 ●

cell viability. Exploring this, would allow for controllable alginate degradation for optimal dismantling of the scaffold and in parallel, providing a suitable environment for cell adhesion, viability, proliferation, and subsequent differentiation and maturation.

6.2 Aims and objectives

The aim of this chapter was to evaluate the LEGO® bio-printer's resolution on the microscale and explore strategies for controllable alginate degradability.

The objectives of this chapter are:

1. Bio-print a tiered multi-bio-ink multi-layered structure with encapsulated live fluorescently stained keratinocytes.
2. Evaluate the resolution of the bio-printed structure through Lightsheet microscopy imaging by observing:
 - a. structural maintenance,
 - b. demarcation of each layer
 - c. encapsulation quality of fluorescently labelled keratinocytes on the microscale.
3. Scaffold removal of 2D and 3D alginate structures with different concentrations of calcium chelators using sodium citrate and EDTA.
4. Explore the degradation times necessary to fully degrade structures through timelapse video observation.
5. Explore the effect of the degraded alginate/calcium chelator solutions on keratinocyte viability up to 24 hours.

6.3 Materials and Methods

6.3.1 Preparation for imaging multi-bio-ink 3D bio-printed structures via Lightsheet Microscopy (LSFM)

6.3.1.1 hTERT/Ker-CT Keratinocyte staining

hTERT/Ker-CT keratinocyte cells were detached, and 30 million cells were stained with CellMask™ Deep Red Plasma Membrane Stain (Thermo) and 30 million cells were stained with Green CellMask™ (Thermo) before encapsulation and resuspension in the alginate/CaCO₃/DMEM solution at a cell density of 10⁷ cells/mL, each. CellMask™ plasma membrane stains are amphipathic molecules, containing both lipophilic and hydrophilic structures allowing for simultaneous membrane penetration and anchoring in live cells. Cell-encapsulated droplets were extruded as described in **Chapter 3, Section 3.3.3**.

6.3.1.2 Experimental 3D bio-printing of encapsulated cells

Monodisperse alginate droplets containing two pre-stained hTERT/Ker-CT keratinocyte cell populations, were 3D bio-printed using the LEGO® custom-built 3D bio-printer into a multi-layered squared lattice and extruded in a 50 mm Petri dish onto a glass coverslip in air. After bio-printing, the excess mineral oil and acetic acid were removed, and the cell-laden 3D structure was gently washed with PBS twice before manipulation and imaging.

6.3.1.3 Light Sheet Microscopy material preparation for image acquisition

Glass capillary devices did not allow for long term hold of full 3D bio-printed structures due to its hydrophilicity. A custom-made device to optimize sample entrapment and sample bio-punching was fashioned using a FEP tubing instead (**Figure 6.1 A**). This consisted of a 1 mL plastic syringe attached to a 4 mm and 3 mm external and internal diameter FEP tube,

● CHAPTER 6 ●

respectively. The syringe ensured optimal vacuum action on the bio-punched sample whilst the FEP tube serves as a transparent polymer that has a similar refractive index to water, making it a suitable alternative to glass. Parafilm held both objects together to prevent air from escaping. A razor-sharp seamless cutting tip (4 mm diameter) removed from a bio-punch device (KAI MEDICAL) was connected to the end of the FEP tube using parafilm (MERCK) to aid in cutting and removing a bio-printed sample. Alternatively, the end of the FEP tube was sharpened using a pencil sharpener. Both allowed to take a biopsy and subsequently extract the sample into the FEP tube.

Prior to this, the FEP tubing had to be straightened to avoid any sample displacements. After cutting the desired length of tubing, a soldering metal was straightened by hand and inserted into the tube, then heated to 180°C in a heating chamber for 1 hour. The soldering metal was carefully removed resulting in a straightened FEP tube (**Figure 6.1 B**). To remove excess dust and dirt from the FEP tube, it was flushed twice with 1 M NaOH. The tubes were then placed in 50 mL Falcon tubes containing 0.5 M NaOH and were ultrasonicated for 10 minutes. FEP tubes were flushed with dH₂O and 70% ethanol twice before placing them back in 50 mL Falcon tubes containing 70% ethanol. They were ultrasonicated again for 10 minutes then flushed several times with dH₂O before storing them in Falcon tubes filled with dH₂O.

A sample from the 3D-bio-printed construct was taken using the custom-made syringe/FEP/bio-punch device and was entrapped in the FEP tube (**Figure 6.1 A 3**). The entire device was inserted into the liquid filled chamber for image acquisition. Light Sheet Fluorescent Microscopy (Zeiss Lightsheet z. 1) was used for image acquisition using a 5x magnification with excitation wavelengths for the Green and Deep Red CellMask™ dyes at 495 nm and 528 nm, respectively. Optical slices of 10 - 15 µm were taken for the full length of the FEP tube. The Zeiss ZEN software was utilized to visualize the cell-laden droplets and 3D reconstitution/grouped Z projection was carried out using Image J.

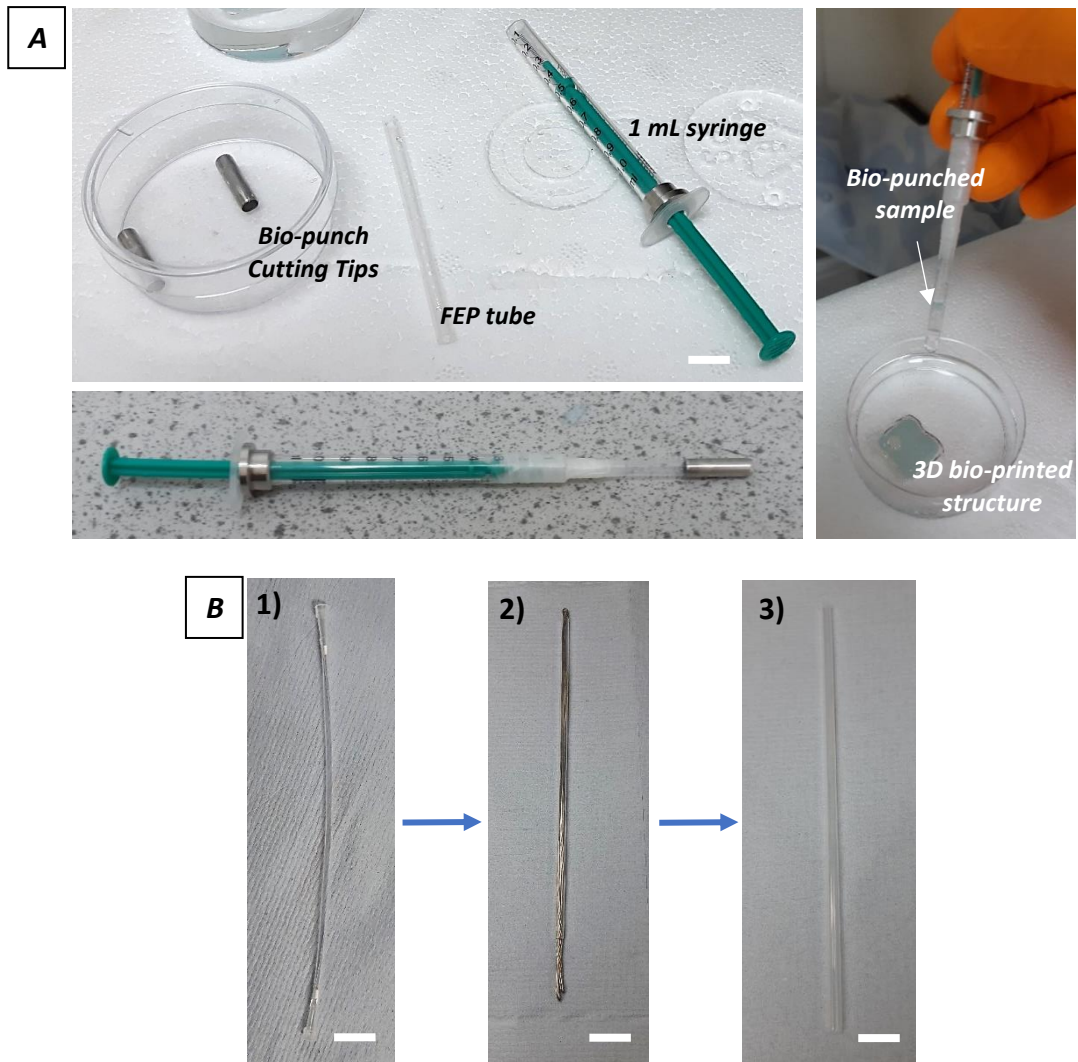


Figure 6.1 FEP tube preparation for Light Sheet Fluorescent Microscopy imaging.

(A) A custom-made device to simultaneously bio-punch, withdraw and use as a capillary for LSMF imaging was fashioned. Scale bar = 10 mm. (B) Prior to imaging, the FEP was straightened and cleaned: (1) the FEP tube of 4 mm and 3 mm ED and ID, respectively, was cut to a desired length. (2) A soldering metal was inserted in the tube and heated to 180°C in a heating chamber for 1 hour. (3) After discarding the soldering metal, the tube was cleaned and kept in dH₂O. Scale bar = 10 mm

6.3.2 Alginate droplet degradation with EDTA and sodium citrate

Two calcium chelators were used to remove the alginate scaffold: Ethylenediaminetetraacetic acid (EDTA) and sodium citrate ($\text{Na}_3\text{C}_6\text{H}_5\text{O}_7$). A series of increasing concentrations of calcium chelator solutions were prepared in calcium-free, pyruvate-free, and glutamine-free DMEM media (Thermo) and Keratinocyte Basal Medium (KBM). EDTA concentrations of 1 mM, 2.5 mM, 4 mM and 8 mM and sodium citrate concentrations of 5 mM, 10 mM, 50 mM, and 100 mM were prepared.

Alginate droplet degradation was tested on three printed shapes: a 10 mm diameter single-layer circle outline printed onto a glass cover slip sitting in a 50 mm Petri dish, a 14 mm diameter 2-layered, or 3-layered concentric circle printed on a Polyethylene Terephthalate (PET) Millicell™ hanging cell culture insert with pore size of 3.0 μm used in 6-well plates (MERCK). To improve droplet degradation visualisation, 3 mL bromothymol blue was added to the alginate solution used for the single layer printed outline. However, the 3D structures were bio-printed using the conventional alginate solution used previously in this study. For the 2D circle outline, 200 μL of each chelating agent solution was added onto the printed alginate droplets. 3D bio-printed structures were transferred from the 50 mm Petri dish to a 6 well plate and submerged into the calcium chelator solution, as illustrated (**Figure 6.2**).

The average degradation times (complete structure degradation) were recorded by video using a Brunel Eyecam fitted in a Zeiss stereomicroscope. For the 2D outline print, six tests were carried out for each different chelation solution and concentration, each test contained 10 runs totalling 480 prints. The dissolved alginate-chelator solutions were systematically collected for cell biocompatibility testing. Three repeats were carried out for each calcium chelator solution tested on the 3D 2- and 3-layered concentric circles. Time lapse videos of alginate degradation were generated using Fiji (ImageJ).

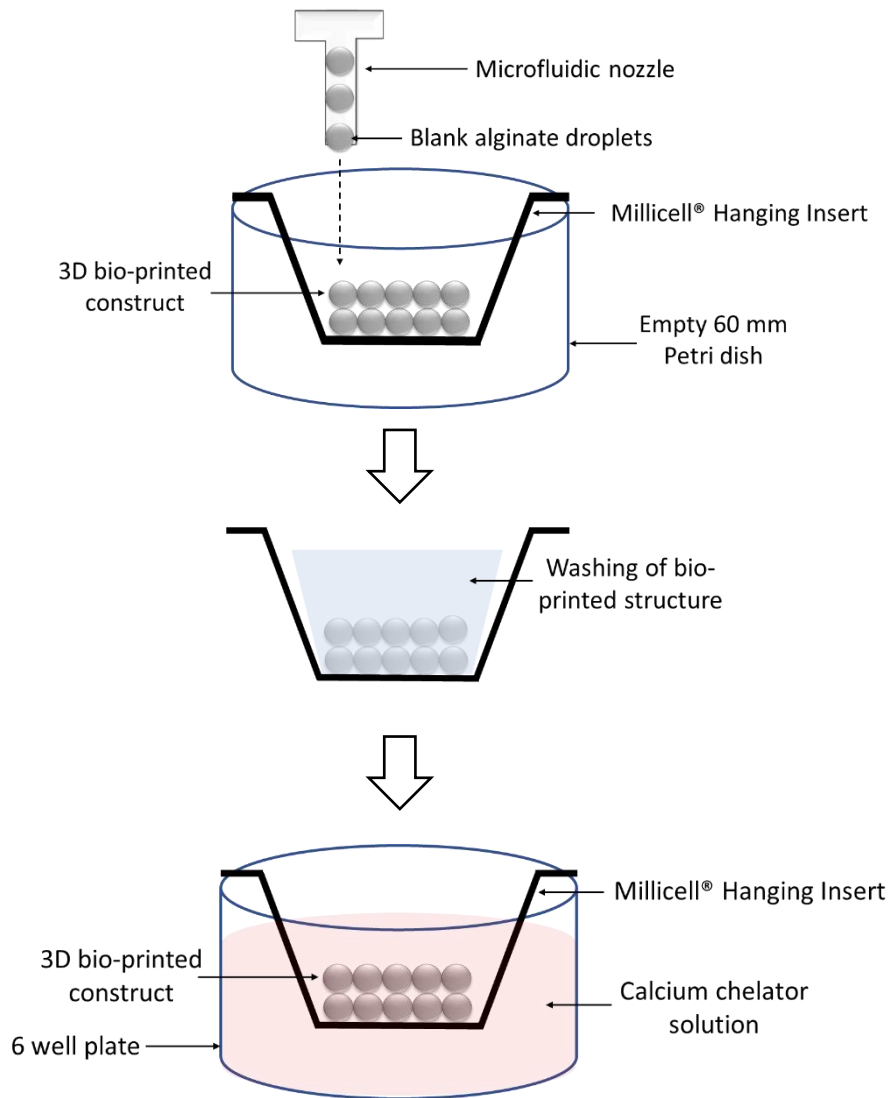


Figure 6.2 Schematic representation of blank alginate droplet degradation bio-printed in Millicell® hanging inserts.

Alginate droplets are produced in 2 or 3-layered concentric circles directly printed in air and in Millicell® hanging inserts sitting in a 50 mm petri dish. The 3D bio-printed structure is then washed and transferred into a 6 well plate for scaffold removal and time lapse imaging.

6.3.3 Investigating the biocompatibility of the dissolved bio-material (alginate/calcium chelator solutions) on keratinocytes

HaCaT cells were seeded at 50 000 cells per well in a 96 well-plate for 24 hours and kept at 37°C and 5% CO₂ to allow attachment prior to experimentation. HaCaT cells were then

incubated with 100 μL of the dissolved-alginate-EDTA or dissolved-alginate-sodium citrate solutions for zero, 30 minutes, 2 hours, and 24 hours in 96-well plates. CellTiter-Blue[®] assay (Promega[®]) was then used to determine cell viability. An amount of 20 μL of the CellTiter-Blue[®] reagent was added to each well and incubated for 2.5 hours to allow the reaction to occur, following Promega[™] protocol guidelines. The “Zero” condition consisted of HaCaT cells incubated with dissolved calcium chelator solutions, but directly incubated with CellTiter-Blue[®]. The control condition contained HaCaT cells and DMEM medium alone. The experiment was conducted once, with ten technical repeats for each calcium chelator solution concentration. Fluorescence intensity scans were taken using a TECAN Infinite Microplate reader at an excitation wavelength of 579 nm and emission wavelength of 584 nm. Average fluorescence was calculated for each solution at the various time points.

6.3.4 Statistics

Data are represented as mean \pm SD. Statistical significance was determined by the independent samples Student t-test, whereby $p < 0.05$ was considered statistically significant.

6.4 Results

6.4.1 Multi-bio-ink 3D bio-printing of a patterned structure containing live keratinocytes

The ability to bio-print complex multi-layered and multi-bio-ink constructs has been demonstrated in the previous chapter by incorporating and patterning colored cell-sized fluorescent beads. Microscopic images revealed successful demarcation of layers, structure maintenance and precise deposition of individual droplets. Generating 3D tissue models relies on the ability to incorporate live cells with similar bio-printing resolution as demonstrated with the cell-sized beads. Hence, since the goal is to produce a 3D bio-printed skin model, a similar tiered construct was bio-printed by incorporating fluorescently labelled hTERT/Ker-CT keratinocyte cells. In addition to the macroscopic assessment conducted in the previous chapter, it was necessary to evaluate the bio-printed construct with higher detail using a microscopic imaging platform. This would inform on the overall printing resolution on the individual droplet scale and short-term cell viability. Indeed, the CellMask™ stain solely labels a live cell's membrane.

The keratinocyte cell-laden construct was bio-printed as an 18-layered squared lattice consisting of: 8 bottom layers of green CellMask™ membrane-stained hTERT/Ker-CT, 4 blank layers, and 6 top layers of deep-red CellMask™ membrane-stained hTERT-KER-CT (**Figure 6.3. A & B**). Two hours post-bio-printing, a section of the bio-print was excised and extracted using a biopsy puncture device, then mounted into the lightsheet microscopy chamber for imaging (**Figure 6.3. C**). Full-depth Z scans of the excised section were taken and imaged. The large size of the excised section required gradual imaging from bottom to the top and subsequent stitching to generate a full image of the bio-print (**Figure 6.3. D**). Lightsheet microscopy images revealed a maintained and successfully layered 3D construct, showing the different colored CellMask™ stained populations in defined spatial positions within each layer (**Figure 6.3. D**). The shape of droplets is distinguishable and droplet-droplet distances show promising data for potential cell-cell interactions for subsequent tissue maturation. However, some areas show larger droplet-droplet distances and holes, which result from the methodology

● CHAPTER 6 ●

used to extract the biopsy sample. The expression of CellMask™ dyes demonstrate the high viability of encapsulated cells throughout the entirety of the multi-layered structure. Overall, this result demonstrates the LEGO® 3D bio-printer's precision in depositing cell-laden droplets with high spatial precision in 3D. Furthermore, the short-term high keratinocyte cell viability and droplet-droplet proximity is promising in generating relevant skin models in the near future.

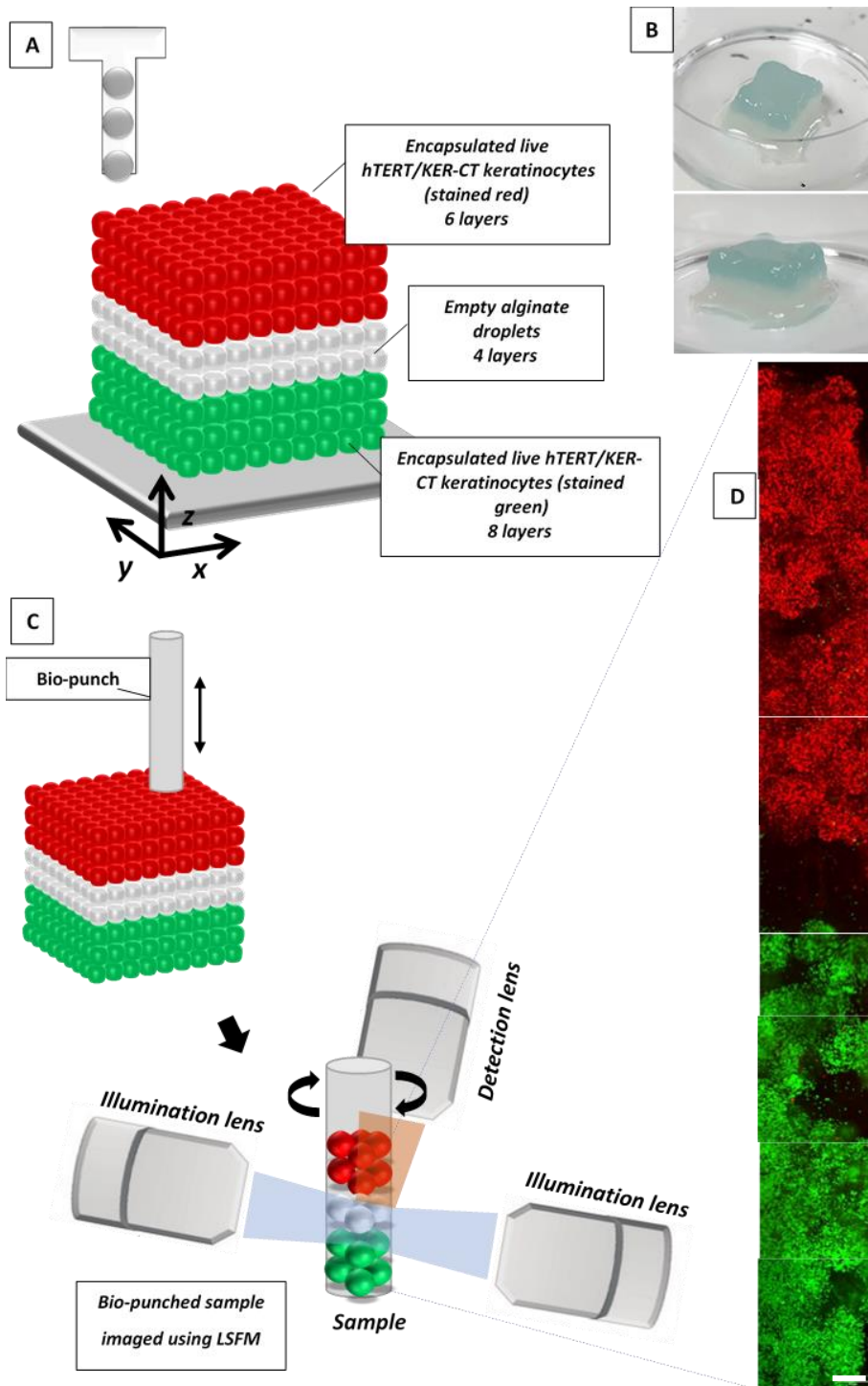


Figure 6.3 Multi-bio-ink bio-printing with encapsulated live hTERT/Ker-CT cells imaged by light-sheet microscopy.

(A) Schematic illustration of a three-bio-ink multi-layer squared lattice print with bio-ink layers containing no cells (4 layers middle) or live hTERT/Ker-CT cells with membranes stained with green (8-layers bottom) or red (6 layers top) fluorescent CellMask™. (B) The resulting bio-construct imaged macroscopically from a top- and side-view. (C) A sample tissue of the bio-construct is excised using a custom-made capillary biopsy punching device for 3D lightsheet imaging. The sample is inserted into the lightsheet chamber, illuminated with illumination lens, and detected for image capture. (D) Lightsheet microscopy stitched images of the 3D bio-printed excised section showing maintenance of stained cell positioning within the 3D printed architecture and positive cell viability. Scale bar = 500 μm .

6.4.2 Evaluating the degradation rates of a 2D patterned alginate structure using calcium chelators

Two calcium chelators known to degrade alginate were used: (1) sodium citrate and (2) Ethylenediaminetetraacetic acid (EDTA). For this, simple 2D lines (one layer) were bio-printed and degradation times were assessed through time-lapse videos and average degradation time quantifications using different calcium chelator concentrations. A simple 2D shape (one layer) was tested at first to gain a better understanding of the average time it would require for full degradation.

6.4.2.1 Sodium Citrate

Alginate droplets printed in a single 2D line were incubated with four different sodium citrate/DMEM solutions to investigate the necessary time required to fully degrade the structure. At 5 minutes, time lapse images revealed no significant degradation at 5- and 10-mM sodium citrate (**Figure 6.4.**). However, an increase in degradation rate was observed when incubated with 10 mM sodium citrate as shown at 10 minutes (**Figure 6.4**). Average complete degradation was achieved at 19 minutes with 10 mM sodium citrate in contrast to a partial degradation with 5 mM sodium citrate. At 5 mM sodium citrate, an average of 15 extra minutes were required for complete degradation (**Figure 6.7**). As expected, the presence of more citrate ions resulted in faster and increased calcium chelation, and subsequently lower average degradation times.

Doubling the concentration of sodium citrate from 5 to 10 mM resulted in decreasing the average degradation time by roughly 40% (**Figure 6.7**). However, increasing the sodium citrate concentration from 50 mM to 100 mM decreased the average degradation time by only 20%, as demonstrated in the time lapse images and graph (**Figures 6.5 & 6.7**). Alginate droplet degradation was visible as early as 2.5 minutes in contrast to 10 minutes using 5- and 10-mM sodium citrate. No statistical significance in average degradation rates was observed between 50- and 100-mM sodium citrate ($p>0.05$), in contrast to differences found between 5- and 10-mM sodium citrate, 5- and 50-mM sodium citrate, and 10- and 50-mM sodium

citrate ($p < 0.05$) (Figure 6.7). To ensure that degradation was solely due to the calcium chelators and not the DMEM or dH₂O, negative controls were conducted, demonstrating no degradation up to 1 hour incubation (Figure 6.6). At a 5 mM sodium citrate concentration, degradation times resulted in 35 minutes and were deemed too slow for a simple 2D structure, whereas 100 mM sodium citrate showed no significant increase in average degradation times compared to 50 mM. Therefore, 5 mM and 100 mM were removed from the remainder of the study.

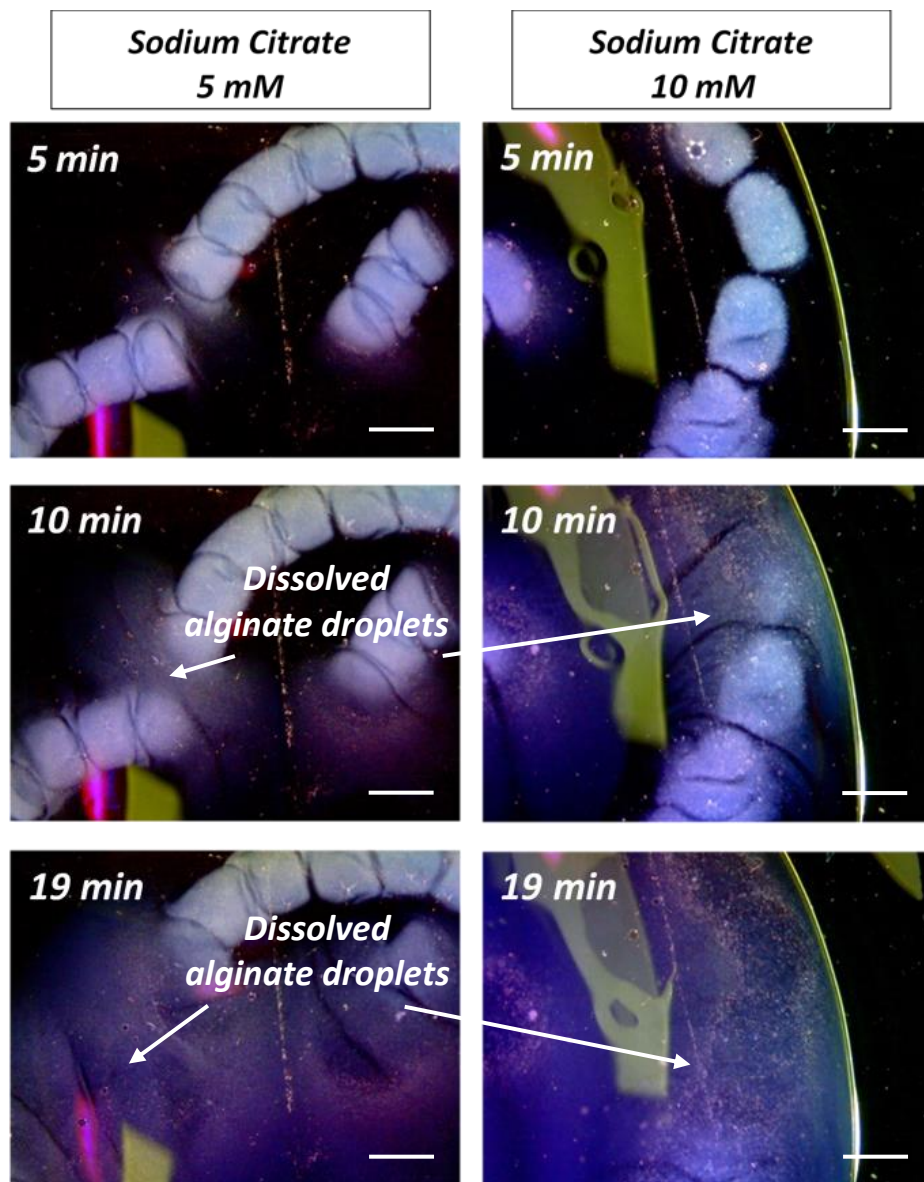


Figure 6.4 Time lapse images of alginate droplet degradation at 5, 10, and 19 minutes, using 5 mM and 10 mM sodium citrate solutions.

Alginate droplets were bio-printed in a single concentric line. Alginate dissolution is observed using a stereoscope. Dissolution occurs when the visible outer perimeter of droplets gradually disappear, the white colour intensity decreases, and when the droplet expands in shape. Scale bar = 1 mm (Produced by Ameer Alshukri).

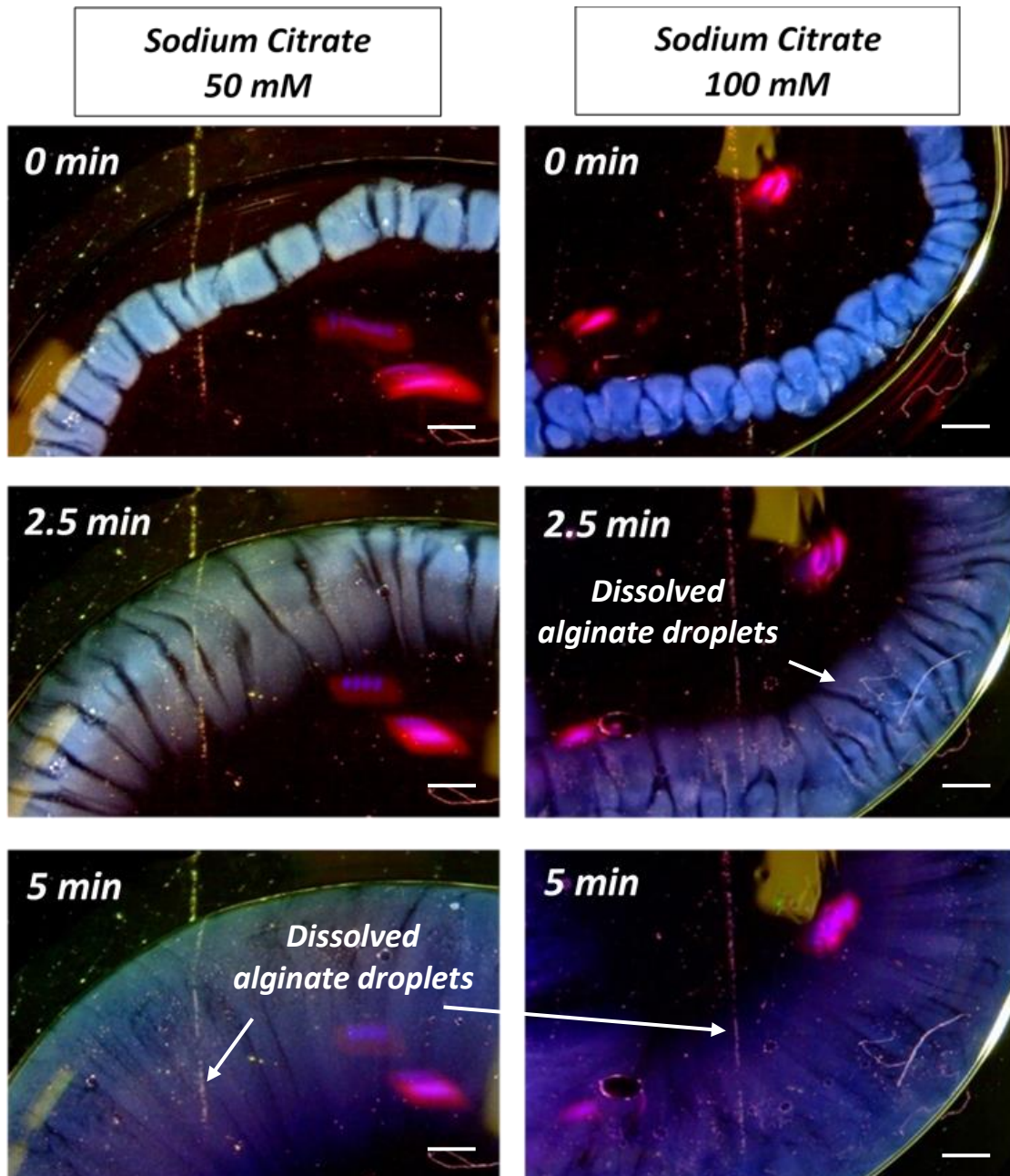


Figure 6.5 Time lapse images of alginate droplet degradation at 0, 2.5, and 5 minutes, using 50mM and 100mM sodium citrate solutions.

Alginate droplets were bio-printed in a single concentric line. Alginate dissolution is observed using a stereoscope. Dissolution occurs when the visible outer perimeter of droplets gradually disappear, the white colour intensity decreases, and when the droplet expands in shape. Scale bar = 1 mm.

(Produced by Ameer Alshukri).

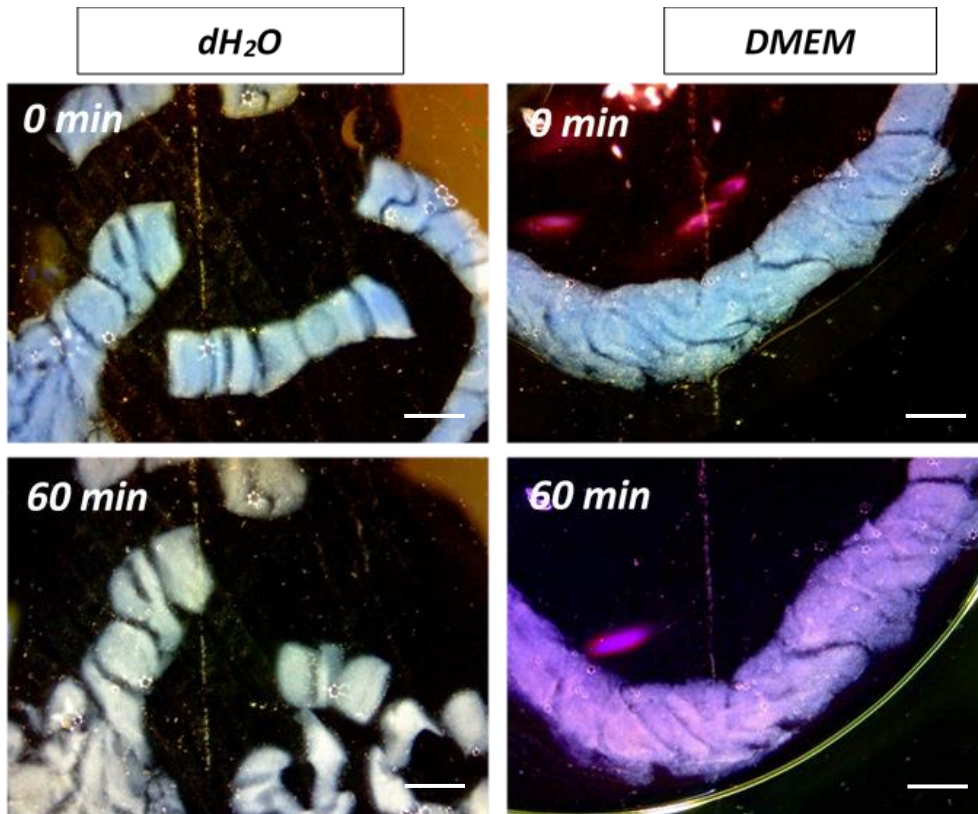


Figure 6.7 Control time lapse images of alginate droplets exposed to dH_2O and Ca^{2+} -free DMEM for 60 minutes.

Alginate dissolution is observed using a stereoscope. Dissolution occurs when the visible outer perimeter of droplets gradually disappear, the white colour intensity decreases, and when the droplet expands in shape. Scale bar = 1 mm. (Produced by Ameer Alshukri).

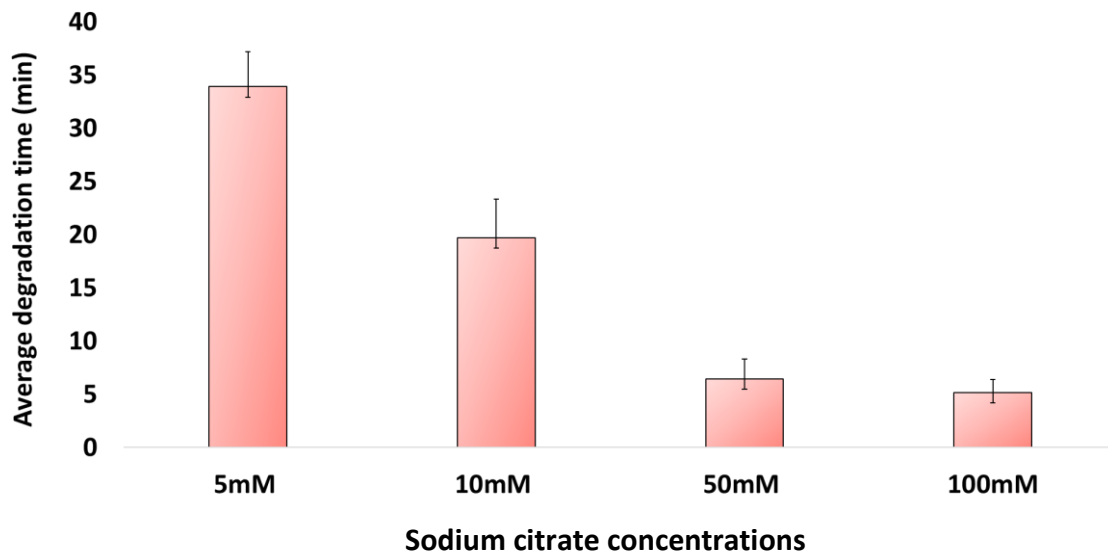


Figure 6.6 Alginate droplet degradation times with varying concentrations of sodium citrate. Complete alginate degradation times in minutes (min) (i.e., disappearance of outer visible droplet perimeter, decreased white colour intensity, and complete loss of droplet structure) were evaluated when alginate droplets were exposed to different concentrations of sodium citrate. Data are represented as mean \pm SD. Independent Samples t-test. ($n=3$) (Produced by Ameer Alshukri).

6.4.2.2 EDTA

A range of EDTA concentrations from 1 to 8 mM were tested for alginate droplet degradation times, similar to the Sodium citrate. As expected, the lowest concentration of EDTA, at 1 mM demonstrated the slowest degradation rate, reaching a complete average time above 20 minutes (**Figure 6.8 & 6.10**). Whilst a partial degradation was observed at 18 minutes for 1 mM EDTA, a complete degradation had already occurred when increasing the concentration to 2.5 mM EDTA, demonstrated in the time lapse images (**Figure 6.8**). Images also demonstrated that at 2.5 mM a partial structure degradation was observable at 10 minutes whilst no visible degradation was yet observed for 1 mM EDTA. Despite no significant difference found in the average complete degradation times between 1 and 2.5 mM EDTA, a trend in the degradation rate decrease is observable when incubating with 2.5 mM EDTA. Due to these reasons, it was decided to remove 1 mM EDTA from further experiments. was removed from the study.

Surprisingly, the fastest average degradation time was observed with 4 mM EDTA and not 8 mM, resulting in an average of 15 and 26 minutes, respectively (**Figure 6.10**). At 15 minutes, no degradation was yet observed using 8 mM EDTA, whilst full degradation was observed with 4 mM EDTA (**Figure 6.9**). It was speculated that a reduction in pH due to high concentrations of EDTA was the reason for a prolonged degradation time, reducing the ability of EDTA to chelate Ca^{2+} ions. Indeed, the shift in colour of phenyl red in the cell culture medium DMEM to yellow indicates a reduction in pH. The effect of pH change on alginate degradation was therefore explored in the next section. Whilst no significant average degradation times were observed between 1, 2.5, and 4 mM EDTA, a visible decreasing trend in average degradation times are seen from 1 to 4 mM EDTA.

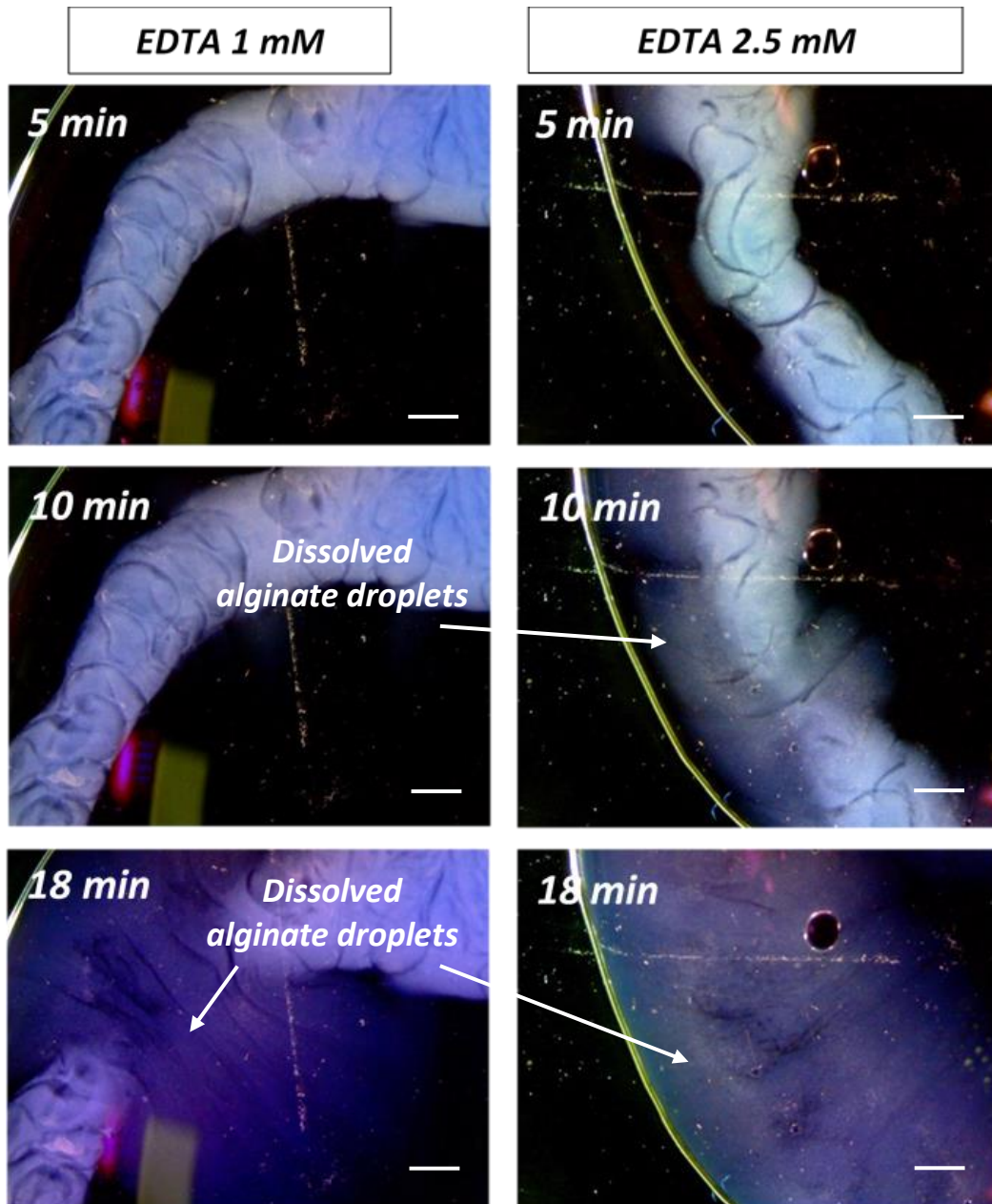


Figure 6.8 Time lapse images of alginate degradation at 5, 10, and 18 minutes using 1 mM and 2.5 mM EDTA solutions.

Alginate dissolution is observed using a stereoscope. Dissolution occurs when the visible outer perimeter of droplets gradually disappear, the white colour intensity decreases, and when the droplet expands in shape. Scale bar = 1 mm. (Produced by Ameer Alshukri).

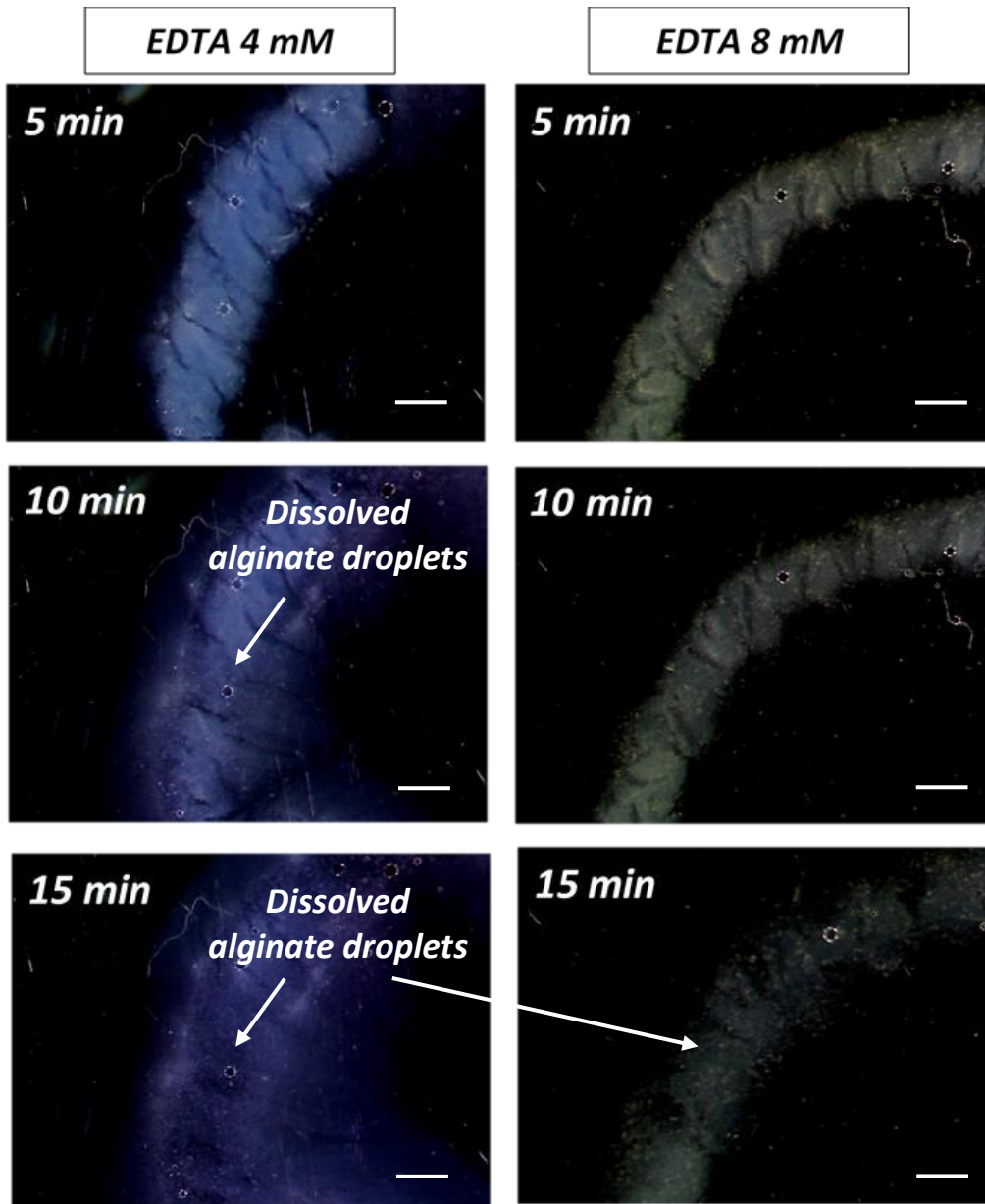


Figure 6.9 Time lapse images of alginate degradation at 5, 10, and 15 minutes using 4 mM and 8 mM EDTA solutions.

Alginate dissolution is observed using a stereoscope. Dissolution occurs when the visible outer perimeter of droplets gradually disappear, the white colour intensity decreases, and when the droplet expands in shape. Scale bar = 1 mm. (Produced by Ameer Alshukri).

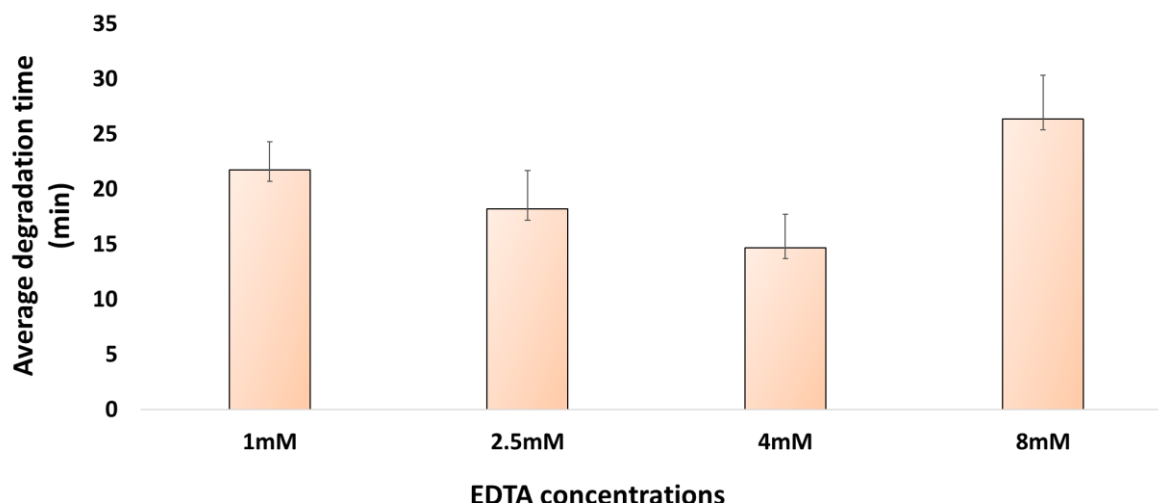


Figure 6.10 Alginate droplet degradation times with varying concentrations of EDTA. Complete alginate degradation times in minutes (min) (i.e., disappearance of outer visible droplet perimeter, decreased white colour intensity, and complete loss of droplet structure) were evaluated when alginate droplets were exposed to different concentrations of EDTA. Data are represented as mean \pm SD. Independent Samples t-test. (n=3) (Produced by Ameer Alshukri).

6.4.2.3 Exploring the effect of pH variations on alginate degradation rates

The pH of all EDTA solutions was tested whereby 8 mM EDTA resulted in the lowest value of pH=5. Concentrations at 1 and 2.5 mM resulted in pH values close to 7 whereas 4 mM EDTA showed a value of 6.5 (data not shown), thus confirming a reduction of pH when increasing EDTA concentration. A colour shift in phenyl red was not observed when varying sodium citrate concentrations suggesting no changes in pH, hence, the effect of pH changes on alginate degradation for sodium citrate was not investigated (**Appendix A-14**).

The effect of pH variation on the ability of EDTA to chelate Ca^{2+} ions and subsequently degrade alginate droplets was investigated. For this, the pH 5 EDTA solution was compared to a neutral pH EDTA solution for alginate degradation. Furthermore, an acidic pH of 2.5 for 4 mM EDTA was compared to the pH 6.5 4 mM EDTA solution. Average alginate degradation time was reduced to 15 minutes from the previously measured 26 minutes (**Figure 6.11 A**). Reducing the pH to 2.5 in the 4 mM EDTA solution increased the average degradation time to 33 minutes in contrast to the 14 minutes (**Figure 6.11 B**). Increasing the pH for the 8 mM EDTA

solution resulted in a similar average degradation time as the 4 mM EDTA solution (**Figure 6.11 C**). Therefore, 8 mM EDTA was removed from the remainder of the study due to no significant differences when compared to using less concentrated EDTA. Results demonstrated that pH variations in the EDTA solutions significantly impacts the degradation rates of alginate.

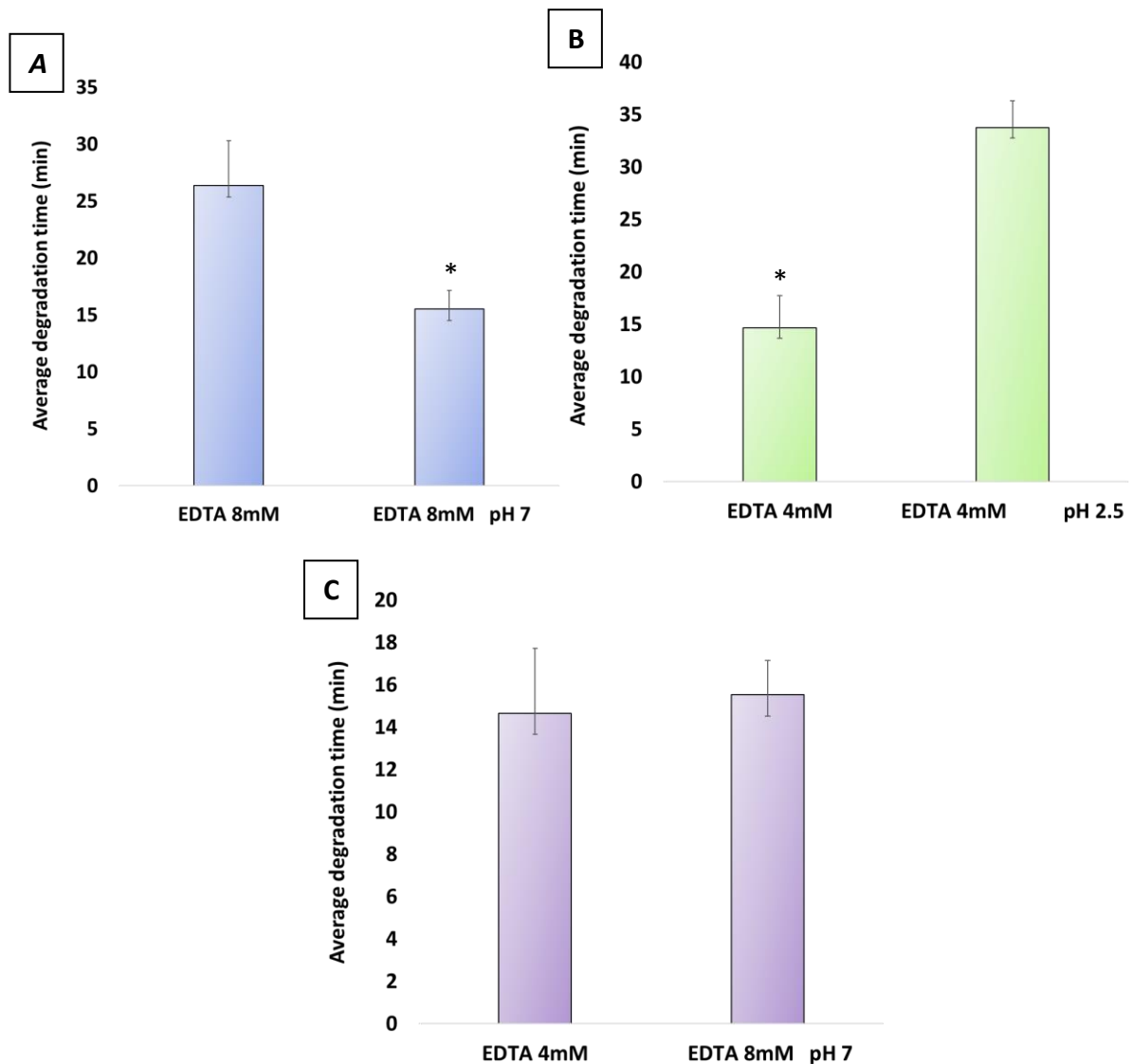


Figure 6.11 Effect of pH adjustments for 4 mM and 8 mM EDTA solutions on the average alginate droplet degradation times.

(A) Sodium hydroxide (NaOH) was added to an 8mM EDTA solution to achieve a neutral pH. Average degradation times were compared between pH 5 and pH 7 8 mM EDTA. (B) Hydrochloric acid (HCl) was added to a 4 mM EDTA solution to reduce the pH to 2.5. Average degradation times were compared between pH 6.5 and pH 2.5 of a 4 mM EDTA solution. (C) Average degradation times were compared between 4 mM EDTA and neutral pH 8 mM EDTA. Data are represented as mean \pm SD. Independent samples t-test. ($p < 0.05$, *). ($n = 3$). (Produced by Ameer Alshukri).

6.4.3 Investigating the effect of the dissolved bio-material solution on keratinocyte viability

Achieving the balance between alginate degradation times and keratinocyte viability is a crucial step in the post-bio-printing process. Four solutions were selected from the previous results: 2.5- & 4-mM EDTA and 10- & 50-mM sodium citrate. The previously dissolved cell-free alginate-chelator solutions were extracted and incubated with cultured 2D monolayers of HaCaT cells for 0, 30 minutes, 2 hours, or 24 hours. This specific mixture was used to replicate the environment keratinocytes would be exposed to when bio-printing and degrading alginate scaffolds. Indeed, 3D bio-printed encapsulated keratinocytes will be subjected to a solution of calcium chelator/medium to degrade alginate, within an environment also containing excess mineral oil and acetic acid.

HaCaT cells were therefore exposed to the dissolved alginate-calcium chelator solutions for different times then treated with 20 μ L of the CellTiter-Blue[®] reagent for 2.5 hours to determine cell viability quantification. The control condition contained HaCaT cells and DMEM only resulting in significantly less fluorescence reading compared to the “Zero” condition which contained HaCaT cells + dissolved alginate-calcium chelator solutions incubated directly with the CellTiter-Blue[®] reagent. This demonstrates that the dissolved alginate-calcium chelator solution potentially increases fluorescence reading alone. Hence, it was only possible to directly compare HaCaT cell viabilities within the same treatment group. For example, the 24-hour exposure time of HaCaT cells to the dissolved alginate-2.5 mM EDTA solution can only be compared to 2 hours, 30 minutes, and Zero times of that same solution. Results demonstrated a decrease in cell viability with longer exposure times to the dissolved solutions (**Figure 6.12**). Although no statistical significance was observed, a general trend in cell viability decrease is clear. This may imply potential detrimental effects when exposed to dissolved alginate-calcium chelator solutions above 24 hours. However, previous preliminary results in this chapter demonstrated rapid degradation of single printed lines that did not exceed 20 minutes for all four tested calcium chelator solutions, meaning that cell viability will be minimally impacted during alginate dissolution.

● CHAPTER 6 ●

To potentially minimise prolonged exposure of keratinocytes to calcium chelators whilst ensuring rapid degradation, 2.5 mM EDTA and 50 mM sodium citrate were selected for the following experiments. It was decided to remove 4 mM EDTA and 10 mM sodium citrate for several reasons: (1) a non-significant average degradation time and cell viability between 2.5 and 4 mM EDTA, (2) (2) a significantly faster average degradation time of 50 mM sodium citrate compared to 10 mM, (3) the favourable documented effect of 50 mM sodium citrate on alginate degradation and cell viability in the literature (Wu et al. 2016; Freeman and Kelly 2017), and (4) the potential detrimental effects of EDTA on dermal components and cells such as fibroblasts and collagen type I (Wong et al. 2019).

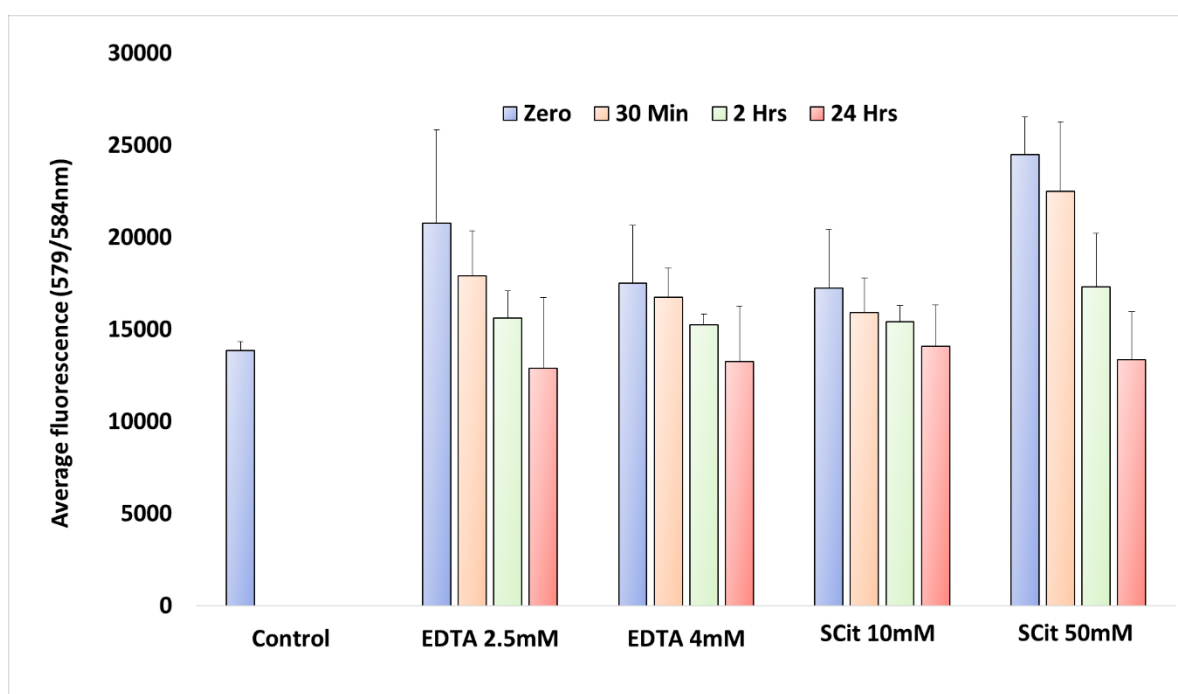


Figure 6.12 Effect of dissolved alginate-calcium chelator solutions (bio-material) on keratinocyte viability over time.

HaCaT cells were incubated for 0, 30 minutes, 2, and 24 hours in a dissolved alginate-calcium chelator solution collected from previously dissolved alginate droplets. The control condition contains HaCaT cells and DMEM medium only. The "Zero" condition contained HaCaT cells that have been exposed to the dissolved alginate/calcium chelator solution and incubated with the CellTiter-Blue® at the same time. Data are represented as mean \pm SD. Independent Samples t-test. (n=3) (Produced by Ameer Alshukri).

6.4.4 Evaluating the degradation rates of large 3D bio-printed structures using calcium chelators

It is anticipated that large complex cell-laden 3D constructs will be bio-printed in the near future in the aim to develop 3D human skin models. Therefore, it is important to ensure alginate dissolution of larger multi-layered structures which are expected to dissolve at lower rates in contrast to simple 2D constructs. For this, a 2-layered concentric circle of 14 mm diameter containing cell-free alginate droplets was bio-printed into a Millicell® hanging insert. The construct was then completely submerged in a calcium chelating solution (4 mM EDTA and 50 mM sodium citrate) prepared Keratinocyte Basal Medium (KBM) hTERT/Ker-CT media. Hanging inserts were used to replicate the recipient in which keratinocytes would be 3D bio-printed and facilitates the transport of the bio-printed structure from one well to the other.

Incubation of bio-printed structure in 2.5 mM EDTA for 1 hour resulted in incomplete degradation of alginate droplets as evidenced by time lapse images (**Figure 6.13**). Indeed, droplets generally retained their structural integrity before and after manual agitation of the well. However, a complete structure degradation was observed when incubating with 50 mM sodium citrate (**Figure 6.13**). Alginate degradation is evidenced by the collapse or disintegration of the structure as opposed to the integral structure, as indicated with the black arrows (**Figure 6.13**). Manual agitation of the well was necessary in order to visualize whether the structure was fully degraded. Although complete degradation was observed at 1 hour, it is possible that this occurs earlier. This was repeated with a 3-layered concentric circle bio-printed structure of 14 mm diameter, whereby full degradation was observed after 30 minutes, confirming earlier degradation (**Figure 6.14**). Furthermore, time lapse images revealed an outside-to-inside dissolution motion, indicating controlled degradation of larger structures.

In line with literature findings, 50 mM sodium citrate demonstrated a more suitable solution for alginate degradation times and cell viability. However, finding the balance between scaffold degradation times, required time for keratinocyte adherence, precise cell location deposition and high cell viability are still under investigation. So far, alginate scaffold

● CHAPTER 6 ●

degradation is controllable, and the results presented in this chapter demonstrate the necessary time and calcium chelator concentrations necessary to degrade simple and complex structures. These results are informative and are further exploitable for future optimisation of the system.

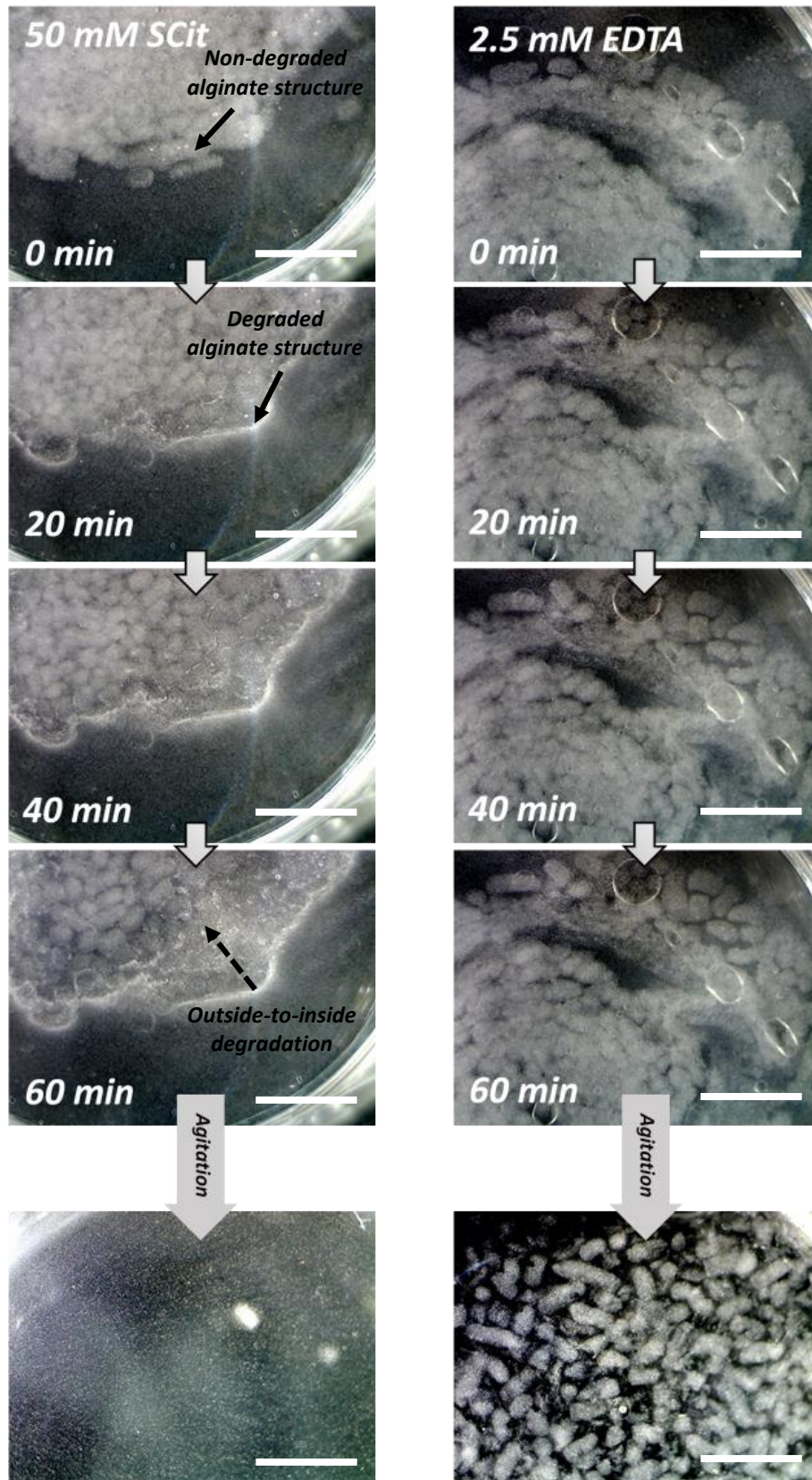


Figure 6.13 Time lapse images showing the degradation of large 3D bio-printed alginate structures using 2.5 mM EDTA and 50 mM sodium citrate solutions.

A 2-layered concentric circle pattern measuring 14 mm in diameter was bio-printed in Millicell® hanging inserts, washed then submerged in calcium chelating solutions for 1 hour. The hanging insert was then agitated to visualise extent of degradation. Scale bar = 10 mm.

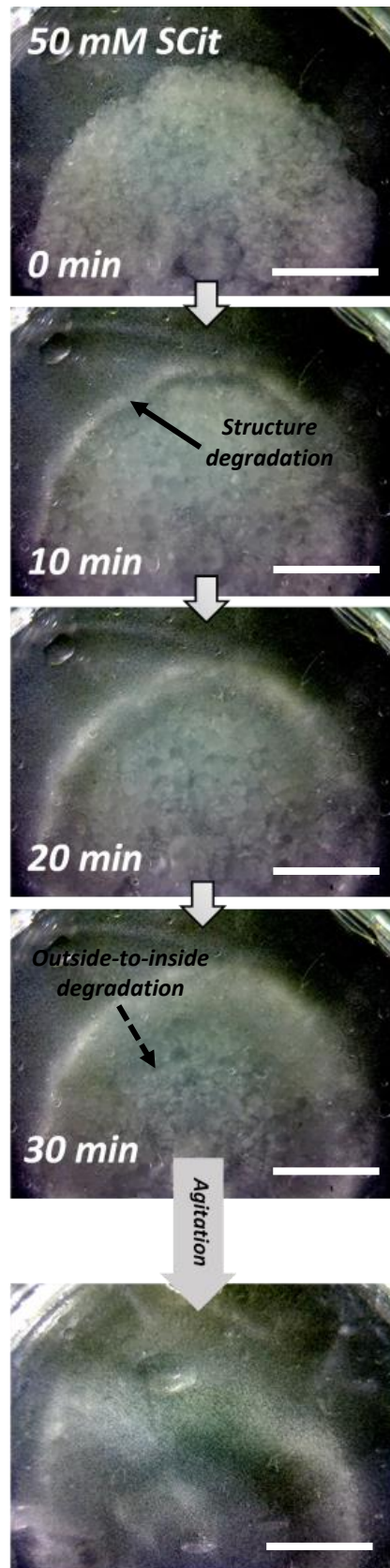


Figure 6.14 Time lapse images showing the degradation of a large 3D bio-printed alginate structure using 50 mM sodium citrate. A 3-layered concentric circle measuring 14 mm in diameter was bio-printed and dissolved in a Millicell® hanging insert in 30 minutes. Scale bar = 10 mm.

6.5 Discussion

The 3D bio-printing of a multi-layered, multi-bio-ink patterned structure, containing live keratinocytes, with high spatial deposition precision at the micrometre scale and high reproducibility has been demonstrated in this chapter. Furthermore, alginate degradation rate was explored on various bio-printed shapes using a range of concentrations from two commonly used calcium chelator agents. Finally, the effect of the degraded solution containing dissolved alginate-calcium chelator, mimicking the 3D bio-printed environment, was tested on keratinocyte biocompatibility.

In anticipation of 3D bio-printing a human skin model, it was important to validate the LEGO® 3D bio-printer's patterning resolution on both the macro- and microscale. Bio-printing multi-layered keratinocytes labelled with different CellMask™ colours was intended to demonstrate high-resolution patterning of two different cell populations, akin to incorporating fibroblasts and keratinocytes, for example, in bio-printed skin models (Lee et al. 2014; Min et al. 2017). A similar study conducted by Graham et al., demonstrated the bio-printing of various patterned structures containing two cell populations (Graham et al. 2017). Another example is shown in Ma et al.'s study who used a digital light processing (DLP) bio-printer for the patterning of human pluripotent stem cells and supporting cells in hexagonal shapes resembling liver lobule structures (Ma et al. 2016). So far, only a tiered layered square lattice containing live cells was produced in this project. However, in the previous chapter, the LEGO® bio-printer's ability to pattern a variety of shapes was demonstrated, promising the patterning of more shapes with the potential of incorporating several cell populations.

A major challenge of bio-printing a large structure was finding an imaging platform capable of imaging a full extract without disrupting the structure's organisation. Ideally, the imaging platform would provide a full optical sectioning (z-stacks) of the structure and can span the extremities. Whilst light-sheet microscopy was capable of providing such possibilities, it was not intended for large biopsy extracts (Reynaud et al. 2008; Power and Huisken 2017). Indeed, the provided glass capillaries can hardly accommodate samples that exceed their width. Furthermore, extracting a full section of the bio-printed structure proved

very difficult with the light-sheet glass capillaries provided, often resulting with significant distortion of the bio-print. Therefore, a device capable of both extracting a bio-printed section without distortion and inserting it into the light-sheet chamber for imaging was designed (**Section 6.3.1.3, Figure 6.1**). The FEP tube-syringe device proved more efficient than the glass capillary by maintaining the overall structure of the bio-print. However, a certain level of distortion was still visible, as shown in the stitched result in Figure 6.3 D. This may be caused by the effect of the extracting device on the structure, whereby the action of withdrawal into the FEP tube may have caused minor shifting of the droplets. Indeed, layer thicknesses do not entirely represent the real dimensions of the bio-printed design. This is evidenced by a significantly smaller blank layer thickness compared to the green and red layers and some areas showing no droplets at all. This can also be caused by the fact that blank droplets may be more easily distorted compared to cell-laden droplets. Furthermore, some green and red stained cells were found in the wrong layers at closer analysis, comparable to the macroscopic images taken of the tiered structure found in **Chapter 5 (Section 5.4.3)**. Despite these challenges, the light-sheet microscopy provided an efficient tool in imaging a large bio-printed construct with a high degree of resolution. The optical sectioning of the structures full depth revealed high droplet-droplet and cell-cell proximity. This can be highly advantageous, as studies have revealed that spheroids placed at close proximity can fuse to generate self-assembled larger tissues (Mironov et al. 2009). Furthermore, achieving resolutions at the “cellular” level can potentially facilitated cell-cell communications and recapitulate complex biological functions (Sun et al. 2017; Chung et al. 2018). To this date, no other study has taken high-resolution images of large 3D bio-printed extracts (Moukachar et al., Corrections in progress for submission to *Advanced Materials Technologies*).

The majority of 3D bio-printing studies resort to scaffold-based bio-ink materials that closely mimic the natural microenvironment and allow to promote cell adhesion, proliferation, and differentiation (Pati et al. 2014; Freeman and Kelly 2017; Hospodiuk et al. 2017; Kim et al. 2019). For example, the development of skin tissue using 3D bio-printing commonly requires the presence of collagen type I that simultaneously provides structural properties and promotes keratinocyte and fibroblast adhesion, proliferation and differentiation (Lee et al. 2009; Lee et al. 2014; Baltazar et al. 2020). Lee et al. fabricated a skin tissue through a layer-by-layer bio-printing of collagen droplets followed by fibroblast-

laden and keratinocyte—laden droplets, with rapid gelation between each layer (Lee et al. 2014). Thus, collagen type I provides a natural microenvironment for keratinocytes and fibroblasts, promoting cell proliferation and tissue maturation *in vitro* (Sugihara et al. 1991). In this study, alginate hydrogel was used solely as a structural carrier which provides no biological anchors for keratinocyte adhesion. Therefore, cell-encapsulation in an inert environment will undoubtedly lead to low cell viability and limited proliferation (Derby 2008; Pati et al. 2014). To circumvent this, keratinocyte droplets would be bio-printed on a collagen type I coated hanging insert, that would promote cell adhesion after alginate degradation. At the same time, alginate would be degraded in a controlled manner post-bio-printing, to allow cell liberation. Wu et al. conducted a similar strategy by bio-printing human corneal epithelial cells in a collagen/gelatine/alginate hydrogel. Alginate was then slowly degraded to allow cell proliferation and high cell viability (Wu et al. 2016). Alternatively, studies have also shown that alginate chains can be functionalised with arginine-glycine-aspartic acid (RGD) peptides which allow cells to adhere via integrin binding and subsequently proliferate (Yu et al. 2010; Utech et al. 2015). Hence, each droplet can act as individual units of growth in a 3D microenvironment.

The choice of using sodium citrate and EDTA as calcium chelator agents stems from their use to degrade alginate in previous studies (**Table 6.1**) (Bonaventure et al. 1994; Shoichet et al. 1996; Rowley et al. 1999; Masuda et al. 2003; Schloßmacher et al. 2013; Wu et al. 2016). Average degradation time of single droplets using 50 mM sodium citrate was observed at roughly 5 minutes, which is six times faster than the study reported by Schloßmacher et al. using 55 mM sodium citrate on 1 mm alginate beads (Schloßmacher et al. 2013). Surprisingly, Schloßmacher et al. used an alginate solution of 1.2%, which is lower than the 2% used in this study. This discrepancy can be explained by the presence of culture medium (DMEM) with the sodium citrate in this study as opposed to using PBS. According to a review by Ching et al., pH fluctuations and ionic concentrations can significantly impact alginate swelling (Ching et al. 2017). Increased ionic concentrations of Mg^{2+} can accelerate swelling, and subsequently dissociation, which is found in the DMEM formulation. In another study, Masuda et al. completely degraded alginate beads from a 1.2% low viscosity alginate solution in 55 mM sodium citrate + 0.15 M NaCl solution in 20 minutes (Masuda et al. 2003). Similarly, this was four times slower than the observed rate in this study, possibly confirming

the role of DMEM in accelerating alginate degradation. Surprisingly, a 100 mM sodium citrate solution did not significantly accelerate the degradation rate compared to 50 mM. This may imply that the amount of Ca^{2+} present in the structure is the limiting factor and not the amount of available citrate to sequester Ca^{2+} ions. Furthermore, the diffusion rate of the chelating solution, hence the citrate ions, through the alginate pores can also limit accessibility of citrate ions. Indeed, the control test whereby alginate droplets were incubated with DMEM, demonstrated that it required 1 hour for the DMEM to diffuse into the droplets, as evidenced by the colour change of the droplets (**Figure 6.6**).

According to Wu et al. alginate degradation rate is a controllable process by varying sodium citrate concentrations, as demonstrated similarly in this study (Wu et al. 2016). However, degradation rates were significantly different between studies. Despite degrading bio-printed structures with similar dimensions (10 mm diameter circle of 1 mm height vs. 30 x 30 mm and 0.8 mm height), degradation rates were significantly faster in this study. One explanation may be the difference in the bio-printed hydrogel composition. The presence of alginate, gelatine, and collagen together may limit sodium citrate diffusion rates as opposed to having alginate only. At a sodium citrate to alginate mol/mol ratio of 66.7%, full degradation was reached after roughly 10 days, whereas in this study, full degradation requires 5 minutes only when using a 55% ratio (50 mM sodium citrate to 2% alginate). This may be further confirmed by other studies that required only 20 – 30 minutes to degrade individual alginate droplets with 50 – 55 mM sodium citrate (Shoichet et al. 1996; Masuda et al. 2003; Schloßmacher et al. 2013). However, none of these studies explored the rate of degradation precisely, and only intended to fully dissolve the alginate without time course experiments. Hence, alginate may have degraded earlier than the reported times. In 2013, Visser et al. bio-printed tissue constructs comprised of synthetic (Polyvinyl alcohol (PVA) & Polycaprolactone (PCL)) and natural polymers (alginate & gelatine-methacryloyl (gelMA)) whereby the 10% alginate was completely degraded with 130 mM sodium citrate within 1 hour (Visser et al. 2013). Another justification of these disparities can be associated to differences in alginate properties, characterised by different molecular weights (MW) and different guluronic and mannuronic acid residues ratio (G/M ratio) (Kong et al. 2004; Freeman and Kelly 2017). Freeman et al. demonstrated that the degradation of high MW alginate was significantly slower than low MW alginate by using a combination of sodium citrate and EDTA

● CHAPTER 6 ●

(50 mM and 20 mM, respectively). Furthermore, alginate crosslinked with calcium carbonate degraded significantly slower than those crosslinked with calcium chloride or calcium sulphate (Freeman and Kelly 2017). Indeed, the relative stiffness of the alginate can be tuned by varying the ionic crosslinking to alginate ratio, which may be differently impacted by the chelating agents. From these studies, it is clear that there are multiple variables that influence the degradation rate of alginate. Overall, the use of sodium citrate demonstrated the possibility for controllable alginate degradation rates, which are useful to optimise cell liberation and subsequent adhesion. Furthermore, time-lapse imaging revealed a progressive wave-like degradation, which may be due to heterogenous or unequal alginate gelling from droplet to droplet.

The rationale for selecting EDTA concentrations ranging from 1 to 8 mM stem from preliminary results, whereby the short-term effect of EDTA on HaCaT adhesion was explored. Briefly, HaCaT cells were detached with trypsin and then treated in an EDTA-DMEM (Ca^{2+} -free) solution for 15 minutes at concentrations of 0.9, 5, 50, 100, and 250 mM. A control consisted of an incubation with trypsin-EDTA (0.9 mM) for 15 minutes, as would normally occur for cell detachment and sub-culturing. Cells were then centrifuged and washed twice with PBS before seeding back in a 6 well plate. Cells were given 24 hours to adhere before analysis. Results demonstrated that incubation with EDTA >5 mM could potentially prevent cell adhesion (**Appendix A-15**). At ≥ 50 mM EDTA, cell attachment was scarce, and cells were seen floating. Despite reseeding the cells with low Ca^{2+} -containing DMEM, that was not enough to re-establish cell adhesion. However, increasing the Ca^{2+} in the medium could theoretically circumvent this. These preliminary results demonstrated the importance of Ca^{2+} -mediated cell adhesion of HaCaT cells, and keratinocytes (Bikle et al. 2012; Elsholz et al. 2014).

Surprisingly, other studies reported the use of considerably higher EDTA concentrations to degrade alginate. For example, Chueh et al. dissolved patterned alginate hydrogels using 100 mM EDTA whilst Freeman et al. used a combination of 20 mM EDTA and 50 mM sodium citrate (Chueh et al. 2010; Freeman and Kelly 2017). Again, concentrations may vary depending on the study's aim, composition of the hydrogel structure, crosslinking properties used, alginate MW, etc. Overall, EDTA showed slower degradation times compared to sodium citrate in this study. The reduction in pH caused by the increase in EDTA salts has

been observed in the colour shift of the phenyl red colour in the DMEM (**Appendix A-14**). The low pH measured in the 8 mM EDTA solution resulted in slower degradation times, which may be explained by several reasons: (1) keeping alginate droplets in low pH levels can potentially resume liberation of Ca^{2+} ions from excess CaCO_3 present from the bio-ink. Therefore, alginate polymer chain crosslinking would be continuously gelling and increasing in matrix strengthening; (2) EDTA salts not only reduce pH of the solution but are poorly soluble in low pH levels. Hence, less EDTA is dissolved and subsequently less EDTA molecules available for Ca^{2+} chelation; (3) Studies have reported that alginate degradation is pH sensitive and low pH suppresses carboxyl group dissociation, in turn decreasing alginate degradation rate (Wu et al. 2010; Ching et al. 2017). Average degradation rates of alginate in this study using sodium citrate and EDTA are significantly faster than those reported in the literature (Masuda et al. 2003; Visser et al. 2013; Wu et al. 2016; Freeman and Kelly 2017). However, the complex interplay of multiple variables affecting degradation rates makes it difficult to directly compare results. Despite the differences, this study along with previous reports demonstrate the possibility to control alginate degradation rates by using a combination of chelating agents and varying concentrations and solution composition. A table recapitulating the different approaches previously reported for alginate degradation using sodium citrate and EDTA (**Table 6.1**).

Dissolved alginate-calcium chelator solutions were meant to mimic a similar environment to cell-laden bio-printed droplets undergoing alginate degradation. A general trend demonstrating decreased viability with longer exposure times to dissolved alginate-EDTA/sodium citrate solutions was seen (**Figure 6.12**). However, no significant impact was observed on cell viability, as reported in previous studies (Schloßmacher et al. 2013; Wu et al. 2016; Freeman and Kelly 2017). Interestingly, Wu et al. found an increase in cell proliferation when bio-printed structures were incubated in a sodium citrate-medium solution up to 8 days, measured by an increased presence of markers of proliferation. This discrepancy can be associated to the presence of collagen in their bio-printed structure, which is known to promote cell adhesion and proliferation, as opposed to seeded cells in this study. Additionally, different cell types may show differences in sensitivity to the microenvironment, hence Wu et al. used human corneal epithelial cells whilst the HaCaT keratinocyte cell line was used in this study. It is speculated that a controlled degradation of alginate whilst simultaneously

● CHAPTER 6 ●

allowing cells to adhere in a highly nutritious environment can promote important cellular functions.

Calcium chelator	Alginate structure, properties, and concentrations	Concentration	Incubation times	Impact on cell viability (when applicable)	Study
Sodium citrate	Gelatine-Alginate-Collagen (3D bio-printed constructs) (1%)	55 mM originally (Concentrations varied by altering the mole ratio of sodium citrate/alginate)	Up to 20 days at a mole ratio of 1:4 (SCit:alginate) and 50 minutes at a 10:1 ratio (SCit:alginate)	Increase in cell proliferation with 66.7% SCit	(Wu et al. 2016)
	Alginate beads (1.2% - low viscosity)	55 mM	20 minutes	No negative impact	(Masuda et al. 2003)
	Alginate disks (1% and 2%)	77.5 mM	20 – 30 minutes	No negative impact	(Rowley et al. 1999)
	Alginate/silica beads (1.2%)	55 mM	30 minutes	No negative impact	(Schloßmacher et al. 2013)
	Alginate/Agarose beads (2%)	50 mM	24 hours	No negative impact	(Shoichet et al. 1996)
	Alginate/Agarose beads (2%)	130 mM	1 hour	No negative impact	(Visser et al. 2013).
	Alginate/GelMA-gellan/PCL/PVA (3D bio-printed structure) (10%)				No negative impact
EDTA	Alginate beads	50 mM	-	No negative impact	(Bonaventure et al. 1994).
	Patterned alginate hydrogels in microchannels (3%)	100 mM	-	No cells involved	(Chueh et al. 2010).

Table 6.1 Reports of alginate degradation approaches using sodium citrate and EDTA. The table describes the alginate structures, properties, and concentrations used in each study; the concentrations of calcium chelators used; the incubation times of alginate in the calcium chelator solutions, and the impact on cell viability post-degradation (if cells were involved in the study).

● CHAPTER 6 ●

Schloßmacher and Masuda et al. reported no impact of alginate degradation with 55 mM sodium citrate on cell viability after 1 hour, as found in this study (Masuda et al. 2003; Schloßmacher et al. 2013). Upcoming work requires exploring viability and proliferation of encapsulated keratinocytes with and without alginate degradation. The viability test was conducted only once in this study due to time limitations, requiring more repeats to generate more conclusive data. Furthermore, a control containing dissolved alginate-calcium chelator solutions only would be necessary to quantify the level of fluorescence induced without cell presence. Finally, exploring the effect of dissolved alginate-EDTA/sodium citrate solutions on hTERT/Ker-CT would be more informative, following previous findings demonstrating its improved phenotype and genotype compared to HaCaT cells (Smits et al. 2017).

Degradation of large structures with 50 mM sodium citrate required roughly 30 minutes for full degradation, whilst only a partial degradation was observed with 2.5 mM EDTA after 60 minutes (**Figure 6.13 & 6.14**). Using 50 mM sodium citrate, this was 5 – 6 times faster than dissolving individual droplets in a 2D line. Interestingly, an outside-to-inside degradation movement was observed, which may be due to steric hindrance and gradual diffusion of calcium chelators into the structure (Chen et al. 2002). This can be an advantage for controlled cell liberation using the defined wave of alginate degradation from the outer structure towards the middle. Preliminary studies made it difficult to verify the extent of degradation, therefore it was necessary to briefly agitate the construct after a specific time. A major difference between the degradation of the 2D printed line and larger 3D constructs was the amount of calcium chelator agent used. The 2D construct was degraded by adding 200 µL vs. completely submerging the 3D construct in 2 – 3 mL of the calcium chelator solutions. This was necessary as bio-printed keratinocyte-laden structures would require full immersion to ensure full degradation of the construct. Whether this method is optimal for skin bio-printing is still debatable, as no previous reports have resorted to this strategy. Wu et al. bio-printed a similar sized structure which was immersed in a sodium citrate and medium solution (66.7% sodium citrate to alginate mole ratio) and degraded in 10 days with high cell viability and proliferation (Wu et al. 2016).

Attempting a similar strategy to Wu et al., whereby bio-printed keratinocytes are slowly liberated onto a collagen coated hanging insert with the optimal medium formulation for cell

growth and survival may be an alternative to fast degradation. Indeed, degradation of alginate in 30 minutes using 50 mM sodium citrate may be too fast for keratinocyte adhesion and may also disrupt cell spatial positioning. Alternatively, alginate may be functionalised with the RGD peptide to allow cell adhesion within the droplets, as mentioned previously (Utech et al. 2015). Keratinocytes could potentially form spheroids which can fuse into tissue structures, whilst simultaneously treating the bio-printed construct with sodium citrate-containing medium to control alginate degradation. This resembles a study conducted by Pourchet et al. in 2017, who generated a bio-printed skin model using a scaffold-free approach. In their study, keratinocytes were bio-printed in a bio-ink mixture consisting of gelatine, alginate, and fibrinogen. Post-printing, gelatine was sacrificed while alginate and fibrinogen resumed crosslinking, providing a structural and cell promoting environment. Indeed, fibrinogen naturally expressed the RGD cell-adhesion peptide, allowing for cell adhesion to the fibrinogen matrix, and subsequently cell-cell interaction, leading to skin maturation (Pourchet et al. 2017). Fibrin, a natural polymer derived from fibrinogen, is a well-established biocompatible scaffold and matrix which has been extensively used to produce tissue engineered skin substitutes (Mazlyzam et al. 2007; Kober et al. 2015; Sánchez-Muñoz et al. 2015; Pourchet et al. 2017; Litvinov et al. 2021).

Fibrin-based bio-ink has been briefly explored in this study, as an alternative to alginate, by two students, Lluan Evans and Gabriela Velasquez. Fibrin polymerisation occurs in the presence of the naturally derived thrombin enzyme which overall provides cells with a gentler environment in contrast to reduced pH induced by the acetic acid and high Ca^{2+} concentrations used for alginate crosslinking. Fibrin degradation is easily achieved by treating it with plasminogen and plasmin enzymes, naturally produced in the blood. Interestingly, early studies have reported that during wound healing, basal keratinocytes strongly express plasminogen activators, which are known to catalyse plasmin activity (Szabo et al. 2004). Furthermore, plasmin has been reported to both decrease keratinocyte proliferation and increase migration, playing an important role in epithelial wound healing (Szabo et al. 2004). Vardar et al. recently reported the production of $\sim 150 \mu\text{m}$ sized fibrin-based droplets using a T-junction microfluidic device (Vardar et al. 2018). These findings provide potential strategies that can be exploited in generating fibrin-based bio-ink for skin tissue bio-printing. Incorporating collagen in the current bio-ink provides another route to potentially improving

● CHAPTER 6 ●

structural support as well as providing good biocompatibility (Kim et al. 2011; Yang et al. 2018). Collagen polymerisation can be achieved through various strategies, including chemical, physical, and enzymatic crosslinking, making it possible to incorporate into the microfluidic system (Adamiak and Sionkowska 2020). Kim et al. designed a hybrid alginate-collagen scaffold (core/shell) resulting in high structural stability and providing a dermal substitute *in vivo* (Kim et al. 2011). Despite major advances in natural and synthetic bio-ink development for bio-printing, recent studies have reported the use of decellularized extracellular matrix (dECM) as an optimal source for bio-ink (Kim et al. 2017a). Kim et al. recently developed a highly relevant vascularised and perfusable bio-printed skin model containing an epidermis, dermis, and hypodermis, from skin-derived dECM (Sd-dECM) as a source of bio-ink (Kim et al. 2017b; Kim et al. 2018; Kim et al. 2019). Furthermore, to circumvent the use of commercial transwells and the contraction of collagen during tissue maturation, Kim et al. bio-printed a PCL mesh, on which all skin bio-ink was bio-printed (Kim et al. 2017b; Kim et al. 2019). Extensive studies relating to improved bio-ink formulations and scaffold degradation strategies for skin bio-printing provide a strong foundation to improve on the strategy used in this study.

The next step in this study, was to attempt 3D bio-printing a human skin epidermal model by combining the findings of this study and previously established methodologies in epidermal skin bioengineering (Smits et al. 2017; Roger et al. 2019). Established methodology involved seeding keratinocytes on a dermal equivalent comprising of collagen matrix coated onto the Millicell® hanging transwell insert. In this study, the plan was to coat these hanging inserts with rat collagen type I and bio-print a 2 layered concentric square or circle of alginate droplets encapsulating hTERT/Ker-CT cells onto the coated inserts. Subsequently, the alginate scaffold would dissolve by incubating the hanging insert in a 50 mM SC and KBM solution allowing for keratinocyte adhesion onto the collagen. After incubation in KBM at 37°C and 5% CO₂ for 2 days in the liquid-liquid interface, the insert is lifted to the air-liquid interface with Ca²⁺ supplements to promote epidermal maturation and stratification. Three controls would be prepared in parallel: (1) the first control would contain the same number of cells per well but would be manually seeded without addition of SC, (2) the second control would be similar to control (1) but with addition of 50 mM SC, and (3) the third control would be a native skin section.

● CHAPTER 6 ●

The final experiment that was conducted prior to COVID-19 lockdown regulations, involved an attempt in generating a control skin models through conventional organotypic cell culture, as described in Roger et al.'s study (Roger et al. 2019). However, one attempt was not enough to generate an epidermal model as optimisation of reagents, concentrations and cell numbers were lacking. Microscopic observation did not reveal any tissue maturation, which may be explained by the large pore size of the Millicell® transwell used. Indeed, 3 µm pore size may have resulted in collagen leakage through the pores, leading to non-efficient keratinocyte adhesion, whilst reports suggest a 0.4 µm pore size is more suitable (Sobral et al. 2007).

The results presented in this chapter demonstrated the potential in bio-printing different skin cell populations with high-resolution patterning, using the custom-built LEGO® 3D bio-printer. Light-sheet microscopy revealed high precision in keratinocyte-laden alginate droplet deposition, owing to the previously optimised parameters of the bio-printing platform. Alginate degradation using sodium citrate and EDTA resulted in relatively fast degradation rates for both 2D and 3D bio-printed constructs, in comparison to previous studies. Additionally, the results demonstrate that alginate degradation can be controlled, despite the interplay of multiple variables affecting alginate gelling and degradation. This provided insight on potential strategies for alginate degradation approaches in the future, and subsequently approaches that would enhance cell growth, adhesion, proliferation, and tissue maturation.

Chapter 7 General discussion

7.1 General Commentary

In this thesis, a low-cost, bespoke, and versatile 3D bio-printer prototype has been built by coupling a LEGO® programmable x/y/z stage with a t-junction microfluidic device. The LEGO® stage movements were programmed to move in unison with the microfluidic droplet production frequency to fabricate droplet patterns in 2D and 3D. The LEGO® 3D bio-printer was built and evaluated for the purpose of bio-printing 3D human skin models.

The second chapter explored the optimal calcium levels in the culture medium required to establish four phenotypically differentiated HaCaT cell populations that mimic the four native epidermal layers. This was initially intended for three reasons: Firstly, to gain a better understanding of the role calcium plays in keratinocyte differentiation; secondly, to provide preliminary comparative results of the expression of specific biomarkers of differentiation and proliferation in 2D vs. native skin vs. 3D bio-printed model; finally, to attempt bio-printing the four cell populations in a layer-by-layer fashion from the least differentiated at the bottom (stratum basale), to the most differentiated on top (stratum corneum) with the possibility that the model would mature quicker. Whilst the first two objectives remained in the scope of the project, the final reason was abandoned. This was because a more suitable keratinocyte cell line, hTERT/Ker-CT was identified. Additionally, a higher priority was to dedicate experimental time to optimise the 3D bio-printer prototype and its ability to encapsulate live keratinocytes and efficiently pattern 2D and 3D structures with high reproducibility. However, the work conducted in **Chapter 2** offered valuable experimental tools in molecular biology, including western blot and immunohistochemistry, to study the expression of several important epidermal biomarkers which will be helpful to replicate when evaluating the microarchitecture and structural relevance of the 3D bio-printed skin model in the near future. **Chapter 2** equally discusses the importance of replicating the similar Ca²⁺ gradient found *in vivo* when culturing keratinocytes *in vitro*. Whilst reconstructing 3D human epidermal models through the culturing of keratinocytes at the ALI in a fixed Ca²⁺ concentration environment is sufficient in replicating the minimal microarchitecture of the epidermis, maintaining the different layers in physiological levels of Ca²⁺ is essential in replicating the function of the tissue. This is a challenging step that has not yet been reported,

however, the development of microfluidic devices that can selectively monitor and transport ions through specific compartments of a tissue engineered model holds promise in increasing the model's complexity (Huang et al. 2014).

The versatility and flexibility in the methodologies, strategies, and technologies that can be used to fabricate tissue models represents a major strength in the area of tissue engineering. 3D bio-printing technology is still in its infancy and still requires improvements in resolution, fabricating vascularisation, perfusion, innervation, microstructural and functional recapitulation (Ng et al. 2019). Microfluidics have also provided a valuable platform in producing cell-encapsulated culturing units for 3D cell culture (Huang et al. 2017). Indeed, in **Chapter 3**, a bio-ink was developed which allowed for the encapsulation of live keratinocytes within alginate droplets achieved using droplet-based microfluidics, and resulted in high short-term cell viability, homogeneous cell dispersion, and control over cell density per droplet. This was achieved using a t-junction microfluidic device. Another microfluidic technology, known as organ-on-a-chip device, have also made great advances in reconstructing tissue models, namely liver, lung, kidney, heart, intestine, and skin (Wu et al. 2020). Organ-on-a-chip technology entails controlling and manipulating fluids carrying cells, biomaterials, bioactive molecules, and nutrients in a perfused microscale environment, forming biological functional units. Microfluidic skin-on-a-chip models have been described as the best models that recapitulate physiology and functionality (Klicks et al. 2017). This is mostly due to the continuous fluid flow of medium mimicking the vascular system and fluidic shear stress, providing a stable support of oxygen and nutrients, which in turn promotes cell viability and proliferation for extended periods of time compared to static cultures (O'Neill et al. 2008; Lee et al. 2017b). One of the major advantages of microfluidics is the ability to customise chips and devices through extrusion-based 3D printing or soft lithography, allowing the production of unique fluidic patterns and geometries suited for specific needs of individual experiments (Morgan et al. 2016; Ortseifen et al. 2020). Dr Oliver Castell's lab specialises in the 3D fabrication of microfluidic devices using 3D printing, which presents a great opportunity if integrated in this study. An example of this is shown in **Appendix A-13**, whereby Dr Jin Li 3D printed a microfluidic device capable of fitting in LEGO® bricks, demonstrating the flexibility of fabricating user-definable microfluidic devices. However, the main limitation of microfluidic techniques is the difficulty in scaling up the tissue models to

more relevant sizes (Ma et al. 2018). However, scaling up of tissue-like structures has been demonstrated in this project by combining microfluidics and programmable stage movements, resulting in large cell-laden bio-printed structures, as shown in **Chapter 6, Figure 6.3**, hence overcoming the aforementioned limitation. In another study, Schimek et al. combined the methodology of conventional organotypic skin tissue engineering with a microfluidic device, generating macroscale, well-differentiated, full-thickness skin models for pharmacological testing (Schimek et al. 2018). This was achieved by growing full-thickness skin models in 96-well inserts, which were subsequently transferred onto a microfluidic perfused chip for 24 days. The ability to fabricate custom-designed microfluidic chips that can accommodate several fluidic inputs for different bio-inks has recently been recognised as a cheap alternative to conventional 3D bio-printing nozzles (Richard et al. 2020). Indeed, the incorporation of microfluidics onto a cartesian x/y/z stage for multi-material/multi-cellular fabrication has been recently achieved for bone regeneration, vasculature, tumour, and muscle tissues (Richard et al. 2020). These studies demonstrate the importance of combining technologies and disciplines to overcome known limitations of skin and tissue *in vitro* modelling. The ability to deposit cells in precise locations using the LEGO® bio-printer could open the possibilities in designing a system that incorporates a permeable “vasculature” which can be bio-printed on, in future iterations. The combination of technologies is portrayed in this thesis through its multi-disciplinary nature by combining droplet-based microfluidics and a LEGO® programmable 3D cartesian stage for the fabrication of 3D skin models.

Until 2009, great effort was placed into standardising methodologies for healthy and diseased reconstructed organotypic skin models (MacNeil 2007). These models still met limitations, as they remained oversimplified compared to the native skin. The commercialisation of 3D bio-printers have allowed the fabrication of increasingly relevant 3D skin models, owing to the automated deposition of cells populations into spatially controlled 3D patterns (Tarassoli et al. 2018). In parallel, many developments in printable bio-inks to optimise the functionality of the bio-printed constructs generated were ongoing (Hospodiuk et al. 2017). As a result of such advances, notable efforts in bio-printing skin equivalents that replicate the multi-layered, multi-cellular microarchitecture of the skin were relatively successful. This is notably seen in the recent reports by Baltazar et al. and Kim et al., who managed to fabricate perfusable, vascularised, full-thickness skin models with high structural

● CHAPTER 7 ●

recapitulation of the native skin (Kim et al. 2019; Baltazar et al. 2020). A main drawback of these studies is the limited accessibility, high cost, and high complexity of their bio-printing platforms. The lack of democratised bio-printing platforms can significantly hinder the scientific advances in a number of budget-limited laboratories (Reid et al. 2016). Furthermore, because 3D bio-printing is growing as a valuable tool for 3D tissue engineering (TE), it is important to find strategies that can render this technology accessible on both the hardware and software front. This has been recently recognised by several research groups, who overcame these limitations by adapting off-the-shelf low-cost 3D printers into 3D bio-printers (Seemann et al. 2012; Reid et al. 2016; Kahl et al. 2019; Diederich et al. 2020; Ioannidis et al. 2020). This is commonly achieved by integrating commercial 3D bio-printed nozzles, building one, or incorporating syringes with an automatic extruder piston. Whilst such platforms showed promising bio-printed structures with reasonable to high resolution, adapting a 3D printer into a 3D bio-printer still necessitates engineering and programming expertise. Many biological researchers can be reluctant to build and develop novel technologies. Additionally, it would require specific coding and programming skills to accommodate cell bio-printing using a 3D printer. Hence, the driver of this thesis resides in the concept of democratising a 3D bio-printing platform that can also be simultaneously a tool for tissue fabrication and an engagement tool for novice engineers and programmers.

In this PhD, a low-cost, modular, and flexible 3D bio-printer prototype was built and characterised, although limited time prevented full exemplification of the technology by creation of a multi-layered skin like tissue. The aim was to develop an accessible bio-printing platform and so, based on the ideas of Marc-Andre Bazergui and Thomas Madeya (*NEW EV3Dprinter: LEGO MINDSTORMS 3D Printer (3rd Generation)* Accessed on 17/06/2021), a commercially available LEGO® modular construction kit and robotics (MINDSTORMS® EV3) were used as the programmable x/y/z stage. LEGO®-based hardware and software provides a level of accessibility that not only engages researchers and experienced engineers, but also can provide a valuable engaging or educational platform for lay audience, the younger public and novice programmers and engineers (Kim and Jeon 2007). For example, a recent study reported the precise patterning of bacterial biofilm using a custom-built 3D bio-printer prototype, termed “The Biolinker”, constructed from K’NEX modular toy construction systems (Schmieden et al. 2018). Bacteria-laden alginate gels were patterned in discrete layers with

● CHAPTER 7 ●

high survival rates until 9 days. That was the first work that demonstrated the patterning of biofilm with high spatial control using a 3D bio-printer prototype from toy construction systems. To date, this is the only study that has used modular toy kits for the rapid prototyping of soft matter.

Putting together the hardware of such modular toy construction systems, whether K'NEX or LEGO®, is an engaging and educational activity that is relatable to many, and which benefits from inputs by individuals from a range of disciplines. Indeed, during the PhD studies, three LEGO® 3D bio-printing platforms were built by three students, with different educational backgrounds: Katie Harvey (engineering student), Grace McDermott (tissue engineering master's student), and Lluan Evans (pharmacy student), using a step-by-step LEGO® Digital Designer (LDD) guide. The LEGO® bio-printing platform also requires an understanding of software programming. The programming of the LEGO® stage uses a virtual programming language, dedicated initially to controlling LEGO® robotics, which provides easy-to-follow tutorials that are widely available on streaming platforms, such as YouTube and the official LEGO® page. Katie Harvey, Cameron Pool (pharmacy student with some programming experience), and Eva Roke (engineering student) helped provide a library of programmes for 2D and 3D patterned movements (**Chapters 4 & 5**) and provided extensive instructions and tutorials. The fields of computer science programming and engineering are becoming common and invaluable tools that can inform biological research, especially in tissue engineering applications. Promotion and development of these important fields requires accessible and low-cost tools such as the LEGO® 3D bio-printer developed in this study.

As mentioned previously, a current limitation of 3D skin models is their oversimplification in architecture and function (Ng et al. 2018). Whilst the rate of technological advances may be the cause of this limitation, another explanation may be the lack of standardised methodologies in fabricating skin models (Roger et al. 2019). This results from a huge rise in commercialised skin equivalents, discovery of new biomaterials, cell lines, bio-inks, 3D printing platforms, microfluidic development, etc., which together can generate a wide range of possible strategies and methodologies. For example, biomaterials that have been used for skin bio-printing include, alginate, collagen, fibrin, synthetic polymers, chitosan,

gelatine, etc. (Yan et al. 2018). Different cell lines have also been reported using immortalised cell lines or human primary cells, including mouse NIH 3T3 fibroblasts, human primary dermal fibroblasts, HaCaT keratinocytes, NHEK, and human epidermal melanocytes (Michael et al. 2013; Pourchet et al. 2017; Baltazar et al. 2020). Furthermore, culture conditions differ between labs, including static culture, or a vascularised/perfused system, and differing culture times which can also affect the tissue maturation during post-processing (Derr et al. 2019; Baltazar et al. 2020). At the current stage, the majority of reported bio-printed skin models are evaluated for their microanatomical and structural relevance more than their functional relevance (Tarassoli et al. 2018). Despite recapitulating the major architectural features of the native skin, there is still no guarantee that the models will replicate the native skin's function *in vitro*, which may be hindered if methodologies have not been standardised. Therefore, there is still space for improvement in developing 3D skin models. At the current stage of the project, it is difficult to project whether the LEGO® 3D bio-printer prototype can provide a standardised methodology and requires further exploration. Its iterative nature, however, promises continual development of the platform and eventually a bio-printed skin model.

It was anticipated that a 3D skin model, consisting of a stratified and well-differentiated epidermis using keratinocytes and a dermal substrate, would be bio-printed using the custom-built LEGO® 3D bio-printer. Whilst a number of 3D skin bio-printed models have been reported since 2009, the novelty from this study, would lie in achieving this with the modular and low-cost LEGO® bio-printer prototype. To date, only one study has successfully fabricated a skin model using a custom-built extrusion-based bio-printer adapted from a commercial 3D printer (Cubo et al. 2016a). Therefore, the need for accessible platforms for skin bio-printing is important. Another advantage of the LEGO® bio-printer prototype lies in its modular nature, which can be iterated to accommodate more sophisticated mechanisms and LEGO® pieces for multi-bio-ink bio-printing. This promises to generate more relevant skin models, with the ambition to incorporate different skin cell populations, appendages, and fabricate diseased models.

7.2 *Future work and Limitations*

The LEGO® 3D bio-printer is considered the first prototype (V. 1.0); hence this research is at an early stage. Therefore, there are many avenues for development and improvement, which are discussed below.

Cell line selection is an important parameter to optimise. The hTERT/Ker-CT cell line were identified as more appropriate than HaCaT due to their potential to generate a fully mature stratified epidermal model (van Drongelen et al. 2014; Smits et al. 2017). Therefore, while the use of HaCaT cells in chapters 2, 3, and 6 help in proof of principle, this work needs to be revised and repeated using hTERT cells. This includes establishing 2D culture monolayers in the presence of varying concentrations of calcium to assess the levels of phenotypic differentiation. Although hTERT cells were encapsulated and bio-printed as a multi-layered structure in chapter 6 (**Figure 6.3**), showing short-term viability qualitatively, it is important to replicate the work that has been performed on HaCaT cells (**Chapter 3**), whereby cell viability was quantitatively assessed comparing 2D monolayer seeding vs. 3D cell-encapsulated conditions (**Figures 3.15 & 3.18**), with hTERT cells. Finally, the effect of alginate bio-ink degradation on cell viability conducted on HaCaT cells should also be repeated using hTERT cells (**Figure 6.12**). The reason for the discrepancy in the choice of a keratinocyte cell line throughout the thesis chapters, can be explained by the timescale of the different experiments, which in some cases were conducted in parallel. HaCaT cells were used up to the end of Year 2 of the project and these were then substituted for hTERT cells.

Whilst droplet-based microfluidics offers advantages as a bio-ink for 3D bio-printing providing controllable production of discrete alginate droplets for cell encapsulation, current limitations in the microfluidic t-junction device include frequent clogging due to the insoluble CaCO₃, heterogenous droplet sizes, large droplet sizes, and lack of droplet uniformity in shapes or monodispersity. Future work needs to focus on producing smaller droplets, measuring approximately 200 – 250 µm, for efficient nutrient and oxygen delivery to cells. From a technical perspective, imaging droplets that measure approximately 1000 µm was challenging with conventional microscopic platforms and therefore smaller droplets would

● CHAPTER 7 ●

also allow would also be more easily characterised (Kahl et al. 2019). Due to the large sizes of the droplets in this study, bio-printed constructs are difficult to observe as a whole and image under the available microscope platforms. Clogging was a recurrent problem in this study, primarily due to the insoluble CaCO_3 particles that can settle in the microfluidic tubings and t-junction. Furthermore, extended bio-printing times can lead to increased clogging and ultimately can affect droplet production and reproducibility. Clogging may be reduced or avoided by using a soluble calcium source consisting of a calcium-EDTA soluble complex that releases the calcium ion upon pH reduction (Utech et al. 2015). This may provide both controllable gelling and a reduction in clogging. Improved reproducibility in the size of droplets produced by the microfluidics may be achieved by using an alternative device, such as the flow-focusing system, which has been reported to generate better monodispersity in droplets (Hidalgo San Jose et al. 2018). This may also subsequently allow for a more reproducible density of cells per droplet, resulting in a more uniform deposition of cells by the bio-printer.

Short-term viability of encapsulated keratinocytes was assessed both quantitatively and qualitatively in **Chapter 3 and 6**. Promising results demonstrated high keratinocyte viability when monitored in individual droplets and when bio-printed in larger structures. However, it is also important to investigate the long-term viability of bio-printed keratinocytes in simple patterned constructs first. This can be achieved by transfecting cells stably with fluorescent proteins, such as yellow fluorescent protein (YFP) or green fluorescent protein (GFP), to generate stably-expressing cell lines. Hence, long term culture of 3D bio-printed recombinant keratinocyte-encapsulated alginate hydrogels can be monitored via fluorescence intensity. Furthermore, the effect of long-term culture on alginate hydrogel stability and degradation can also be monitored.

Despite generating bio-printed structures through precise patterning of blank and cell-laden droplets, the decoupling of the LEGO® stage and droplet production i.e., control of the syringe pump being independent from the LEGO® stage, is a notable limitation of this study. Whilst it helped to optimise each platform independently and provide proof of principle, it prevented synchronisation between droplet production and stage movement, and therefore had an overall negative effect on construct resolution. As described in **Chapter 5**, a LEGO®

● CHAPTER 7 ●

syringe driver was built and programmed to combat this and was able to extrude the bio-inks at similar flow rates to those used by the commercial syringe driver (**Figure 5.16**). It is also possible to build several multiplexed LEGO® pumps to accommodate more bio-inks for future iterations of the 3D bio-printer (Almada et al. 2019). Interestingly, multiplexers designed for NXT/EV3 motors are also commercially available at a cost of approximately £40. These can receive signals from multiple LEGO® devices and are therefore able to provide control of the system as an integrated platform (mindsensors, *Multiplexer for NXT/EV3 Motors*, Accessed on 18/06/2021). Future work should continue to develop the coupled LEGO® stage and LEGO® syringe driver and should characterise its functionality, as described in **Chapter 5** for the uncoupled system.

The addition of a LEGO® syringe driver and its integration with the LEGO® stage also requires software developments. During this project, the existing MINDSTORM® programming software encountered several crashes due to the high volumes of files. This, coupled with a desire to increase the complexity of the print, has recently stimulated investigation of a more suitable LEGO® compatible programming software called LabVIEW. Indeed, EV3 robotics are also programmable using LabVIEW, which can access higher virtual memory on 64-bit windows operating system. LabVIEW is an engineering software that also uses VPL for hardware configuration and automated analysis systems. It is an open-source software that has been previously used in multidisciplinary research domains, including bioreactor systems control, real-time image processing of microscopic biological samples, development of brain-machine interface (BMI) research, or biomedical data acquisition (Smith et al. 2000; Degenhart et al. 2011; Burdge and Libourel 2014; Dhawale 2014).

Bio-printed constructs showed good resolution overall, assessed through different imaging platforms. However, this study suffers from a lack of quantitative analysis of bio-printed constructs, which would provide more robust data. Imaging platforms allowed to capture the overall bio-printed structures at the macro- and microscale, qualitatively. This would require measuring the bio-printed structures and determine the dimensional errors in percentage, when compared to the intended design selected. This is commonly found in most studies that have custom-built 3D bio-printers and evaluated the printers capabilities (Kahl et al. 2019; Sanz-Garcia et al. 2020). Furthermore, the bio-printing of several single layers in

forms of outlines or grid structures would also be interesting to generate. Hollow shapes can be potentially produced but have not yet been tested in this study. Hollow cylinders are particularly interesting to produce artificial vasculature (Gao et al. 2015; Sasmal et al. 2018). Indeed, fabrication of cylindrical vessel-like structures consisting of cross-linked alginate hydrogel were previously reported by Gao et al., using extrusion-based 3D bio-printing (Gao et al. 2017).

The aim of the final chapter of this thesis was to exemplify proof of principle and to 3D bio-print a human skin epidermal model using a combination of the LEGO® bio-printer and some established methodologies in epidermal skin bioengineering (Roger et al. 2019). The principal was to bio-print a 2 layered concentric square or circle of alginate droplets encapsulating hTERT/Ker-CT cells onto collagen coated hanging transwell inserts, dissolve the alginate component of the bio-ink and to lift the printed structure to the air liquid interface to promote differentiation. However, it was important to firstly explore the rate of alginate degradation and its impact on keratinocyte viability, as demonstrated in **Chapter 6**. Therefore, it would be more prudent to repeat these experiments and explore longer periods for alginate degradation, which studies have shown to improve overall cell functions (Wu et al. 2016). Whilst alginate provides a biocompatible and structurally viable bio-material for bio-printing, incorporating a second bio-material, such as collagen or fibrin, can be used to promote cell adhesion and growth, whilst alginate can be used as a sacrificial hydrogel with controllable degradation. Secondly, COVID-19 related disruptions and limited time reduced the time available for these experiments, and therefore future studies are now needed to optimise the parameters to generate skin models. Resulting tissues produced using the bio-printer would then be sectioned and stained using haematoxylin and eosin (H&E) to evaluate epidermal microanatomy. Furthermore, epidermal differentiation would be evaluated through immunofluorescence to detect known markers of differentiation and proliferation, such as Involucrin, Keratin 5, Keratin 10, or E-cadherin, as explored in chapter 2 of this thesis. Such results would validate the LEGO® 3D bio-printer's ability to produce relevant human skin epidermal models and would encourage further iterative developments of the custom-built 3D bio-printer towards the ambitious target of printing full thickness human skin models, including a dermis, hypodermis, vascular system, sweat glands, and nerves.

● CHAPTER 7 ●

In the eventuality a 3D bio-printed skin model is not achieved in the future, efforts in generating 3D skin models can still be achieved using droplet-based microfluidics. Indeed, cells have been shown to grow and proliferate for extended periods of time under encapsulated conditions, due to the permeability of hydrogels, allowing for efficient diffusion of nutrients across the polymer network (Hidalgo San Jose et al. 2018). Under the right culture conditions, such droplets have the potential to grow into micrometre sized spheroids that can mimic tissue organisation (Lee et al. 2020; Richard et al. 2020). Indeed, a study reported the production of layered skin micro sized tissues by generating monodisperse collagen type I beads encapsulating normal human fibroblasts using a flow-focusing device, in which normal human keratinocytes were seeded (Morimoto et al. 2013). This resulted in the production of layered skin cell beads expressing an outer layer of keratinocytes, a dermal-epidermal junction, and an inner layer of fibroblasts. These beads have been shown to self-assemble into a larger scale tissue that can be manipulated and evaluated through sectioning (Matsunaga et al. 2011). This methodology has the potential of being combined with the current LEGO® 3D bio-printer for uniform patterning of skin cell beads into moulding chambers, which can mature into skin tissue structures *in vitro*. Additionally, the moulding chambers can be 3D printed to contain a perfused system, allowing for enhanced culture conditions and potentially relevant skin 3D models. The 3D printing of perfusable microfluidic chips is achievable and readily accessible in Dr Oliver Castell's lab (Baxani et al. 2016; Morgan et al. 2016).

In conclusion, the studies presented in this thesis demonstrate the build and development of a versatile, bespoke, and flexible 3D bio-printing platform capable of producing individual alginate droplets with encapsulated live cells and bio-printing a variety of 2D/3D structures with good spatial control. This was achieved by building a low-cost LEGO® x/y/z programmable stage combined with a t-junction microfluidic droplet dispensing device, allowing for precise geometrical positioning of live cell-encapsulated discrete alginate droplets. The LEGO® 3D bio-printer is also capable of printing complex multi-layered structures and patterns of live-cells of different identity within the 3D structure with distinct layers, potentially mimicking biological micro and macrostructures. To date, this is the first use of LEGO® in the application for soft matter 3D printing to create a programmable 3D bio-printer.

References

Abd, E. et al. 2016. Skin models for the testing of transdermal drugs. *Clinical Pharmacology: Advances and Applications* Volume 8, pp. 163–176. Available at: <https://www.dovepress.com/skin-models-for-the-testing-of-transdermal-drugs-peer-reviewed-article-CPAA>.

Adamiak, K. and Sionkowska, A. 2020. Current methods of collagen cross-linking: Review. *International Journal of Biological Macromolecules* 161, pp. 550–560. Available at: <https://doi.org/10.1016/j.ijbiomac.2020.06.075>.

Adams, J.C. and Watt, F.M. 1989. Fibronectin inhibits the terminal differentiation of human keratinocytes. *Nature* 340(6231), pp. 307–309. Available at: <http://www.nature.com/articles/340307a0>.

Agarwal, S. et al. 2020. Current Developments in 3D Bioprinting for Tissue and Organ Regeneration—A Review. *Frontiers in Mechanical Engineering* 6(October). doi: 10.3389/fmech.2020.589171.

Akbari, S. and Pirbodaghi, T. 2014. Microfluidic encapsulation of cells in alginate particles via an improved internal gelation approach. *Microfluidics and Nanofluidics* 16(4), pp. 773–777. Available at: <http://link.springer.com/10.1007/s10404-013-1264-z>.

Al-Shamkhani, A. and Duncan, R. 1995. Radioiodination of Alginate via Covalently-Bound Tyrosinamide Allows Monitoring of its Fate In Vivo. *Journal of Bioactive and Compatible Polymers* 10(1), pp. 4–13. Available at: <http://journals.sagepub.com/doi/10.1177/088391159501000102>.

Alam, H. et al. 2011. Novel function of keratins 5 and 14 in proliferation and differentiation of stratified epithelial cells. Goldman, R. D. ed. *Molecular Biology of the Cell* 22(21), pp. 4068–4078. Available at: <https://www.molbiolcell.org/doi/10.1091/mbc.e10-08-0703>.

Alcinesio, A. et al. 2020. Controlled packing and single-droplet resolution of 3D-printed functional synthetic tissues. *Nature Communications* 11(1), pp. 1–13. Available at: <http://dx.doi.org/10.1038/s41467-020-15953-y>.

Aljohani, W. et al. 2018. Bioprinting and its applications in tissue engineering and regenerative medicine. *International Journal of Biological Macromolecules* 107(PartA), pp. 261–275. Available at: <https://doi.org/10.1016/j.ijbiomac.2017.08.171>.

Almada, P. et al. 2019. Automating multimodal microscopy with NanoJ-Fluidics. *Nature Communications* 10(1), p. 1223. Available at: <http://www.nature.com/articles/s41467-019-09231-9>.

● REFERENCES ●

- Alsberg, E. et al. 2003. Regulating Bone Formation via Controlled Scaffold Degradation. *Journal of Dental Research* 82(11), pp. 903–908. Available at: <http://journals.sagepub.com/doi/10.1177/154405910308201111>.
- Amici, E. et al. 2008. Alginate gelation in microfluidic channels. *Food Hydrocolloids* 22(1), pp. 97–104. Available at: <https://linkinghub.elsevier.com/retrieve/pii/S0268005X07000380>.
- Anton, D. et al. 2015. Three-dimensional cell culture: A breakthrough in vivo. *International Journal of Molecular Sciences* 16(3), pp. 5517–5527. doi: 10.3390/ijms16035517.
- Arai, K. et al. 2011. Three-dimensional inkjet biofabrication based on designed images. *Biofabrication* 3(3). doi: 10.1088/1758-5082/3/3/034113.
- Archambault, M. et al. 1995. Keratinocytes and fibroblasts in a human skin equivalent model enhance melanocyte survival and melanin synthesis after ultraviolet irradiation. *Journal of Investigative Dermatology* 104(5), pp. 859–867. Available at: <http://dx.doi.org/10.1111/1523-1747.ep12607034>.
- Arezou Teimouri et al. 2018. 2D vs. 3D Cell Culture Models for 2D vs. 3D Cell Culture Models for In Vitro Topical (Dermatological) Medication Testing. *Intech* 32(tourism), pp. 137–144. Available at: <https://www.intechopen.com/books/advanced-biometric-technologies/liveness-detection-in-biometrics>.
- Attalla, R. et al. 2019. 3D bioprinting of heterogeneous bi- and tri-layered hollow channels within gel scaffolds using scalable multi-axial microfluidic extrusion nozzle. *Biofabrication* 11(1). doi: 10.1088/1758-5090/aaf7c7.
- Avci, P. et al. 2013. Animal models of skin disease for drug discovery. *Expert Opinion on Drug Discovery* 8(3), pp. 331–355. doi: 10.1517/17460441.2013.761202.
- Baker, B.M. et al. 2013. Microfluidics embedded within extracellular matrix to define vascular architectures and pattern diffusive gradients. *Lab on a Chip* 13(16), pp. 3246–3252. doi: 10.1039/c3lc50493j.
- Baker, B.M. and Chen, C.S. 2012. Deconstructing the third dimension-how 3D culture microenvironments alter cellular cues. *Journal of Cell Science* 125(13), pp. 3015–3024. doi: 10.1242/jcs.079509.
- Baltazar, T. et al. 2020. Three Dimensional Bioprinting of a Vascularized and Perfusable Skin Graft Using Human Keratinocytes, Fibroblasts, Pericytes, and Endothelial Cells. *Tissue Engineering - Part A* 26(5–6), pp. 227–238. doi: 10.1089/ten.tea.2019.0201.
- Baxani, D.K. et al. 2016. Bilayer Networks within a Hydrogel Shell : A Robust Chassis for Artificial Cells and a Platform for Membrane Studies *Angewandte*, pp. 14240–14245. doi: 10.1002/anie.201607571.
- Beckert, B. et al. 2019. Immortalized human hTert/KER-CT Keratinocytes a model system for

● REFERENCES ●

research on desmosomal adhesion and pathogenesis of pemphigus vulgaris. *International Journal of Molecular Sciences* 20(13). doi: 10.3390/ijms20133113.

Behne, M. et al. 2011. Major translocation of calcium upon epidermal barrier insult: imaging and quantification via FLIM/Fourier vector analysis. *Physiology & behavior* 176(1), pp. 139–148. doi: 10.1016/j.physbeh.2017.03.040.

Bell, E. et al. 1979. Production of a tissue-like structure by contraction of collagen lattices by human fibroblasts of different proliferative potential in vitro. *Proceedings of the National Academy of Sciences of the United States of America* 76(3), pp. 1274–1278. doi: 10.1073/pnas.76.3.1274.

Bell, E. et al. 1981. Living Tissue Formed in vitro and Accepted. *Nature* 211(March), pp. 6–8.

Bennett, D. V and Ahrens, M.B. 2016. Chapter 22 A Practical Guide to Light Sheet Microscopy. 1451, pp. 321–331. doi: 10.1007/978-1-4939-3771-4.

Benning, L. et al. 2018. Assessment of hydrogels for bioprinting of endothelial cells. *Journal of Biomedical Materials Research - Part A* 106(4), pp. 935–947. doi: 10.1002/jbm.a.36291.

Berning, M. et al. 2015. Three-Dimensional In Vitro Skin and Skin Cancer Models Based on Human Fibroblast-Derived Matrix. 21(9), pp. 958–970. doi: 10.1089/ten.tec.2014.0698.

Bessler, N. et al. 2019. Nydus One Syringe Extruder (NOSE): A Prusa i3 3D printer conversion for bioprinting applications utilizing the FRESH-method. *HardwareX* 6, p. e00069. Available at: <https://doi.org/10.1016/j.ohx.2019.e00069>.

Bianconi, E. et al. 2013. An estimation of the number of cells in the human body. *Annals of Human Biology* 40(6), pp. 463–471. doi: 10.3109/03014460.2013.807878.

Bikle, D.D. et al. 2012. Calcium regulation of keratinocyte differentiation. *Expert Review of Endocrinology & Metabolism* 7(4), pp. 461–472. Available at: <http://www.tandfonline.com/doi/full/10.1586/eem.12.34>.

Billiet, T. et al. 2014. Biomaterials The 3D printing of gelatin methacrylamide cell-laden tissue-engineered constructs with high cell viability. *Biomaterials* 35(1), pp. 49–62. Available at: <http://dx.doi.org/10.1016/j.biomaterials.2013.09.078>.

Billingham, R.E. and Reynolds, J. 1953. TRANSPLANTATION STUDIES ON SHEETS OF PURE EPIDERMAL EPITHELIUM AND ON EPIDERMAL CELL SUSPENSIONS. *British Empire Cancer Campaign Research Fellow*

Black, A.F. et al. 1998. In vitro reconstruction of a human capillary-like network in a tissue-engineered skin equivalent. *FASEB Journal* 12(13), pp. 1331–1340. doi: 10.1096/fasebj.12.13.1331.

Boehnke, K. et al. 2007. Effects of fibroblasts and microenvironment on epidermal

● REFERENCES ●

- regeneration and tissue function in long-term skin equivalents. 86, pp. 731–746. doi: 10.1016/j.ejcb.2006.12.005.
- Boelsma, E. et al. 1999. Reconstruction of a human skin equivalent using a spontaneously transformed keratinocyte cell line (HaCaT). *Journal of Investigative Dermatology* 112(4), pp. 489–498. Available at: <http://dx.doi.org/10.1046/j.1523-1747.1999.00545.x>.
- Bonaventure, J. et al. 1994. Reexpression of cartilage-specific genes by dedifferentiated human articular chondrocytes cultured in alginate beads. *Experimental Cell Research* 212(1), pp. 97–104. doi: 10.1006/excr.1994.1123.
- Borowiec, A. et al. 2013. Optimal Differentiation of In Vitro Keratinocytes Requires Multifactorial External Control. 8(10), pp. 1–15. doi: 10.1371/journal.pone.0077507.
- Boukamp, P. et al. 1988. Normal keratinization in a spontaneously immortalized aneuploid human keratinocyte cell line. *Journal of Cell Biology* 106(3), pp. 761–771. doi: 10.1083/jcb.106.3.761.
- Boyce, S.T. and Ham, R.G. 1983. Calcium-regulated differentiation of normal human epidermal keratinocytes in chemically defined clonal culture and serum-free serial culture.
- Boyce, S.T. and Lalley, A.L. 2018. Tissue engineering of skin and regenerative medicine for wound care. *Burns & Trauma* 6, pp. 1–10. doi: 10.1186/s41038-017-0103-y.
- Breitkreutz, D. et al. 2013. Skin basement membrane: The foundation of epidermal integrity - BM functions and diverse roles of bridging molecules nidogen and perlecan. *BioMed Research International* 2013. doi: 10.1155/2013/179784.
- Briley, A. and Shapiro, B. 2016. hTERT-immortalized and Primary Keratinocytes Differentiate into Epidermal Structures in 3D Organotypic Culture. *ATCC*, pp. 3–4. doi: 10.13140/RG.2.2.17700.88960.
- Brohem, C.A. et al. 2011. Artificial skin in perspective: Concepts and applications. *Pigment Cell and Melanoma Research* 24(1), pp. 35–50. doi: 10.1111/j.1755-148X.2010.00786.x.
- Burdge, D.A. and Libourel, I.G.L. 2014. Open Source Software to Control Bioflo Bioreactors. Scaria, V. ed. *PLoS ONE* 9(3), p. e92108. Available at: <https://dx.plos.org/10.1371/journal.pone.0092108>.
- Burgeson, R.E. and Christiano, A.M. 1997. The dermal-epidermal junction. *Current Opinion in Cell Biology* 9(5), pp. 651–658. doi: 10.1016/S0955-0674(97)80118-4.
- Cao, N. et al. 2012. Influence of Calcium Ions on Cell Survival and Proliferation in the Context of an Alginate Hydrogel. *ISRN Chemical Engineering* 2012, pp. 1–9. doi: 10.5402/2012/516461.
- Carlson, M.W. et al. 2008. Three-Dimensional Tissue Models of Normal and Diseased Skin.

● REFERENCES ●

- Current Protocols in Cell Biology* 41(1), pp. 1–7. doi: 10.1002/0471143030.cb1909s41.
- Carreras, P. et al. 2020. Droplet microfluidics for the ex vivo expansion of human primary multiple myeloma cells. *Micromachines* 11(3). doi: 10.3390/mi11030261.
- Catros, S. et al. 2011. Laser-assisted bioprinting for creating on-demand patterns of human osteoprogenitor cells and. doi: 10.1088/1758-5082/3/2/025001.
- Celli, A. et al. 2010. The epidermal Ca²⁺ gradient: Measurement using the phasor representation of fluorescent lifetime imaging. *Biophysical Journal* 98(5), pp. 911–921. Available at: <http://dx.doi.org/10.1016/j.bpj.2009.10.055>.
- Chan, A.W.J. et al. 2006. Granulation of subtilisin by internal gelation of alginate microspheres for application in detergent formulation. *Enzyme and Microbial Technology* 38(1–2), pp. 265–272. Available at: <https://linkinghub.elsevier.com/retrieve/pii/S0141022905003716>.
- Chatzinikolaidou, M. 2016. Cell spheroids: the new frontiers in in vitro models for cancer drug validation. *Drug Discovery Today* 21(9), pp. 1553–1560. Available at: <http://dx.doi.org/10.1016/j.drudis.2016.06.024>.
- Chau, D.Y.S. et al. 2013. The development of a 3D immunocompetent model of human skin. *Biofabrication* 5(3), p. 035011. Available at: <https://iopscience.iop.org/article/10.1088/1758-5082/5/3/035011>.
- Chen, S. et al. 2002. Steric effects on diffusion of associated molecules in acetone. *Chemical Communications* 8, pp. 898–899. doi: 10.1039/b200655c.
- Chiarello, E. et al. 2017. Droplet breakup driven by shear thinning solutions in a microfluidic T-junction. *Physical Review Fluids* 2(12), pp. 1–11. doi: 10.1103/PhysRevFluids.2.123602.
- Chimene, D. et al. 2016. Advanced Bioinks for 3D Printing: A Materials Science Perspective. *Annals of Biomedical Engineering* 44(6), pp. 2090–2102. doi: 10.1007/s10439-016-1638-y.
- Ching, S.H. et al. 2017. Alginate gel particles—A review of production techniques and physical properties. *Critical Reviews in Food Science and Nutrition* 57(6), pp. 1133–1152. Available at: <http://dx.doi.org/10.1080/10408398.2014.965773>.
- Choi, C.H. et al. 2007. Generation of monodisperse alginate microbeads and in situ encapsulation of cell in microfluidic device. *Biomedical Microdevices*. doi: 10.1007/s10544-007-9098-7.
- Chou, W.L. et al. 2015. Recent advances in applications of droplet microfluidics. *Micromachines* 6(9), pp. 1249–1271. doi: 10.3390/mi6091249.
- Chueh, B.H. et al. 2010. Patterning alginate hydrogels using light-directed release of caged calcium in a microfluidic device. *Biomedical Microdevices* 12(1), pp. 145–151. doi: 10.1007/s10544-009-9369-6.

● REFERENCES ●

- Chung, H. et al. 2018. Keratinocytes negatively regulate the N-cadherin levels of melanoma cells via contact-mediated calcium regulation. *Biochemical and Biophysical Research Communications* 503(2), pp. 615–620. Available at: <https://doi.org/10.1016/j.bbrc.2018.06.050>.
- Cichorek, M. et al. 2013. Skin melanocytes: Biology and development. *Postepy Dermatologii i Alergologii* 30(1), pp. 30–41. doi: 10.5114/pdia.2013.33376.
- Clausell-Tormos, J. et al. 2008. Droplet-Based Microfluidic Platforms for the Encapsulation and Screening of Mammalian Cells and Multicellular Organisms. *Chemistry and Biology*. doi: 10.1016/j.chembiol.2008.04.004.
- Clayton, K. et al. 2017. Langerhans cells-programmed by the epidermis. *Frontiers in Immunology* 8(NOV), pp. 1–14. doi: 10.3389/fimmu.2017.01676.
- Colombo, I. et al. 2017. HaCaT Cells as a Reliable In Vitro Differentiation Model to Dissect the Inflammatory/Repair Response of Human Keratinocytes. *Mediators of Inflammation* 2017, pp. 1–12. Available at: <https://www.hindawi.com/journals/mi/2017/7435621/>.
- Colosi, C. et al. 2016. Microfluidic Bioprinting of Heterogeneous 3D Tissue Constructs Using Low-Viscosity Bioink. *Advanced Materials* 28(4), pp. 677–684. Available at: <http://doi.wiley.com/10.1002/adma.201503310>.
- Corzo-León, D.E. et al. 2019. An ex vivo human skin model to study superficial fungal infections. *Frontiers in Microbiology* 10(JUN), pp. 1–17. doi: 10.3389/fmicb.2019.01172.
- Costantini, M. et al. 2017. Microfluidic-enhanced 3D bioprinting of aligned myoblast-laden hydrogels leads to functionally organized myofibers in vitro and in vivo. *Biomaterials* 131(April), pp. 98–110. doi: 10.1016/j.biomaterials.2017.03.026.
- Coulman, S.A. et al. 2009. Microneedle mediated delivery of nanoparticles into human skin. *International Journal of Pharmaceutics* 366(1–2), pp. 190–200. doi: 10.1016/j.ijpharm.2008.08.040.
- Coulomb, B. and Dubertret, L. 2002. Skin cell culture and wound healing. *Wound Repair and Regeneration* 10(2), pp. 109–112. doi: 10.1046/j.1524-475X.2002.02104.x.
- Cubo, N. et al. 2016a. 3D bioprinting of functional human skin: production and in vivo analysis. *Biofabrication* 9(1), p. 015006. Available at: <https://iopscience.iop.org/article/10.1088/1758-5090/9/1/015006>.
- Cubo, N. et al. 2016b. 3D bioprinting of skin: a state-of-the-art review on modelling, materials, and processes. *Biofabrication* 8(3), p. 032001. doi: 10.1088/1758-5090/8/3/032001.
- Cuono, C. et al. 1986. Use of Cultured Epidermal Autografts and Dermal Allografts As Skin Replacement After Burn Injury. *The Lancet* 327(8490), pp. 1123–1124. doi: 10.1016/S0140-6736(86)91838-6.

● REFERENCES ●

- Dababneh, A.B. and Ozbolat, I.T. 2014. Bioprinting Technology: A Current State-of-the-Art Review. *Journal of Manufacturing Science and Engineering, Transactions of the ASME* 136(6), pp. 1–11. doi: 10.1115/1.4028512.
- Dai, G. and Lee, V. 2015. Three-dimensional bioprinting and tissue fabrication: prospects for drug discovery and regenerative medicine. *Advanced Health Care Technologies* , p. 23. doi: 10.2147/ahct.s69191.
- Damiati, S. et al. 2018. Microfluidic devices for drug delivery systems and drug screening. *Genes* 9(2), pp. 1–24. doi: 10.3390/genes9020103.
- Degenhart, A.D. et al. 2011. Craniux: A LabVIEW-Based Modular Software Framework for Brain-Machine Interface Research. *Computational Intelligence and Neuroscience* 2011, pp. 1–13. Available at: <http://www.hindawi.com/journals/cin/2011/363565/>.
- Derby, B. 2008. Bioprinting: Inkjet printing proteins and hybrid cell-containing materials and structures. *Journal of Materials Chemistry* 18(47), pp. 5717–5721. doi: 10.1039/b807560c.
- Derr, K. et al. 2019. Fully Three-Dimensional Bioprinted Skin Equivalent Constructs with Validated Morphology and Barrier Function. *Tissue Engineering - Part C: Methods* 25(6), pp. 334–343. doi: 10.1089/ten.tec.2018.0318.
- Dhawale, A.P. 2014. Real-Time Image Processing for Biological Applications Through Morphological Operations using LabVIEW. 3(5), pp. 1262–1265.
- Diederich, B. et al. 2020. A versatile and customizable low-cost 3D-printed open standard for microscopic imaging. *Nature Communications* 11(1). Available at: <http://dx.doi.org/10.1038/s41467-020-19447-9>.
- Ding, H. et al. 2019. 3D Bioprinted GelMA Based Models for the Study of Trophoblast Cell Invasion. *Scientific Reports* 9(1), pp. 1–13. doi: 10.1038/s41598-019-55052-7.
- Dolega, M.E. et al. 2015. Controlled 3D culture in Matrigel microbeads to analyze clonal acinar development. *Biomaterials* 52(1), pp. 347–357. Available at: <http://dx.doi.org/10.1016/j.biomaterials.2015.02.042>.
- Donetti, E. et al. 2020. 3D skin model to investigate the early epidermal morphological psoriatic features. *Journal of Translational Science* 6(4), pp. 1–4. doi: 10.15761/jts.1000361.
- van Drongelen, V. et al. 2014. Barrier Properties of an N/TERT-Based Human Skin Equivalent. *Tissue Engineering Part A* 20(21–22), pp. 3041–3049. Available at: <http://online.liebertpub.com/doi/abs/10.1089/ten.tea.2014.0011>.
- van Duinen, V. et al. 2015. Microfluidic 3D cell culture: From tools to tissue models. *Current Opinion in Biotechnology* 35, pp. 118–126. Available at: <http://dx.doi.org/10.1016/j.copbio.2015.05.002>.

● REFERENCES ●

- Duval, K. et al. 2017. Modeling Physiological Events in 2D vs. 3D Cell Culture. *Physiology* 32(4), pp. 266–277. Available at: <https://www.physiology.org/doi/10.1152/physiol.00036.2016>.
- Eichner, R. et al. 1986. The role of keratin subfamilies and keratin pairs in the formation of human epidermal intermediate filaments. *Journal of Cell Biology* 102(5), pp. 1767–1777. doi: 10.1083/jcb.102.5.1767.
- Elaine Fuchs 1990. Epidermal Differentiation: The Bare Essentials The Program of Terminal Differentiation. *The Journal of Cell Biology* 111(6, Pt.2), pp. 2807–2814. Available at: <https://www.ncbi.nlm.nih.gov/pmc/articles/PMC2116387/pdf/jc11162807.pdf>.
- Elias, P.M. et al. 2008. Epidermal vascular endothelial growth factor production is required for permeability barrier homeostasis, dermal angiogenesis, and the development of epidermal hyperplasia: Implications for the pathogenesis of psoriasis. *American Journal of Pathology* 173(3), pp. 689–699. Available at: <https://linkinghub.elsevier.com/retrieve/pii/S0002944010616422>.
- Elsholz, F. et al. 2014. Calcium - A central regulator of keratinocyte differentiation in health and disease. *European Journal of Dermatology* 24(6), pp. 650–661. doi: 10.1684/ejd.2014.2452.
- England, S. et al. 2017. Bioprinted fibrin-factor XIII-hyaluronate hydrogel scaffolds with encapsulated Schwann cells and their in vitro characterization for use in nerve regeneration. *Bioprinting* 5(May 2016), pp. 1–9. Available at: <http://dx.doi.org/10.1016/j.bprint.2016.12.001>.
- Fan, C. and Wang, D. 2017. Macroporous Hydrogel Scaffolds for Three-Dimensional Cell Culture and Tissue Engineering. *Tissue Engineering Part B: Reviews* 23(5), pp. 451–461. doi: 10.1089/ten.teb.2016.0465.
- Fan, R. et al. 2016. Bio-printing cell-laden Matrigel–agarose constructs. *Journal of Biomaterials Applications* 31(5), pp. 684–692. doi: 10.1177/0885328216669238.
- Faramarzi, N. et al. 2018. Patient-Specific Bioinks for 3D Bioprinting of Tissue Engineering Scaffolds. *Advanced Healthcare Materials* 7(11), p. 1701347. Available at: <http://doi.wiley.com/10.1002/adhm.201701347>.
- Faulkner-Jones, A. et al. 2013. Development of a valve-based cell printer for the formation of human embryonic stem cell spheroid aggregates. *Biofabrication* 5(1). doi: 10.1088/1758-5082/5/1/015013.
- Filocamo, G. et al. 2016. MK-4101, a Potent Inhibitor of the Hedgehog Pathway, Is Highly Active against Medulloblastoma and Basal Cell Carcinoma. *Molecular Cancer Therapeutics* 15(6), pp. 1177–1189. Available at: <http://mct.aacrjournals.org/lookup/doi/10.1158/1535-7163.MCT-15-0371>.

● REFERENCES ●

- Franz, T.J. et al. 2009. Use of excised human skin to assess the bioequivalence of topical products. *Skin Pharmacology and Physiology* 22(5), pp. 276–286. doi: 10.1159/000235828.
- Freeman, F.E. and Kelly, D.J. 2017. Tuning alginate bioink stiffness and composition for controlled growth factor delivery and to spatially direct MSC Fate within bioprinted tissues. *Scientific Reports* 7(1), pp. 1–12. Available at: <http://dx.doi.org/10.1038/s41598-017-17286-1>.
- Fuchs, E. and Raghavan, S. 2002. Getting under the skin of epidermal morphogenesis. *Nature Reviews Genetics* 3(3), pp. 199–209. doi: 10.1038/nrg758.
- Gabriel Villar, Alexander D. Graham, H.B. 2013. A Tissue-Like Printed Material. *Science* 340(6128), pp. 45–48. doi: 10.1126/science.1228297.
- Gaebel, R. et al. 2011. Biomaterials Patterning human stem cells and endothelial cells with laser printing for cardiac regeneration. *Biomaterials* 32(35), pp. 9218–9230. Available at: <http://dx.doi.org/10.1016/j.biomaterials.2011.08.071>.
- Gao, Q. et al. 2015. Biomaterials Coaxial nozzle-assisted 3D bioprinting with built-in microchannels for nutrients delivery. *Biomaterials* 61, pp. 203–215. Available at: <http://dx.doi.org/10.1016/j.biomaterials.2015.05.031>.
- Gao, Q. et al. 2017. 3D Bioprinting of Vessel-like Structures with Multilevel Fluidic Channels. *ACS Biomaterials Science and Engineering* 3(3), pp. 399–408. doi: 10.1021/acsbomaterials.6b00643.
- Garach-Jehoshua, O. et al. 1998. Upregulation of the calcium-dependent protease, calpain, during keratinocyte differentiation. *British Journal of Dermatology* 139(6), pp. 950–957. doi: 10.1046/j.1365-2133.1998.02548.x.
- Garstecki, P. et al. 2006. Formation of droplets and bubbles in a microfluidic T-junction - Scaling and mechanism of break-up. *Lab on a Chip* 6(3), pp. 437–446. doi: 10.1039/b510841a.
- Gazel, A. et al. 2006. Inhibition of JNK promotes differentiation of epidermal keratinocytes. *Journal of Biological Chemistry* 281(29), pp. 20530–20541. doi: 10.1074/jbc.M602712200.
- Gerber, L.C. et al. 2017. Liquid-handling Lego robots and experiments for STEM education and research. *PLoS Biology* 15(3), pp. 1–9. doi: 10.1371/journal.pbio.2001413.
- Ghalbzouri, A. El et al. 2008. Leiden reconstructed human epidermal model as a tool for the evaluation of the skin corrosion and irritation potential according to the ECVAM guidelines. *Toxicology in Vitro* 22(5), pp. 1311–1320. doi: 10.1016/j.tiv.2008.03.012.
- Gibot, L. et al. 2013. Development of a tridimensional microvascularized human skin substitute to study melanoma biology., pp. 83–90. doi: 10.1007/s10585-012-9511-3.
- Golan, T. et al. 2015. Interactions of Melanoma Cells with Distal Keratinocytes Trigger

● REFERENCES ●

Metastasis via Notch Signaling Inhibition of MITF. *Molecular Cell* 59(4), pp. 664–676. Available at: <http://dx.doi.org/10.1016/j.molcel.2015.06.028>.

Graham, A.D. et al. 2017. High-Resolution Patterned Cellular Constructs by Droplet-Based 3D Printing. *Scientific Reports* 7(1), pp. 1–11. Available at: <http://dx.doi.org/10.1038/s41598-017-06358-x>.

Green, H. et al. 1979. Growth of cultured human epidermal cells into multiple epithelia suitable for grafting. *Proceedings of the National Academy of Sciences of the United States of America* 76(11), pp. 5665–5668. doi: 10.1073/pnas.76.11.5665.

Groeber, F. et al. 2016. A first vascularized skin equivalent as an alternative to animal experimentation. *Altex* 33(4), pp. 415–422. doi: 10.14573/altex.1604041.

Gudapati, H. et al. 2014. Alginate gelation-induced cell death during laser-assisted cell printing. *Biofabrication* 6(3), p. 035022. Available at: <https://iopscience.iop.org/article/10.1088/1758-5082/6/3/035022>.

Gudapati, H. et al. 2016. Biomaterials A comprehensive review on droplet-based bioprinting : Past , present and future. *Biomaterials* 102, pp. 20–42. Available at: <http://dx.doi.org/10.1016/j.biomaterials.2016.06.012>.

Guiraud, B. et al. 2014. Characterization of a human epidermis model reconstructed from hair follicle keratinocytes and comparison with two commercially models and native skin. *International Journal of Cosmetic Science* 36(5), pp. 485–493. doi: 10.1111/ics.12150.

Gulyas, M. et al. 2018. Software tools for cell culture-related 3D printed structures. *PLoS ONE* 13(9), pp. 1–11. doi: 10.1371/journal.pone.0203203.

Gungor-Ozkerim, P.S. et al. 2018. Bioinks for 3D bioprinting: An overview. *Biomaterials Science* 6(5), pp. 915–946. doi: 10.1039/c7bm00765e.

Günther, A. and Jensen, K.F. 2006. Multiphase microfluidics: from flow characteristics to chemical and materials synthesis. *Lab Chip* 6(12), pp. 1487–1503. Available at: <http://xlink.rsc.org/?DOI=B609851G>.

Haase, I. et al. 2003. Regulation of keratinocyte shape, migration and wound epithelialization by IGF-1 and EGF-dependent signalling pathways. *Journal of Cell Science* 116(15), pp. 3227–3238. doi: 10.1242/jcs.00610.

Hahn, W.C. et al. 2000. Human keratinocytes that express hTERT and also bypass a p16(INK4a)-enforced mechanism that limits life span become immortal yet retain normal growth and differentiation characteristics. *Molecular and cellular biology* 20(4), pp. 1436–47. Available at: <http://www.pubmedcentral.nih.gov/articlerender.fcgi?artid=85304&tool=pmcentrez&rendertype=abstract>.

● REFERENCES ●

- Haniffa, M. et al. 2015. Human skin dendritic cells in health and disease. *Journal of Dermatological Science* 77(2), pp. 85–92. Available at: <http://dx.doi.org/10.1016/j.jdermsci.2014.08.012>.
- Hay, R.J. et al. 2014. The global burden of skin disease in 2010: An analysis of the prevalence and impact of skin conditions. *Journal of Investigative Dermatology* 134(6), pp. 1527–1534. Available at: <http://dx.doi.org/10.1038/jid.2013.446>.
- Headen, D.M. et al. 2018. Parallel droplet microfluidics for high throughput cell encapsulation and synthetic microgel generation. *Microsystems & Nanoengineering* 4(May 2017), p. 17076. Available at: <http://www.nature.com/articles/micronano201776>.
- Hennings, H. et al. 1980. Calcium Regulation of Growth and Differentiation of Mouse Epidermal Cells in Culture. 19(January), pp. 245–254.
- Hidalgo San Jose, L. et al. 2018. Microfluidic Encapsulation Supports Stem Cell Viability, Proliferation, and Neuronal Differentiation. *Tissue Engineering - Part C: Methods* 24(3), pp. 158–170. doi: 10.1089/ten.tec.2017.0368.
- Hinton, T.J. et al. 2015. Three-dimensional printing of complex biological structures by freeform reversible embedding of suspended hydrogels. *Science Advances* 1(9). doi: 10.1126/sciadv.1500758.
- Hoarau-Véchet, J. et al. 2018. Halfway between 2D and animal models: Are 3D cultures the ideal tool to study cancer-microenvironment interactions? *International Journal of Molecular Sciences* 19(1). doi: 10.3390/ijms19010181.
- Hoffman, R.M. 2010. Histocultures and Their Use. *Encyclopedia of Life Sciences* (October), pp. 1–6. doi: 10.1002/9780470015902.a0002573.pub2.
- Homan, K.A. et al. 2016. Bioprinting of 3D Convulated Renal Proximal Tubules on Perfusable Chips. *Scientific Reports* 6, pp. 1–13. doi: 10.1038/srep34845.
- Hong, S. et al. 2015. 3D Printing of Highly Stretchable and Tough Hydrogels into Complex, Cellularized Structures. *Advanced Materials* 27(27), pp. 4035–4040. doi: 10.1002/adma.201501099.
- Hosokawa, K. et al. 2004. Power-free poly(dimethylsiloxane) microfluidic devices for gold nanoparticle-based DNA analysis. Electronic supplementary information (ESI) available: Sample movie used for flow characterization, mathematical details of the one-dimensional diffusion model. *Lab on a Chip* 4(3), p. 181. Available at: <http://xlink.rsc.org/?DOI=b403930k>.
- Hospodiuk, M. et al. 2017. The bioink: A comprehensive review on bioprintable materials. *Biotechnology Advances* 35(2), pp. 217–239. Available at: <http://dx.doi.org/10.1016/j.biotechadv.2016.12.006>.
- Houghton, P.J. et al. 2005. In vitro tests and ethnopharmacological investigations: Wound

● REFERENCES ●

- healing as an example. *Journal of Ethnopharmacology* 100(1–2), pp. 100–107. doi: 10.1016/j.jep.2005.07.001.
- Huang, C. et al. 2014. Microfluidic chip for monitoring Ca²⁺ transport through a confluent layer of intestinal cells. *RSC Advances* 4(95), pp. 52887–52891. doi: 10.1039/c4ra09370d.
- Huang, H. et al. 2017. Generation and manipulation of hydrogel microcapsules by droplet-based microfluidics for mammalian cell culture. *Lab on a Chip* 17(11), pp. 1913–1932. doi: 10.1039/c7lc00262a.
- Huang, S. et al. 2016. 3D bioprinted extracellular matrix mimics facilitate directed differentiation of epithelial progenitors for sweat gland regeneration. *Acta Biomaterialia* 32, pp. 170–177. Available at: <http://dx.doi.org/10.1016/j.actbio.2015.12.039>.
- Huber, B. et al. 2016. Integration of Mature Adipocytes to Build-Up a Functional Three-Layered Full-Skin Equivalent. *Tissue Engineering - Part C: Methods* 22(8), pp. 756–764. doi: 10.1089/ten.tec.2016.0141.
- Idaszek, J. et al. 2019. 3D bioprinting of hydrogel constructs with cell and material gradients for the regeneration of full-thickness chondral defect using a microfluidic printing head. *Biofabrication* 11(4). doi: 10.1088/1758-5090/ab2622.
- Imamura, Y. et al. 2015. Comparison of 2D- and 3D-culture models as drug-testing platforms in breast cancer. *Oncology Reports* 33(4), pp. 1837–1843. doi: 10.3892/or.2015.3767.
- Ioannidis, K. et al. 2020. A Custom Ultra-Low-Cost 3D Bioprinter Supports Cell Growth and Differentiation. *Frontiers in Bioengineering and Biotechnology* 8(November), pp. 1–13. doi: 10.3389/fbioe.2020.580889.
- Jensen, C. and Teng, Y. 2020. Is It Time to Start Transitioning From 2D to 3D Cell Culture? *Frontiers in Molecular Biosciences* 7(March), pp. 1–15. doi: 10.3389/fmolb.2020.00033.
- Jian, H. et al. 2018. 3D bioprinting for cell culture and tissue fabrication. *Bio-Design and Manufacturing* 1(1), pp. 45–61. Available at: <https://doi.org/10.1007/s42242-018-0006-1>.
- Johnson, B.N. et al. 2015. 3D Printed Anatomical Nerve Regeneration Pathways. *Advanced Functional Materials* 25(39), pp. 6205–6217. Available at: <http://doi.wiley.com/10.1002/adfm.201501760>.
- Johnson, B.N. et al. 2016. 3D printed nervous system on a chip. *Lab on a Chip* 16(8), pp. 1393–1400. doi: 10.1039/c5lc01270h.
- Kahl, M. et al. 2019. Ultra-low-cost 3D bioprinting: Modification and application of an off-the-shelf desktop 3D-printer for biofabrication. *Frontiers in Bioengineering and Biotechnology* 7(JUL), pp. 1–12. doi: 10.3389/fbioe.2019.00184.
- Kang, A.R. et al. 2014. Cell encapsulation via microtechnologies. *Biomaterials* 35(9), pp. 2651–

● REFERENCES ●

2663. Available at: <http://dx.doi.org/10.1016/j.biomaterials.2013.12.073>.

Kang, H. et al. 2016. A 3D bioprinting system to produce human-scale tissue constructs with structural integrity. *Nature Biotechnology* 34(3), pp. 312–319. Available at: <http://dx.doi.org/10.1038/nbt.3413>.

Kang, K. et al. 2018. Three-Dimensional Bioprinting of Hepatic Structures with Directly Converted Hepatocyte-Like Cells. *Tissue Engineering - Part A* 24(7–8), pp. 576–583. doi: 10.1089/ten.tea.2017.0161.

Kapałczyńska, M. et al. 2016. 2D and 3D cell cultures – a comparison of different. *Archives of Medical Science* 14(4), pp. 910–919.

Karimkhani, C. et al. 2017. Global skin disease morbidity and mortality an update from the global burden of disease study 2013. *JAMA Dermatology* 153(5), pp. 406–412. doi: 10.1001/jamadermatol.2016.5538.

Kerimoğlu, O. and Şahbaz, S. 2018. Animal Skin Models for Percutaneous Absorption Studies. *Journal of Biopharmaceutics and Therapeutic Challenges J Biopharm Ther chal* 2(1), p. 1.

Khademhosseini, A. et al. 2008. Microscale technologies for tissue engineering. *Advances in Tissue Engineering* 103(8), pp. 349–369. doi: 10.1142/9781848161832_0017.

Khavari, P.A. 2006. Modelling cancer in human skin tissue. *Nature Reviews Cancer* 6(4), pp. 270–280. Available at: <http://www.nature.com/articles/nrc1838>.

Kim, B.S. et al. 2017a. Decellularized extracellular matrix: A step towards the next generation source for bioink manufacturing. *Biofabrication* 9(3). doi: 10.1088/1758-5090/aa7e98.

Kim, B.S. et al. 2017b. Direct 3D cell-printing of human skin with functional transwell system. *Biofabrication* 9(2), p. 025034. Available at: <https://iopscience.iop.org/article/10.1088/1758-5090/aa71c8>.

Kim, B.S. et al. 2018. 3D cell printing of in vitro stabilized skin model and in vivo pre-vascularized skin patch using tissue-specific extracellular matrix bioink: A step towards advanced skin tissue engineering. *Biomaterials* 168, pp. 38–53. Available at: <https://doi.org/10.1016/j.biomaterials.2018.03.040>.

Kim, B.S. et al. 2019. 3D Cell Printing of Perfusable Vascularized Human Skin Equivalent Composed of Epidermis, Dermis, and Hypodermis for Better Structural Recapitulation of Native Skin. *Advanced Healthcare Materials* 8(7), pp. 1–11. doi: 10.1002/adhm.201801019.

Kim, G. et al. 2011. Coaxial structured collagen-alginate scaffolds: Fabrication, physical properties, and biomedical application for skin tissue regeneration. *Journal of Materials Chemistry* 21(17), pp. 6165–6172. doi: 10.1039/c0jm03452e.

Kim, S.H. and Jeon, J.W. 2007. Programming LEGO Mindstorms NXT with visual programming.

● REFERENCES ●

ICCAS 2007 - *International Conference on Control, Automation and Systems* , pp. 2468–2472. doi: 10.1109/ICCAS.2007.4406778.

Kimutai, L.K. et al. 2002. Modulations in Epidermal Calcium Regulate the Expression of Differentiation-Specific Markers., pp. 1128–1136. doi: 10.1046/j.1523-1747.2002.19512.x.

Klicks, J. et al. 2017. In vitro skin three-dimensional models and their applications. *Journal of Cellular Biotechnology* 3(1), pp. 21–39. doi: 10.3233/jcb-179004.

Knight, E. and Przyborski, S. 2015. Advances in 3D cell culture technologies enabling tissue-like structures to be created in vitro. *Journal of Anatomy* 227(6), pp. 746–756. doi: 10.1111/joa.12257.

Kober, J. et al. 2015. Generation of a Fibrin Based Three-Layered Skin Substitute. *BioMed Research International* 2015, pp. 1–8. Available at: <http://www.hindawi.com/journals/bmri/2015/170427/>.

Koch, L. et al. 2010. Laser Printing of Skin Cells and Human Stem Cells. *Tissue Engineering Part C: Methods* 16(5), pp. 847–854. Available at: <https://www.liebertpub.com/doi/10.1089/ten.tec.2009.0397>.

Koch, L. et al. 2012. Skin tissue generation by laser cell printing. *Biotechnology and Bioengineering* 109(7), pp. 1855–1863. doi: 10.1002/bit.24455.

Kodet, O. et al. 2015. Melanoma cells influence the differentiation pattern of human epidermal keratinocytes. *Molecular Cancer* 14(1), p. 1. Available at: <http://molecular-cancer.biomedcentral.com/articles/10.1186/1476-4598-14-1>.

Kolarsick, P.A.J. et al. 2011. Anatomy and Physiology of the Skin. *Journal of the Dermatology Nurses' Association* 3(4), pp. 203–213. Available at: <http://content.wkhealth.com/linkback/openurl?sid=WKPTLP:landingpage&an=01412499-201107000-00003>.

Kolesky, D.B. et al. 2016. Three-dimensional bioprinting of thick vascularized tissues. *Proceedings of the National Academy of Sciences* 113(12), pp. 3179–3184. Available at: <http://www.pnas.org/lookup/doi/10.1073/pnas.1521342113>.

Kong, H.J. et al. 2004. Controlling degradation of hydrogels via the size of cross-linked junctions. *Advanced Materials* 16(21), pp. 1917–1921. doi: 10.1002/adma.200400014.

Köster, S. et al. 2008. Drop-based microfluidic devices for encapsulation of single cells. *Lab on a Chip* 8(7), p. 1110. Available at: <http://xlink.rsc.org/?DOI=b802941e>.

Kumamoto, J. et al. 2018. Mathematical-model-guided development of full-thickness epidermal equivalent. *Scientific Reports* 8(1), pp. 1–8. Available at: <http://dx.doi.org/10.1038/s41598-018-36647-y>.

● REFERENCES ●

- Kuo, I.Y. and Ehrlich, B.E. 2015. Signaling in muscle contraction. *Cold Spring Harbor Perspectives in Biology* 7(2), pp. 1–14. doi: 10.1101/cshperspect.a006023.
- Kyle, S. et al. 2017. ‘Printability’ of Candidate Biomaterials for Extrusion Based 3D Printing: State-of-the-Art’. *Advanced Healthcare Materials* 6(16). doi: 10.1002/adhm.201700264.
- Langhans, S.A. 2018. Three-dimensional in vitro cell culture models in drug discovery and drug repositioning. *Frontiers in Pharmacology* 9(JAN), pp. 1–14. doi: 10.3389/fphar.2018.00006.
- Lee, B.B. et al. 2013. Size and shape of calcium alginate beads produced by extrusion dripping. *Chemical Engineering and Technology* 36(10), pp. 1627–1642. doi: 10.1002/ceat.201300230.
- Lee, D.Y. et al. 2000. A new skin equivalent model: Dermal substrate that combines de-epidermized dermis with fibroblast-populated collagen matrix. *Journal of Dermatological Science* 23(2), pp. 132–137. doi: 10.1016/S0923-1811(00)00068-2.
- Lee, J. et al. 2017a. A desktop multi-material 3D bio-printing system with open-source hardware and software. *International Journal of Precision Engineering and Manufacturing* 18(4), pp. 605–612. doi: 10.1007/s12541-017-0072-x.
- Lee, J.M. et al. 2020. Generation of tumor spheroids using a droplet-based microfluidic device for photothermal therapy. *Microsystems and Nanoengineering* 6(1), pp. 0–9. Available at: <http://dx.doi.org/10.1038/s41378-020-0167-x>.
- Lee, K.Y. and Mooney, D.J. 2012. Alginate: Properties and biomedical applications. *Progress in Polymer Science (Oxford)* 37(1), pp. 106–126. doi: 10.1016/j.progpolymsci.2011.06.003.
- Lee, S. et al. 2017b. Construction of 3D multicellular microfluidic chip for an in vitro skin model. doi: 10.1007/s10544-017-0156-5.
- Lee, V. et al. 2014. Design and Fabrication of Human Skin. *Tissue Engineering Part C: Methods* 20(6), pp. 473–484. doi: 10.1089/ten.tec.2013.0335.
- Lee, W. et al. 2009. Multi-layered culture of human skin fibroblasts and keratinocytes through three-dimensional freeform fabrication. *Biomaterials* 30(8), pp. 1587–1595. Available at: <http://dx.doi.org/10.1016/j.biomaterials.2008.12.009>.
- Leighton, J. 1951. A sponge matrix method for tissue culture; formation of organized aggregates of cells in vitro. *Journal of the National Cancer Institute* 12(3), pp. 545–561.
- Leighton, J. et al. 1967. Collagen-coated cellulose sponge: Three-dimensional matrix for tissue culture of Walker tumor 256. *Science* 155(3767), pp. 1259–1261. doi: 10.1126/science.155.3767.1259-a.
- Leinonen, P.T. et al. 2009. Reevaluation of the normal epidermal calcium gradient, and analysis of calcium levels and ATP receptors in hailey-hailey and darier epidermis. *Journal of Investigative Dermatology* 129(6), pp. 1379–1387. doi: 10.1038/jid.2008.381.

● REFERENCES ●

- Lemaître, G. et al. 2004. Expression profiling of genes and proteins in HaCaT keratinocytes: Proliferating versus differentiated state. *Journal of Cellular Biochemistry* 93(5), pp. 1048–1062. doi: 10.1002/jcb.20212.
- Li, H. et al. 2016a. Rheological study on 3D printability of alginate hydrogel and effect of graphene oxide. *International Journal of Bioprinting* 2(2), pp. 54–66. doi: 10.18063/IJB.2016.02.007.
- Li, J. et al. 2016b. Recent advances in bioprinting techniques: Approaches, applications and future prospects. *Journal of Translational Medicine* 14(1), pp. 1–15. doi: 10.1186/s12967-016-1028-0.
- Li, L. et al. 1995. Chelation of intracellular Ca²⁺ inhibits murine keratinocyte differentiation in vitro. *Journal of Cellular Physiology* 163(1), pp. 105–114. Available at: <http://doi.wiley.com/10.1002/jcp.1041630112>.
- Li, W.J. et al. 2002. Electrospun nanofibrous structure: A novel scaffold for tissue engineering. *Journal of Biomedical Materials Research* 60(4), pp. 613–621. doi: 10.1002/jbm.10167.
- Litvinov, R.I. et al. 2021. Fibrinogen and Fibrin. *Subcellular Biochemistry* 96(04), pp. 471–501. doi: 10.1007/978-3-030-58971-4_15.
- Liu, H. and Zhang, Y. 2009. Droplet formation in a T-shaped microfluidic junction. *Journal of Applied Physics* 106(3). doi: 10.1063/1.3187831.
- Liu, K. et al. 2006. Shape-controlled production of biodegradable calcium alginate gel microparticles using a novel microfluidic device. *Langmuir* 22(22), pp. 9453–9457. doi: 10.1021/la061729+.
- Liu, L. et al. 2013. Preparation of monodisperse calcium alginate microcapsules via internal gelation in microfluidic-generated double emulsions. *Journal of Colloid and Interface Science* 404, pp. 85–90. Available at: <http://dx.doi.org/10.1016/j.jcis.2013.04.044>.
- Liu, N. et al. 2016. 3D bioprinting matrices with controlled pore structure and release function guide in vitro self-organization of sweat gland. *Scientific Reports* 6(October), pp. 1–8. doi: 10.1038/srep34410.
- Ma, J. et al. 2018. Bioprinting of 3D tissues/organs combined with microfluidics. *RSC Advances* 8(39), pp. 21712–21727. doi: 10.1039/c8ra03022g.
- Ma, X. et al. 2016. Deterministically patterned biomimetic human iPSC-derived hepatic model via rapid 3D bioprinting. *Proceedings of the National Academy of Sciences of the United States of America* 113(8), pp. 2206–2211. doi: 10.1073/pnas.1524510113.
- MacNeil, S. 2007. Progress and opportunities for tissue-engineered skin. *Nature* 445(7130), pp. 874–880. Available at: <http://www.nature.com/articles/nature05664>.

● REFERENCES ●

- Malak, M. et al. 2020. Monitoring calcium-induced epidermal differentiation in vitro using multiphoton microscopy. *Journal of Biomedical Optics* 25(07), p. 1. doi: 10.1117/1.jbo.25.7.071205.
- Malmqvist, K.G. et al. 1983. Proton-Induced X-Ray Emission Analysis - a New Tool in Quantitative Dermatology. *Scanning Electron Microscopy* (pt 4), pp. 1815–1825.
- Mapanao, A.K. and Voliani, V. 2020. Three-dimensional tumor models: Promoting breakthroughs in nanotheranostics translational research. *Applied Materials Today* 19, p. 100552. Available at: <https://doi.org/10.1016/j.apmt.2019.100552>.
- Marcom, P.K. 2017. 3D in vitro model for breast cancer research using magnetic levitation and bioprinting method. *Genomic and Precision Medicine: Primary Care: Third Edition* 4417329, pp. 181–194. doi: 10.1016/B978-0-12-800685-6.00010-2.
- Maretzky, T. et al. 2008. ADAM10-mediated E-cadherin release is regulated by proinflammatory cytokines and modulates keratinocyte cohesion in eczematous dermatitis. *Journal of Investigative Dermatology* 128(7), pp. 1737–1746. doi: 10.1038/sj.jid.5701242.
- Marrero, B. et al. 2009. Generation of a tumor spheroid in a microgravity environment as a 3D model of melanoma. *In Vitro Cellular and Developmental Biology - Animal* 45(9), pp. 523–534. doi: 10.1007/s11626-009-9217-2.
- Marshall, K.A. and Walker, T.W. 2019. Investigating the dynamics of droplet breakup in a microfluidic cross-slot device for characterizing the extensional properties of weakly-viscoelastic fluids. *Rheologica Acta* 58(9), pp. 573–590. doi: 10.1007/s00397-019-01152-0.
- Martinez, C.J. et al. 2012. A Microfluidic Approach to Encapsulate Living Cells in Uniform Alginate Hydrogel Microparticles. *Macromolecular Bioscience* 12(7), pp. 946–951. doi: 10.1002/mabi.201100351.
- Masuda, K. et al. 2003. A novel two-step method for the formation of tissue-engineered cartilage by mature bovine chondrocytes: The alginate-recovered-chondrocyte (ARC) method. *Journal of Orthopaedic Research* 21(1), pp. 139–148. doi: 10.1016/S0736-0266(02)00109-2.
- Matsunaga, Y.T. et al. 2011. Molding cell beads for rapid construction of macroscopic 3D tissue architecture. *Advanced Materials* 23(12), pp. 90–94. doi: 10.1002/adma.201004375.
- Mazlyzam, A.L. et al. 2007. Reconstruction of living bilayer human skin equivalent utilizing human fibrin as a scaffold. *Burns* 33(3), pp. 355–363. doi: 10.1016/j.burns.2006.08.022.
- Mazutis, L. et al. 2015. Microfluidic Production of Alginate Hydrogel Particles for Antibody Encapsulation and Release. *Macromolecular Bioscience* 15(12), pp. 1641–1646. doi: 10.1002/mabi.201500226.
- McGrath, J.A. and Uitto, J. 2010. Anatomy and Organization of Human Skin. In: *Rook's*

● REFERENCES ●

Textbook of Dermatology. Oxford, UK: Wiley-Blackwell, pp. 1–53. Available at: <http://doi.wiley.com/10.1002/9781444317633.ch3>.

Meier, F. et al. 2000. Human Melanoma Progression in Skin Reconstructs. *The American Journal of Pathology* 156(1), pp. 193–200. Available at: <https://linkinghub.elsevier.com/retrieve/pii/S0002944010647190>.

Menon, G.K. et al. 1985. Ionic calcium reservoirs in mammalian epidermis: Ultrastructural localization by ion-capture cytochemistry. *Journal of Investigative Dermatology* 84(6), pp. 508–512. doi: 10.1111/1523-1747.ep12273485.

Menon, G.K. 2002. New insights into skin structure: Scratching the surface. *Advanced Drug Delivery Reviews* 54(SUPPL.). doi: 10.1016/S0169-409X(02)00121-7.

Menon, G.K. and Elias, P.M. 1991. Ultrastructural Localization of Calcium in Psoriatic and Normal Human Epidermis. *Archives of Dermatology* 127(1), pp. 57–63. doi: 10.1001/archderm.1991.01680010067010.

Micallef, L. et al. 2008. Effects of extracellular calcium on the growth- differentiation switch in immortalized keratinocyte HaCaT cells compared with normal human keratinocytes., pp. 143–151. doi: 10.1111/j.1600-0625.2008.00775.x.

Michael, S. et al. 2013. Tissue Engineered Skin Substitutes Created by Laser-Assisted Bioprinting Form Skin-Like Structures in the Dorsal Skin Fold Chamber in Mice. *PLoS ONE* 8(3). doi: 10.1371/journal.pone.0057741.

Michel, M. et al. 1999. Characterization of a new tissue-engineered human skin equivalent with hair. *In Vitro Cellular and Developmental Biology - Animal* 35(6), pp. 318–326. doi: 10.1007/s11626-999-0081-x.

Mieremet, A. et al. 2017. Improved epidermal barrier formation in human skin models by Chitosan modulated dermal matrices. *PLoS ONE* . doi: 10.1371/journal.pone.0174478.

Min, D. et al. 2017. Bioprinting of biomimetic skin containing melanocytes. (April), pp. 1–7. doi: 10.1111/exd.13376.

Miri, A.K. et al. 2018. Microfluidics-Enabled Multimaterial Maskless Stereolithographic Bioprinting. *Advanced Materials* 30(27), p. 1800242. Available at: <http://doi.wiley.com/10.1002/adma.201800242>.

Miri, A.K. et al. 2019. Effective bioprinting resolution in tissue model fabrication. *Lab on a Chip* 19(11), pp. 2019–2037. doi: 10.1039/c8lc01037d.

Mironov, V. et al. 2009. Organ printing: Tissue spheroids as building blocks. *Biomaterials* 30(12), pp. 2164–2174. Available at: <http://dx.doi.org/10.1016/j.biomaterials.2008.12.084>.

Moll, R. et al. 1982. The catalog of human cytokeratins: Patterns of expression in normal

● REFERENCES ●

- epithelia, tumors and cultured cells. *Cell* 31(1), pp. 11–24. doi: 10.1016/0092-8674(82)90400-7.
- Moll, R. et al. 2008. The human keratins: Biology and pathology. *Histochemistry and Cell Biology* 129(6), pp. 705–733. doi: 10.1007/s00418-008-0435-6.
- Moon, S. et al. 2010. Layer by Layer Three-dimensional Tissue Epitaxy by Cell-Laden Hydrogel Droplets. *Tissue Engineering Part C: Methods* 16(1), pp. 157–166. Available at: <https://www.liebertpub.com/doi/10.1089/ten.tec.2009.0179>.
- Morgan, A.J.L. et al. 2016. Simple and Versatile 3D Printed Microfluidics Using Fused Filament Fabrication., pp. 1–17. doi: 10.1371/journal.pone.0152023.
- Morimoto, Y. et al. 2013. Construction of 3D, Layered Skin, Microsized Tissues by Using Cell Beads for Cellular Function Analysis. *Advanced Healthcare Materials* 2(2), pp. 261–265. doi: 10.1002/adhm.201200189.
- Moroni, L. et al. 2018. Biofabrication: A Guide to Technology and Terminology. *Trends in Biotechnology* 36(4), pp. 384–402. doi: 10.1016/j.tibtech.2017.10.015.
- Moser, R. et al. 2016. From playroom to lab: Tough stretchable electronics analyzed with a tabletop tensile tester made from toy-bricks. *Advanced Science* 3(4), pp. 1–9. doi: 10.1002/advs.201500396.
- Müller, I. and Kulms, D. 2018. A 3D organotypic melanoma spheroid skin model. *Journal of Visualized Experiments* 2018(135), pp. 1–9. doi: 10.3791/57500.
- Murphy, S. V and Atala, A. 2014. 3D bioprinting of tissues and organs. *Nature Publishing Group* 32(8), pp. 773–785. Available at: <http://dx.doi.org/10.1038/nbt.2958>.
- Ng, K.W. et al. 2009. Development of an ex vivo human skin model for intradermal vaccination: Tissue viability and Langerhans cell behaviour. *Vaccine* 27(43), pp. 5948–5955. doi: 10.1016/j.vaccine.2009.07.088.
- Ng, W.L. et al. 2016. Skin Bioprinting : Impending Reality or Fantasy ? *Trends in Biotechnology* 34(9), pp. 689–699. Available at: <http://dx.doi.org/10.1016/j.tibtech.2016.04.006>.
- Ng, W.L. et al. 2018. Proof-of-concept: 3D bioprinting of pigmented human skin constructs. *Biofabrication* 10(2). doi: 10.1088/1758-5090/aa9e1e.
- Ng, W.L. et al. 2019. Print Me An Organ! Why We Are Not There Yet. *Progress in Polymer Science* 97, p. 101145. Available at: <https://doi.org/10.1016/j.progpolymsci.2019.101145>.
- Nicholas, M.N. et al. 2016. Methodologies in creating skin substitutes. *Cellular and Molecular Life Sciences* 73(18), pp. 3453–3472. doi: 10.1007/s00018-016-2252-8.
- Nie, J. et al. 2018. 3D printed Lego® -like modular microfluidic devices based on capillary driving. *Biofabrication* 10(3). doi: 10.1088/1758-5090/aaadd3.

● REFERENCES ●

- Niehues, H. et al. 2018. 3D skin models for 3R research: The potential of 3D reconstructed skin models to study skin barrier function. *Experimental Dermatology* 27(5), pp. 501–511. doi: 10.1111/exd.13531.
- Niehues, H. and van den Bogaard, E.H. 2018. Past, present and future of in vitro 3D reconstructed inflammatory skin models to study psoriasis. *Experimental Dermatology* 27(5), pp. 512–519. doi: 10.1111/exd.13525.
- Niessen, C.M. 2007. Tight Junctions / Adherens Junctions : Basic Structure and Function. *Journal of Investigative Dermatology* 127(11), pp. 2525–2532. Available at: <http://dx.doi.org/10.1038/sj.jid.5700865>.
- O'Neill, A.T. et al. 2008. Characterization of microfluidic human epidermal keratinocyte culture. *Cytotechnology* 56(3), pp. 197–207. doi: 10.1007/s10616-008-9149-9.
- Okabe, S. et al. 2014. Acetic acid induces cell death: An in vitro study using normal rat gastric mucosal cell line and rat and human gastric cancer and mesothelioma cell lines. *Journal of Gastroenterology and Hepatology (Australia)* 29(S4), pp. 65–69. doi: 10.1111/jgh.12775.
- Okochi, M. et al. 2013. Cell behavior observation and gene expression analysis of melanoma associated with stromal fibroblasts in a three-dimensional magnetic cell culture array. *Biotechnology Progress* 29(1), pp. 135–142. Available at: <http://doi.wiley.com/10.1002/btpr.1642>.
- Okubo, N. et al. 2019. Cost-effective microvalve-assisted bioprinter for tissue engineering. *Bioprinting* 13(December 2018), p. e00043. Available at: <https://doi.org/10.1016/j.bprint.2019.e00043>.
- Ortseifen, V. et al. 2020. Microfluidics for Biotechnology: Bridging Gaps to Foster Microfluidic Applications. *Frontiers in Bioengineering and Biotechnology* 8(November), pp. 1–12. doi: 10.3389/fbioe.2020.589074.
- Ozbolat, I.T. and Hospodiuk, M. 2016. Current advances and future perspectives in extrusion-based bioprinting. *Biomaterials* 76, pp. 321–343. Available at: <http://dx.doi.org/10.1016/j.biomaterials.2015.10.076>.
- Pakhomova, C. et al. 2020. Software for bioprinting. *International Journal of Bioprinting* 6(3), pp. 41–61. doi: 10.18063/ijb.v6i3.279.
- Pampaloni, F. et al. 2007. The third dimension bridges the gap between cell culture and live tissue. *Nature Reviews Molecular Cell Biology* 8(10), pp. 839–845. Available at: www.nature.com/reviews/molcellbio.
- Parenteau, N.L. et al. 1992. The organotypic culture of human skin keratinocytes and fibroblasts to achieve form and function. *Cytotechnology* 9(1–3), pp. 163–171. doi: 10.1007/BF02521744.

● REFERENCES ●

- Pati, F. et al. 2014. Printing three-dimensional tissue analogues with decellularized extracellular matrix bioink. *Nature Communications* 5. doi: 10.1038/ncomms4935.
- Pedde, R.D. et al. 2017. Emerging Biofabrication Strategies for Engineering Complex Tissue Constructs. 1606061, pp. 1–27. doi: 10.1002/adma.201606061.
- Peng, W. et al. 2016. Bioprinting towards Physiologically Relevant Tissue Models for Pharmaceuticals. *Trends in Biotechnology* 34(9), pp. 722–732. Available at: <http://dx.doi.org/10.1016/j.tibtech.2016.05.013>.
- Pereira, F.D.A.S. et al. 2018. Commercial 3D Bioprinters. *3D Printing and Biofabrication* , pp. 535–549. doi: 10.1007/978-3-319-45444-3_12.
- Pit, A.M. et al. 2015. Droplet manipulations in two phase flow microfluidics. *Micromachines* 6(11), pp. 1768–1793. doi: 10.3390/mi6111455.
- Poncelet, D. 2006. Production of Alginate Beads by Emulsification/Internal Gelation. *Annals of the New York Academy of Sciences* 944(1), pp. 74–82. Available at: <http://doi.wiley.com/10.1111/j.1749-6632.2001.tb03824.x>.
- Pourchet, L.J. et al. 2017. Human Skin 3D Bioprinting Using Scaffold-Free Approach. *Advanced Healthcare Materials* 6(4), pp. 1–8. doi: 10.1002/adhm.201601101.
- Power, R.M. and Huisken, J. 2017. A guide to light-sheet fluorescence microscopy for multiscale imaging. *Nature Methods* 14(4), pp. 360–373. doi: 10.1038/nmeth.4224.
- Proksch, E. et al. 2008. The skin: An indispensable barrier. *Experimental Dermatology* 17(12), pp. 1063–1072. doi: 10.1111/j.1600-0625.2008.00786.x.
- Prunieras, M. et al. 1976. The culture of skin. A review of theories and experimental methods. *Journal of Investigative Dermatology* 67(1), pp. 58–65. doi: 10.1111/1523-1747.ep12512483.
- Pupovac, A. et al. 2018. Toward Immunocompetent 3D Skin Models. *Advanced Healthcare Materials* 7(12), pp. 1–11. doi: 10.1002/adhm.201701405.
- Ramadan, Q. and Ting, F.C.W. 2016. In vitro micro-physiological immune-competent model of the human skin. *Lab on a Chip* 16(10), pp. 1899–1908. doi: 10.1039/c6lc00229c.
- Ranamukhaarachchi, S.A. et al. 2016. A micromechanical comparison of human and porcine skin before and after preservation by freezing for medical device development. *Scientific Reports* 6(August), pp. 1–9. Available at: <http://dx.doi.org/10.1038/srep32074>.
- Randall, M.J. et al. 2018. Advances in the Biofabrication of 3D Skin in vitro: Healthy and Pathological Models. *Frontiers in Bioengineering and Biotechnology* 6(October). doi: 10.3389/fbioe.2018.00154.
- Régnier, M. et al. 1997. Integration of Langerhans cells into a pigmented reconstructed human epidermis. *Journal of Investigative Dermatology* 109(4), pp. 510–512. doi: 10.1111/1523-

● REFERENCES ●

1747.ep12336627.

Reid, J.A. et al. 2016. Accessible bioprinting : adaptation of a low-cost 3D-printer for precise cell placement and stem cell differentiation. *Biofabrication* 8(2). doi: 10.1088/1758-5090/8/2/025017.

Reid, J.A. et al. 2019. A 3D bioprinter platform for mechanistic analysis of tumoroids and chimeric mammary organoids. *Scientific Reports* 9(1), pp. 1–10. doi: 10.1038/s41598-019-43922-z.

Reijnders, C.M.A. et al. 2015. Development of a Full-Thickness Human Skin Equivalent in Vitro Model Derived from TERT-Immortalized Keratinocytes and Fibroblasts. *Tissue Engineering - Part A* 21(17–18), pp. 2448–2459. doi: 10.1089/ten.tea.2015.0139.

Reynaud, E.G. et al. 2008. Light sheet-based fluorescence microscopy: More dimensions, more photons, and less photodamage. *HFSP Journal* . doi: 10.2976/1.2974980.

Rheinwald, J.G. and Green, H. 1975. Serial cultivation of strains of human epidermal keratinocytes: the formation of keratinizing colonies from single cell. *Cell* 6(3), pp. 331–343. Available at: <https://linkinghub.elsevier.com/retrieve/pii/S0092867475800018>.

Rheinwald, J.G. and Green, H. 1977. Epidermal growth factor and the multiplication of cultured human epidermal keratinocytes. *Nature* 265(5593), pp. 421–424. doi: 10.1038/265421a0.

Rice, R.H. and Green, H. 1979. Presence in human epidermal cells of a soluble protein precursor of the cross-linked envelope: Activation of the cross-linking by calcium ions. *Cell* 18(3), pp. 681–694. doi: 10.1016/0092-8674(79)90123-5.

Richard, C. et al. 2020. The emerging role of microfluidics in multi-material 3D bioprinting. *Lab on a Chip* 20(12), pp. 2044–2056. doi: 10.1039/c9lc01184f.

Roehm, K.D. and Madhally, S. V. 2018. Bioprinted chitosan-gelatin thermosensitive hydrogels using an inexpensive 3D printer. *Biofabrication* 10(1). doi: 10.1088/1758-5090/aa96dd.

Roger, M. et al. 2019. Bioengineering the microanatomy of human skin. *Journal of Anatomy* 234(4), pp. 438–455. doi: 10.1111/joa.12942.

Rosbach, K. et al. 2016. Histamine H4 receptor knockout mice display reduced inflammation in a chronic model of atopic dermatitis. *Allergy* 71(2), pp. 189–197. Available at: <http://doi.wiley.com/10.1111/all.12779>.

Rossow, T. et al. 2012. Controlled synthesis of cell-laden microgels by radical-free gelation in droplet microfluidics. *Journal of the American Chemical Society* 134(10), pp. 4983–4989. doi: 10.1021/ja300460p.

● REFERENCES ●

- Rowley, J.A. et al. 1999. Alginate hydrogels as synthetic extracellular matrix materials. *Biomaterials* 20(1), pp. 45–53. doi: 10.1016/S0142-9612(98)00107-0.
- Ryan, A.J. et al. 2016. Towards 3D in vitro models for the study of cardiovascular tissues and disease. *Drug Discovery Today* 21(9), pp. 1437–1445. Available at: <http://dx.doi.org/10.1016/j.drudis.2016.04.014>.
- Sackmann, E.K. et al. 2014. The present and future role of microfluidics in biomedical research. *Nature* 507(7491), pp. 181–189. Available at: <http://dx.doi.org/10.1038/nature13118>.
- Sakaguchi, M. et al. 2003. S100C/A11 is a key mediator of Ca²⁺-induced growth inhibition of human epidermal keratinocytes. *Journal of Cell Biology* 163(4), pp. 825–835. doi: 10.1083/jcb.200304017.
- Sánchez-Muñoz, I. et al. 2015. The Use of Adipose Mesenchymal Stem Cells and Human Umbilical Vascular Endothelial Cells on a Fibrin Matrix for Endothelialized Skin Substitute. *Tissue Engineering Part A* 21(1–2), pp. 214–223. Available at: <https://www.liebertpub.com/doi/10.1089/ten.tea.2013.0626>.
- Sanz-Garcia, A. et al. 2020. A versatile open-source printhead for low-cost 3d microextrusion-based bioprinting. *Polymers* 12(10), pp. 1–18. doi: 10.3390/polym12102346.
- Sasmal, P. et al. 2018. 3D bioprinting for modelling vasculature. *Microphysiological Systems* 1, pp. 1–1. doi: 10.21037/mps.2018.10.02.
- Schimek, K. et al. 2018. Bioengineering of a Full-Thickness Skin Equivalent in a 96-Well Insert Format for Substance Permeation Studies and Organ-On-A-Chip Applications. *Bioengineering* 5(2), p. 43. Available at: <http://www.mdpi.com/2306-5354/5/2/43>.
- Schloßmacher, U. et al. 2013. Alginate/silica composite hydrogel as a potential morphogenetically active scaffold for three-dimensional tissue engineering. *RSC Advances* 3(28), pp. 11185–11194. doi: 10.1039/c3ra23341c.
- Schmieden, D.T. et al. 2018. Printing of Patterned, Engineered E. coli Biofilms with a Low-Cost 3D Printer. *ACS Synthetic Biology* 7(5), pp. 1328–1337. doi: 10.1021/acssynbio.7b00424.
- Schoop, V.M. et al. 1999. Epidermal organization and differentiation of HaCat keratinocytes in organotypic coculture with human dermal fibroblasts. *Journal of Investigative Dermatology* 112(3), pp. 343–353. Available at: <http://dx.doi.org/10.1046/j.1523-1747.1999.00524.x>.
- Schröder, H. et al. 2016. Transdermal drug targeting and functional imaging of tumor blood vessels in the mouse auricle. *FASEB Journal* 30(2), pp. 923–932. doi: 10.1096/fj.15-279240.
- Schumacher, M. et al. 2014. Efficient keratinocyte differentiation strictly depends on JNK-induced soluble factors in fibroblasts. *Journal of Investigative Dermatology* 134(5), pp. 1332–1341. Available at: <http://dx.doi.org/10.1038/jid.2013.535>.

● REFERENCES ●

- Sears, N.A. et al. 2016. A Review of Three-Dimensional Printing in Tissue Engineering. *Tissue Engineering Part B: Reviews* 22(4), pp. 298–310. doi: 10.1089/ten.teb.2015.0464.
- Seemann, R. et al. 2012. Droplet based microfluidics. *Reports on Progress in Physics* 75(1), p. 016601. Available at: <https://iopscience.iop.org/article/10.1088/0034-4885/75/1/016601>.
- Seo, E. et al. 2005. Analysis of calcium-inducible genes in keratinocytes using suppression subtractive hybridization and cDNA microarray. 86, pp. 528–538. doi: 10.1016/j.ygeno.2005.06.013.
- Seo, M. et al. 2012. HaCaT Keratinocytes and Primary Epidermal Keratinocytes Have Different Transcriptional Profiles of Cornified Envelope-Associated Genes to T Helper Cell Cytokines. *Biomolecules and Therapeutics* 20(2), pp. 171–176. Available at: <http://koreascience.or.kr/journal/view.jsp?kj=OOOMB4&py=2012&vnc=v20n2&sp=171>.
- Serex, L. et al. 2018. Microfluidics: A new layer of control for extrusion-based 3D printing. *Micromachines* 9(2). doi: 10.3390/mi9020086.
- Seth, D. et al. 2017. Global Burden of Skin Disease: Inequities and Innovations. *Current Dermatology Reports* 6(3), pp. 204–210. doi: 10.1007/s13671-017-0192-7.
- Shah, R.K. et al. 2008. Designer emulsions using microfluidics. *Materials Today* 11(4), pp. 18–27. Available at: [http://dx.doi.org/10.1016/S1369-7021\(08\)70053-1](http://dx.doi.org/10.1016/S1369-7021(08)70053-1).
- Sharma, R. et al. 2020. 3D Bioprinting Pluripotent Stem Cell Derived Neural Tissues Using a Novel Fibrin Bioink Containing Drug Releasing Microspheres. *Frontiers in Bioengineering and Biotechnology* 8(February), pp. 1–12. doi: 10.3389/fbioe.2020.00057.
- Shiple, G.D. et al. 1986. Reversible inhibition of normal human prokeratinocyte proliferation by type beta transforming growth factor-growth inhibitor in serum-free medium. *Cancer research* 46(4 Pt 2), pp. 2068–71. Available at: <http://www.ncbi.nlm.nih.gov/pubmed/2418960>.
- Shoichet, M.S. et al. 1996. Stability of hydrogels used in cell encapsulation: An in vitro comparison of alginate and agarose. *Biotechnology and Bioengineering* 50(4), pp. 374–381. Available at: [https://onlinelibrary.wiley.com/doi/10.1002/\(SICI\)1097-0290\(19960520\)50:4%3C374::AID-BIT4%3E3.0.CO;2-I](https://onlinelibrary.wiley.com/doi/10.1002/(SICI)1097-0290(19960520)50:4%3C374::AID-BIT4%3E3.0.CO;2-I).
- Sigaux, N. et al. 2019. 3D Bioprinting: principles, fantasies and prospects. *Journal of Stomatology, Oral and Maxillofacial Surgery* 120(2), pp. 128–132. Available at: <http://dx.doi.org/10.1016/j.jormas.2018.12.014>.
- Simpson, C.L. et al. 2011. Deconstructing the skin: Cytoarchitectural determinants of epidermal morphogenesis. *Nature Reviews Molecular Cell Biology* 12(9), pp. 565–580. doi: 10.1038/nrm3175.
- Singh, A. et al. 2015. Topically Applied Hsp90 Inhibitor 17AAG Inhibits UVR-Induced

● REFERENCES ●

- Cutaneous Squamous Cell Carcinomas. *Journal of Investigative Dermatology* 135(4), pp. 1098–1107. Available at: <https://linkinghub.elsevier.com/retrieve/pii/S0022202X15372067>.
- Skardal, A. and Atala, A. 2015. Biomaterials for Integration with 3-D Bioprinting. *Annals of Biomedical Engineering* 43(3), pp. 730–746. doi: 10.1007/s10439-014-1207-1.
- Smalley, K.S.M. et al. 2006. LIFE ISN'T FLAT: TAKING CANCER BIOLOGY TO THE NEXT DIMENSION. *In Vitro Cellular & Developmental Biology - Animal* 42(8), p. 242. Available at: <http://link.springer.com/10.1290/0604027.1>.
- Smith, W.D. et al. 2000. LabVIEW™ Facilitates Interdisciplinary Team Projects in Graduate Biomedical Engineering Courses. *International Journal of Engineering Education* 16(3), pp. 234–243.
- Smits, J.P.H. et al. 2017. Immortalized N/TERT keratinocytes as an alternative cell source in 3D human epidermal models. *Scientific Reports* 7(1), pp. 1–14. doi: 10.1038/s41598-017-12041-y.
- Snyder, J.E. et al. 2011. Bioprinting cell-laden matrigel for radioprotection study of liver by pro-drug conversion in a dual-tissue microfluidic chip. *Biofabrication* 3(3). doi: 10.1088/1758-5082/3/3/034112.
- Sobral, C.S. et al. 2007. Human keratinocytes cultured on collagen matrix used as an experimental burn model. *Journal of burns and wounds* 7(June 2014), p. e6. Available at: <http://www.ncbi.nlm.nih.gov/pubmed/18091983%0Ahttp://www.pubmedcentral.nih.gov/articlerender.fcgi?artid=PMC2064970>.
- Sohrabi, S. et al. 2020. Droplet microfluidics: Fundamentals and its advanced applications. *RSC Advances* 10(46), pp. 27560–27574. doi: 10.1039/d0ra04566g.
- Sorrell, J.M. et al. 2004. Site-matched papillary and reticular human dermal fibroblasts differ in their release of specific growth factors/cytokines and in their interaction with keratinocytes. *Journal of Cellular Physiology* 200(1), pp. 134–145. Available at: <https://onlinelibrary.wiley.com/doi/10.1002/jcp.10474>.
- Sriram, G. et al. 2015. European Journal of Cell Biology Fibroblast heterogeneity and its implications for engineering organotypic skin models in vitro. *European Journal of Cell Biology* 94(11), pp. 483–512. Available at: <http://dx.doi.org/10.1016/j.ejcb.2015.08.001>.
- Stone, H.A. et al. 2004. Engineering flows in small devices: Microfluidics toward a lab-on-a-chip. *Annual Review of Fluid Mechanics* 36(March), pp. 381–411. doi: 10.1146/annurev.fluid.36.050802.122124.
- Ströbel, S. et al. 2016. Characterization of a novel in vitro 3D skin microtissue model for efficacy and toxicity testing. *Toxicology Letters* 258, pp. S156–S157. Available at: <https://linkinghub.elsevier.com/retrieve/pii/S0378427416317453>.

● REFERENCES ●

- Su, M.J. et al. 1994. 1,25-Dihydroxyvitamin D₃ potentiates the keratinocyte response to calcium. *The Journal of biological chemistry* 269(20), pp. 14723–9. Available at: <http://www.ncbi.nlm.nih.gov/pubmed/7910167>.
- Suea-Ngam, A. et al. 2019. Droplet microfluidics: From proof-of-concept to real-world utility? *Chemical Communications* 55(67), pp. 9895–9903. doi: 10.1039/c9cc04750f.
- Sugihara, H. et al. 1991. Reconstruction of the skin in three-dimensional collagen gel matrix culture. *In Vitro Cellular & Developmental Biology - Animal* 27(2), pp. 142–146. doi: 10.1007/BF02631000.
- Sugiura, S. et al. 2005. Size control of calcium alginate beads containing living cells using micro-nozzle array. *Biomaterials* 26(16), pp. 3327–3331. doi: 10.1016/j.biomaterials.2004.08.029.
- Sullivan, M.T. and Stone, H.A. 2008. The role of feedback in microfluidic flow-focusing devices. *Philosophical Transactions of the Royal Society A: Mathematical, Physical and Engineering Sciences* 366(1873), pp. 2131–2143. doi: 10.1098/rsta.2008.0003.
- Sun, J. and Tan, H. 2013. Alginate-based biomaterials for regenerative medicine applications. *Materials* 6(4), pp. 1285–1309. doi: 10.3390/ma6041285.
- Sun, Q. et al. 2017. Ex vivo construction of human primary 3D-networked osteocytes. *Bone* . doi: 10.1016/j.bone.2017.09.012.
- Sun, T. et al. 2006. Culture of skin cells in 3D rather than 2D improves their ability to survive exposure to cytotoxic agents. 122, pp. 372–381. doi: 10.1016/j.jbiotec.2005.12.021.
- Sütterlin, T. et al. 2017. A 3D self-organizing multicellular epidermis model of barrier formation and hydration with realistic cell morphology based on EPISIM. *Scientific Reports* 7(March), pp. 1–11. doi: 10.1038/srep43472.
- Suvarnapathaki, S. et al. 2018. Generation of cell-laden hydrogel microspheres using 3D printing-enabled microfluidics. *Journal of Materials Research* 33(14), pp. 2012–2018. doi: 10.1557/jmr.2018.77.
- Szabo, I. et al. 2004. Plasmin promotes keratinocyte migration and phagocytic-killing accompanied by suppression of cell proliferation which may facilitate re-epithelialization of wound beds. *Clinical and Developmental Immunology* 11(3–4), pp. 233–240. doi: 10.1080/17402520400001710.
- Szymański, Ł. et al. 2020. A simple method for the production of human skin equivalent in 3D, multi-cell culture. *International Journal of Molecular Sciences* 21(13), pp. 1–11. doi: 10.3390/ijms21134644.
- Takayama, S. et al. 1999. Patterning cells and their environments using multiple laminar fluid flows in capillary networks. *Proceedings of the National Academy of Sciences* 96(10), pp.

● REFERENCES ●

- 5545–5548. Available at: <http://www.pnas.org/cgi/doi/10.1073/pnas.96.10.5545>.
- Tan, W.H. and Takeuchi, S. 2007. Monodisperse alginate hydrogel microbeads for cell encapsulation. *Advanced Materials* 19(18), pp. 2696–2701. doi: 10.1002/adma.200700433.
- Tarassoli, S.P. et al. 2018. Skin tissue engineering using 3D bioprinting: An evolving research field. *Journal of Plastic, Reconstructive and Aesthetic Surgery* 71(5), pp. 615–623. Available at: <https://doi.org/10.1016/j.bjps.2017.12.006>.
- Tice, J.D. et al. 2003. Formation of Droplets and Mixing in Multiphase Microfluidics at Low Values of the Reynolds and the Capillary Numbers. *Langmuir* 19(22), pp. 9127–9133. doi: 10.1021/la030090w.
- Tobin, D.J. 2006. Biochemistry of human skin—our brain on the outside. *Chem. Soc. Rev.* 35(1), pp. 52–67. Available at: <http://xlink.rsc.org/?DOI=B505793K>.
- Tu, C.L. et al. 2008. Inactivation of the calcium sensing receptor inhibits E-cadherin-mediated cell-cell adhesion and calcium-induced differentiation in human epidermal keratinocytes. *Journal of Biological Chemistry* 283(6), pp. 3519–3528. doi: 10.1074/jbc.M708318200.
- Tu, C.L. and Bikle, D.D. 2013. Role of the calcium-sensing receptor in calcium regulation of epidermal differentiation and function. *Best Practice and Research: Clinical Endocrinology and Metabolism* 27(3), pp. 415–427. Available at: <http://dx.doi.org/10.1016/j.beem.2013.03.002>.
- Ura, H. et al. 2004. An in vitro outgrowth culture system for normal human keratinocytes. *Journal of Dermatological Science* 35(1), pp. 19–28. doi: 10.1016/j.jdermsci.2004.03.005.
- Utech, S. et al. 2015. Microfluidic Generation of Monodisperse, Structurally Homogeneous Alginate Microgels for Cell Encapsulation and 3D Cell Culture. *Advanced Healthcare Materials* 4(11), pp. 1628–1633. doi: 10.1002/adhm.201500021.
- Valyi-Nagy, I.T. et al. 1993. Undifferentiated keratinocytes control growth, morphology, and antigen expression of normal melanocytes through cell-cell contact. *Laboratory investigation; a journal of technical methods and pathology* 69(2), pp. 152–9. Available at: <http://www.ncbi.nlm.nih.gov/pubmed/8350597>.
- Vardar, E. et al. 2018. Microfluidic production of bioactive fibrin micro-beads embedded in crosslinked collagen used as an injectable bulking agent for urinary incontinence treatment. *Acta Biomaterialia* 67, pp. 156–166. Available at: <https://doi.org/10.1016/j.actbio.2017.11.034>.
- Vaughan, M.B. et al. 2009. H-Ras expression in immortalized keratinocytes produces an invasive epithelium in cultured skin equivalents. *PLoS ONE* 4(11). doi: 10.1371/journal.pone.0007908.
- Velasco, D. et al. 2012. Microfluidic Encapsulation of Cells in Polymer Microgels. *Small* 8(11), pp. 1633–1642. Available at: <http://doi.wiley.com/10.1002/smll.201102464>.

● REFERENCES ●

- Velasco, D. et al. 2018. 3D human skin bioprinting: a view from the bio side. *Journal of 3D Printing in Medicine* 2(3), pp. 141–162. Available at: <https://www.futuremedicine.com/doi/10.2217/3dp-2018-0008>.
- Vertrees, R.A. et al. 2009. Tissue Culture Models., pp. 159–182. Available at: http://link.springer.com/10.1007/978-0-387-89626-7_18.
- Vidal Yucha, S.E. et al. 2019. Human Skin Equivalent Demonstrates Need for Neuro-Immuno-Cutaneous System. *Advanced Biosystems* 3(1), pp. 1–16. doi: 10.1002/adbi.201800283.
- Visser, J. et al. 2013. Biofabrication of multi-material anatomically shaped tissue constructs. *Biofabrication* 5(3). doi: 10.1088/1758-5082/5/3/035007.
- Vörsmann, H. et al. 2013. Development of a human three-dimensional organotypic skin-melanoma spheroid model for in vitro drug testing. *Cell Death and Disease* 4(7). doi: 10.1038/cddis.2013.249.
- Wagner, E.F. et al. 2010. Psoriasis: what we have learned from mouse models. *Nature Reviews Rheumatology* 6(12), pp. 704–714. Available at: <http://www.nature.com/articles/nrrheum.2010.157>.
- Wang, J.X. et al. 2016. Crosstalk in skin: melanocytes, keratinocytes, stem cells, and melanoma. *Journal of Cell Communication and Signaling* 10(3), pp. 191–196. Available at: <http://dx.doi.org/10.1007/s12079-016-0349-3>.
- Wang, K. et al. 2011. Generation of micromonodispersed droplets and bubbles in the capillary embedded T-junction microfluidic devices. *AIChE Journal* 57(2), pp. 299–306. Available at: <http://doi.wiley.com/10.1002/aic.12263>.
- Wang, Z. et al. 2012. Enhanced Keratinocyte Proliferation and Migration in Co-culture with Fibroblasts. 7(7), pp. 1–12. doi: 10.1371/journal.pone.0040951.
- Ward, T. et al. 2005. Microfluidic flow focusing: Drop size and scaling in pressure versus flow-rate-driven pumping. *Electrophoresis* 26(19), pp. 3716–3724. doi: 10.1002/elps.200500173.
- Warhol, M.J. et al. 1985. Immuno-ultrastructural localization of involucrin in squamous epithelium and cultured keratinocytes. *Journal of Histochemistry and Cytochemistry* 33(2), pp. 141–149. doi: 10.1177/33.2.2578499.
- Watt, F.M. et al. 1984. Calcium-induced reorganization of desmosomal components in cultured human keratinocytes. *Journal of Cell Biology* 99(6), pp. 2211–2215. doi: 10.1083/jcb.99.6.2211.
- Werner, S. et al. 2007. Keratinocyte-fibroblast interactions in wound healing. *Journal of Investigative Dermatology* 127(5), pp. 998–1008. Available at: <http://dx.doi.org/10.1038/sj.jid.5700786>.

● REFERENCES ●

- Wilson, A.F.D.Æ.V.G. et al. 2007. In vitro culture conditions to study keratinocyte differentiation using the HaCaT cell line. *Cytotechnology* 54(2), pp. 77–83. doi: 10.1007/s10616-007-9076-1.
- Włodarczyk-Biegun, M.K. and del Campo, A. 2017. 3D bioprinting of structural proteins. *Biomaterials* 134, pp. 180–201. doi: 10.1016/j.biomaterials.2017.04.019.
- Woelfle, U. et al. 2010. Triterpenes Promote Keratinocyte Differentiation In Vitro, Ex Vivo and In Vivo: A Role for the Transient Receptor Potential Canonical (subtype) 6. *Journal of Investigative Dermatology* 130(1), pp. 113–123. Available at: <https://linkinghub.elsevier.com/retrieve/pii/S0022202X15345310>.
- Wojtowicz, A.M. et al. 2014. The importance of both fibroblasts and keratinocytes in a bilayered living cellular construct used in wound healing. doi: 10.1111/wrr.12154.
- Wong, C.W. et al. 2019. In Vitro Expansion of Keratinocytes on Human Dermal Fibroblast-Derived Matrix Retains Their Stem-Like Characteristics. *Scientific Reports* 9(1). doi: 10.1038/s41598-019-54793-9.
- Woodcock-Mitchell, J. et al. 1982. Immunolocalization of keratin polypeptides in human epidermis using monoclonal antibodies. *Journal of Cell Biology* 95(2), pp. 580–588. doi: 10.1083/jcb.95.2.580.
- Wu, C. et al. 2010. Bioactive inorganic-materials/alginate composite microspheres with controllable drug-delivery ability. *Journal of Biomedical Materials Research - Part B Applied Biomaterials* 94(1), pp. 32–43. doi: 10.1002/jbm.b.31621.
- Wu, Q. et al. 2020. Organ-on-a-chip: recent breakthroughs and future prospects. *BioMedical Engineering OnLine* 19(1), p. 9. Available at: <https://biomedical-engineering-online.biomedcentral.com/articles/10.1186/s12938-020-0752-0>.
- Wu, Z. et al. 2016. Bioprinting three-dimensional cell-laden tissue constructs with controllable degradation. *Nature Publishing Group* (April), pp. 1–10. Available at: <http://dx.doi.org/10.1038/srep24474>.
- Wysocki, A.B. 1999. Skin anatomy, physiology, and pathophysiology. *The Nursing clinics of North America* 34(4), pp. 777–97, v. Available at: <http://www.ncbi.nlm.nih.gov/pubmed/10523436>.
- Xia, Z. et al. 2018. Tissue and Organ 3D Bioprinting. *SLAS Technology* 23(4), pp. 301–314. doi: 10.1177/2472630318760515.
- Xie, Y. et al. 2010. Development of a three-dimensional human skin equivalent wound model for investigating novel wound healing therapies. *Tissue Eng Part C Methods* 16(5), pp. 1111–1123. doi: 10.1089/ten.TEC.2009.0725.
- Xie, Z. and Bikle, D.D. 2007. The recruitment of phosphatidylinositol 3-kinase to the E-

● REFERENCES ●

- cadherin-catenin complex at the plasma membrane is required for calcium-induced phospholipase C- γ 1 activation and human keratinocyte differentiation. *Journal of Biological Chemistry* 282(12), pp. 8695–8703. doi: 10.1074/jbc.M609135200.
- Xu, C. et al. 2012. Scaffold-free inkjet printing of three-dimensional zigzag cellular tubes. *Biotechnology and Bioengineering* 109(12), pp. 3152–3160. doi: 10.1002/bit.24591.
- Xu, F. et al. 2010. A droplet-based building block approach for bladder smooth muscle cell (SMC) proliferation. *Biofabrication* 2(1). doi: 10.1088/1758-5082/2/1/014105.
- Xu, S. et al. 2005. Generation of monodisperse particles by using microfluidics: Control over size, shape, and composition. *Angewandte Chemie - International Edition* . doi: 10.1002/anie.200462226.
- Yan, W.C. et al. 2018. 3D bioprinting of skin tissue: From pre-processing to final product evaluation. *Advanced Drug Delivery Reviews* 132, pp. 270–295. Available at: <https://doi.org/10.1016/j.addr.2018.07.016>.
- Yang, X. et al. 2018. Collagen-alginate as bioink for three-dimensional (3D) cell printing based cartilage tissue engineering. *Materials Science & Engineering C* 83(September 2017), pp. 195–201. Available at: <https://doi.org/10.1016/j.msec.2017.09.002>.
- Yang, Y. et al. 2015. Development and validation of in vitro-in vivo correlation (IVIVC) for estradiol transdermal drug delivery systems. *Journal of Controlled Release* 210, pp. 58–66. Available at: <http://dx.doi.org/10.1016/j.jconrel.2015.05.263>.
- Yu, J. et al. 2010. The use of human mesenchymal stem cells encapsulated in RGD modified alginate microspheres in the repair of myocardial infarction in the rat. *Biomaterials* 31(27), pp. 7012–7020. Available at: <http://dx.doi.org/10.1016/j.biomaterials.2010.05.078>.
- Yuspa, S.H. et al. 1989. Expression of murine epidermal differentiation markers is tightly regulated by restricted extracellular calcium concentrations in vitro. *Journal of Cell Biology* 109(3), pp. 1207–1217. doi: 10.1083/jcb.109.3.1207.
- Zhang, C. et al. 2020. Preparation of alginate hydrogel microparticles using droplet-based microfluidics: a review of methods. *arXiv* , pp. 1–29. Available at: <http://arxiv.org/abs/2009.06898>.
- Zhang, H. et al. 2007. Exploring Microfluidic Routes to Microgels of Biological Polymers. *Macromolecular Rapid Communications* 28(5), pp. 527–538. Available at: <http://doi.wiley.com/10.1002/marc.200600776>.
- Zhang, Y.S. et al. 2017. 3D Bioprinting for Tissue and Organ Fabrication. *Annals of Biomedical Engineering* 45(1), pp. 148–163. doi: 10.1007/s10439-016-1612-8.
- Zhang, Z. and Michniak-Kohn, B.B. 2012. Tissue engineered human skin equivalents. *Pharmaceutics* 4(1), pp. 26–41. doi: 10.3390/pharmaceutics4010026.